AFOSR-TR. 85-1026

mechanical and aerospace engineering

mechanical engineering, aerospace engineering, energy systems engineering, engineering science, materials science

INVESTIGATION OF MATERIAL PROBLEMS FOR HIGH TEMPERATURE, HIGH POWER SPACE ENERGY-CONVERSION SYSTEMS

(Second Annual Progress Report)

GRANT AFOSR-83-0067

For the period
5/01/84 to 4/30/85

DTIC
ELECTE
DEC 10 1985
A

Contributors:

Dean L. Jacobson, James F. Morris, Mysore Ramalingam,
Shlomo Snir, Charles Bice, Derek Tang, Kurt Von Braun, Joe Vittengel

ATTENTION:

Major Joseph W. Hager
Program Manager
Electronic and Material Sciences

College of Engineering & Applied Sciences
Arizona State University
Tempe, Arizona 85287

85 12 6 120   CR-R 85014

AD-A162 227

REPORT DOCUMENTATION PAGE	READ INSTRUCTIONS BEFORE COMPLETING FORM

1. REPORT NUMBER	2. GOVT ACCESSION NO.	3. RECIPIENT'S CATALOG NUMBER
AFOSR·TR· 85-1026	AD-A161 119	

4. TITLE (and Subtitle)	5. TYPE OF REPORT & PERIOD COVERED
Investigation of Material Problems for High-Temperature High-Power Space Energy-Conversion Systems	Second Annual Report May 24 - April 85
	6. PERFORMING ORG. REPORT NUMBER
	CR-R-85014

7. AUTHOR(s)	8. CONTRACT OR GRANT NUMBER(s)
D.L. Jacobson, James F. Morris, Mysore Ramalingam, Shlomo Snir, Charles Bice, Derek Tang, Kurt von Braun, Joe Vittengel	AFOSR-83-0067

9. PERFORMING ORGANIZATION NAME AND ADDRESS	10. PROGRAM ELEMENT, PROJECT, TASK AREA & WORK UNIT NUMBERS
Mechanical and Aerospace Engineering Arizona State University	61102F 2306/A2

11. CONTROLLING OFFICE NAME AND ADDRESS	12. REPORT DATE
Air Force Office of Scientific Research AFOSR/NE - Bolling Air Force Base, DC	May 1985
	13. NUMBER OF PAGES

14. MONITORING AGENCY NAME & ADDRESS(if different from Controlling Office)	15. SECURITY CLASS. (of this report)
Building 410 Bolling AFB Washington, DC. 20332-6448	Unclassified
	15a. DECLASSIFICATION/DOWNGRADING SCHEDULE

16. DISTRIBUTION STATEMENT (of this Report)

Approved for public release;
distribution unlimited.

DTIC
ELECTE
DEC 10 1985
A

17. DISTRIBUTION STATEMENT (of the abstract entered in Block 20, if different from Report)

Approved for public release;
distribution unlimited.

18. SUPPLEMENTARY NOTES

19. KEY WORDS (Continue on reverse side if necessary and identify by block number)

20. ABSTRACT (Continue on reverse side if necessary and identify by block number)

This is the annual report for grant AFOSR 83-0067. The period covered is May 10, 1984 to April 30, 1985. The contents detail work done on the investigation of material problems for high-temperature, high-power space energy conversion systems. The specific areas of research include investigations of methods of decreasing creep at the high temperatures encountered

DD FORM 1473 EDITION OF 1 NOV 65 IS OBSOLETE
S/N 0102-014-6601

in the space environment; investigations for improving the properties of refractory metals, tungsten in particular, by alloy additions of rhenium, thoria and hafnium carbide; ~~the~~ > and development of emissivity data for materials of interest at elevated temperatures.

In general the baseline system of tungsten, rhenium alloys is being researched to improve recrystallization characteristics, creep resistance ~~and other important~~ > etc. ~~properties.~~ Impurity distributions and their deleterious phenomena are studied. Micro-alloying with thorium and hafnium is being evaluated because of their obvious influences on recrystallization; impurity segregation and embrittlement; solution, precipitation and dispersion strengthening; as well as other effects of their intensive gettering capabilities. The alloys

The alloys being studied are sintered and swaged into rods and wires for various high-temperature mechanical and electronic testing. ~~Among the testing devices are a~~ include: a high-temperature thermionic-emission microscope; a specially designed high-temperature vacuum tensile-testing machine; a specially designed and built zone refiner for ~~some~~ possible refining conventional metallographic procedures; SEM, TEM and Auger surface analyses. A specialized quadrupole mass spectrometer is being instrumented for determination of high-temperature vaporization and thermionic characteristics of the alloys.

During the past year the analytical equipment has been developed and testing begun on the alloys. Research studies on critical areas such as creep have continued.

Annual Report on

Investigation of Material Problems for High-Temperature,
High-Power Space Energy Conversion Systems

Grant AFOSR-83-0067

for the Period
5/01/84 to 4/30/85

for

Air Force Office of Scientific Research
AFOSR/NE Bld. 410
Bolling AFB
Washington, D.C. 20332

Attn.:
Major Joseph W. Hagar
Program Manager
Electronic and Material Sciences

TABLE OF CONTENTS

LIST OF FIGURES

LIST OF TABLES

I. INTRODUCTION

This is the annual report for grant AFOSR 83-0067. The period covered is May 10, 1984 to April 30, 1985. The contents detail work done on the investigatin of material problems for high-temperature, high-power space energy conversin systems. The specific areas of research include investigations of methods of decreasing creep at the high temperatures encountered in the space environment; investigations for improving the properties of refractory metals, tungsten in in particular by alloy additons of rhenium, thoria and hafnium carbide; the development of emissivity data for materials of interest at elevated temperatures.

In general the baseline system of tungsten, rhenium alloys is being researched to improve recrystallization characteristics, creep resistance and other important properties. Impurity distribution and their deleterious phenomena are studied. Thorium and hafnium are being evaluated because of their obvious influences on recrystallization, impurity segregatin and embrittlement, solution, dispersion strengthening and gettering capabilities.

The alloys being studied are sintered and swaged into rods and wires for various high temperature mechanical and electronic testing. Among the testing devices are a high temperature thermionic emission microscope, a specially designed high-temperature vacuum tensile testing machine, a specially designed and built zone refiner for some possible refining, conventional metallographic procedures, SEM, TEM, and Auger surface analyses. A specialized quadrupole mass spectrometer is bein ginstrumented for determnation of high temperature vaporization and thermodynamic characteristics of the alloys.

During the past year, the anayltical equipment has been developed and testing begun on the alloys. Research studies on critical areas such as creep have continued.

Contributers to the reported work include; Jim Morris, Mysore Ramalingam, Charles Bice, Shlomo Snir, Derek Tang, Kurt von Braun, Joe Vittengel, and Dean Jacobson.

II. DECREASED CREEP FOR INCREASED SPACE POWER

2.1 ABSTRACT

The Air Force Office of Scientific Research reaffirmed in its 1982 Conference on Prime Power for High-Energy Space Systems "that materials would be a critical requirement for progress toward high power in space." Correspondingly high spacecraft weights, particularly for greater waste-heat rejection, force operating temperatures upward and emphasize the necessity of decreased creep for increased space power. In fact alloys capable of nearly ultimate metal performance will soon be essential. In this spirit the following paper examines recent developments in the understanding and description of mechanisms contributing to or detracting from creep. A discussion of various creep categories and related processes ensues. Then methods of counteracting creep receive some attention. And a specific approach to decreased creep in high-temperature, low-vapor-pressure space ultralloys terminates the presentation with predictions of improved ductility, increased recrystallization resistance and simplified processing.

2.2 REQUIRED MATERIAL IMPROVEMENTS FOR FUTURE SPACE POWER

The Proceedings of the AFOSR Special Conference on Prime Power for High-Energy Space Systems states prefatorially [2.1], "it was readily anticipated prior to the conference that materials would be a critical requirement for progress toward high power in space." And in fact 15 presentations swelled the "Materials" session of that 1982 conference. Most of those emphasized resistance to high temperatures and irradiation.

Previously the materials-workshop chairman for a NASA-convened conference on Future Orbital Power Systems Technology Requirements had also stressed thermal performance [2.2]: "If there is a single general trend that applies to the various combinations of heat sources and conversion methods, it is the one toward higher source temperature and higher sink temperature--and consequently lighter weight systems. For this reason the workshop felt that high-temperature-materials data was of prime importance...."

In addition to enabling greater power generation ultimate materials offer higher probabilities of withstanding high-power reception. Increased short-term toleration of burn-through, thermal-shock and/or radiation effects from extremely high-power-density electromagnetic and particle beams could be crucially advantageous. Because technologies for beam generation lead those for concentration, collimation and control considerably, partial and secondary beam exposures are definite possibilities. And in such situations ultimate material capabilities could mean survival.

More generally, in the long-range view of material-technology growth, movement toward the ultimate is inevitable, motivational and of course immediately desirable: Just as superalloys allowed terrestrial engineers greater freedom, ultralloys will enable space engineers to reach new orbits

of creative thought. Just as prototypic tungsten, rhenium (W,Re) alloys evolved from the pre-1973 space-nuclear-reactor (SNR) program, improved versions of these ultralloys will contribute to multimegawatt SNR capabilities in the future [2.3 to 2.35]. And the superior thermophysicochemical characteristics of such alloys will open previously inaccessible areas of mission and spacecraft innovation.

Particularly necessary space-power capabilities derive from high-temperature resistance to creep and recrystallization [2.31 to 2.35]. And fortunately techniques that inhibit creep and recrystallization often improve ductility—the lack of which erects a major barrier to W,Re ultralloy applications. So more ductile alloys that resist high-temperature creep and recrystallization are metallic combinations that can unlock design doors to space-power expansion.

2.3 SOME HIGH-TEMPERATURE-MATERIALS CREEP BACKGROUND

Perhaps the preceding section implies that research on high-temperature creep and recrystallization spun off from the space program. Such an inference is of course erroneous. True, Sherby in his 1962 paper, "Factors Affecting the High-Temperature Strength of Polycrystalline Materials," credits "the Aeronautical Research Laboratories, Wright-Patterson Air Force Base, Ohio, for support of a program on a study of the elastic properties of materials at elevated temperatures and on the role of elastic properties in the high temperature creep strength" [2.36]. But in his description of "high temperature deformation...characterized by (a) breakdown of the grains into subgrains, (b) grain boundary shearing and grain boundary migration and (c) fine slip difficult to resolve under ordinary microscopic techniques" Sherby cites much work beginning in the 1930's and one 1917 publication. In particular he refers to a 1938 paper wherein "Kanter...developed a creep law which was truly remarkable in that he suggested the importance of both diffusion and elastic properties on creep...." Diffusional creep effects received considerable attention from Sherby in this and his 1968 contribution to Progress in Materials Science, Volume 13 (Incorporating Progress in Metal Physics) [2.37,2.169 references].

Lattice diffusion quite naturally appeared to be the simple basis for diffusional creep initially. Nabarro proposed this mechanism in 1948 [2.38], and two years later Herring provided the appropriate detailed analysis for "Nabarro, Herring creep" [2.39]. For steady states at suitable conditions to render lattice diffusion rate-determining the Nabarro, Herring theory predicts creep admirably.

But under other conditions this theoretic model underestimates creep rates greatly. Recognizing this deficiency Coble suggested in 1963 that

accelerated diffusion along grain boundaries can accommodate polycrystalline deformation [2.40,2.41]. And of course in regions where neither grain-boundary nor lattice diffusion exhibits negligible effects on creep the Coble and Nabarro, Herring expressions combine effectively to describe their compounded contributions. However these mechanisms fail to apply when grain sizes grow excessively large which occurs for example in operations near melting points. Then with similarly low stresses lattice diffusion controls creep according to the Harper, Dorn theory [2.42].

At the other extreme creep apparently proceeds intragranularly and increases exponentially with high stress values (note the end of "High-Stress Creep"). The exponential stress dependence persists through many orders of magnitude in creep rate [2.43]. This enigmatic regime continues to provoke speculative examination [2.44 to 2.47]. But for obvious reasons the lower creep ranges are more important practically and therefore receive greater attention. Under high as well as low stresses pure metals and their solid solutions undergo seemingly similar deformation processes.

Between the high and low creep regions pure metals react to deformation through a recovery process such as dislocation climb [2.48,2.49]. Here the required vacancy diffusion proceeds through the lattice or more rapidly through dislocation cores, the latter often termed "pipe diffusion." However for solid solutions Weertman theorized that accommodation occurs with dislocation glide with a lower-power stress dependency than that for pure metals [2.37,2.50]. Now lattice-solute-diffusion as well as pipe-diffusion coefficients become considerations--although applicability of the latter is not experimentally verified [2.47]. Some solid solutions undergo transitions from dislocation climb at lower stresses to viscous glide at higher stresses and then back to climb near the top of the intermediate

creep range [2.51]. High-temperature-climb inhibition by stacking faults from dislocation splitting appears to impede creep in face-centered-cubic (FCC) and hexagonal-close-packed (HCP) metals compared with body-centered-cubic (BCC) structures (where dislocations "are in general not believed to be extended"). But although stacking-fault energy is important, apparently another reason for reduced FCC and HCP creep lies in lower atomic-diffusion rates: Impeded transport occurs in the closely packed crystals and their widely extended or severely distorted dislocations [2.37,2.52].

Whether diffusionally accommodated or not, grain-boundary sliding is a dominant deformation mode in high-temperature creep [2.53 to 2.57]. Important variables in this process in addition to the basic material chemistry, grain size and morphology, temperature and stress are additive and impurity chemistry, grain-boundary segregation and intergranular particle size and distribution. Grain-boundary-sliding effects are of prime importance in the nucleation, growth, aggregation, load shedding, integration and macrocrack generation of intergranular cavities. And of course this cavitation train travels a direct track to the final fracture. So intergranular cavity nucleation and growth are significant advanced stages of high-temperature creep that depend on plastic flow and diffusion.

2.4 DIFFUSION EFFECTS IN HIGH-TEMPERATURE CREEP

Creep in a particular material depends directly on the diffusion mechanism that predominates under prevailing thermal, mechanical and morphological conditions:

$$\dot{\varepsilon} = Cf(T,\sigma,d)D \qquad\qquad [2.1]$$

Here the steady-state strain rate $\dot{\varepsilon}$ equals the product of a morphochemophysical constant C and a function of absolute temperature T,

applied stress σ and grain size d as well as the pertinent diffusion coefficient D = D_o exp(-Q/RT) involving frequency factor D_o, activation energy Q and the gas constant R.

The diffusion assignation to this point appears rather -- diffuse. But the lack of definition derives from the gamut of diffusion processes available in a simple metal. Over ten years ago Gjostein presented an experimentally verified diffusion-coefficient order for FCC metals [2.58]: Exemplary values at half the absolute melting temperature ($0.5T_m$) for the logarithm of the diffusion coefficient (m^2/sec) are approximately -19 for FCC lattices, -14.7 for FCC dissociated dislocations, -12.2 for FCC grain boundaries as well as for undissociated dislocations and -11.4 for FCC surfaces. The Gjostein inverted-homologous-temperature correlations average diffusion-coefficient data for a wide variety of metals, surfaces and large-angle grain boundaries. Here "undissociated" refers to results for edge-dislocation entities on small-angle tilt boundaries without partial dislocations as well as stacking-fault ribbons which characterize the term "dissociated" [2.59].

Thus for temperatures considerably below T_m diffusion coefficients for surfaces, grain boundaries, undissociated then dissociated dislocations and finally lattices, respectively, satisfy the following expression.

$$D_s > D_b = D_{d,u} > D_{d,d} > D_\ell \qquad [2]$$

Although this general order derives from FCC results it probably represents other crystal structures generically. In fact the $0.5T_m$ value for the BCC log D_b is about -13.4. However the apparent lack of stacking faults in BCC dislocations presumably precludes $D_{d,d}$ leaving only $D_{d,u}$ or just D_d to

symbolize dislocation-core or pipe diffusion D_p. For solid solutions interdiffusion of solute atoms also requires an appropriate diffusivity D_i. So equation [1] invites the assignment of the dominant diffusion coefficient or coefficients with subsequent utilization of the pertinent preceding subscripts such as $D_\ell = D_{\ell o} \exp(-Q_\ell/RT)$ for lattice or intragranular transport.

D_ℓ often appears as D_v denoting "volume diffusion" and rationally connoting vacancy diffusion: Migrations by vacancies (Schottky defects), interstitialcies (Frenkel defects) and position exchange offer possibilities for self or substitutional diffusion as opposed interstitial diffusion of inordinately small particles. Of course generation of interstitialcies yields a like number of vacancies which in turn promote vacancy diffusion. And as implied and supported by experimental findings lattice diffusion occurs primarily through vacancy effects.

But Balluffi reaches a similar conclusion for "Grain Boundary Diffusion Mechanisms in Metals, "the subject of his 1982 Institute of Metals Lecture (59):

> This lecture will attempt to review our current knowledge of the atomistic mechanisms responsible for these grain boundary diffusion phenomena. Relevant aspects of the structure of grain boundaries and the point and line defects which may exist in grain boundaries are described first. The important experimental observations are then discussed. Diffusion models are then taken up, and it is concluded that the atomic migration occurs by a point defect exchange mechanism which, in at least the vast majority of boundaries in simple metals, most likely involves grain boundary vacancies. The grain boundary sources and/or sinks required to support divergences in the atomic (vacancy) fluxes are grain boundary dislocations. Phenomena therefore occur which resemble the Kirkendall Effect in the bulk lattice in certain respects. Additional topics are discussed which include effects of boundary structure on boundary diffusion and the question of whether or not boundary diffusion is faster along migrating than stationary boundaries.

And in addition to the importance of grain-boundary as well as lattice transport in the low-creep region, vacancy diffusion along the cores of dislocations supports recovery processes such as viscous glide and dislocation climb in the intermediate-creep range [2.47].

However a pipe model also appears best adapted to predict small-angle boundary diffusion [2.60]. Peterson [2.61] supports this observation with experimental data [2.60,2.62 to 2.66] in his 1983 paper on "grain-boundary diffusion in metals." And of course he agrees with Balluffi that dissociated dislocations and stacking faults are relatively ineffective diffusion paths compared with their undissociated counterparts. Evidence favors "a rather well localized vacancy" activity in a three-dimensional process for the appropriate dislocation-core-diffusion modelling [2.64,2.65]. Peterson also asserts that "the effective width of a boundary for grain-boundary diffusion is about two atomic planes. Gleiter computed such grain-boundary dislocation widths and reveals that separate-dislocation modeling applies only for boundaries with orientation dependencies of energy such as small-angle geometries [2.57] -- although Turnbull and Hoffman indicate applicabilities to 16° or possibly 28°" [2.60]. Peterson also observes that diffusion along moving grain boundaries apparently can be orders of magnitude greater than along stationary ones. And he discusses grain-boundary-diffusion impurity effects with special attention to segregation.

Thus very important diffusion effects on creep involve solute, additive and/or impurity segregation at lattice interruptions such as dislocations, grain boundaries and surfaces. Diffusion driven by chemical-potential gradients segregates foreign elements within the primary metal. Then those

segregated materials affect lattice, dislocation and grain-boundary
diffusion processes which in turn influence creep [2.68]:

> Cases of retarded Herring-Nabarro creep are analyzed
> in terms of the efficacy of grain boundaries as
> sources and sinks for vacancies: strongly bound
> segregant atoms at grain boundaries affect the
> mobility of defects and hence control the operation
> of vacancy sources. Recently, observations have
> been made on the effect of strongly segregating
> solutes on grain boundary diffusivity. such
> behavior influences Coble creep rates, producing a
> general retardation. Here we assess the magnitude
> of the effect induced by various surface active
> species on grain boundary diffusivity and
> consequently on Coble creep; predictions show that
> in general, small amounts of highly surface active
> impurities induce a remarkable inhibition of this
> form of creep.

Here Hondros and Henderson [2.68] point to a mechanism capable of exerting
profound influences not only on creep-research results but also on the
ultimate development, production, fabrication and positive or negative
performance of ultralloys.

Exemplary of this observation is the extreme segregation of exceedingly
low overall concentrations of oxygen to grain boundaries in VIA-group
metals--and the resultant embrittlement [2.69 to 2.71]. In this vein
Honeycombe [2.69] discusses impressive effects of "micro-alloying" to
increase not only creep strength but also ductility and recrystallization
resistance. This was the subject Honeycombe (Goldsmiths' Professor of
Metallurgy, Cambridge University) treated in his "Commemorative Lecture by
the Twenty-Eighth Gold Medalist of the Japan Institute of Metals" in Tokyo
on April 2, 1983. So the importance of these implications are certainly
appreciated internationally. In fact the well-known Soviet expert on
ultralloys Savitsky [2.9, 2.28, 2.29] dwelled on the strong influences of
fractions of an atomic percent of hafnium and zirconium carbides on the

"phase composition, structure, and properties of vacuum-melted W-C(Zr,Hf,Nb,Ta,Re) alloys in his invited" lecture held on the 9th Plansee Seminar, Reutte, 1977" [2.72]: "It has been established that high mechanical properties of tungsten alloys at temperatures up to 2000-2500°C are associated with the formation of dispersed, thermodynamically stable precipitates of high-melting-point Me carbides or Me-C complexes." Savitsky et alii emphasized gratifying results for very small quantities of such carbides in W,Re ultralloys: "ZrC and HfC formation in W alloys radically (by 300-600°) shifts the onset of structural changes upon recrystallization into the high-temperature region." And because recrystallization is a diffusion-controlled phenomenon of course the previously mentioned accompanying increases in creep strength are also very substantial.

Before departing this section on "diffusion effects in high-temperature creep" two sources for lattice, grain-boundary and surface diffusion coefficients deserve mentioning. The pertinent references [2.73 and 2.74] both originated with Rice et alii in the Brown University Division of. Engineering. And in addition to Acta Metallurgica they appear in Perspectives in Creep Fracture edited by Ashby and Brown of the Cambridge University Engineering Laboratories [2.75].

2.5 GENERIC CREEP

High-temperature creep like recrystallization proceeds through thermally activated processes such as diffusion in the inexorable drive toward reduction of the total free energy G [2.71, 2.76, 2.77]. Perhaps better terminology for the Gibbs function G is "thermodynamic potential" or "free enthalpy" [2.78 to 2.80]:

$$G = H - TS = U - TS + PV = F + PV \tag{2.3}$$

with enthalpy H, absolute temperature T, entropy S, internal energy U, pressure P, volume V and Helmholtz function F also called "work content" or again "free energy."

In any event $-\Delta G$ equals the net or available work for an isothermal reversible change -- or under such conditions the maximum work at constant temperature W_T minus the external work of expansion against a constant pressure $P\Delta V$:

$$\Delta G = W_T - P\Delta V = H - T\Delta S \tag{2.4}$$

And in systems involving other than P,V work effects those intensive and extensive quantities undergo replacement by or coordination with electric intensity and polarization in capacitive effects, magnetic field and magnetization in magnetic materials, electromotive force and charge in electric cells, surface tension and area in superficial films as well as tensile force and length in elongated wires.

But in usual chemical thermodynamics $G = f(T,P,n_1,n_2,....)$ for $n_1,n_2,...$ amounts of substances 1,2,... in the system phase yields a very important partial molal property, the chemical potential μ:

$$\left(\frac{\partial G}{\partial n_1}\right)_{P,T,n_1,n_2,....} = \mu_1 \tag{2.5}$$

And component 1 tends to escape from regions of its higher chemical potentials to regions of its lower chemical potentials. Therefore chemical-potential differences indicate escaping or migrating tendencies of a system constituent [2.81].

Admittedly Fick's First Law for flow rate $dN/dt = -AD_c \partial c/\partial x$ and Fick's Second Law $\partial c/\partial t = D_c \partial^2 c/\partial x^2$ purport to describe diffusional effects entirely as functions of concentration c. However Fick's First and Second

Laws fail to explain "uphill" diffusion that increases rather than decreases concentration -- such as grain-boundary segregation. Because, as previously observed, diffusion is a thermally activated process dedicated to the diminution of total free enthalpy, atoms migrate in directions leading to overall system equilibrium -- not necessarily to concentration homogeneity. And in a chemical system, equilibrium obtains when the chemical potential of each species is the same throughout.

Therefore the gradient of chemical potential $\partial\mu/\partial x$ not of concentration drives diffusion:

$$dN/dt = - AD_\mu \partial\mu/\partial x \tag{2.6}$$

with the chemical-potential diffusion coefficient D_μ as a function of its concentration counterpart D_c

$$D_\mu = cD_c \ \partial \ln c/\partial\mu = cD_{co}e^{-\Delta H/RT} \ \partial \ln c/\partial\mu \tag{2.7}$$

Here $\mu = \mu^\circ + RT \ln a$ where $\mu^\circ = \mu$ for the pure component and activity $a = \gamma c$ with activity coefficient γ. Of course $D_c = D_{co} \exp(-\Delta H/RT)$ is the Arrhenius diffusion-constant expression with frequency factor D_{co} and activation enthalpy ΔH. Thus as expected diffusion driven by chemical-potential gradients grows exponentially with increasing temperature. And further generalization requires consideration of the total thermodynamic potential. For example electronic migration depends on the sum of the chemical potential and the motive (similar to the electric potential) -- or the total electrochemical potential of the electron phase [2.81]. Scaled migrational similarity prevails for ionic phases. Analogously, stress concentrations promote vacancy movement and countercurrent atom flux. So

diffusional effects under generalized service conditions often become quite complex.

And as the preceding section indicates, diffusion is a major factor in high-temperature creep. In reality several creep processes may proceed effectively together -- in parallel and/or in series. Then the resultant creep rate depends on the relationship of such mechanisms: If they occur independently the fastest process controls the overall creep rate. If they operate in an interdependent sequence the slowest mechanism dictates the creep rate [2.82]. Langdon et alii further define metallic creep behaviors as class M and class A [2.83]: Class M is characteristic of pure metals where several processes proceed independently resulting in higher powers of stress dependency for higher strain rates. Class A characterizes solid-solution alloys and "designates a different behavior observed only under certain conditions" [2.47]. In the intermediate stress range class-M-to-A as well as class-A-to-M transitions occur when limiting conditions are met. In addition to solution effects, precipitate and dispersion strengthening exert profound influences on creep characteristics of metals. But these modifications progress toward great creep complexity which is reality in many situations involving impurities as well as additives.

From a much simpler viewpoint typical pure metal creep curves depict the time trace of strain during plastic deformation caused by prolonged loading: Generally the ε, t plot begins with instantaneous elastic elongation. Then a transient or primary stage occurs with initially high, then decreasing creep while the metal hardens and develops stress-dependent substructures. Next a steady-state or secondary stage obtains with a constant creep rate and essentially stable substructures. Finally the

runaway or teritiary stage prevails often with grain-boundary-cavity and neck formations followed by ultimate failure.

Such creep characteristics correlate well against homologous temperatures T/T_m. Because various thermally activated processes increase solid-particle freedom culminating in fusion, their ascendancy temperatures gauged against the melting point T_m imply activation energies for those mechanisms. Thus in creep effects thermally activated influences remain small below ~ $0.3T_m$. "Creep becomes an important deformation mechanism above $0.3-0.5$ T_m" [2.84]. Although creep-activation energies (Q_c's) often plateau between 0.2 and 0.4 T_m, depending on strain rates, these levels generally fall below those for self diffusion Q_{sd}'s [2.37, 2.85]. Generally Q_c's approximate Q_{sd}'s for metals from In to W, metal halides and oxides (citations in 37) at temperatures higher than 0.4 to 0.5 T_m -- again depending on strain rate or stress. In this upper region approaching T_m Q_c's tend to rise slightly with increasing T because of the decreasing elastic modules E: Actually logarithmic plots of $\dot{\epsilon}/D_{sd}$ versus σ/E effect tighter correlations than their $\dot{\epsilon}$, σ counterparts in general [2.37].

These generalizations engender familiarity with "generic creep," which of course can produce both positive and negative results. But the following section on particular creep effects should compensate somewhat for the preceding general approach.

2.6 SPECIFIC CREEP

An interesting creep definition arrives here as a quotation of a paraphrastic observation by Murr [2.77]: "As Ashby pointed out [2.86] the total creep process may be regarded either as deformation by grain boundary sliding with diffusion maintaining the integrity of the interface, or as deformation by mass transport with grain boundary sliding accommodating the

incompatibilities which would otherwise appear in the interface." In any event, more specifically, in any creep event the applied stress σ deforms the subject material element at a characteristic strain rate $\dot{\varepsilon}$. For one-percent deformation in about a third of century $\dot{\varepsilon} \sim 10^{-11}$ second^{-1}, which is a reasonable expectation in many applications. But much creep testing and experience develop strain rates many orders of magnitude faster than 10^{-11} second^{-1}.

Traditionally, graphic creep presentations display the logarithm of $\dot{\varepsilon}$ over about ten cycles against the logarithm of σ over about three cycles -- although the final stage of creep often spans many orders of $\dot{\varepsilon}$ magnitude itself. Tradition also dictates dividing creep stress into low, intermediate and high regimes -- with the rate of increasing $\dot{\varepsilon}$ growing greater in each successive division for pure metals. To this point no compelling rationale for thwarting such customs has arisen.

2.6.1 Low-Stress Creep

2.6.1.1 Nabarro, Herring Creep

Nabarro, Herring creep [2.38, 2.39] results directly from stress-intensified vacancy migrating from grain boundaries under tension to others under compression. This low-stress small-grain intragranular transport phenomenon precludes diffusion-accommodated dislocation movement but more aptly approximates Newtonian viscous-fluid behavior. Additional detailed descriptions of Nabarro, Herring creep appear in references 2.37, 2.47, 2.76 as well as 2.38 and 2.39 which provide an appropriate expression for the steady-state strain rate:

$$\dot{\varepsilon} = \frac{C_{NH}b^{3}\sigma}{kT\,d^{2}} D_{\ell o}e^{-Q_{\ell}/RT} \qquad (2.8)$$

The symbols are those given for equations [2.1] and [2.2] with the addition of Boltzmann's constant k and the Burgers vector b [2.80].

Nabarro, Herring creep depends on grain boundaries as sources and sinks of vacancies but on lattice or volume diffusion. Thus as might be expected the Nabarro, Herring mechanism dominates low-stress creep for small grain sizes in the high-temperature regions.

2.6.1.2 Coble creep

Coble creep [2.40] rises in importance as temperatures decrease for low-stress small-grain metals. Now rapid diffusion along the grain boundaries predominates over the much greater diffusional areas available to intragranular or lattice transport. And Coble creep proceeds in accordance with the following equation.

$$\dot{\epsilon} = \frac{C_C \ b^3 \sigma}{kT \ d^3} D_{bo} e^{-Q_b/RT} \tag{2.9}$$

So Coble and Nabarro, Herring creep become equivalent at a temperature influenced strongly by the difference in lattice and grain-boundary diffusion activation energies (eq. (2)):

$$T = \frac{Q_\ell - Q_b}{R \ln\left[\left(\frac{C_{NH}}{C_C}\right) \left(\frac{D_{\ell o}}{D_{bo}}\right) \left(\frac{d}{b}\right) \right]} \tag{2.10}$$

And of course in the region where both contribute significantly as well as independently equations (2.8) and (2.9) combine effectively:

$$\dot{\epsilon} = \frac{b^3 \sigma}{kT d^3}\left(C_{NH} D_{\ell o} e^{-Q_\ell/RT} + \left(\frac{b}{d}\right) C_C D_{bo} e^{-Q_b/RT}\right) \tag{2.11}$$

This expression again emphasizes that reducing grain size increases these forms of low-stress creep and favors Coble deformation in particular.

2.6.1.3 Harper Dorn Creep

Harper, Dorn creep [2.42] in contrast deletes grain-size dependence and applies well for deforming single-crystal, bicrystal and large-grained metals at low stresses:

$$\dot{\varepsilon} = \frac{C_{HD}b\sigma}{kT} D_{\ell o} e^{-Q_\ell/RT} \tag{2.12}$$

Equations (2.8) and (2.12) predict a transition from Nabarro, Herring to Harper, Dorn creep in a critical grain-size range [2.47]:

$$d = \left(\frac{C_{NH}}{C_{HD}}\right)^{1/2} b \approx 1.5 \times 10^{6} b \tag{2.13}$$

In turn eqs. (2.9) and (2.12) indicate a change from Coble to Harper, Dorn creep at

$$d = b\left(\frac{C_C D_{bo}}{C_{HD} D_{\ell o}}\right)^{1/3} e^{-(Q_b - Q_\ell)/3RT} \approx 1.4 \times 10^{4} b^{2/3}(\delta D_b/D_\ell)^{1/3} \tag{2.14}$$

where δ is the grain-boundary width [2.47, 2.87]. Langdon et alii estimate that Harper, Dorn creep prevails typically above grain sizes of 300 to 500 μm [2.47, 2.88] with substructures of uniformly randomly distributed dislocations in densities independent of stress and with no evident subgrains [2.47, 2.89].

2.6.2 Intermediate-Stress Creep

2.6.2.1 Low-Temperature Creep Accompanied by Dislocation Climb.

Low-temperature creep accommodated by dislocation climb depends on pipe diffusion which is considerably more rapid than lattice transport at lower thermal levels (eq. (2.2)). And in addition to its reduced energy of activation, pipe diffusion occurs through the intragranular dislocation density which increases with the second power of applied stress [2.90]. So low-temperature intermediate-stress creep with dislocation-climb accommodation exhibits the greatest stress dependency in its range:

$$\dot{\varepsilon} = \frac{C_{LTC} b \sigma^7}{kT \sigma^6} D_{do} e^{-Q_d/RT} \tag{2.15}$$

This effect eventuates as stress increases toward the upper limit of the intermediate range at temperatures near $0.5\ T_m$. Of course "low" and "high" temperature designations here are relative, referring to extremes for elevated-temperature deformation.

2.6.2.2 High-Temperature Creep with Dislocation-climb Accommodation

High-temperature creep with dislocation-climb accommodation connotes the ascendancy of vacancy diffusion through the lattice. As previously noted this steady-state strain rate obtains with the attainment of a persisting arrangement of relatively uniform subgrains. Within the subgrains which vary in size inversely with σ the dislocation density again increases with σ^2 similar to its intragranular counterpart in low-temperature deformation with climb recovery [2.91]. But because volume vacancy diffusion prevails the dislocation-density effect is extraneous in the stress exponent of the creep-rate equation:

$$\dot{\epsilon} = \frac{C_{HTC} \, b\sigma^3}{kTG^4} \, D_{\ell o} \, e^{-Q_\ell/RT} \tag{2.16}$$

This expression applies not only to pure metals but also to solid-solution alloys deforming with dislocation-climb accommodation.

2.6.2.3 Low-Temperature Creep with Viscous Glide

Low-temperature creep with viscous glide is a solid-solution postulate of Langdon, "but in practice this low-temperature behavior has not been reported experimentally" [2.47]. In "viscous glide" "the rate of dislocation motion is dictated by the velocity with which solute atoms can be dragged along with the dislocations" [2.37]. In any event if such a process were dependent on vacancy diffusion along dislocation cores within the grains the intragranular-dislocation-density proportionality to σ^2 would again increase the applied-stress exponent over that for high-temperature dislocation glide. Then the low-temperature viscous-glide postulation becomes the following equation.

$$\dot{\epsilon} = \frac{C_{LTG} \, b\sigma^3}{kTG^4} \, D_{d\ell o} \, e^{-Q_{d\ell}/RT} \tag{2.17}$$

Apparently, "although in principle there is also the possibility of diffusion along the dislocation cores at low temperatures," the effect is negligible in "the viscous glide of dislocations with solute atom atmospheres."

2.6.2.4 High-Temperature Creep with Dislocation Glide

High-temperature creep with dislocation glide, however, develops in solid-solution alloys:

$$\dot{\varepsilon} = \frac{C_{HTG}\, b\sigma^3}{kTG^2}\, D_{\ell\ell o}\, e^{-Q_{\ell\ell}/RT} \tag{2.18}$$

There only dislocation climb accommodates intermediate-stress deformation. But both climb and glide mechanisms operate in metallic solid solutions. In fact Langdon et alii indicate these are sequential phenomena leading to process transitions within the intermediate-stress range for solid-solution creep [2.47,2.83,2.92,2.93]. By equating (2.16) and (2.18), correlating the result with experimental data [2.92] and determining the stress at which "gliding dislocations break away from their solute-atom atmospheres [2.93] they bracket the viscous-glide regime: "It follows that class A behavior with n ~ 3 (stress power) is restricted in solid-solution alloys to a range of normalized stresses which is given by

$$\psi \left(\frac{kT}{eGb^3}\right)\left(\frac{1}{c}\right)^{1/2}\left(\frac{\bar{D}}{D_\ell}\right)^{1/2}\left(\frac{Gb}{\Gamma}\right)^{3/2} < \frac{\sigma}{G} < \frac{W_m^2\, c}{5Gb^3 kT} \tag{2.19}$$

where $\psi \sim 3 \times 10^{-7}$." Also e is the solute, solvent size difference; c, solute concentration; $\bar{D}$, solute-atom interdiffusion coefficient; Γ, solid-solution stacking-fault energy; and incidentally ψ is a dimensionless constant estimated from the experimental data (Al,5% Mg at 827K) as ~ 3×10^{-7}; subsequent analyses...have yielded values for ψ of ~ 2×10^{-7}."

So Langdon et alii establish transitions from high-temperature climb to viscous glide, then back to the dislocation-climb mechanism again -- all within the intermediate-stress region for solid-solution creep.

2.6.3 High-Stress Creep

"The high-stress range...is not well understood....high-stress creep begins where the power law breaks down.... Creep data at high stresses will generally give a linear relation when plotted as log $\dot{\varepsilon}$ against stress....

The resulting slope is a strong function of the material....the start of the upsweep of the creep rate...is independent of the material being investigated. Although possibly entirely unrelated it is of interest to note that this particular relation, $\dot{\varepsilon}/D = 10^9$, was proposed by Cottrell [2.94] as the criterion for the occurrence of the Portevin-Le Chatelier effect (serrated stress-strain curves) in interstitially alloyed body-centered-cubic metals; in this case D is the diffusion coefficient of the interstitial atom.... It would also appear that contemporary creep theories cannot explain why high stress creep begins at a creep rate equal to $10^9 D$." These 1968 observations by Sherby and Burke [2.37] apparently still apply. Little additional information accrued in the interim -- although Sherby et alii published results in 1980 indicating that above the power-law breakdown, normalized creep rates grow exponentially with stress through up to fifteen orders of magnitude [2.95].

In 1981 Langdon stated [2.47], "At high stresses there is an exponential dependence on stress of the form

$$\dot{\varepsilon} \propto \exp(B\sigma) \tag{2.19}$$

where B is a constant, p = 0 (grain-size exponent) because the deformation process relates to a lattice mechanism, and the activation energy is of the order of the value for lattice self-diffusion Q_ℓ." But in 1983 Langdon commented [2.47], "In addition pipe diffusion tends to dominate under these ('power-law breakdown') conditions so that the activation energy is closer to Q_p than Q_ℓ." He also cited "speculations" on high-stress creep [2.45,2.46) and emphasized its incipience:

$$\sigma/G = 2 \times 10^{-3} \ (91) \quad \text{and} \quad \dot{\varepsilon}/D = 10^9 \ \text{cm}^{-2} \ (44) \tag{2.20}$$

Thus probably because of a lack of practical interest in power-law breakdown the 1968 observations by Sherby and Burke apparently still apply.

Grain-Boundary Sliding

In contrast to the neglected power-law-breakdown technology grain-boundary sliding attracts much attention [2.53 to 2.57] -- particularly in relation to intergranular-cavity nucleation, growth and integration to macrocrack formation with propagation eventuating in fracture [2.54 to 2.56, 2.73 to 2.75). To explain cavity production reference 56 details finite-element analyses that determine stress concentrations at hard grain-boundary-particle apices and triple-grain junctions in alloys creeping with low grain-boundary-sliding resistance, typical above 0.4 T_m. However for general purposes "an evaluation of deformation models for grain-boundary sliding" seems appropos [2.53]: Such a discussion precludes intragranular processes independent of grain-boundary mechanisms. Either the grain-boundary effects take the form of creep that elongates grains in the tensile-stress direction with lattice [2.38,2.39] and/or grain-boundary [2.40] vacancy diffusion -- "grain-boundary sliding with diffusional accommodation" [2.96] termed lifshitz sliding [2.53,2.97]. Or they manifest as grains slipping past each other, communicating through their mutual boundaries, without granular distortion -- termed Rachinger sliding [2.53,2.97].

2.6.4.1 Intrinsic Sliding

Intrinsic sliding involves basically only two primary plane surfaces unimpeded by secondary granular effects such as triple-grain junctions (triple points). This model applies in a strict sense only to bicrystals sliding either on surface irregularities such as ledges or through boundary

processes such as dislocation climb and glide. For grain-boundary sliding accommodated by materials transport between ledges Ashby et. alii provide an appropriate expression for the intrinsic velocity v_s [2.96, 2.98, 2.99]:

$$v_s = \frac{8\delta b^3 \tau}{kTh^2} D_b + \frac{8\delta b \tau}{kT} D_b \text{(as h} \rightarrow \text{ atomic height)} \tag{2.21}$$

with previously defined symbols except shear stress τ and ledge height h. For such intrinsic Lifshitz sliding Langdon and Vastava observe that "this type of flow is adequately modeled for polycrystalline materials by the theories of Nabarro-Herring and Coble for diffusion creep, and it does not in general lead to cavity formation" [2.53].

More important in processes leading to fracture is intrinsic Rachinger sliding involving dislocation glide and climb in boundaries hindered by the steps there [2.100]:

$$v_s = \beta \frac{\delta b \tau}{kT} D = \pm \left(\frac{\psi \Omega^{2/3}(1+\tan\alpha \cot\gamma)}{x \tan\alpha \cot\gamma} \right) \frac{\delta b \tau}{kT} D \tag{2.22}$$

where ψ is reciprocal dislocation spacing; Ω, atomic volume ($\sim b^3$); x, diffusion-path length ($\sim 10 b_b$ with boundary-dislocation Burgers vector b_b); α and γ are angles orienting the boundary and axis of rotation. For sliding through dislocation climb only the boundary-plane shear-strain rate $\dot{\gamma}_{bs}$ results from another model [2.101]:

$$\dot{\gamma}_{bs} = \frac{2c_j \rho_{bd} b_b^3 \tau}{\psi \zeta kT} D_b \tag{2.23}$$

with jog concentration c_j, moving grain-boundary-dislocation density ρ_{bd}, number of b_b's in the dislocation-climb distance for each added atom ψ [2.1 to 2.10] and a constant for b_b orientation relative to the boundary $\zeta(\sim 0.5)$.

Although intrinsic sliding is a Newtonian viscous process the indicated unit stress exponents are generally greater experimentally than this theoretical value [2.53,2.101].

2.6.4.2 Extrinsic Sliding

Extrinsic sliding in contrast applies to polycrystalline materials and therefore includes secondary granular effects such as accommodation at triple grain junctions [2.49, 2.53, 2.102 to 2.108]. Folding at triple points often accommodates grain-boundary sliding as described by Gifkins [2.102]:

$$\dot{\varepsilon}_{bs} = 2\,C_F F\,\frac{y\lambda b\sigma^{4\cdot 5}}{kTd^2 G^{3\cdot 5}}\,D_\ell \tag{2.24}$$

Here C is "the constant in the standard rate equation for lattice creep by dislocation climb," $3^{0\cdot 5}\pi^2/8b^{1\cdot 5}N^{0\cdot 5}$ for "climb at the head of dislocation pileups" and $-1/6\pi^{0\cdot 5}b^{1\cdot 5}N^{0\cdot 5}$ for "climb at multipoles" with N as the active-dislocation-source number density [2.49,2.53,2.103]. F is a triple-point-sliding stress-concentration factor; y, the triple-point-fold width; and λ, the subgrain size equal to $\Lambda bG/\sigma$ with another constant Λ [2.53]. Incorporating this λ equivalent Langdon suggests another version of (2.24):

$$\dot{\varepsilon}_{bs} = 2C_F F\Lambda\,\frac{yb^2\sigma^{3\cdot 5}}{kTd^2 G^{2\cdot 5}}\,D_\ell \tag{2.25}$$

Thus the activation energy for this extrinsic-sliding model is that for lattice self-diffusion $(D_\ell = D_{\ell o}\,\exp(-Q_\ell/RT))$.

Gifkins, author of (2.24), collaborated with Raj and Ashby in the development of (2.21) which Crossman and Ashby modified to apply to polycrystalline boundary sliding with intragranular plastic-flow accommodation [2.104]:

$$\dot{\varepsilon}_{bs} = \frac{8\delta b^3 \sigma}{3kTh^2 d} D_b \tag{2.26}$$

Here the activation energy is that for grain-boundary diffusion
$(D_b = D_{bo} \exp(-Q_b/RT))$. Gifkins [2.105] asserts that another solution to
this problem based on grain-boundary coherency [2.106] lacks experimental
applicability -- perhaps because it is a limiting version of the model
[2.53, 2.107). In any event Ashby et alii have contributed heavily to grain-
boundary-sliding technology.

However an early unique contribution from Langdon provides an
expression for polycrystalline sliding accommodated by grain-boundary
cavitation and cracking [2.108]:

$$\dot{\varepsilon}_{bs} = C_c \frac{b^2 \sigma^2}{kTdG} D_\ell \tag{2.27}$$

This equation and (2.26) indicate grain-boundary-sliding rates inversely
proportional to grain size; (2.25) shows the reciprocal of squared grain
size. And the stress exponent varies from one through two to 3.5 (or 4.5).
In this vein Langdon states [2.53], "Published experimental results on
grain-boundary sliding are tabulated, and it is shown that there are wide
variations in apparent dependence of sliding on stress and temperature....it
is concluded that none of the models is entirely consistent with
experimental data."

2.7 CREEP EFFECTS IN DIFFUSIVE INTERGRANULAR CAVITATION

As previously stated, grain-boundary sliding is a primary process in
the nucleation, growth and coalescence of intergranular cavities. But to
properly assess the importance of boundary sliding Argon et alii provide
some background and context in their 1983 and '84 papers [2.55]:

> The mechanistic details of intergranular fracture
> in creeping alloys have recently been critically

assessed by Argon [2.54]. Here we will be interested only in the mechanisms of cavity nucleation and growth....Since at elevated temperatures point defect concentrations and mobilities are both high, cavity nucleation has been considered as a classical nucleation process of a vacant phase by the agglomeration of vacancies on stressed interfaces. The theoretical models for such nucleation (2.109 to 2.111) result in a reciprocal time $\dot{\rho}$ for cavity nucleation that is of this form,

$$\dot{\rho} = \dot{\rho}_0 \exp(-\Delta G^*/kT)$$

$$= (2\pi r^* D_b \delta/\Omega^{4/3}) \exp(\sigma_n \Omega/kT) \exp(\exp-\Delta G^*/kT) \qquad (2.28)$$

where r^* and ΔG^* are the radius and free energy of the critical size cavity at its saddle point configuration, nucleated under local normal stress σ_n at temperature T and where $D_b \delta$ is the linear diffusive conductance of the grain boundary...Ω the atomic volume.... These threshold stresses are of the same order as the cohesive strength of high quality interfaces at low temperatures that need to be reached in ductile fracture to form cavities [2.111,2.112]. Thus the formation of cavities at elevated temperatures is not significantly relaxed. Similar results can be obtained for other metals and for ceramics [2.113]. Since the service stresses at which intergranular fracture occurs are more than a factor of 20 lower, it is necessary to conclude that stress concentrations are needed to cavitate a grain boundary. Grant and coworkers [2.114,2.115] have demonstrated experimentally that intergranular cavitation required both grain boundary sliding and grain boundary particles, that cavities form preferentially at grain boundary particles, and that when particles are scrupulously removed, cavities do not form even though boundary sliding is present.

So intergranular cavitation requires stress concentration that results from grain-boundary sliding over hard grain-boundary particles. But polycrystalline grain-boundary sliding alone, over inherent triple points, fails to generate cavities.

With these salient observations Argon et alii attacked the problem of stress concentration during grain-boundary sliding [2.56,2.111,2.116]. They

analyzed "two apparent sources of intergranular stress concentration:
nondeformable grain-boundary particles and triple grain junctions both of
which have been amply demonstrated to be of importance in creep fracture
[2.117,2.118]. We have discussed earlier [2.111] that these two problems
are complementary in nature and in timing. While the first problem of
stress concentration around grain-boundary particles is the dominant one, it
exists with full intensity only during short, transient period of rapid
sliding. The second problem of stress concentration at triple grain
junctions, on the other hand, builds up gradually as the shear tractions on
slanted boundaries are reduced to zero. Both analysis [2.111] and
experiments [2.111,2.117] indicate that the first problem is important in
cavity nucleation and the second in rapid coalescence of already-formed
cavities to form wedge cracks.... In the special case of modeling
intergranular cavitation that we are interested in it is necessary to apply
some modifications to these stress fields by considering the stress-
smoothing effect of diffusional flow between portions of a boundary under
high tensile stress and adjacent portions under high compressive stress"
[2.56].

Argon [2.55] gauges this "stress-smoothing effect" against "a critical
diffusion length [2.112]":

$$L = (D_b \delta_b \Omega \sigma_e / kT \dot{\epsilon}_e)^{1/3} \tag{2.29}$$

Needleman and Rice [2.74] "show that coupling between creep and diffusion
can be expressed in terms of a stress and temperature dependent material
length scale L introduced by Rice [2.119], where" the expression is
identical to eq. (29). They assert that "when the length L is
large...compared to cavity radius (a) and half-spacing (b), plastic creep

flow effects can be neglected. On the other hand...when L is small compared to the spacing, coupled creep-diffusion effects are important, and the ratio of cavity growth rate to the prediction based on the rigid-grains (Hull-Rimmer) model is found to be a rapidly increasing function of the ratio a/L." Also argon observed that "it must be concluded that cavity formation is distinctly favored near the apex regions of grain boundary particles provided that these particles are of a size in excess of the critical diffusion length so that the stress concentrations cannot be effectively leveled down by diffusional flow around the particles" [2.55].

So eq. (2.29) predicts the incipience of nucleation and of plastic-creep-flow influence on the growth of intergranular cavities: Thus the Argon, Rice diffusion-length expression appears to be an important tool in the technology development for grain-boundary cavitation.

Creation of cavity nuclei eludes detailed experimental verification because characteristic nucleation diameters approximate 2×10^{-9} meter -- about ten crystal-ionic diameters. And the smallest cavities detected with more or less conventional microscopy are about 10^{-7} meter [2.54,2.55]. In fact nucleation radii are quite close to the grain-boundary-segregation thickness for oxygen in commercial molybdenum which required as imaging atom probe with a high-resolution time-of-flight spectrometer for elucidation. But such field-ionization-microscopic techniques seem somewhat unadaptable to creeping cavitation studies [2.69,2.70].

Another complication in cavity-nucleation observation is the tendency of nuclei to grow very rapidly because of elastic dilation in the stress concentrations at the generating apices of grain-boundary particles: An order of magnitude cavity-size increase resulting in abrupt stress-concentration reduction is a reasonable estimate [2.55]. So the probability

of freezing-in nucleation for later dissection and submicroscopic inspection is low. However many detailed studies of other nuclei-generating processes are also difficult. Tout au contraire cavity-growth investigations seem considerably simpler. But Argon stated in 1983 [2.55], "In spite of much success in understanding of cavity growth that has evolved over the past decade, there are still large discrepancies between experiment and theory that require attention."

Thus although a detailed accounting of progress in grain-boundary-cavitation technology appears unwarranted in this general paper, further appraisals in the near future should prove very illuminating.

2.8 ANOTHER GRAIN-BOUNDARY-SLIDING MANIFESTATION: SUPERPLASTICITY

Superplasticity enables alloys to extend hundreds even thousands of percent without failure or even necking down. Because such deformation capability offers obvious processing advantages, if it is precluded under service conditions, the USSR investigated superplasticity intensively beginning in the mid 1940's. Soviet scientists and engineers published numerous papers and reference books on this phenomenon. Finally after publications of surveys of the USSR work the US became interested in superplasticity in the 1960's. By now reviews of this technology each containing well over a hundred referential citations are commonplace [2.120,2.121).

In the latter John Gittus (United Kingdom Atomic Energy Authority, Harwell), Editor-in-Chief of "The International Journal of Structural Mechanics and Materials Science," presents a simple informative 1983 description [2.121]:

> ...Superplasticity is a widespread phenomenon
> exhibited by very many metals and alloys. Indeed
> it is probably possible to produce the superplastic
> state in most common alloy systems. The prime

requirement is a fine stable grain size which can
be produced in two main ways:

a) By pinning the grain boundaries, for example
   with a fine precipitate.

b) By having about 50% of a second phase present in
   a finely distributed form. The grain size at
   equilibrium is then approximately equal to the
   size of the second phase particles.

Deformation in superplastic materials occurs by a
mechanism which is quite distinct from the
homogeneous straining process that characterizes
normal flow. In the latter case...every grain
exhibits the same strain as the polycrystal in
which it is situated; grains do not change partners
during deformation by homogeneous flow. By
contrast in the superplastic process the grains or
particles of the alloy flow like grains of sand in
an hourglass. Individual grains make fluctuating
changes in shape so as to prevent the formation of
voids at the grain boundaries. But even after very
large deformations the grains do not elongate and
remain more or less in the same equiaxed state as
at the beginning of deformation. Instead of
deforming the grains slide over one another, and it
is this process of heterogenous straining which
causes the material to be in the same state after a
large deformation as it was initially. As there
has been little significant change in state there
is no particular reason why rupture should
supervene even after very large extensions. In
many fine-grained single-phase superplastic alloys
the deformation process is very simple. It seems
to involve sliding at the grain boundaries by the
movement of grain boundary dislocations. The
formation of grain boundary voids is prevented by
the climb of boundary dislocations on certain
facets of the grains. Deposition of matter onto
the climbing dislocations permits the small changes
in shape that are needed to accommodate mismatch at
the boundaries of grains that are translating
relative to one another.

Langdon quantifies the "fine stable grain size" requirement as "typically
(but not necessarily) less than about 10 μm in size" [2.120].

Both Gittus and Langdon mention an often-referenced expression for
superplastic stress σ as the product of a constant and the strain rate
$\dot{\varepsilon}$ raised to a power m ("the strain-rate sensitivity"):

$$\sigma = K\dot{\varepsilon}^{m}$$

(2.30)

Of course K is not a constant but rather a complex function which includes at the very least the temperature dependency. In any event (30) is equivalent to the power law from creep technology $\dot{\epsilon} = f(T, \ldots)\sigma^n$ where $n=m^{-1}$.

A more general superplasticity form for α and β phases (exemplary of brass) appears in the Gittus review well-referenced to Suery [2.121,2.122]:

$$\dot{\epsilon}_\beta = A_\beta \frac{\sigma^n}{L_\beta^{\bar{a}}} e^{-Q_\beta/RT} \qquad (2.31)$$

Here "A_β is a constant"; L_β, the β-phase grain size; Q_β, "the activation energy (apparent)"; and other symbols are as previously noted. The global law of behavior is then written

$$\dot{\epsilon}_g = h(\alpha) \frac{\sigma^n}{L_\beta^{\bar{a}}} e^{-Q_\beta/RT} \qquad (2.32)$$

where if $g(\alpha)$ ($h(\alpha)$) is a function of the proportion of α phase

$$h(\alpha) = A_{\beta g} g(\alpha) \text{ "} \qquad (2.33)$$

For Cu,Zn alloys with 58 to 61% Cu and volume fractions of α phase from ⌄.24 to 0.71 at 600°C Gittus modifies (2.32) yielding

$$\dot{\epsilon}_g = h(\alpha) \left(\frac{\sigma}{L_\beta}\right)^2 e^{-115\pm10\left(kJ \text{ mole}^{-1}K^{-1}\right)/RT} \qquad (2.34)$$

In a later section Gittus proposes a "model for superplastic deformation of brass" based on a dislocation climb mechanism controlled by diffusion α,β interfaces rather thán β grain boundaries [2.121,2.122]:

$$\dot{\varepsilon} = \frac{2b^3\sigma^2}{kTL_\beta^3 G} D_{Io} \, e^{-Q_I/RT}$$

(2.35)

Here the subscript I denotes interfacial diffusional characteristics.

Equation (2.35) resembles the generalized equations for creep and for grain-boundary sliding. Accordingly Langdon concludes with considerable referential support, "Microscopic evidence indicates some intragranular dislocation activity in the superplastic region II, but the dominant deformation mechanism appears to be grain boundary sliding." He tabulates and plots much experimental data to verify his viewpoint. He also observes [2.123], "It is now firmly established that superplastic materials exhibit very high elongations to failure over rather limited ranges of strain rate which are typically in the vicinity of 10^{-3} to $10^{-2}s^{-1}$, and there is a reduction in fracture strains at both lower and high strain rates." In a subsequent paper on superplastic flow Langdon states (2.124), "Within region II most of the experimental data indicate a stress exponent (n) close to 2, an exponent (p) of the inverse grain size close to 2 and a activation energy (Q) close to the value for grain boundary diffusion Q_{gb}." So eq. (2.35) appears prototypically reasonable in form and numbers as a description of the superplastic manifestation of grain-boundary sliding.

2.9 COUNTERACTING CREEP

Perhaps the most obvious and possibly the most difficult method to reduce creep is through the use of thermomechanically critical elements each constructed entirely of a single crystal. Of course such monocrystalline entities should operate with their minimum-creep directions aligned with the maximum stress -- taking advantage of their morphological anisotropy. An example of this application occurs in turbine blades produced as single crystals.

Another approach to decrease creep involves utilization of materials with high melting points. This too is quite obvious because of the use of homologous temperatures (T/T_m) in the general descriptions of creep and solid-diffusion phenomena. Many papers on high-temperature deformation begin with a phrase such as "typically at or above about $0.5T_m$ where T_m is the absolute melting point" [2.47]. Thus among the high-melting metals W $(T_m = 3653K)$ and Re $(T_m = 3453K)$ excel as anticreep prospects.

Apparently the basic bonding configuration of W as well as Mo and Cr also contributes to creep resistance: Transition metals especially those of the VI-A group combine usual metallic interatomic bonds with covalent components [2.11,2.125,2.126]. And covalent bonding greatly impedes dislocation motion, substantially enhancing creep resistance. Some speculate dubitably that this facet of VI-A metals may increase brittleness though either inherent covalent characteristics or heightened susceptibility to impurity effects [2.11]. In any event the nature of interatomic bonding is important in counteracting creep.

In this same vein a high activation energy for self-diffusion is of course effective in opposing creep through the inhibition of diffusional capabilities -- reduction of self-diffusion coefficients. Apparently W exhibits the highest activation energies for lattice and grain-boundary self-diffusion of all metals [2.74,2.127]. So in a general thermophysicochemical sense W and W alloys appear to offer maximum metallic creep resistance.

Much more generally solute, precipitation and dispersion strengthening effects fortify creep resistance and often improve ductility while opposing recrystallization. Solute atoms that concentrate at dislocations drag against movements such as climb and glide and thereby reduce creep. Defect

atoms with high interaction energies are particularly effective in this role. Solutes that cause greatest alterations in lattice parameters and shear moduli per fractional gram-atom addition are the most effective solution strengtheners in general.

Precipitation strengthening with considerably less than one percent of HfC in W ultralloys, solution strengthened by a few, several or more percent Re, is the subject of many of the references cited in the introductory section. HfC is a very stable,extremely high-melting (>4100K precipitate. Precipitating such coherent particles from molten solutions into very-low-solubility states within the solidified-alloy matrix strengthens in particular through increased opposition to movements of dislocations and grain boundaries. However precipitates generally decrease in effectiveness as they approach their solvi. Therefore very high solvus temperatures, very low solubilities and very small component diffusional tendencies are desirable for materials providing precipitation strengthening.

A similar approach with higher-temperature capabilities relies on dispersion strengthening with fine well-distributed particles of strong high-melting essentially insoluble materials. Excellent examples are ThO_2 in W and W,Re alloys which are also referenced repeatedly in the introductory section: "The dispersed phase commonly used with tungsten is thorium dioxide, which thermodynamically is the most stable oxide" [2.128] and "has a melting point of 3300°C which is the highest of all oxides" [2.129]. Such particle dispersions reduce mobilities of grain boundaries, subboundaries and dislocations -- decreasing creep, increasing ductility and raising recrystallization temperatures. But dispersing these particles effectively is a problem. Of course dispersoid size, spacing,

concentration, stability and other variables of microstructural and chemical interactions influence creep-inhibiting capabilities [2.130].

Conversion of deleterious segregated impurities to productive separate phases through in situ reactions with micro-alloying agents offers a very promising approach to creep inhibition [2.69,2.130]. For example an imaging atom probe reveals that O in commercial Mo drops from -2a/o at the grain boundaries to several ppm about 1 nm into the grains [2.69,2.70]. Such segregation also occurs with C in metals [2.70]. And in may cases overall concentrations of these impurities measure only ten of parts per million -- but can exceed 100 ppm. Effects of these micro-impurities are often profound: Exempli gratia, the most embrittling "interstitial" for VI-A metals (W, Mo and Cr) is C, then O, next N and finally H [2.71]. The order reverses for VA metals (Ta, Nb and V). And numerous references indicate that interstitial-impurity levels of C or O in W or Mo effect substantial property alterations. But very small additions of pure Th and/or Hf should "getter" segregated O and C resulting in the "formation of a separate phase with one or more of the alloying agents. The phase may be uniformly distributed in the grains (not in this case) or preferentially nucleated at dislocations, grain boundaries or interphase interfaces" [2.69]. So micro-alloying of this type can convert harmfully segregated impurities into fine stable high-melting dispersions strategically located to counteract creep, inhibit recrystallization and yet improve ductility.

This method may also be effective in suppression of cavity nucleation. Argon indicates [2.55], "Uniformly larger area fractions of particles on all grain boundaries, i.e. reduced ℓ/p (particle spacing-to-size) ratios lower the stress concentration and should retard cavity formation -- provided that all boundaries are uniformly and densely covered with particles. Since

there is little current understanding on how to govern such uniform precipitation of hard spheres along grain boundaries, this possibility appears difficult to achieve." Of course the preceding paragraph proposes such a particle distribution.

Thus this section discusses mechanisms for counteracting not only creep -- but also intergranular cavitation.

2.10 AN APPROACH TO DECREASED CREEP

Space-power growth aims at continuously increasing temperature levels that will eventually surmount the asymptotic capabilities of ultimate materials. Therefore alloys that circumscribe the greatest potentialities of metallic combinations to serve in space will eventuate -- better sooner than later and rather here than there.

The ultimate refractory metal for space applications is W: It offers the highest metallic melting point, the highest recrystallization temperature, the highest self-diffusion activation energies, partially covalent bonding, the lowest vapor pressure...and great high-temperature strength. Some point to the higher W density as a detriment. But its much greater strengths enable W to meet stress requirements at high temperatures with less weight than its competitors. In general arguing rationally against W as the primary space-ultralloy component is difficult, if not impossible, and often humorous.

The most probable secondary metal is Re -- not only because of the salubrious "rhenium effect" in W but also because it approaches W in refractory metallic capabilities: Re is the next-highest-melting metal, with great strength and a very low vapor pressure -- comparable with that of Ta. Re also provides σ-phase (-WRe) precipitation strengthening as well as synergistic solution strengthening in W [2.35]. Of course Re also raises the recrystallization temperature of W and improves its ductility considerably especially with small amount of σ-phase precipitation.

In addition to Re solution effects HfC precipitation strengthening and ThO_2 dispersion strengthening separately are well known. They too increase W and W,Re-alloy recrystallization temperatures and ductility. And their synergistic effects warrant intensive investigation. But the use of pure Th

and/or Hf in nearly stoichiometric amounts to convert deleterious segregated O and C in W,Re alloys into productive separate phases "preferentially nucleated at dislocations, grain boundaries or interphase interfaces" requires immediate attention [2.32 to 2.35 and 2.130].

In powdered metallurgical methods very small quantities of comparatively low-melting (1960K) Th (and/or Hf 2400K or Zr 2130K) might serve to chemically activate sintering of W, Re powders at greatly reduced temperatures. During the sintering process the Th (and/or Hf or Zr) film would tend to spread over the W, Re-particle surfaces with their segregated O and C because of their great mutual affinities. [2.31 to 2.35 and 2.130]. And for the same reason of course the distributed Th (and/or Hf or Zr) would tend to getter these embrittling superficial impurities and deposit them in very refractory separate-phase particles "preferentially nucleated at dislocations, grain boundaries or interphase interfaces." Simultaneously, "gettering" grain-boundary-segregated and reacted O and C from the W particles should liberate W metal from superficial oxide and carbide compounds, increase its intergranular transport and thereby enhance its propensities to sinter (Balluffi, Coble...). But the resulting very refractory Th (and/or Hf or Zr) oxide and carbide particles should also strongly inhibit undesirable grain growth.

These mechanisms are of course not those proposed for conventional chemically activated sintering postulated for the simple model of a pure activator (Ni, Pd, Pt...) interacting predominantly intergranularly with pure-refractory-metal particles [2.131 to 2.138]. Based on this practically unattainable idealization "the electron concentration concept predicts the transition metals with nearly complete d electron subshells (i.e., Ni, Pd and Pt (8, 10 and 9 electrons out of 10 maximally)) to be better sintering

activators" [2.131, 2.132). Mechanistically "activated sintering of refractory metals with certain transition metal additives occurs because the additive lowers the energy barrier for refractory atom transport. The lower activation energy results in increased diffusion of the refractory metal through the additive. The additive remains segregated at the particle-particle contact points because of the unipolar solubility relationship. That is the refractory metal is soluble in the additive, but the additive is relatively insoluble in the refractory metal. The segregated lower melting additive provides a rapid short-circuit mass transport path throughout the sintering process" [2.137].

This isolated idealized refractory-metal, activator-metal relationship certainly simplifies theoretic considerations and provides heuristic value. But W powder used in supporting experiments contained 73 ppm C, 180 ppm N and 2090 ppm O [2.132]; a later Mo powder contained 18 ppm C and 1258 ppm O. For such impurities extreme grain-boundary segregation is probable as discussed in "Diffusion Effects in High-Temperature Creep." Also there the "strong influences of fractions of an atomic percent" of additives, impurities and reaction products on thermophysicochemical properties of refractory alloys received brief but emphatic attention [2.61,2.68 to 2.72, 2.130].

Apparently segregated impurities and micro-alloying agents deserve if not demand at least as much attention as pure refractory-metal, activator-metal combinations. In fact P, S, Cu and even Ni "segregation to interphase boundaries in liquid-phase sintered tungsten alloys" not only affect the sintering process impressively but also weaken the resulting W, Ni, Cu and W, Ni, Fe compactions [2.139]. So although Th (and/or Hf or Zr) fail to meet the pure-metal requirements of "nearly complete d electron subshells"

(two d electrons each) and "of the unipolar solubility relationship," they offer solutions to some very practical problems: They getter the boundary segregated and reacted O, C and other impurities that separate the nearly pure refractory metal from any activator metal. And they provide interfacially dispersed stable refractory-compound precipitates.

Amounts of segregated O and C to react with appropriately adjusted quantities of Th (and/or Hf or Zr) might be varied in original melt compositions [2.72] or by chemisorption on particles prior to sintering [2.140,2.141]. Suitable levels for truly efficient dispersion improvements are usually fractions of an atomic percent. Th (and/or Hf or Zr) reaction with O and C at very low concentrations in W,Re-alloy melts with subsequent precipitation is also a possibility. But of course the much higher vaporization tendencies of the micro-alloying agents compared with those of W and Re present a problem. Finally if these localized reaction techniques fall short of optimum ThO_2 and HfC requirements for W, Re, additive ultralloys, conventional addition methods can make up the differences. But such adjustments add to improvements already effected by gettering deleterious impurities and strategically dispersing them through micro-alloying with Th (and/or Hf or Zr).

Thus, compared with relatively inefficient random dispersion methods, the preceding highly specific approach to removing a problem and replacing it with an asset -- at the desired location [2.55] -- deserves further investigation. This is particularly true when the solution promises not only decreased creep for increased space power but also greater ductility and recrystallization resistance as well as improved powder-metallurgy processing.

2.11   REFERENCES

2.1   A. Hyder and P. Turchi: Preface to the Proceedings of the AFOSR
       Special Conference on Prime Power for High-Energy Space Systems,
       Norfolk, Virginia, February 1982.

2.2   NASA Lewis Research Center Conference: Future Orbital Power Systems
       Technology Requirements, NASA CP-2058, September 1978.

2.3   V. Barth: Physical and Mechanical Properties of Tungsten and
       Tungsten-Base Alloys, Battelle Report 127, March 1960.

2.4   G. Hoppin: Investigation of Joining the Refractory Metals Tungsten
       and Niobium, GE Contract with WADD, Materials Central, USAF, 1960 to
       1962.

2.5   IIT: Research on Development and Application of a Theory for Plastic
       Deformation of Cemented Alloys, Armour Research Foundation contract
       with WAL, U.S. Army, 1960 to 1962.

2.6   H. Ogden: Development of a Ductile Tungsten Sheet Alloy, BMI
       contract with Bu Weps, Navy, 1960 to 1962.

2.7   J. Ratliff, W. Gibeaut and H. Ogden: Tungsten Research and
       Development Review 1960-1962, Battelle DMIC Report 193, October 1963.

2.8   F. Foyle: Thoriated Rhenium-Tungsten Alloys for Electron Tube
       Applications, 7th National Conference on Tube Techniques, National
       Conference on Tube Techniques, National Advisory Group on Electron
       Devices, September 1964.

2.9   E. Savitsky, M. Tylkina and K. Pavarova: Rhenium Alloys,
       Izdatel'stvo "Nauk", Moscow, 1965.

2.10   P. Raffo and W. Klopp: Mechanical Properties of Solid-Solution and
       Carbide-Strengthened Arc-Melted Tungsten Alloys, NASA TN D-3248,
       February 1966.

2.11   M. Pridantsev: Structures and Properties of Heat-Resistant Metals
       and Alloys, Izdatel'stvo "Nauk", Moscow, 1967.

2.12   W. Klopp: Review of Ductilizing of Group VIa Elements by Rhenium and
       Other Solutes, NASA TN D-4955, 1968.

2.13   D. Novick: A Field Ion Microscope Investigation of the Tungsten-
       Rhenium-Oxygen System, Columbia University Ph.D. dissertation,
       University Microfilms, Ann Arbor, 1968.

2.14   D. Jacobson and A. Campbell: The Characteristics of Bare and
       Cesiated CVD 75 Percent Tungsten/(sic) 25 Percent Rhenium Electrodes,
       Record of the 1969 IEEE Thermionic-Conversion Specialists Conference
       (IEEE TCSC), October 1969.

2.15   V. Wilson: A Review of Thermionic Converter Tests, IEEE TCSC, 82,
       October 1969.

2.16   R. Hall, P. Raffo, W. Witzke and W. Klopp: Carbide Strengthening of
Tungsten and Molybdenum Alloys, Aerospace Structural Materials, NASA
LeRC Conference, November 1969.

2.17   M. Garfinkle: Effect of Rhenium Alloying on Lattice Dilation of
Group VI-A Refractory Metals, Mettallurgical Transactions, Volume 1,
April 1970.

2.18   R. Yoda, T. Itagaki and T. Hamada: Some Properties of Tungsten-
Rhenium Alloys, Japan Institute of Metals Journal, Volume 34,
November 1970.

2.19   M. Majdic and G. Wirth: Uber das Rekristallisationsverhalten Einer
mit Thorium-Oxid Dispersionsgeharteten Wolfram-Rhenium-Legierung im
Vergleich zu Reinem Wolfram, Journal of Less-Common Metals, Volume
24, 1971.

2.20   W. Klopp and W. Witzke: Mechanical Properties of a Tungsten -23.4
Percent Rhenium -0.27 Percent Hafnium-Carbon Alloy, Journal of Less-
Common Metals, Volume 24, 1971, also NASA TN D-6328.

2.21   R. Hilbert, V. Storhok, W. Chubb and D. Keller: Controlling the
High-Temperature Swelling of Uranium Oxide, IEEE Conference Record of
1971 Thermionic Conversion Specialist Conference (IEEE TCSC), October
1971.

2.22   M. Gavrilyuk: The Nature of Cold Brittleness in Refractory Metals of
Group VIa, Metallovedenie i Termicheskaya Obrabotka Metallov, Number
1, January 1972.

2.23   D. Jacobson: Emission Characteristics of Some Dilute Tungsten
Alloys, Metallurgical Transactions, Volume 3, May 1972.

2.24   W. Chubb, V. Storhok and D. Keller: Factors Affecting the Swelling
of Nuclear Fuels at High Temperatures, Nuclear Technology, Volume 18,
June 1973.

2.25   D. Quataert, C. Busse and F. Geiger: Long Time Behavior of High
Temperature Tunsten-Rhenium Heat Pipes with Lithium or Silver as
Working Fluid, Paper 4-4, Proceedings of the Interantional Heat Pipe
Conference, Stuttgent, 1973.

2.26   W. Witzke: The Effects of Composition on Mechanical Properties of W-
4Re-Hf-C Alloys, Metallurgical Transactions, Volume 5, February 1974,
also NASA TND-7210, April 1973.

2.27   W. Witzke: Effects of Composition on Mechanical Properties of W-4
Re-Hf-C Alloys, Metallurgical Transactions, Volume 5, February 1974
(also NASA TN D-7210).

2.28   Ye. Savitsky, V. Bykov, K. Povarova, L. Alekseyeva, S. Budagovskiy,
P. Makarov and I. Kondakhchan: Effect of Alloying with Niobium,
Rhenium and Osmium on the Physical Properties of Cast Tungsten Alloys

of Rare Metals with Special Physicochemical Properties, "Nauka" Press, 1975.

2.29   Ye. Savitsky, V. Cheokhovskoy, K. Povarova, V. Zaychenko, P. Makarov and V. Petukhov: Study and Applications of Rhenium Alloys, Issledovaniye i Prcmeneniye Splavov Reniya, "Nauka" Press, 1975.

2.30   E. Marmer, O. Gurvich and L. Mal'tseva: High-Temperature Materials, Freund Publishing, Holon, Israel, 1976.

2.31   J. Morris: Tungsten Rhenium Alloys in Space Nuclear Reactors, Air Force AFWAL TM-   , Arizona State University ERC-R-82005 (transmitted October, 1981).

2.32   J. Morris: Direct-Energy-Conversion Implications of Space Nuclear Reactors, Proceedings of the 17th IECEC, August 1982.

2.33   J. Morris: Ultralloys for Current and Future Space Power, Air Force AFWAL TM-   , Arizona State University ERC-R-83025 (transmitted June 1983).

2.34   J. Morris: Ultralloys for Nuclear Thermionic Conversion, 18th IECEC, August 1983.

2.35   J. Morris: Better, Cheaper In-Core Thermionic Energy Conversion with Pre-1973 Ultralloys, 19th IECED, August 1984.

2.36   O. Sherby: Factors Affecting the High Temperature Strength of Polycrystalline Solids, Acta Metallurgica 10, 135, 1962.

2.37   O. Sherby and P. Burke: Mechanical Behavior of Crystalline Solids at Elevated Temperature; Progress in Materials Science, Volume 13 (Incorporating Progress in Metal Physics), 324 to 390, 1968 (Porgamon Press).

2.38   F. Nabarro: in the Report of a Conference on Strength of Solids, The Physical Society, 75 to 90, 1948 (London).

2.39   C. Herring: Diffusional Viscosity of a Polycrystalline Solid, Journal of Applied Physics 21, 437 1950.

2.40   R. Coble: A Model for Boundary Diffusion Controlled Creep in Polycrystalline Materials, Journal of Applied Physics 34, 1679, 1963.

2.41   R. Coble: in High-Strength Materials, 706 to 723, Wiley and Sons, 1965.

2.42   J. Harper and J. Dorn: Viscous Creep in Aluminum Near Its Melting Temperatures, Acta Metallurgica 5, 654, 1957.

2.43   H. Luthy, A. Miller and O. Sherby: The Stress and Temperature Dependence of Steady-State Flow at Intermediate Temeprature for Pure Polycrystalline Aluminum, Acta Metallurgica 28, 169, 1980.

2.44 O. Sherby and C. Young: Factors Influencing the Strain-Rate, Temperature Dependence of the Flow Stress in Polycrystalline Solids; Rate Processes in Plastic Deformation of Materials (J. Li and A. Mukherjee, editors), 497, 1975 (ASM, Metals Park, Ohio).

2.45 W. Nix and B. Ilschner: Mechanisms controlling Creep of Single-Phase Metals and Alloys, Proceedings of the International Conference of Strength of Metals and Alloys (ICSMA), 1503, 1980 (Pergamon Press).

2.46 A. Arieli and A. Mukherjee: Power-Law Breakdown During High-Temperature Creep of FCC Metals, Creep and Fracture Engineering Materials and Structures, 97 to 111, 1981 (Pineridge Press, Swansea).

2.47 T. Langdon: Deformation at High Temperatures, Strength of Materials and Alloys (ICSMA 6), 1105 to 1119 1983 (Pergamon Press). Also Deformation of Polycrystalline Materials at High Temperatures, Proceedings of the 2nd Risø International Symposium on Metallurgy and Materials Science, September 1981.

2.48 J. Weertman: Theory of Steady-State Creep Based on Dislocation Climb, Journal of Applied Physics 26, 1213, 1955.

2.49 J. Weertman: Steady-State Creep Through Dislocation Climb, Journal of Applied Physics 28, 362, 1957.

2.50 J. Weertman: Creep of Indium, Lead and Some of Their Alloys with Various Metals, Transactions of the Metallurgical Society of AIME 218, 207, 1960.

2.51 F. Mohamed and T. Langdon: Transition from Dislocation Climb to Viscous Glide in Creep of Solid-Solution Alloys, Acta Metallurgica 22, 779, 1974.

2.52 J. Weertman: Theory of the Influence of Stacking-Fault Width of Split Dislocations on High-Temperature Creep Rate. Transactions of the Metallurgical Society of AIME 233, 2069, 1965.

2.53 T. Langdon and R. Vastava: An Evaluation of Deformation Models for Grain Boundary Sliding, Special Technical Publication (STP) 765, 435 to 451, American Society for Testing and Materials (ASTM), 1982.

2.54 A. Argon: Mechanisms and Mechanics of Fracture in Creeping Alloys, Recent Advances in Creep and Fracture of Engineering Materials and Structures, 1 to 51, 1982 (Pineridge Press, Swansea).

2.55 A. Argon: Intergranular Cavitation in Creeping Alloys, Scripta Metallurgica 17, 5, 1983.

2.56 C. Lau, A. Argon and F. McClintock: Stress Concentrations Due to Sliding Grain Boundaries in Creeping Alloys, STP 803 Volume 1, 1-551 to 1-572, ASTM, 1984.

2.57 M. Ashby and H. Frost: Deformation Mechanism Maps: Further Development and Case Studies, CUED/C/MATS/TR.90 Dec. 1981, Cambridge University.

2.58   N. Gjostein: Diffusion, The American Society for Metals, Metals Park, OH, 1973.

2.59   R. Balluffi:, Grain-Boundary Diffusion Mechanisms in Metals, Metallurgical Transactions A 13A, 2069, 1982.

2.60   D. Turnbull and R. Hoffman: The Effect of Relative Crystal and Boundary Orientations on Grain Boundary Diffusion Rates, Acta Metallurgica 2, 419, 1954.

2.61   N. Peterson: Grain-Boundary Diffusion in Metals, International Metals Review 28, 65 to 91, 1983.

2.62   S. Couling and R. Smoluchowski: Anisotropy of Diffusion in Grain Boundaries, Journal of Applied Physics 25, 1538, 1954.

2.63   B. Okkerse: Self-Diffusion of Gold (compared with Cu, Ag and Pb): Physical Review 103, 1246, 1956 (Also B. Okkerse, T. Tiedema and W. Burgers: Acta Metallurgica 3, 300, 1955).

2.64   R. Hoffman: Anisotropy of Grain Boundary Self Diffusion, Acta Metallurgica 4, 97, 1956.

2.65   W. Upthegrove and M. Sinnott: Grain Boundary Self-Diffusion of Nickel, Transations of the American Society for Metals 50, 1031, 1958.

2.66   R. Canon and J. Stark: Analysis of Penetration Data from Grain Boundary Diffusion Experiments, Journal of Applied Physics 40, 4361, 1969.

2.67   H. Gleiter: The Nature of Dislocations in High-Angle Grain Boundaries, Philosophical Magazine 36, 1109, 1977.

2.68   E. Hondros and P. Henderson: Role of Grain Boundary Segregation in Diffusional Creep, Metallurgical Transactions A 14A 521, 1983.

2.69   R. Honeycombe: Some Aspects of Micro-Alloying, Commemorative Lecture by the 28th Gold Medalist of the Japan Institute of Metals, Transactions of the Japan Institute of Metals 24, 177, 1983.

2.70   A. Waugh and M. Southon: Surface Analysis and Grain-Boundary Segregation Measurements Using Atom-Probe Techniques, Surface Science 89, 718, 1979.

2.71   F. Haessner (Editor): Recrystallization of Metallic Materials, Dr. Riederer Verlag GMbH, Stuttgart, 1978.

2.72   Ye. Savitsky, K. Povarova, P. Makarov and Ye. Zavarzina: Phase Composition, Structure and Properties of Vacuum-Melted W·C(Zr, Hf, Nb, Ta, Re) Alloys, Planseeberichte fur Pulvermetallurgie, Bd. 25, 168 to 185, 1977 (9th Plansee Seminar, Reutte).

2.73   T. Chuang, K. Kagawa, J. Rice and L. Sills: Overview No. 2, Nonequilibrium Models for Diffusive Cavitation of Grain Interfaces, Acta Metallurgica 27, 265 to 284, 1979.

2.74   A. Needleman and J. Rice: Overview No. 9, Plastic Creep Flow Effects in the Diffusive Cavitation of Grain Boundaries, Acta Metallurgica 28, 107 to 124, 1980.

2.75   M. Ashby and L. Brown (Editors):   Perspectives in Creep Fracture, Pergamon Press, 1983.

2.76   J. Tien and G. Ansell: Alloy and Microstructural Design, Academic Press, 1976.

2.77   L. Murr: Interfacial Phenomena in Metals and Alloys, Addison-Wesley Publishing Company, 1975.

2.78   O. Martin: A Derivation for the Thermochemical Equilibrium, Chemical Abstracts 37, 2250, 1943.

2.79   J. Rose: Dynamic Physical Chemistry, Pitman Press, 1961.

2.80   D. Gray (editor):   American Institute of Physics Handbook, McGraw-Hill Book Company, 1963.

2.81   G. Hatsopoulos and E. Gyftopoulos: Thermionic Energy Conversion, Volume II: Theory, Technology and Application, MIT Press, 1979.

2.82   T. Langdon and F. Mohamed: Characteristic of Independent and Sequential Creep Processes, Journal of the Australian Institute of Metals 22, 189 to 199, 1977.

2.83   P. Yavari, F. Mohamed and T. Langdon: Creep and Substructure Formation in an Al, 5% Mg Solid-Solution Alloy, Acta Metallurgica 29, 1495 to 1507, 1981.

2.84   C. Gandhi and M. Ashby: Overview No. 5, Fracture-Mechanism Maps for Materials Which Cleave: FCC, BCC and HCP Metals and Ceramics, Acta Metallurgia 27, 1565 to 1602, 1979.

2.85   C. Barrett, A. Ardell and O. Sherby: Influence of Modulus on the Temperature Dependence of the Activation Energy for Creep at High Temperatures, Transactions of the Metallurgical Society of AIME 230, 201, 1964.

2.86   M. Ashby: Boundary Defects and Atomistic Aspects of Boundary Sliding and Diffusional Creep, Sruface Science 31, 498, 1972.

2.87   T. Langdon and P. Yavari: An Investigation of Harper-Dorn Creep-II The Flow Process, Acta Metallurgia 30, 881, 1982.

2.88   P. Yavari and T. Langdon: Transition from Nabarro-Herring to Harper-Dorn Creep at Low Stress Levels, Scripta Metallurgica 11, 863, 1977.

2.89   P. Yavari, D. Miller and T. Langdon: An Investigation of Harper-Dorn Creep-I Mechanical and Microstructural Characteristics, Acta Metallurgica 30, 871, 1982.

2.90   S. Robinson and O. Sherby: Mechanical Behavior of Polycrystalline Tungsten at Elevated Temperature, Acta Metallurgica 17, 109, 1969.

2.91   J. Bird, A. Mukerjee and J. Dorn: Correlations Between High-Temperature Creep Behavior and Structure, Quantitative Relation Between Properties and Microstructure, Israel University Press, Jerusalem, 1969 (D. Brandon and A. Rosen, Editors).

2.92   F. Mohamed and T. Langdon: Transition from Dislocation Climb to Viscous Glide in Creep of Solid-Solution Alloys, Acta Meta. 22, 779, 1974.

2.93   P. Yayari and T. Langdon: An Examination of the Breakdown in Creep by Viscous Glide in Solid Solution Alloys at High Stress Levels, Acta Metallurgica 30, 281, 1982.

2.94   A. Cottrell in Relation of Properties to Microstructures, American Society for Metals, 131, 1954.

2.95   H. Luthy, A. Miller and O. Sherby: The Stress and Temperature Dependence of Steady-State Flow at Intermediate Temperature for Pure Polycrystalline Aluminum, Acta Metallurgica 28, 169, 1980.

2.96   R. Raj and M. Ashby: On Grain Boundary Sliding and Diffusional Creep, Metallurgical Transactions 2, 1113, 1971.

2.97   W. Cannon: The Contribution of Grain Boundary Sliding to Axial Strain During Diffusion Creep, Philosophical Magazine 25, 1489, 1972.

2.98   M. Ashby, R. Raj and R. Gifgins: Diffusion Controlled Sliding at a Serrated Grain Boundary, Scripta Metallurgica 4, 737, 1970.

2.99   M. Ashby: Boundary Defects and Atomistic Aspects of Boundary Sliding and Diffusional Creep, Surface Science 31, 498, 1972.

2.100   R. Gates: The Role of Grain Boundary Dislocations in Grain Boundary Sliding, Acta Metallurgica 21, 855, 1973.

2.101   R. Pond, D. Smith and P. Southerden in Proceedings of the 4th International Conference of Strength of Metals and Alloys 1, 378, 1976 (Laboratoire de Physique du Solide, E.N.S.M.I.M., Nancy, France).

2.102   R. Gifkins: Superplasticity, Creep and Grain-Boundary Sliding, Scripta Metallurgical 7, 27, 1973.

2.103   J. Weertman: Dislocation Climb Theory of Steady-State Creep, Transactions of the American Society for Metals 61, 681, 1968.

2.104 F. Crossman and M. Ashby: The Nonuniform Flow of Polycrystals by Grain-Boundary Sliding Accommodated by Power-Law Creep, Acta Metallurgica 23, 425, 1975.

2.105 R. Gifkins: The Effect of Grain Size and Stress Upon Grain-Boundary Sliding, Metallurgical Transactions A 8A, 1507, 1977.

2.106 M. Speight: The Role of Grain-Boundary Sliding in the Creep of Polycrystals, Acta Metallurgica 24, 725, 1976.

2.107 I.-W. Chen and A. Argon: Grain Boundary and Interphase Boundary Sliding in Power-Law Creep, Acta Metallurgica 27, 749, 1979.

2.108 T. Langdon: Grain Boundary Sliding as a Deformation Mechanism During Creep, Philosophical Magazine 22, 689, 1970.

2.109 R. Raj and M. Ashby: Intergranular Fracture at Elevated Temperature, Acta Metallurgica 23, 653, 1975.

2.110 R. Raj: Nucleation of Cavities at Second Phase Particles in Grain Boundaries, Acta Metallurgica 26, 995, 1978.

2.111 S. Argon, I.-W. Chen and C. Lau in Creep-Fatigue-Environment Interactions, 46, 1980 (edited by R. Pelloux and N. Stoloff, AIME, New York).

2.112 S. Argon: Formation of Cavities from Nondeformable Second-Phase Particles in Low Temperature Ductile Fracture, Journal of Engineering Materials and Technology 98, 60, 1976.

2.113 A. Evans: in Recent Advances in Creep and Fracture of Engineering Materials and Structures, 53, 1982 (edited by B. Wilshire and D. Owen, Pineridge Press, Swansea, U.K.).

2.114 N. Grant and A. Mullendorz: Deformation and Fracture at Elevated Temperatures, M.I.T. Press, Cambridge, Massachusetts, 1965.

2.115 I. Servi and N. Grant: Creep and Stress Rupture Behavior of Aluminum as a Function of Purity, Transactions of AIME (Journal of Metals) 230, 909, 1951.

2.116 A. Argon, I-W. Chen and C. Lau in Three-Dimensional Constitutive Relations and Ductile Fracture, 23, 1981 (edited by S. Nemat-Nasser, North Holland Publishing, Amsterdam).

2.117 I-W. Chen and A. Argon: Creep Cavitation in 304 Stainless Steel, Acta Metallurgica 29, 1321, 1981.

2.118 N. Grant: in Fracture, Volume 3, 483 to 533, 1971 (edited by H. Liebowitz, Academic Press, New York).

2.119 J. Rice: Time Dependent Fracture of Materials at Elevated Temperatures (S. Wolf, Editor), US Department of Energy Report CONF 79023 UC-25, 130, 1979 (Germantown, Md.).

2.120 T. Langdon: The Mechanical Properties of Superplastic Materials, Metallurgical Transactions A 13A, 689, 1982.

2.121 J. Gittus: Superplasticity: A Review of Data, ResMechanica 7, 127 to 201, 1983.

2.122 M. Suery: Metallurgie et Rheologie des Alliages Superplastiques Biphases, PhD Thesis, University of Metz, 1979.

2.123 T. Langdon: Fracture Processes in Superplastic Flow, Metal Science 16, 175, 1982.

2.124 T. Langdon: The Significance of the Dimensionless Constant in the Rate Equation for Superplastic Flow, Metallurgical Transactions A 13A, 2059, 1982.

2.125 V. Trefilov: Physical Nature of Brittle Failure of Metals, 26, 1965 (Kiev, USSR).

2.126 T. Kontorova: Plasticity of Metals, Translated from Problemy Prochnosti, Number 10, 107, 1977.

2.127 G. Samsonov: Comments on the Electronic Mechanism of Diffusion Processes in Metals and Alloys, Protective Coatings on Metals (USSR Translation) 4, 3, 1972.

2.128 R. Jaffee and G. Hahn: Structural Considerations in Developing Refractory Alloys, DMIC Report 182 (BMI), January 1963.

2.129 C. Lynch (NPAFB, Editor): Handbook of M _erials Science, CRC Press, 1974.

2.130 J. Morris: Ultralloys for High-Temperature High-Power Applications in Space, DOE Contract PE-AC21-83-MC20418, August 1984 (Arizona State University CR-R-84043).

2.131 G. Samsonov, I. Pryadko and L. Pryadko: A Configurational Model of Matter, Consultants Bureau, 1973 (New York).

2.132 R. German and Z. Munir: Enhanced Low-Temperature Sintering of Tungsten, Metallurgical Transactions A 7A, 1873, 1976.

2.133 P. Zovas, R. German, K. Kwang and C. Li: Activated and Liquid-Phase Sintering -- Progress and Problems, Journal of Metals 35, 28, 1983.

2.134 R. German: Diffusional Activated Sintering-Densification Microstructure and Mechanical Properties, The Interantional Journal of Powder Metallurgy and Powder Technology 19, 277, 1983.

2.135 C. Li and R. German: The Properties of Tungsten Processed by Chemically Activated Sintering, Metallurgical Transactions A 14A, 2031, 1983.

2.136 R. German and K. Churn: Sintering Atmosphere Effects on Ductility of W-Ni-Fe Heavy metals, Metallurgical Transactions A 15A, 747, 1984.

2.137   P. Zovas and R. German: Retarded Grain Boundary Mobility in Activated Sintered Molybdenum: Metallurgical Transactions A 15a, 1103, 1984.

2.138   R. German and B. Rabin: Enhanced Sintering Through Second Phase Additions, 1984 Powder Metallurgy Group Conference, October 1984, Harrogate, UK.

2.139   C. Lea, B. Muddle and D. Edmonds: Segregation to Interphase Boundaries in Liquid-Phase Sintered Tungsten Alloys, Metallurgical Transactions A 14A, 667, 1983.

2.140   T. Noda, T. Kainuma and M. Okada: Effect of Oxygen on Intergranular Brittlement of Molybdenum, Journal of the Japan Institute of Metals 48, 25, 1984

2.141   T. Noda, T. Kainuma and M. Okada: Oxygen Desorption from Grain Boundaries of Molybdenum During Vacuum Heating, Journal of Japan Institute of Metals 48, 30, 1984.

III. MATERIAL PROBLEMS FOR HIGH-TEMPERATURE, HIGH-POWER SPACE-CONVERSION SYSTEMS -- TABLES.

A presentation in table form points out some specific concerns for high-temperature application, especially regarding ductility and recrystallization.

Table 3.1

MATERIAL PROBLEMS FOR HIGH-TEMPERATURE, HIGH-POWER

SPACE ENERGY-CONVERSION SYSTEMS

TRENDS TOWARD HIGHER POWER -

HIGHER TEMPERATURES FOR LIGHTER WEIGHTS

MORE-REFRACTORY MATERIALS

FABRICATION AND SERVICE PROBLEMS

Table 3.2

MATERIAL PROBLEMS FOR HIGH-TEMPERATURE, HIGH-POWER

SPACE ENERGY-CONVERSION SYSTEMS

CERAMICS OFFER LIMITED FABRICATION

AND SERVICE ADAPTABILITY.

REFRACTORY ALLOYS MUST ADAPT

THEMSELVES AND CERAMICS TO

SYSTEM FABRICATION AND

SERVICE REQUIREMENTS.

Table 3.3

MATERIAL PROBLEMS FOR HIGH-TEMPERATURE, HIGH-POWER

SPACE ENERGY-CONVERSION SYSTEMS

MAJOR DIFFICULTIES FOR ULTIMATE REFRACTORY ALLOYS

DUCTILITY (FABRICATION AND SERVICE)

RECRYSTALLIZATION (FABRICATION AND SERVICE)

OTHER PROBLEMS INTENSIFIED BY HIGH

TEMPERATURE AND HARD VACUUM

(STRENGTH, CREEP, VAPORIZATION

THERMAL EXPANSION, DIFFUSION,

CHEMICAL REACTION...)

Table 3.4

MATERIAL PROBLEMS FOR HIGH-TEMPERATURE, HIGH-POWER
SPACE ENERGY-CONVERSION SYSTEMS

ULTIMATE REFRACTORY ALLOYS COMPRISE

ULTIMATE REFRACTORY COMPONENTS.

HIGHEST-MELTING, LEAST-VAPORIZING METALS

METAL	MELTING, K	2000K TORR
BODY-CENTERED-CUBIC (BCC)		
TUNGSTEN (W)	3650	4×10^{-12}
TANTALUM (T_A)	3270	5×10^{-11}
MOLYBDENUM (M_0)	2890	2×10^{-7}
NIOBIUM (N_B)	2750	5×10^{-9}
HEXAGONAL CLOSE-PACKED (HCP)		
RHENIUM (R_E)	3450	1×10^{-10}
OSMIUM (O_S)	~ 3300	~ 3×10^{-10}
RUTHENIUM (R_U)	~ 2700	1×10^{-6}
FACE-CENTERED-CUBIC (FCC)		
IRIDIUM (I_R)	2720	2×10^{-7}
RHODIUM (R_H)	2240	~ 1×10^{-4}

Table 3.5

MATERIAL PROBLEMS FOR HIGH-TEMPERATURE, HIGH-POWER

SPACE ENERGY-CONVERSION SYSTEMS

HIGHEST-MELTING, LEAST-VAPORIZING METAL CRYSTALS

BCC: TUNGSTEN

HCP: RHENIUM

FCC: IRIDIUM

DELETERIOUS INTERSTITIAL IMPURITIES

OXYGEN, CARBON, NITROGEN AND HYDROGEN

EFFECTIVE LOW-VAPOR-PRESSURE GETTERS FOR INTERSTITIALS

HAFNIUM AND THORIUM (MULTIPLY BENEFICIAL

DISPERSED REFRACTORY INTERSTITIAL PRODUCTS)

PRIMARY PROBLEMS

DUCTILITY

RECRYSTALLIZATION (NUCLEATION OR PRIMARY

RECRYSTALLIZATION AND GRAIN GROWTH)

Table 3.6

MATERIAL PROBLEMS FOR HIGH-TEMPERATURE, HIGH-POWER

SPACE ENERGY-CONVERSION SYSTEMS

DUCTILITY: TRACE-IMPURITY EFFECTS

INTERSTITIALS (ESPECIALLY GRAIN-BOUNDARY-SEGREGATED

INTERSTITIAL PRODUCTS) GREATLY REDUCE

DUCTILITY (IN THE FOLLOWING ORDERS).

VIA GROUP (C_R, M_O, W): CARBON (MOST EMBRITTLING),

OXYGEN, NITROGEN AND HYDROGEN

VA GROUP (V, N_B, T_A): HYDROGEN (MOST EMBRITTLING),

NITROGEN, OXYGEN AND CARBON

RECRYSTALLIZATION GREATLY REDUCES DUCTILITY BY

LOCALIZING BRITTLE INTERSTITIAL PRODUCTS IN GRAIN

BOUNDARIES AND INCREASING THEIR INTERGRANULAR

CONCENTRATIONS THROUGH GRAIN-GROWTH REDUCTION

OF THE TOTAL INTERGRANULAR SURFACE.

Table 3.7

MATERIAL PROBLEMS FOR HIGH-TEMPERATURE, HIGH-POWER

SPACE ENERGY-CONVERSION SYSTEMS

DUCTILITY AND RECRYSTALLIZATION OF HIGH-PURITY REFRACTORY METALS

o W(BCC), R_E(HCP) AND I_R(FCC) WERE SELECTED AS HIGHEST-MELTING, LEAST-
   VAPORIZING EXAMPLES OF THEIR CRYSTAL SPECIES.

o W (VIA), R_E (VIIA) AND I_R (VIII) REPRESENT DIFFERENT CHEMICAL GROUPS.

o FEW RECRYSTALLIZATION RESULTS EXIST FOR HIGH-PURITY W, R_E AND I_R.

o ZONE REFINING PURIFIES W, R_E AND I_R BY IMPURITY VAPORIZATION AS WELL
   AS SEGREGATION.

o LOW VAPORIZATION OF W, R_E AND I_R ENABLES VERY-HIGH-TEMPERATURE
   OBSERVATION OF RECRYSTALLIZATION BY THERMIONIC-EMISSION MICROSCOPY.

o W, R_E AND I_R ARE EXCELLENT C_S-DIODE ELECTRODES: W, 25 R_E SERVES WELL
   IN HIGH-TEMPERATURE HEAT PIPES ("HIGH-TEMPERATURE, HIGH-POWER SPACE
   ENERGY-CONVERSION SYSTEMS").

o R_E AND I_R BOTH IMPROVE DUCTILITY AND RECRYSTALLIZATION RESISTANCE IN
   HIGH-STRENGTH, LOW-CREEP W ALLOYS.

o W, R_E AND I_R COULD BE MAJOR COMPONENTS IN ULTIMATE SPACE ALLOYS.

Table 3.8

MATERIAL PROBLEMS FOR HIGH-TEMPERATURE, HIGH-POWER

SPACE ENERGY-CONVERSION SYSTEMS

RECRYSTALLIZATION AND DUCTILITY STUDIES

(POLY-, BI- AND SINGLE-CRYSTAL SAMPLES)

HIGH-TEMPERATURE STUDIES

ZONE REFINING

ISOTHERMAL ANNEALING

THERMIONIC-EMISSION MICROSCOPY

MASS SPECTROMETRY AND SPECTROPHOTOMETRY

HOT HARDNESS AND ELECTRICAL RESISTIVITY

ROOM-TEMPERATURE STUDIES

STANDARD METALLOGRAPHY

ELECTRON TRANSMISSION MICROSCOPY

CHEMICAL ANALYSES (AUGER, ELECTRON PROBE....)

TENSILE, BENDING, HARDNESS, RESISTIVITY....

THEORETIC AND CORRELATIVE ANALYSES

Table 3.9

RECRYSTALLIZATION

CRYSTALLINE EQUILIBRIUM -

OBTAINS PRACTICALLY AT THE CENTER OF

A HUGE PURE FLAWLESS SINGLE CRYSTAL.

THERMODYNAMICALLY UNSTABLE LATTICE STATES -

RESULT FROM CHEMICAL IMPURITIES AND

PHYSICAL IMPERFECTIONS SUCH AS

POINT DEFECTS, DISLOCATIONS AND

GRAIN BOUNDARIES AS WELL AS EXTERNAL SURFACES.

FREE-ENERGY REDUCTION -

DRIVES RECRYSTALLIZATION AND ITS

"ZONE-REFINING" PROCLIVITIES.

Table 3.10

RECRYSTALLIZATION

REARRANGEMENT AND REDUCTION OF LATTICE IMPERFECTIONS

BELOW THE MATERIAL MELTING POINT LOWERS FREE ENERGY:

1. AGGLOMERATION, REACTION, ULTIMATELY ANNIHILATION OF POINT DEFECTS:

2. SHRINKAGE OF DISLOCATION LOOPS AND DISLOCATION ANNIHILATION:

3. DISLOCATION REARRANGEMENT IN LOW-FREE-ENERGY CONFIGURATIONS:

4. IMPERFECTION REACTIONS PRODUCING LATTICE REGIONS CAPABLE OF GROWTH;

5. GRAIN-BOUNDARY ABSORPTION OF POINT DEFECTS AND DISLOCATIONS:

6. DIMINUTION OF THE TOTAL INTERGRANULAR SURFACE.

1 AND 2 ARE "RECOVERY." 3 CAN BE EITHER "POLYGONIZATION" YIELDING
SUBGRAINS WITH LOW-ANGLE BOUNDARIES OR "NUCLEATION." 4 IS "NUCLEATION,"
ALSO TERMED "PRIMARY RECRYSTALLIZATION." 5 AND 6 ARE "GRAIN GROWTH."

Table 3.11

RECRYSTALLIZATION

COMPRISES

"NUCLEATION" OR "PRIMARY RECRYSTALLIZATION"

AND

"GRAIN GROWTH."

HOWEVER

"FORMATION AND MIGRATION OF LARGE-ANGLE BOUNDARIES"

SEEMS A MORE APPROPRIATE DEFINITION BECAUSE

"SOME RECRYSTALLIZATION PROCESSES OCCUR WITHOUT NUCLEATION."

Table 3.12

RECRYSTALLIZATION

NUCLEATION IS THE SELECTIVE GROWTH OF
HIGHLY MISORIENTED SUBGRAINS THROUGH
BOUNDARY MIGRATION AND/OR
COALESCENCE – AS INDICATED BY EXTENSIVE OBSERVATIONS,

KINETICS OF SUCH SUBGRAIN
COALESCENCE AND BOUNDARY-MIGRATION PROCESSES ARE
COMPARATIVELY UNCERTAIN.

Table 3.13

RECRYSTALLIZATION

GRAIN-GROWTH VELOCITY
EQUALS THE PRODUCT OF THE
BOUNDARY MOBILITY AND THE
RESULTANT DRIVING FORCE.

COLD WORK PRODUCES A DRIVING
FORCE EQUAL TO THE FREE-ENERGY-
DENSITY DIFFERENCE ACROSS THE
INTERGRANULAR REGION WHICH
IS PROPORTIONAL TO THE
IMPERFECTION-DENSITY DIFFERENCE
ACROSS THE MIGRATING BOUNDARY.

Table 3.14

RECRYSTALLIZATION

DRIVING FORCES FOR GRAIN-BOUNDARY MIGRATION

ORIGIN	EQUATION	ESTIMATED MAGNITUDE (N/m^2)
STORED ENERGY	$\Delta\rho F$	10^7
REVERSED-CAPILLARY	$2\gamma f/r$	10^6
ELECTRIC	λE	10^5
CAPILLARY	$2\gamma/r$	10^4
SURFACE ENERGY	$2\Delta\gamma/d$	10^4
MAGNETIC	$(\frac{1}{2})\Delta\mu H^2$	10^3
MECHANICAL	$\theta\sigma$	10^3
TEMPERATURE GRADIENT	$\delta S_V T$	10^2
ELASTIC ENERGY	$(\frac{1}{2})\Delta s\sigma^2$	10^2
ELECTROMIGRATION	$2nq\rho Z^*J$	10^2

MASTELLER AND BAUER: RECRYSTALLIZATION OF METALLIC MATERIALS

Table 3.15

RECRYSTALLIZATION

DRIVING-FORCE SYMBOLS

$\Delta\rho$ = DIFFERENCE BETWEEN DISLOCATION DENSITY (M^{-2}) IN TWO ADJACENT GRAINS DEFINING THE BOUNDARY, Γ = DISLOCATION LINE ENERGY (J/m), γ = RADIUS OF CURVATURE OF BOUNDARY (M), λ = NET ELECTRIC CHARGE PER UNIT BOUNDARY AREA (C/m^2), E = ELECTRIC FIELD (V/m), $\Delta\gamma$ = DIFFERENCE BETWEEN SURFACE ENERGY OF TWO ADJACENT GRAINS DEFINING THE BOUNDARY (J/m^2), d = SPECIMEN THICKNESS (m), $\Delta\mu$ = DIFFERENCE BETWEEN MAGNETIC PERMEABILITY IN TWO ADJACENT GRAINS DEFINING THE BOUNDARY (H/m), H = MAGNETIC FIELD (A/m), θ = MISORIENTATION BETWEEN GRAINS DEFINING A (LOW-ANGLE) BOUNDARY (RADIANS), σ = STRESS FIELD (Pa), n = NUMBER OF ATOMS PER GRAIN BOUNDARY AREA (M^{-2}), S = ENTROPY ($J/°Cm^3$), ∇ T = TEMPERATURE GRADIENT (°C/m), Δs = DIFFERENCE BETWEEN ELASTIC COMPLIANCE CONSTANTS IN TWO ADJACENT GRAINS DEFINING THE BOUNDARY (m^2/N), q = ELASTIC CHARGES (C), ρ = ELECTRICAL RESISTIVITY (Ωm), Z^* = (NORMALIZED) DIFFERENCE BETWEEN (ELECTRON) SCATTERING CROSS SECTIONS IN THE ACTIVATED AND GROUND STATES (DIMENSIONLESS), J = CURRENT DENSITY (A/m^2), AND δ = GRAIN BOUNDARY THICKNESS.

Table 3.16

RECRYSTALLIZATION

DRAGGING FORCES, WHICH

OPPOSE GRAIN-BOUNDARY MIGRATION,

DERIVE FROM

SOLUTE ATOMS,

PRECIPITATES,

DISPERSED PARTICLES,

SURFACE GROOVES . . . .

PINNING CAN RESULT FROM

CONCENTRATED DRAG CONFIGURATIONS.

Table 3.17

RECRYSTALLIZATION

SPECIFIC MOBILITY (INVERSE DRAG COEFFICIENT) CHARACTERIZES BOUNDARY MIGRATION FOR EACH DRIVING FORCE.

MOBILITIES CAN BE COMPLEX FUNCTIONS OF VELOCITY.

APPROPRIATE MOBILITY SUMMATIONS CORRESPOND TO RESULTANTS OF DRIVING AND DRAGGING FORCES.

Table 3.18

RECRYSTALLIZATION

THERMAL ACTIVATION

$\Delta g = \Delta h - T \Delta s \longrightarrow$ $\longleftarrow \Delta g \longrightarrow$

BOUNDARY MIGRATION

NET ATOM FLOW

LATTICE 1 (VERY THIN BOUNDARY) LATTICE 2

FREE ENERGY

DISTANCE
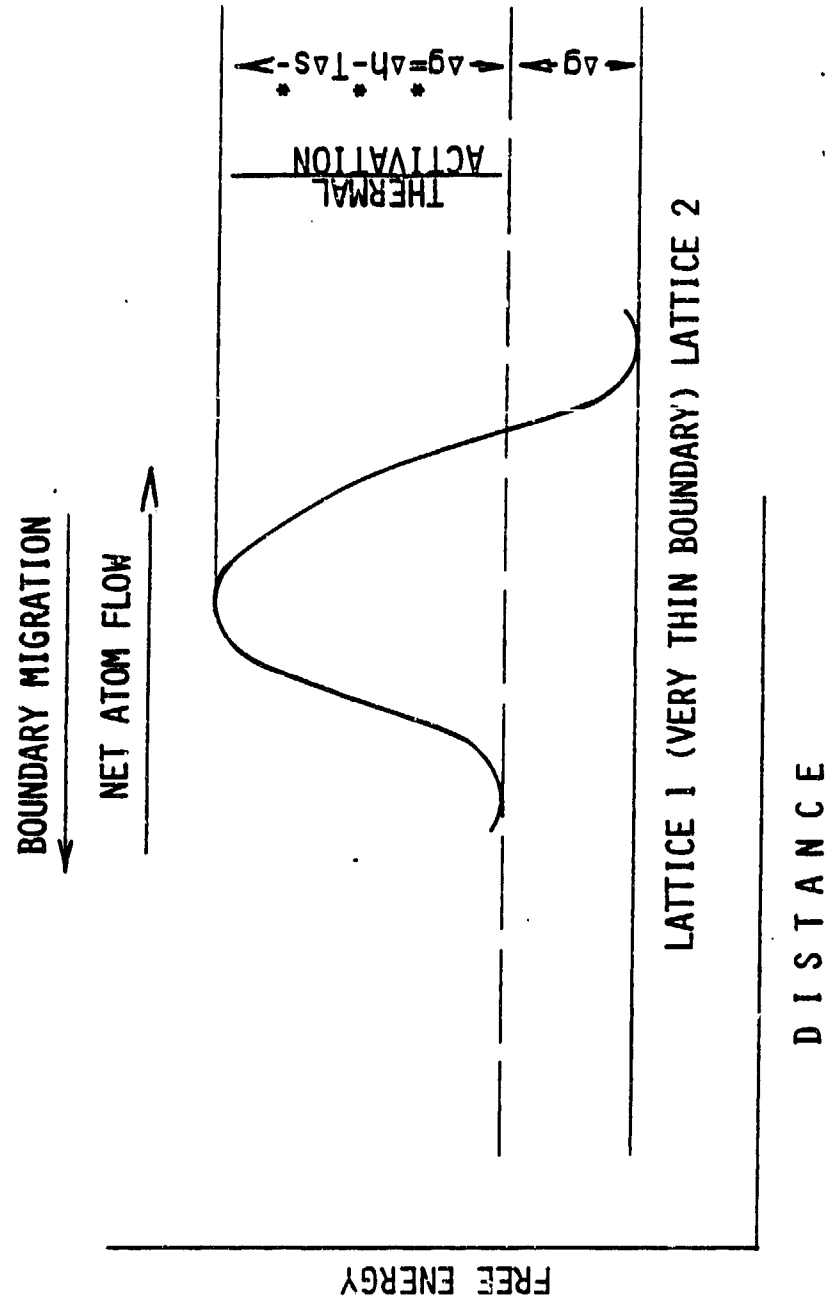
Table 3.19

RECRYSTALLIZATION
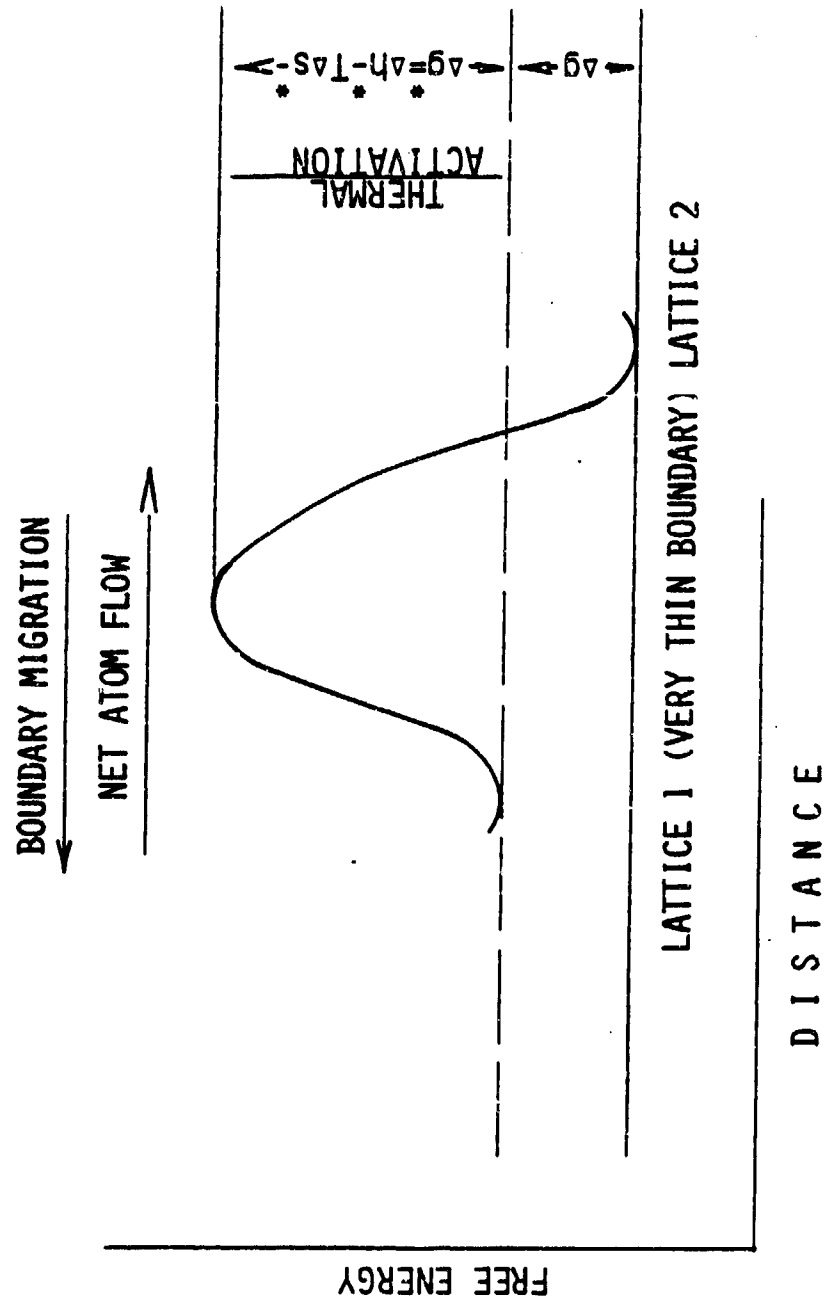
Table 3.20

RECRYSTALLIZATION

1-TO-2 ATOM FLOW →

$\nu_1 \exp(-g^*/kT)$

2-TO-1 ATOM FLOW →

$\nu_2 \exp[-(\Delta g^* + \Delta g)/kT]$

$\nu_1 = \nu_2 = \nu$ = LATTICE-ATOM OSCILLATORY FREQUENCY

NET BOUNDARY-

MIGRATION RATE $= v = \nu \lambda [1 - \exp(-\frac{\Delta g}{kT})] \exp(-\frac{\Delta g^*}{kT})$

λ = EFFECTIVE ATOM DISPLACEMENT THROUGH THE BOUNDARY

$\Delta g/kT << 1$ FOR PURE-METAL RECRYSTALLIZATION

BOUNDARY-MIGRATION RATE $= v = \nu \lambda (\frac{\Delta g}{kT}) \exp(-\frac{\Delta g^*}{kT})$

Table 3.21

RECRYSTALLIZATION

CRYSTAL-STEP MODEL FOR GRAIN BOUNDARY MIGRATION

<u>ASSUMPTIONS:</u> CLOSELY PACKED (FCC) PLANES END AT BOUNDARIES IN PERIODIC STEPS HAVING KINKS WHICH CAN RELEASE OR RECEIVE ATOMS THAT DIFFUSE THROUGH INTERGRANULAR REGIONS. Δg^* IS THE SUM OF FREE ENERGIES FOR TRANSITIONS OF SUCH ATOMS; δ IS THE GRAIN-BOUNDARY WIDTH, GREATER THAN SINGLE-JUMP λ. f_1 AND f_2 ARE POSITIVE FUNCTIONS OF STEP DENSITIES ON OPPOSING BOUNDARY SURFACES AND OF VACANCY EFFECTS. THEN –

$$\psi = \frac{\lambda}{\delta} [1 + \frac{\lambda}{\delta} (\frac{1}{f_1} + \frac{1}{f_2})]^{-1} < 1$$

AND –

GRAIN-BOUNDARY MIGRATION RATE $= v = \psi \nu \lambda (\frac{\Delta g}{kT}) \exp (- \frac{\Delta g^*}{kT})$

Table 3.22

RECRYSTALLIZATION

VACANCY MODELS FOR GRAIN-BOUNDARY MIGRATION

ASSUMPTIONS: MIGRATION VELOCITY INCREASES WITH RISING BOUNDARY
VACANCY FRACTION C_m - AS INDICATED BY NUMEROUS EXPERIMENTS:
DIFFUSION JUMPS ACROSS BOUNDARIES OCCUR THROUGH VACANCY-SITE
CHANGING PROCESSES. BECAUSE INSTANTANEOUS C_m's DEPEND ON VACANCY
INJECTION, COLLECTION AND EJECTION MECHANISMS, THEY ARE COMPLEX
FUNCTIONS OF BOUNDARY VELOCITIES AND TEMPERATURES AS WELL AS
VACANCY SOURCE AND SINK EFFECTS. THEN -

GRAIN-BOUNDARY
MIGRATION RATE

$$= V = C_m \, \nu \, \lambda \, \left(\frac{\Delta g}{kT}\right) \exp\left(-\frac{\Delta g^\star}{kT}\right)$$

Table 3.23

RECRYSTALLIZATION

-SATURATION MODEL FOR GRAIN-BOUNDARY MIGRATION

ASSUMPTIONS: DISLOCATION PROCESSES PROPOSED BY
LI (1961) AND MODIFIED BY GRABSKI (1969) RESULT
IN ALLOWED MATERIAL TRANSPORT ONLY ACROSS AN
"ACTIVE CROSS SECTION" FRACTION σ OF THE GRAIN-
BOUNDARY SURFACE. THUS SATURATION LIMITS THE
MIGRATION VELOCITY:

GRAIN-BOUNDARY
MIGRATION RATE $\equiv V = \sigma \nu \lambda \left(\frac{\Delta g}{kT}\right) \exp\left(-\frac{\Delta g^*}{kT}\right)$

Table 3.24

RECRYSTALLIZATION

GRAIN GROWTH OF TWO-PHASE ALLOYS

(HORNBOGEN: METALL 29, 247, 1975)

ELEVATED TEMPERATURES ACCENTUATE RECRYSTALLIZATION OF TWO-PHASE MICROSTRUCTURES DRIVEN BY INTERFACIAL ENERGY DENSITIES WHICH ARE FUNCTIONS OF GRAIN SIZE $r_{\alpha\alpha}$. THEN FOR BOUNDARY ($D_{\alpha\alpha}$ OR $D_{\alpha\beta}$), DISLOCATION-CORE PIPE (D_p) OR VOLUME (D_V) DIFFUSION SIMPLE GROWTH, TIME LAWS OBTAIN:

$r_{\alpha\alpha} \propto (D_{\alpha\alpha}t)^1$ PRIMARY OR SECONDARY RECRYSTALLIZATION

$r_{\alpha\alpha} \propto (D_{\alpha\alpha}t)^{\frac{1}{2}}$ GRAIN GROWTH (RARELY OBSERVED)

$r_p \propto (D_V t)^{\frac{1}{3}}$ DISPERSED-PARTICLE GROWTH (OFTEN SEEN)

$r_{\alpha\beta} \propto (D_{\alpha\beta}t)^{\frac{1}{4}}$ DUPLEX-STRUCTURE GROWTH (GRAIN-SIZE DIFFUSION DISTANCES FOR DUPLEX MICROSTRUCTURES RESULT IN RELATIVELY STABLE FINE-GRAINED ALLOYS.)

Table 3.25

RECRYSTALLIZATION

THERMAL STABILITY OF DUPLEX ALLOYS

(HORNBOGEN: METALL 29, 247, 1975)

NORMAL-GRAIN AND DUPLEX-STRUCTURE GROWTHS

SUCCUMB TO DISPERSED-PARTICLE CONTROL WHEN

DRIVING AND PINNING FORCES ARE EQUAL. THEN -

$$r_{\alpha\alpha}^{crit.}(t) = A \cdot \frac{r_p(t)}{f} = A^* \cdot \frac{(D_\gamma t)^{1/3}}{f}$$

WHERE A's ARE GEOMETRIC FACTORS DEPENDENT ON

LOCAL-PARTICLE SHAPE AND SIZE DISTRIBUTIONS.

THE DISPERSED-PARTICLE VOLUME FRACTION f THAT

STABILIZES GROWTH DECREASES CONSIDERABLY WITH

PREDOMINANT GRAIN-BOUNDARY PARTICULATE LOCATION.

Table 3.26

RECRYSTALLIZATION

APPROXIMATE THERMAL BOUNDARIES FOR ALLOYS

HALF THE ABSOLUTE MELTING POINT ($0.5T_M$) OFTEN INDICATES IMPORTANT INCIPIENCE OF THERMALLY ACTIVATED PROCESSES.

BELOW $0.3T_M$ TO $0.4T_M$ SHORT-RANGE (ELECTRONIC, STACKING-FAULT, LOCAL-ORDER) INTERACTIONS GENERALLY DOMINATE.

LONGER-RANGE SOLUTE, DISLOCATION INTERACTIONS CONTINUE THEIR INFLUENCES TO $0.5T_M$ OR HIGHER.

ABOVE $0.75T_M$ to $0.8T_M$ INCREASED MOBILITY OF SOLUTE ATOMS GREATLY REDUCES THEIR HINDRANCE OF DISLOCATION MOVEMENT.

ARRHENIUS RELATIONS FOR GRAIN-BOUNDARY MIGRATION VELOCITIES OFTEN BREAK AT $\sim 0.8T_M$ AND EXHIBIT MUCH LOWER ACTIVATION ENERGIES IN THE HIGHER-TEMPERATURE RANGE.

REFRACTORY-DISPERSION STRENGTHENING GENERALLY EXCELS FOR APPLICATIONS OF ALLOYS NEAR THEIR MELTING POINTS.

Table 3.27

RECRYSTALLIZATION WITH ITS DIRECT AND SIDE EFFECTS

EXERTS COMPLEX INFLUENCES ON STRENGTH, CREEP, COMPATIBILITY...

AND DUCTILITY OF REFRACTORY ALLOYS. SUCH PROPERTIES ARE MAJOR

CONSIDERATIONS IN ULTRATHERMAL APPLICATIONS.

BUT DUCTILITY - AND RECRYSTALLIZATION - ARE PRIMARY

PARAMETERS IN THE CAPABILITY OF REFRACTORY ALLOYS TO ADAPT

THEMSELVES AND CERAMICS TO FABRICATION AND SERVICE REQUIREMENTS.

AND IN THAT LIGHT THIS PRESENTATION DISCUSSED THE

GENERAL BACKGROUND, APPROACH AND ANALYTIC CONTEXT FOR THE STUDY

OF REFRACTORY-ALLOY RECRYSTALLIZATION AS A CRITICAL MECHANISM

IN MATERIAL PROBLEMS FOR HIGH-TEMPERATURE, HIGH-POWER SPACE

ENERGY-CONVERSION SYSTEMS.

IV. TUNGSTEN, RHENIUM ADDITIVE ALLOYS FOR HIGH TEMPERATURE SPACE APPLICATIONS.

4.1 ABSTRACT

Some of the primary needs for crucial future space applications are increasing power levels and densities. Refractory, additive alloys of ultimate thermal capabilities promise to provide these increasing power levels and densities. The high temperatures possible with such ultralloys enable greater heat rejection, hence lighter, denser, more mobile space systems. Great creep strengths, minimal vaporization rates, high recrystallization temperatures, substantial conductivity, fabricability, serviceability and ductility are prime requisites. The most refractory element, tungsten (W) would be the obvious choice but brittleness impedes progress with this super metal. However, in combination with rhenium (Re) as well as very low concentrations of hafnium carbide (HfC) and thoria (ThO_2), W becomes fabricable, ductile even after welding and improves in resistance to creep and recrystallization. W, Re combinations exhibit local ductility maxima at about 3% Re and at about 15%-18% Re. ThO_2 and HfC additions in the order of 1 and 0.3% respectively, further heighten W, Re ductilities, creep strengths and recrystallization temperatures.

We propose to investigate these ultralloys by standard characterization, metallographic and strength of materials procedures as well as by sophisticated and accurate high temperature methods such as thermionic emission and high temperature, high vacuum mechanical testing. Some anticipated advancements appear possible with W, Re, ThO_2, HfC alloys for high temperature space applications.

4.2 INTRODUCTION

There are a variety of potential missions, such as space based manufacturing, high capacity communications, outer planetary orbiters and lunar and planetary bases that appear to demand compact high power, very long life power units which are independent of sunlight. In general, the most intensive energy processing in any spacecraft occurs in the source and conversion systems for primary space power. There, higher temperatures translate into less weight, greater capability and increased mobility essential, particularly in military missions.

4.2.1 Projected space requirements for high temperature materials

Cohen [4.1] presents a tabulation of potential high power requirements for the United States national defense. For space based systems, high power levels must be achieved at significantly higher values of specific power (W/kg) and energy (W-Hr/kg) than are presently available to satisfy defense needs for survivability. Table 4.1 gives a list of the potential high power requirements.

The Soviet development of Space Nuclear Reactors [4.2] (SNR's) aims at military goals. The USSR-SNR program is aimed at achieving prime power sources at Megawatt levels and beyond and quite obviously the US-SNR program is also expected to follow suit and develop these high energy source systems for defense utilization. The SP-100 program [4.3] contemplates the advantages of the demonstrated technology accumulation for in-core Thermionic Energy Conversion (IC-TEC) in the selection of an appropriate SNR [4.4] approach. Such current and prospective developments of high temperature, high power space energy conversion systems pose critical material problems.

APPLICATION	POWER LEVEL
SPACE-BASED RADARS	5 TO 400 Kw
SURVEILLANCE	30 TO 100 Kw
COMMUNICATIONS	100 Kw
OTV (NEP)	>100 Kw
JAMMERS	70 to 200 Kw
LASERS	10 TO 100 Mw PULSED
PARTICLE BEAMS	10 TO 100's Mw PULSED
ADVANCED CONCEPTS	1 TO 100's Mw PULSED

Table 4.1 Department of defense potential high power requirements.

Accordingly, ultimate alloys are extremely important and almost mandatory for future orbital power systems technology requirements [4.5]. If there is a single general trend that applies to the various combinations of heat sources and conversion methods, it is the one toward higher source temperature and higher sink temperature and consequently lighter weight systems. Higher sources and sink temperatures means developing materials with superior properties at high tempeatures and for this, high temperature materials data is of prime importance. This emphasizes anticipating and solving material problems for high temperature space applications.

4.2.2 Characteristics of ultimate space materials

At high temperatures, ceramic materials become more electrically conductive and this precludes their effective use to transfer heat to energy converters while blocking electric transport. Even when solid insulators function adequately at high temperatures, their comparitive mechanical intransigence limits the fabricability and service adaptability. Thus refractory alloys must in general accomodate ceramics as well as themselves to system fabrication and service requirements. However, refractory alloys suffer from ductility deficiencies and recrystallization effects. Other complications arise from intensified influences of high temperatures and hard vacuum on strength, creep, diffusion, segregation, chemical reaction, vaporization and other thermophysical phenomena.

To start with, we can examine the highest melting, least vaporizing metals listed in Table 4.2.

ATOMIC NUMBER	MATERIAL (SYMBOL)	APPROXIMATE MELTING POINT, °K	APPROXIMATE VAPOR PRESSURE AT 2000°K, TORR
40	ZIRCONIUM (Zr)	2130	2×10^{-6}
41	NIOBIUM (Nb)	2760	5×10^{-9}
42	MOLYBDENUM (Mo)	2890	2×10^{-7}
43	TECHNETIUM (Tc)	2400	3×10^{-7}
44	RUTHENIUM (Ru)	2700	1×10^{-6}
72	HAFNIUM (Hf)	2400	2×10^{-6}
73	TANTALUM (Ta)	3270	5×10^{-11}
74	TUNGSTEN (W)	3640	4×10^{-12}
75	RHENIUM (Re)	3450	1×10^{-10}
76	OSMIUM (Os)	3320	$< 3 \times 10^{-10}$
77	IRIDIUM (Ir)	2720	2×10^{-7}
90	THORIUM (Th)	1960	3×10^{-6}
	ALUMINA (Al$_2$O$_3$)	2320	6×10^{-6}
	THORIA (ThO$_2$)	3490	APPROXIMATELY EQUAL TO THAT OF MOLYBDENUM

*"HIGHEST OF THE OXIDES"

| | HAFNIUM CARBIDE (HfC) | 4120 | OVER TWO ORDERS OF MAGNITUDE LOWER THAN THAT OF MOLYBDENUM, NEARLY FOUR WITH EXCESS CARBON |

Table 4.2 List of high melting, low vaporizing materials.

4.2.2.1 The primary components, tungsten and rhenium

Tungsten is the most refractory metal. Iridium and rhenium added to tungsten increase its ductility, strength and resistance to creep and recrystallization, as will be seen later.

Tungsten is a body centered cubic element with a 2000°K vapor pressure of 4×10^{-12} torr and a melting point of 3683°K. Its ductile to brittle transition occurs well above room temperature and it begins to recrystallize below 40% of its melting point which further complicates manufacturing and service. Even today, brittleness and difficult fabricability often overshadow the peerless high temperature properties of W.

Rhenium strengths apparently are the only ones among the metals to approach or exceed those of W. However, in contrast to tungsten, ductile rhenium results from vacuum annealing. But rhenium exhibits extremely high work hardenability with very little deformation, often requiring repeated vacuum annealing during fabrication.

W-Re, W-Ru, W-Hf, W-Hf-C and WB were some of the alloy systems investigated by General Electric Company [4.6] for their flow and fracture behavior at various temperatures. Each of the alloys was initially prepared by a vacuum melting and was then extruded and rolled to a sheet material for subsequent mechanical property evaluations. The most significant finding from the property studies was the exceptional combination of strength and ductility shown by a W-27%Re alloy with some sigma phase present in the as rolled structure. The solubility of rhenium in tungsten is about 26% as shown in Figure 4.1. The dbt temperature for this alloy in either the wrought or fine-grained recrystallized condition was about -100°F and the corresponding yield strength was approximately 400,000 psi. Thus Re

Hf-W   Hafnium-Tungsten
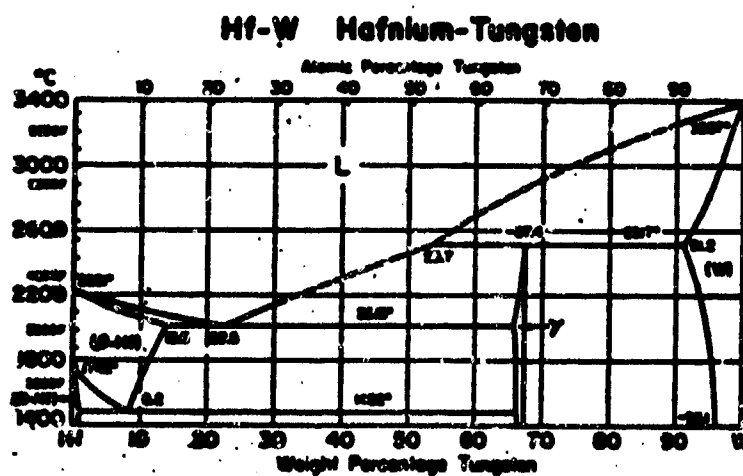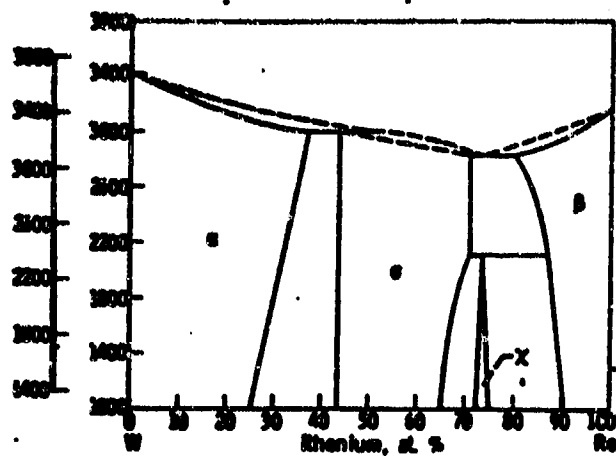
Fig. 4.1   Some relevant phase diagrams.

solution strengthening with ɤ-phase precipitation strengthening greatly improves the overall fabrication and service characteristics of W.

J. R. Stephens [4.7] and W. R. Witzke investigated the effects of temperature and composition on alloy softening in the Group VIA metals Cr, Mo and W alloyed with Re. They made hardness measurements at various temperatures for fourteen alloys in each system. Their results showed that alloy softening was similar in all three alloy systems and occured at Re concentrations of less than 16 at%. A sharp temperature dependence of hardness was observed in concentrated alloys that exhibited alloy softening. The results for W-Re are shown in Figure 4.2 a and b.

In fact, the softening of tungsten with rhenium was established as early as 1959 by K. Sedlatschek [4.8] and H. Braun. Figure 4.3a indicates that α-solid solution alloys with 25 to 30% Re are more ductile at 1000°C than pure tungsten or tungsten with lower percentages of rhenium. Figure 4.3b shows the relationship between cold ductility and rhenium content for W-Re alloys. This curve shows a maximum ductility at 30% rhenium. They also found that the high temperature hardness of W-Re alloys was excellent compared to that of W which deteriorates rapidly with temperature.

The softening of tungsten when alloyed with rhenium was clearly exhibited when A. V. Longunov [4.9] and Kovalev investigated the thermophysical properties of W-Re cast alloys. They found that the thermal conductivity of the alloy was lower than that of pure W as shown in Figure 4.4 at all temperatures and this was attributed to the softening of the parent material.

An atomic-resolution study of homogeneous radiation-induced precipitation in a neutron irradiated W-10%Re alloy, at Cornell University in 1983 revealed that there was a significant alteration of the

Fig. 4.2b   Hardness dependence
of W-Re
alloy on temperature.

Fig. 4.2a   Hardness dependence of W on
Re content.

Fig. 4.3b   Influence of rhenium
on the cold workability of tungsten.

Fig. 4.3a   Ductility of W-Re
alloys at 1000° C.

microstructure of this alloy as a result of the fast neutron irradiation. Precipitates with α-phase precipitation in core promise better space nuclear reactors and thermionic energy conversion capablities.

4.2.2.2 The additive ThO_2

Interstitial impurities generally tend to diminish ductility, but some of them can produce beneficially dispersed refractory products through reactions with low pressure vapor getters such as thorium and hafnium. Thorium is the best getter for oxygen. The proposal of adding ThO_2 to W, Re alloys was initiated when it was found that the unactivated ThO_2 had work functions of 6.3 eV bare and 1.0 eV cesiated. Great gains in ductility, hot strength and recrystallization resistance for ThO_2 additions to W, Re ultralloys have already received attention. Particle dispersions strongly influence mobilities of grain boundaries and subboundaries, redistribution of dislocation and other effects that affect the formation of recrystallization nuclei and initial growth. Thus dispersed particles such as ThO_2 change recrystallization temperatures as complex functions of the dispersed size, spacing, concentration, stability and other variables of microstructural interaction. As shown in Fig. 4.5 [4.10] ThO_2 is a very stable oxide which has a melting point of 3300°C. Thoriated tungsten is generally obtained by flashing a W filament containing 0.5-1.5% ThO_2 at a high temperature (2700°K), which reduces some of the oxide to metallic thorium. This is then followed by heating at 2100-2200°K, thus causing diffusion of thorium to the surface where it forms a monatomic layer which possesses much higher electron emission than pure W. At temperatures above 2000°K the thorium evaporates at a rate which exceeds that of diffusion to the surface with a resultant decrease in eletron emissivity.
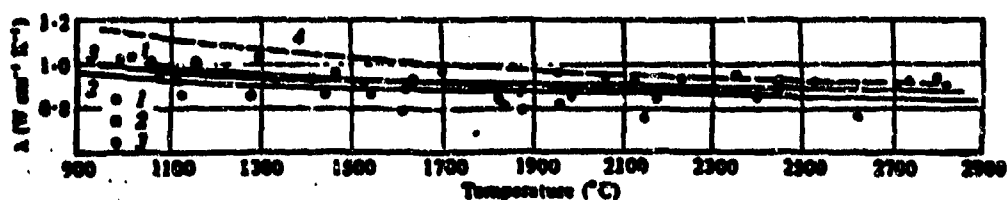
Fig. 4.4   Thermal conductivity of W-5%Re cast alloy:1 Heat 140;

2 Heat 141; 3 Heat 142;4 pure tungsten.
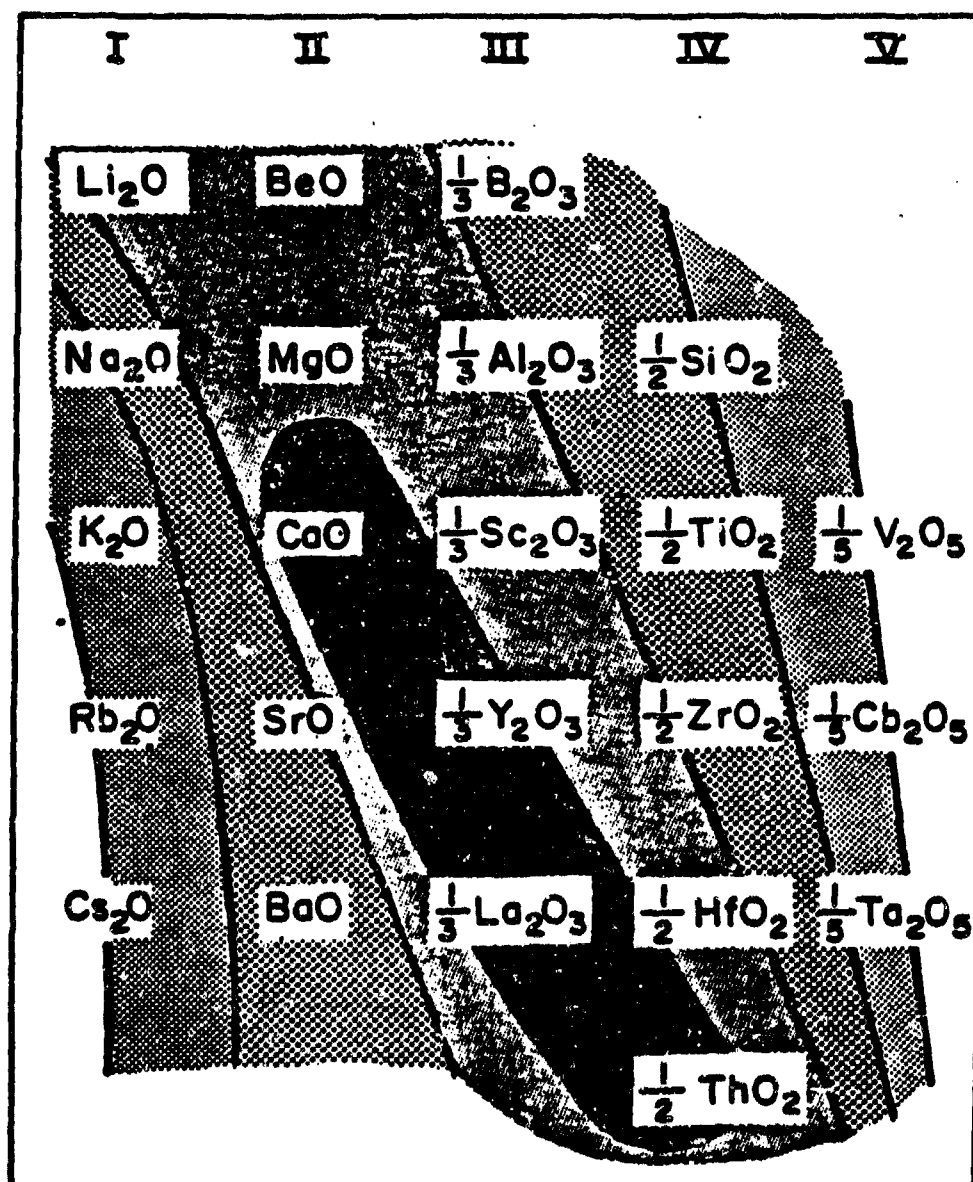
Fig. 4.5   Stability relationships of refractory oxides.

A DMIC report compiled by V. D. Barth [4.11] illustrates the strengthening of tungsten wire by ThO_2. The effect of ThO_2 addition is already seen in Fig. 4.6, a plot of ultimate tensile strength vs. temperature. Two percent of ThO_2 was found to increase the elevated temperature yield strength to 41,000 psi from an original value of 11,000 psi and the UTS from 22,000 psi to 42,000 psi.

H. G. Sell [4.12] and R. Stickler evaluated $W-5Re-2ThO_2$ alloys in regard to solid solution and dispersion strengthening. They determined the effect of Re and ThO_2 dispersion in W, on the DBTT and modes of fracture. The maximum temperature at which the testing was done was 1000°C. The results are shown in Fig. 4.7. They found that Re concentrations from 3 to 10% in solid solution significantly strengthens W, increasingly, with increasing Re concentration. The coarse ThO_2 dispersion did not retard recrystallization, and adds considerably to the strength of W-Re alloys by grain refinement. ThO_2 addition effected increases of ⁻4000 psi on W-Re alloys.

Figure 4.8 [4.13] shows the change in microstructure of a pure tungsten filament heated by alternating current. When large grains extending across the filaments develop, the filaments become very brittle and break apart under the stresses produced by the thermal expansion on heating and cooling. Consequently, second phase particles of thoria are doped into the tungsten to limit this grain growth. The effectiveness of a small amount of ThO_2 in limiting grain growth in tungsten is illustrated in Fig. 4.9.

Given that the thoria particles are randomly distributed, if volume fraction of thoria particles = f and radius of thoria particles = r, the number of particles intercepted by $1cm^2$ area = $3f/2\pi r^2$ (4.1). Force restraining grain boundary motion = $3f\pi rY(1+\cos\alpha)$ (4.2).
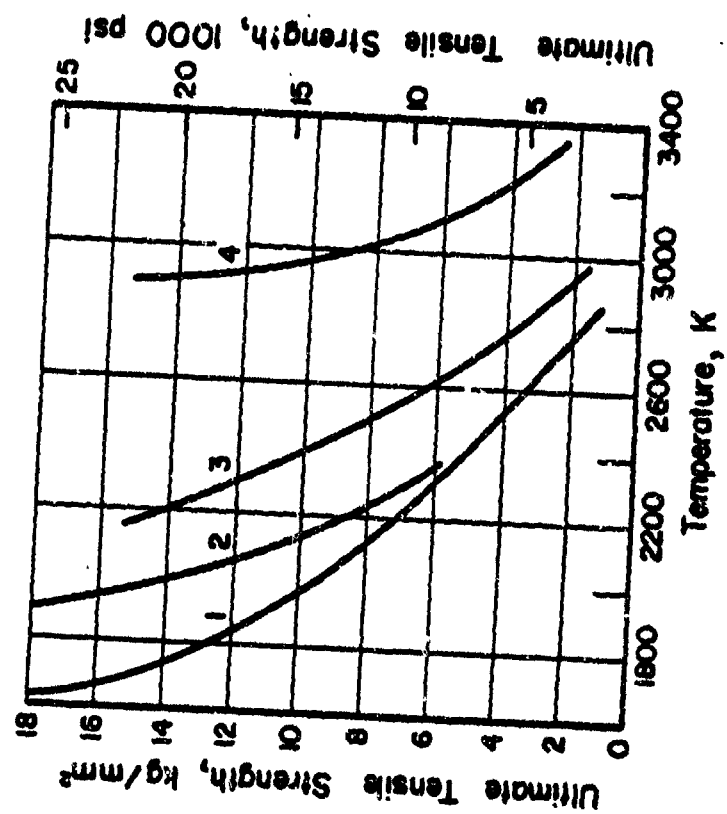
Fig. 4.6   Strengthening of tungsten wires with ThO$_2$.

Fig. 4.8 Change in microstructure of a pure tungsten filament heated by alternating current.

Fig. 4.7 Temperature dependence of ductility of swaged and 0.5hr./2400°C annealed tungsten and tungsten alloy rods.
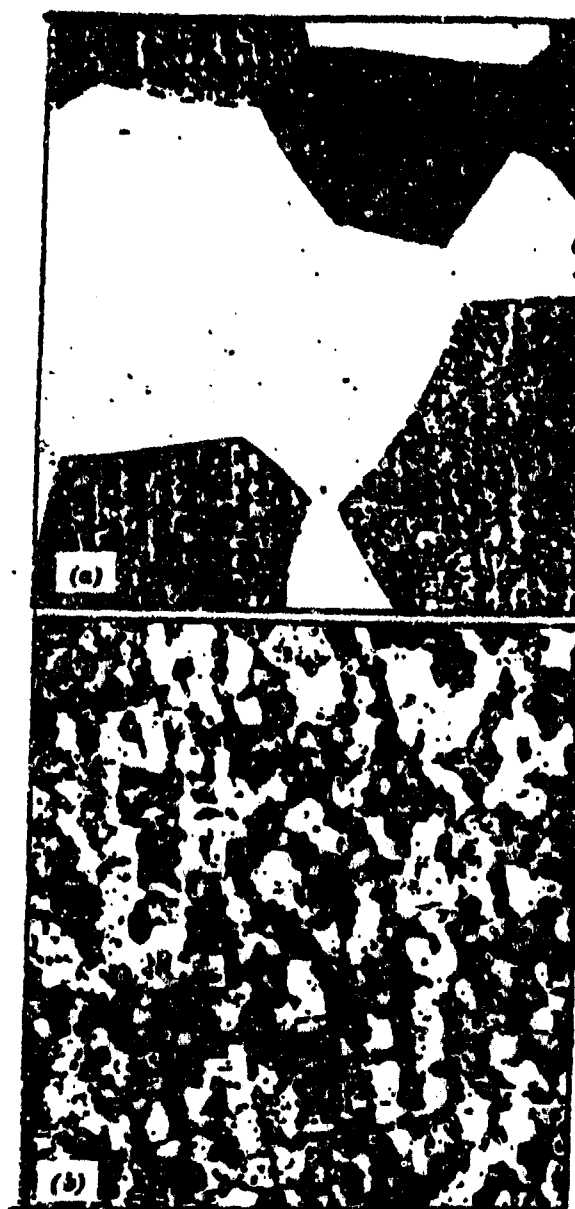
Fig. 4.9. Tungsten rods annealed
at 2700°C for 2 mts. a) Pure,
b) 0.75% ThO$_2$ added,. 100X.

When the force balances the pressure force due to curvature, grain growth will stop and we will get a limiting grain size given by

$$R = \frac{4r}{3f(1+\cos\alpha)}$$ (4.3)

assuming spherical interfaces of radius R. Thus we see that the limiting grain size depends upon the volume fraction, the radius and the contact angle α of the second phase particles.

4.2.2.3 The additive HfC

Hafnium is an excellent getter for carbon in W, Re alloys. Impressive increases in ductility, hot strength and recrystallization resistance have been found for HfC dispersed W, Re ultralloys. The noted Soviet refractory alloy expert Savitsky has commented that HfC formation in W alloys radically shifts the onset of structural changes upon recrystallization into the high temperature region. In addition to this, HfC in W alloys is thermodynamically very stable. Hf and C solubilities in W are low and so grain boundary segregation might be expected. But through appropriate microalloying, reaction of grain-boundary segregated C and Hf should be advantageous rather than detrimental.

J. Wadsworth [4.14] examined the behavior of molybdenum and tungsten based alloys which are strengthened by hafnium carbide. He established, by calculating the amounts of hafnium carbide available for precipitation in the molybdenum and tungsten based alloys, it was possible to demonstrate that excess hafnium does not have a "solute-weakening" effect as had been claimed. Instead, a trend of improved creep strength and high temperature tensile strength with an increase in the amount of HfC available for precipitation was, observed.

Space nuclear reactor growth based on in core thermionic energy conversion requires substantially improved TEC and considerably higher temperatures than those presently proposed. This is only possible through the use of W, Re ultralloys with ThO_2 and HfC. $W-3Re-1ThO_2-0.3HfC$, $W-10Re-1ThO_2-0.3HfC$, $W-25Re-1ThO_2-0.3HfC$, $W-30Re-1ThO_2-03HfC$, are all possible candidates for emitters in ICTEC with wide potentialities. Verification of such potentialities should derive from research related to W, Re, additive ultralloys presently supported by the Department of Energy and the Air Force at Arizona State University.

4.3 PROPOSED RESEARCH ON TUNGSTEN, RHENIUM ADDITIVE ALLOYS

It has already been esablished that rhenium percentages between two and five, at about ten and near twenty-five in tungsten alloys maximizes ductility locally and tungsten, 25% rhenium offers higher creep strength than tungsten to over 1600°C. It has greater ductility and recrystallization resistance. Additions of thoria and hafnium carbide in the order of 1 and 0.3% respectively, further increase creep strengths, ductilities and recrystallization temperatures of tungsten, rhenium alloys. Thus, parametric evaluations of tungsten with 3, 10, 25 and 30% rhenium, each in turn modified with one percent thoria and 0.3% hafnium carbide will be used as the basis for the research work.

Until 1975, data on pure W, Re alloys prepared by powder metallurgy were lacking. But investigators still resorted to powder metallurgy techniques as it was the only practical method of producing W alloys containing a ThO_2 dispersion. Fusion processes such as electron-beam melting or arc casting would be beneficial because the impurity concentrations in such alloys are low, but the prohibitive cost and the fact that ThO_2 decomposes at the melting temperature of W and its dilute alloys,

prevent them from being used for making W, Re, ThO$_2$, HfC alloys. Further, sintered samples have a small grain size and this reduces recrystallization processes with the surface impurities of O$_2$, N$_2$, and C forming resistance to diffusion and grain growth. As a result, it was decided that we would investigate sintered samples of W with 3, 10, 25 and 30% rhenium in the thermionic microscope and mechanical testing facility and follow this up with identical investigations on each of the above mentioned alloys with 1% ThO$_2$ and 0.3% HfC added to it.

4.3.1 Scientific approach to the reseach problem

The scientific approach to the research will be to develop general theories for high temperature mateials for producing high quality and long life. Recrystallization, ductility, strength vapor pressures work function, compositional stability and other phenomena will be considered which are vital to high temperature energy converters. Techniques for producing and sustaining the desired properties will be investigated from a microscopic, mechanistic point of view with regard to the desired properties. Limited theoretical and experimental information exists for such systems and a typical base line system will be examined in order to test the theories and models developed.

It is proposed to add getters to react with the O$_2$ and C and improve the high temperature strength and ductility through the combined effects of solid solutions and dispersion strengthening. Recrystallization is the formation and migration of large angle boundaries for alloys shown in Table 4.2. Most of these approximate thermal boundaries have been encountered by those who work with high temperature alloys. Recognition of these transitions emphasizes that direct and side effects of recrystallization exert abstruse influences on strength, creep, compatibility and ductility of

<u>Tab</u> <u>3</u> <u>Approximate thermal boundaries for alloys</u>
<u>(recrystallisation)</u>.

Half the absolute melting point (0.5T_M) often indicates incipience of thermally activated processes.

Below 0.3T_M to 0.4T_M short-range (electronic, stacking-fault, local-order)interactions generally dominate.

Longer-range solute, dislocation interactions continue their influences to 0.5T_M or higher.

Above 0.75T_M to 0.8T_M increased mobility of solute atoms greatly reduced their hindrance of dislocation movement.

Arrhenius relations for grain-boundary migration velocities often break at 0.8T_M and exhibit much lower activation energies in the higher-temperature range.

Refractory-dispersion strengthening generally excels for applications of alloys near their melting points.

refractory alloys. Ductility and recrystallization are often critical parameters in the capability of ultralloys to adapt themselves and ceramics to fabrication and service requirements. Thus a better understanding of refractory alloy recrystallization, is a crucially essential part of overcoming the material problems for high temperature, high power space energy conversion systems.

4.3.2 Scientific merits of the proposed research

Significant discrepancies in our understanding of refractory metal and other high temperature materials, involving such behaviors as embrittlement, vaporization and recrystallization, prohibit mechanism description and counteraction as well as property prediction for elemental systems suitable for high temperatures, hence higher power production in space energy converters. It is proposed here that a few of the most important phenomena be investigated. Theories and models will be developed and a base line material system will be used for examining them. The base line will be selected with the best present knowledge in order to begin to establish relationships between the basic mechanisms, alloying gettering and thermal history in predicting subsequent physical property behavior. High temperature phenomena are often only inferred through room temperature observations following high temperature treatment. The proposed work employs real time investigation of high temperature surface characteristics and electron emission to obtain information on complex transport and reaction mechanisms.

Some very enlightening information should result from observing high temperature size and surface composition changes of grains in sintered samples of W, Re with appropriate additions. The primary additive (rhenium) reduces and controls embrittlement and recrystallization. The gettering

additive may affect the base metal ductility and recrystallization. Since refractory oxides vaporize and disintegrate at high temperatures in vacuum, sintered samples of particles with and without bake-out pre-treatment deserve attention. The getters should produce very stable oxides and carbides. So in high temperature, vacuum service, the refractory should experience contention between oxygen and nitrogen clean-up by refractory oxide and nitride vaporization as well as disintigration and by the formation of stable gettered products.

4.4 THERMIONIC EMISSION CHARACTERISTICS AND SURFACE COMPOSITIONS OF W, Re AND W, Re, ThO₂, HfC ALLOYS

This section deals with the information on the research to be conducted on the W, Re and W, Re, ThO_2, HfC alloys using a thermionic microscope in order to obtain the thermionic emission characteristics of the sintered samples. The theory of electron emission and applications of the microscope are discussed and a sequential procedure for all the research activities involved has been established. In addition to the research using the thermionic microscope, related thermionic emission research activities have also been mentioned.

4.4.1 Introduction to Thermionic Emission Microscopy

Thermionic emission microscopy is the oldest form of electron microscopy where the specimen itself serves as a source of electrons. Electrons emitted from the surface of a flat bulk specimen is focussed through a suitable lens system and then projected at a usable magnification onto a flourescent screen. The result is a metallographic type image of the kind usually associated with optical microscopy. The design and operation of a thermionic emission microscope requires coordination of two physical processes. The first process is electron emission from a specimen, while

the second involves the formation of an image with these electrons. The two major characteristics that exemplify the usefullness of the thermionic emission microscope as a Research Tool are; a) the fact that it represents a magnification range which bridges that between optical microscopy and the more conventional types of electron microscopy, and b) it is more suited to elevated temperature operation than other forms of microscopy.

Specific experimental areas [4.15] where the thermionic emission microscope can be readily applied as a useful Research Tool are indicated in Table 4.4.

4.4.1.1 Electron emission

The Sommerfield model for the behavior of electrons in a metal provides the simplest view of the theory of operation of a thermionic emission microscope. This is indicated schematically in Fig. 4.10. Here, it is seen that the potential within the metal is assumed zero while that outside the metal is given some finite value, V. According to this model, electrons can occupy energy states within the metal up to the level E_f, the Fermi Energy. The probability that a particular state is occupied is given by the Fermi function,

$$f(E) = \frac{1}{\exp[(E-E_f)/kT] + 1} \tag{4.4}$$

At $T = 0°K$, $f(E) = e^{-\infty} + 1 = \frac{1}{1} = 1$ for $E < E_f$. This means that all quantum states are occupied at absolute zero while all quantum states at energies greater than E_f are unoccupied.

Table 4.4 Applications of the thermionic emission microscope.

1. High temperatures phase transformations in metallic and non-metallic systems.
2. Grain growth occurring at elevated temperatures in metallic and non-metallic systems.
3. Recrystallization in those systems where it occurrs at a sufficiently high temperature.
4. Cold work in the refractory metals, such as tungsten, molybdenum and niobium.
5. Relative interfacial energy studies in systems where the systems are in equilibrium at elevated temperatures.
6. Diffusion studies in systems at elevated temperatures.
7. Segregation studies in cast or wrought materials.
8. Surface adsorption of gases and activator atoms on metallic surfaces.
9. Sintering mechanisms in powder metallurgical compacts.
10. Solidification studies im metals.
11. Oxidation studies of metal surfaces under controlled conditions.
12. Study of electron emission from surfaces. Also work function studies of different crystal orientations.
13. Cathode studies for the activation process in coated cathodes.
14. Effect of strain on the above mentioned phenomena.
15. Creep in metals at elevated temperatures.
16. Study of the distribution of inorganic constituents within the cells os tissue.

4.4.1.2 Work function

The energy difference between the Fermi Energy and the potential outside of the metal is the <u>work function</u> of the metal ϕ.

Either an electron absorbs a quantum of energy or it does not. The energy E of a photon is proportional to the frequency ν of the light or

$$E = h\nu \qquad (4.5)$$

If an electron is given an amount of energy $h\nu$, then in order to escape from the metal, it must use up an amount $e\phi$ of this energy. The maximum energy an electron can have left after it gets out of the surface is

$$K_{max} = h\nu - e\phi \qquad (4.6)$$

The thermionic emission microscope is a device where the specimen is heated up to a high temperature (at least 1400°C) by electron bombardment and the electrons given out by the surface collected by a Faraday cage by the imposition of a suitable potential difference. The Faraday cage current can be related to the sample electron current density by the equation;

$$J_0 = \frac{I \cdot M^2}{A_c} \qquad (4.7)$$

The current density J_0 can then be used to calculate the effective work function ϕ from the well known Richardson-Dushman equation

$$J_0 = AT^2 \exp[-\phi/kT] \qquad (4.8)$$

A derivation of this equation using the principles of Classical Thermodynamics, has been presented in Appendix 4.1.

4.4.2 Objectives of the ongoing research on thermionic emission

a) Fabricate sintered alloys of W with 0%, 3%, 10%, 25%, and 30% of Re in button form of about 0.4" in dia. with a porosity of about 7 to 8%.

b) Fabricate sintered alloys in the above form and hot swage it down to 0.25" dia. to reduce the porosity to less than 0.1%.

c) Perform thermionic emission microscope examination of the samples in a) & b) above at 1600 to 2200°K in suitable intervals.

d) For each test,

   i)   Observe grain size, grain growth and document by photographic enlargements.

   ii) Measure emission of grains in the thermionic microscope and calculate the work function.

   iii) Perform emission scans of surfaces to determine work function variation from grain to grain.

Repeat for W, Re, ThO$_2$, HfC alloys.

4.4.3 Literature survey

E. Eichen [4.16], who has spent a considerable amount of time in reviewing the work done on Thermionic emission, has compiled a lot of his findings and presented the information in a tabular form indicating the references of people who studied the emission characteristics of materials ranging from aluminum oxide to zirconium. Up to this time, however, most of the work had been done in the development of the thermionic emission microscope as a metallurgical research tool. Figures 4.11 and 4.12 are typical emission micrographs of an iron 0.3% carbon alloy at 800°C and polycrystalline alumina.

A typical thermionic energy converter schematic [4.17] is shown in Fig. 4.13, and Fig. 4.14 gives the performance and topping temperatures for thermionic energy conversion with 30 A/cm^2, 10% back emission, and negligible, inter-electrode loss.

D. Jacobson [4.18], thermally stabilized and recrystallized a polycrystalline molybdenum sample. Quantitative measurements of the emission from each individual grain were obtained using the electron emission microscope. The effective work function of each grain was calculated and the crystallographic orientation of each grain was determined using Laue back reflection techniques. A polar plot of the effective work function vs. crystallographic orientation is shown in Fig. 4.15.

The effective work functions of nine tungsten-base alloys were measured by D.L. Jacobson [4.19]. The second constituents were: 1) 5% Re, 2) 15% Re, 3) 2.5% Os, 4) 5% Os, 5) 1% Ir, 6) 2% Ir, 7) 5% Ta, 8) 10% Ta, and 9) 20% Ta. Work functions were determined from the vacuum emission vehicle and thermionic emission microscope measurements. Mosaics of each surface were produced from the microscope, which show the grain structure of the alloys and some anamolous emission areas. Some exceptionally high base work functions were observed from samples with small alloy additions. Table 4.5 gives the effective work functions of tungsten alloy electrodes from vacuum emission vehicle generated Schottky plots. Fig. 4.16 is a typical Schottky plot from Vacuum emission vehicle measurements. Table 4.6 is a comparison of effective work functions as determined from vacuum emission vehicle and thermionic emission microscope measurements.

A. Modinos [4.20], a mathematician from the University of Waterloo, Canada, presented a semi-empirical theory of the electronic work function of the different faces of tungsten. An adjustable parameter relates to the
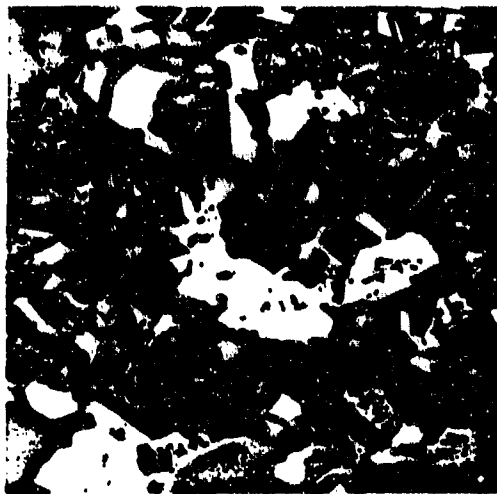
Fig. 4.11. Thermionic emission micrograph of an Iron-0.3% C alloy at 800°C. Mag. 660X.
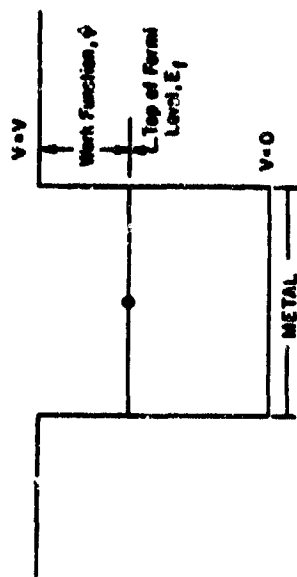
Fig.4:10. Schematic view of the potential field of a metal.
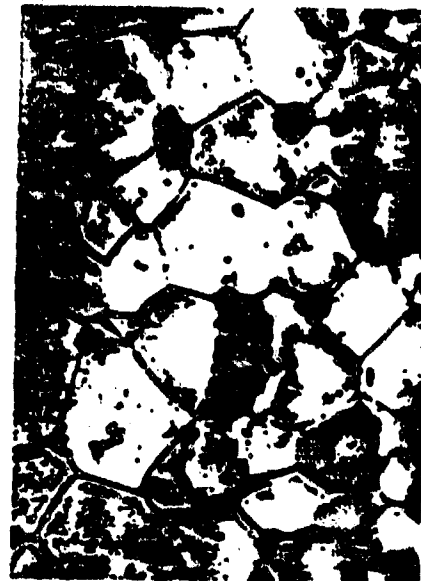
Fig. 4.12. Emission micrograph of polycrystalline alumina using Hydrogen ions.
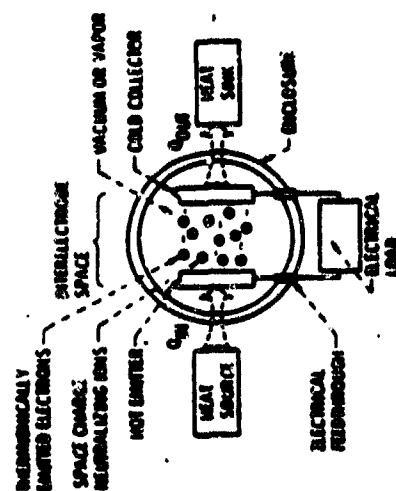
Fig.4.14 Polar plot of ϕ effective in (110) zone for a polycrystalline Mo sample. (1789 °C).

Fig. 4.13 Thermionic energy converter. (Operating Principle)

isotropic contribution to the work function, and is determined from a self-consistent calculation of the band-structure of the energy levels in the bulk of the metal. The calculated work functions were in reasonably good agreement with available experimental data. He suggested that the measured work function

$$\phi(lmn) = \phi^\circ + \phi_d(lmn) \tag{4.9}$$

where ϕ° is the isotropic contribution and ϕ_d is the surface dipole contribution due to the formation of an electrostatic dipole layer. Table 4.7 gives the surface dipole contributions to the work function for different orientations.

J. Jaskie and D.L. Jacobson [4.21] investigated experimentally the relationship between bulk composition, surface composition and thermionic work function in the Yttrium-Boron system. These results were compared with other rare Earth-Boride systems. A Richardson plot for the 3 Y-B compounds tested is shown in Fig. 4.17 and Fig. 4.18 gives the estimated behavior of work function within 2 phase regions. Table 4.8 gives the composition data summary and the work functions for the 3 Y-B compounds.

C.V. Landrith [4.22] used the thermionic emission microscope to determine the effective work function of a molybdenum ceramic eutectic, Mo-LaCrO$_3$. Measurements were made at temperatures up to 1881°K, and at pressures in the range of 1 to 45 x 10^{-7} torr. The mean effective work functions of 4 grains on the surface of the Mo-LaCrO$_3$ was in the range of 4.74 to 4.81 eV. A typical emission micrograph of Mo-LaCrO$_3$ is shown in Fig. 4.19.

A. Subramanian [4.25], investigated the effect of alloying elements such as tungsten on the emission properties of LaB$_6$. The average B to La

Fig.4.15 Performance and topping temperatures for thermionic energy conversion with 30Amps/cm^2..,10% back emission and negligible inter electrode loss.

Fig.4.17 Richardson plots for
Y-B compounds.
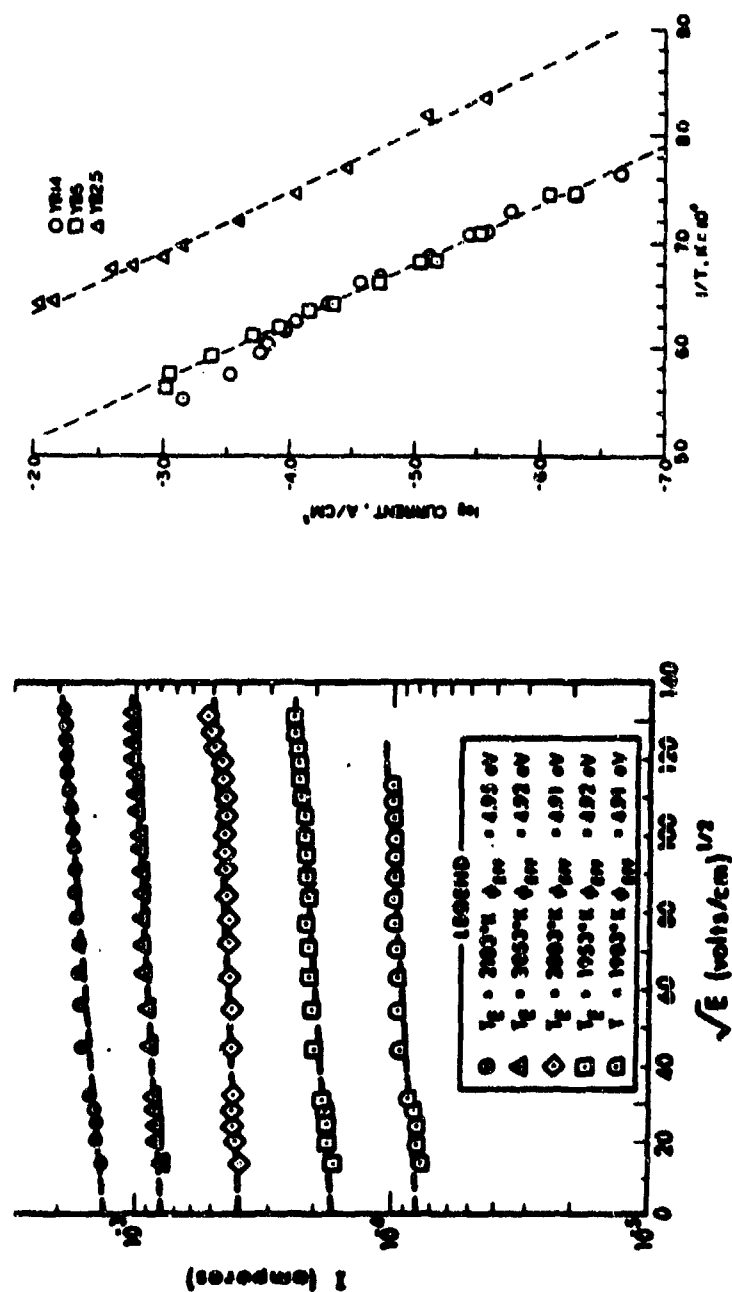
Fig. 4.16 Schottky plots of W-5%Re
from vacuum(vehicle)emission
measurements.

Table 4.5 Effective work function of tungsten alloy electrodes
from vacuum emission vehicle generated Schottky plots.

Table 4.6. Comparison of effective work functions as determined from
vacuum emission vehicle and thermionic emission microscope data.

Face	$D(\mu)$ (Å)	$\beta=0.015, E=6\,eV\,Å^{-3}, \phi^0=3.955\,eV$		$\beta=0.015, E=7.246\,eV\,Å^{-3}, \phi^0=3.766\,eV$		$\beta=0.006, E=8.82\,eV\,Å^{-3}, \phi^0=3.854\,eV$	
		$\sigma_D(\mu)$ (eV)	$\phi(\mu)$ (eV)	$\sigma_D(\mu)$ (eV)	$\phi(\mu)$ (eV)	$\sigma_D(\mu)$ (eV)	$\phi(\mu)$ (eV)
(110)	2.234	1.245	5.20	1.503	5.269	1.492	5.345
(100)	1.598	1.008	4.963	1.213	4.979	1.155	5.009
(112)	1.299	0.856	4.811	1.034	4.800	0.946	4.800
(111)	0.912	0.697	4.562	0.734	4.500	0.644	4.598
(123)	0.844	0.556	4.511	0.667	4.433	0.588	4.442
(012)	0.705	0.449	4.404	0.542	4.308	0.446	4.320
(233)	0.673	0.423	4.378	0.511	4.277	0.437	4.291
(122)	0.524	0.304	4.259	0.367	4.133	0.398	4.162
(116)	0.512	0.295	4.250	0.355	4.131	0.398	4.152

Table 4.7. Surface dipole contribution to the work function.

Nominal composition	Analyzed composition	Surface phases	Interior phases	Density, g/cm³	ϕ, eV
2.5	3.0	$YB_2 + YB_4$	YB_4		3.28
5.0	5.1	$YB_4 + YB_6$	$YB_6 + YB_4$	2.56	3.93
14.0	11.7	$YB_{12} > YB_6$	$Y_{12} > YB_6$	2.91	3.98

Table 4.8. Composition data summary.

Fig. 4.19 Emission
micrograph of
Mo-LaCro$_3$.
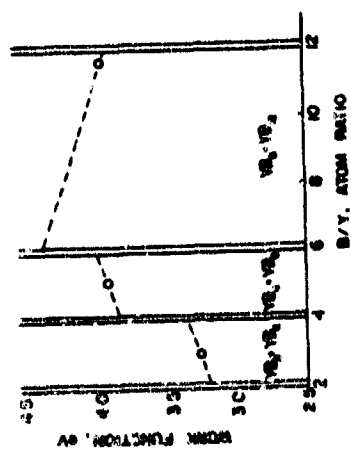
Fig. 4.18 Estimated beh-
avior of work fun--
ction within two
phase regions.

ratio was found to be 6.03 and tungsten was detected to the extent of 0.3 to 0.5 weight %. The effective work function ranged from 3.88 eV to 4.29 eV at a temperature of 1573°K. It was found that the presence of tungsten lowered the emission and hence increased the work function of LaB_6. Figure 4.20 is a Richardson Plot for the La-B-W Alloy system and Fig. 4.21 shows the variation of work function with temperature.

4.4.4 Techniques involved and facility support for sample preparation and testing

4.4.4.1 Material procurement

The moment it was decided that we investigate sintered W, Re and W, Re, ThO_2, HfC alloys, at least 50 different suppliers were contacted all over the country but only one supplier,

Rhenium Alloys Inc.

1329 Taylor St., Box 245

Elyria, Ohio 44035

agreed to make the samples for us, at a fairly high price. To date, we have received the alloys in 3 different configurations indicated in Table 4.9. The second set of alloys with the same configurations but with 1% ThO_2 and 0.3% HfC added to them are being manufactured and the shipment is expected in June 1985.

4.4.4.2 Sample preparation

The material which was originally in button form, roughly 0.4 inches in diameter and 0.5 inches long was first turned down to 0.375 inches diameter using a four-faceted tungsten-carbide cutting tool. Because of the brittle nature of the alloys, the turned surface had a lot of dents due to particles
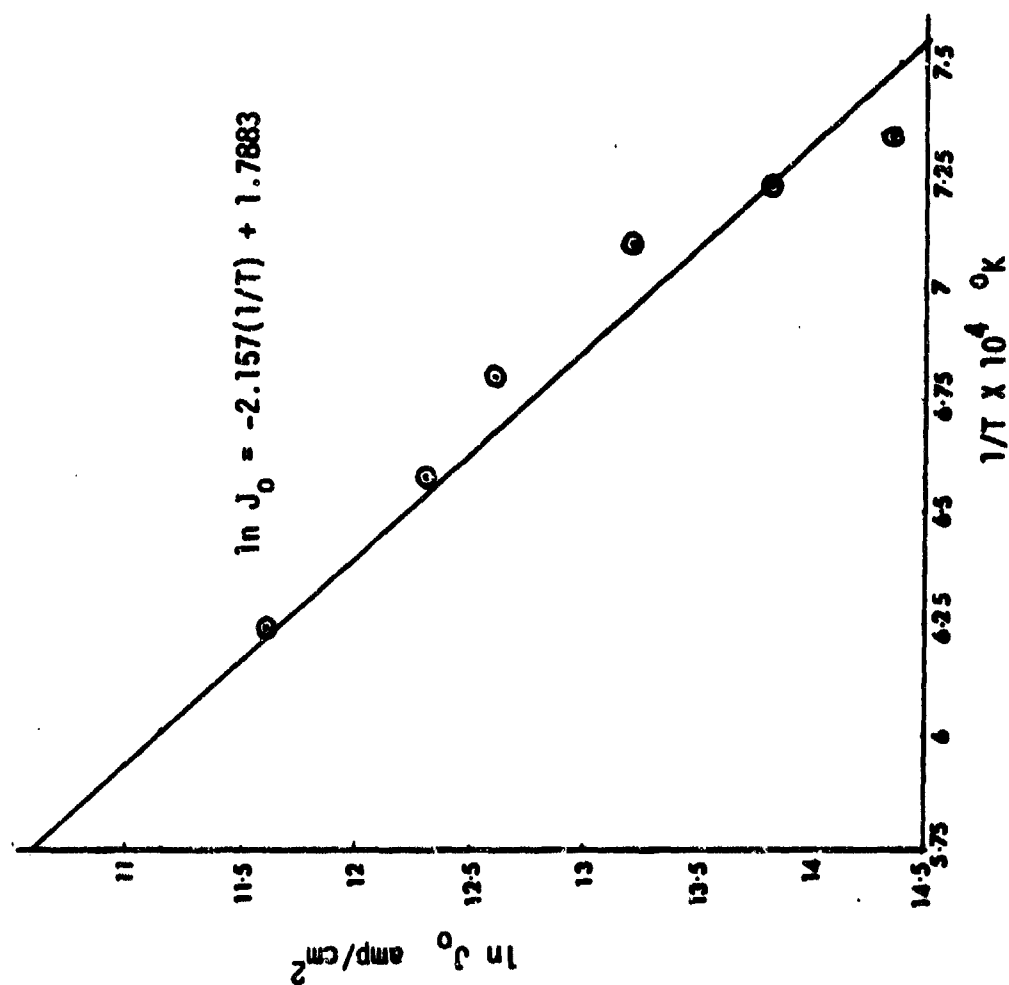
Fig.4.20 Richardson plot for La-B-K alloy system.

$$\ln J_0 = -2.157(1/T) + 1.7883$$
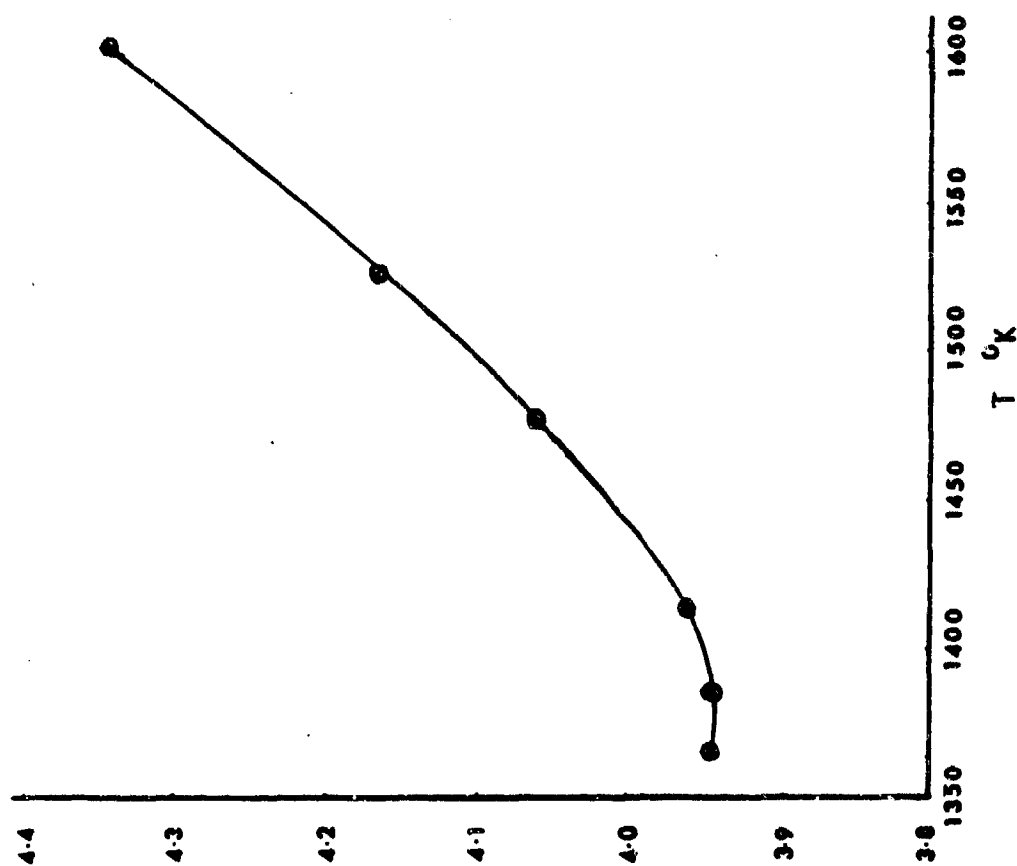
Fig 4.21 Variation of
work function with
temperature for La-
B--W alloy.

Table 4.9   Materials procured from Rhenium Alloys Inc.

Composition :

    W + 0% Re
    W + 3% Re
    W + 10%Re   Sintered from W & Re powder.
    W + 25%Re
    W + 30%Re

Configurations :

1. Button form : 0.4 ins. diameter, 0.5 ins. long density = 92-93%, five pieces.

2. Rods : 0.25 ins. diameter, 12 ins. length, hot swaged from a larger diameter, density = 100% ,.five rods.

3. Wires : 20 mil. diameter except for the 30% Re alloy, length = 36 ins. diameter of W, 30% Re wire = 50 mil.

Materials source : Rhenium Alloys Inc.
    Box 245. 1329 Taylor street,
    Elyria, Ohio- 44035.

chipping off from the surface. The surface was eventually finished on the Electrical Discharge Machine as shown in Fig. 4.22. The electrode for this purpose was designed and fabricated using copper rods and is also shown in the figure along with the fixture for mounting in the E.D.M. The material · s then sliced down using a special diamond cutter to form buttons 0.375 inches in diameter and 0.100 inches thick for use in the thermionic microscope. The EDM was used once again to drill the Hohlraum (or black enclosure) which had a diameter of 0.020 inches and a length of 0.200 inches thereby satisfying the condition of an Isothermal Black enclosure with a L/D ratio of 10:1.

4.4.4.3 Sample characterization

Sample characterization was done on each one of the alloys in order to determine and check the composition and the homogenity of each alloy.

(i) Electron microprobe analysis

A small bit (2 mm x 2 mm x 1 mm) was cut using the diamond cutter and submitted to the Chemistry Department at Arizona State University to have it analysed in the electron microprobe facility. The results of the analysis, as indicated in Table 4.10, show that the alloys with lower percentages of rhenium were inhomogeneous and modification in the fabrication process was essential.

(ii) Metallography

Each of the five samples were polished using Emery paper of varying grades and then lapped with Lev. Alumina, 1.0 µm. Alumina and finally 0.05 µm. Alumina solutions. Photomicrographs were taken using the optical microscope. Microhardness testing was then done on the polished samples using Murakami·s Reagent and photomicrographs taken again to determine grain
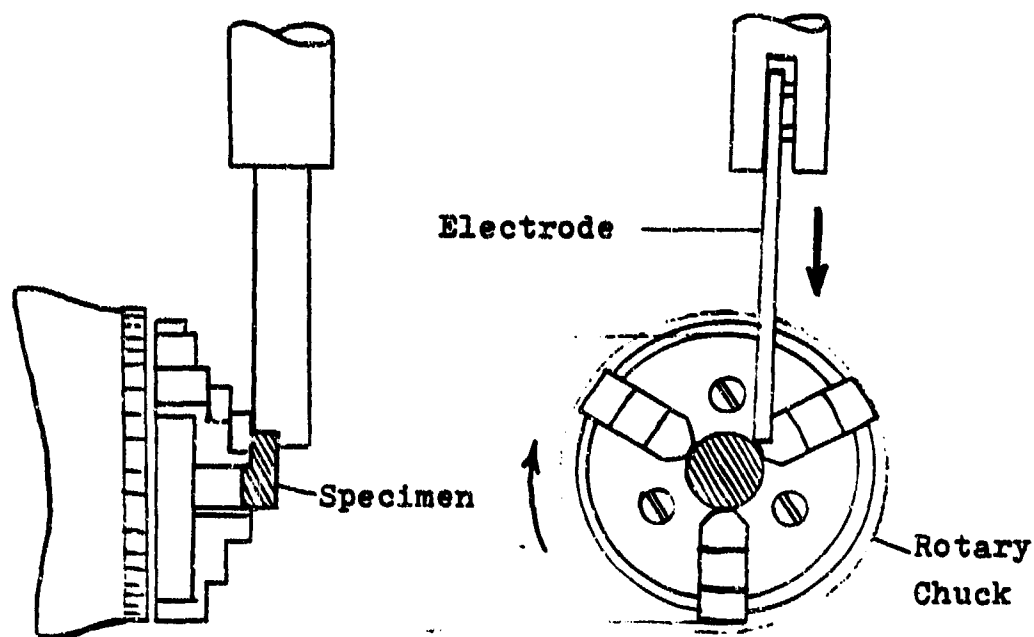
Some specifications of the EDM.

    Type: Servomet.

    Cabinet size: 29"wx28^3/8 "dx22^1/2"h.

    Power: 200-250V, 10amp. 50/60 cycles.

    Work tank aperture: 11.75" x 7.5".

    Work tank depth : 13".

    Capacity: 4.15 Imp. Gals.

    Total surface below paraffin: 1.875"min.,8.375" max.

    Maximum height of work piece: 7.375".

    Work table lift: 5.375".

    Travel of servohead: 4.625".

Fig. 4.22 Details of electrical discharge machining.

Table 4.10 Results of electron microprobe analysis.

Concentrations at different positions.

Elements	1	2	3	4	5
W	0.997	0.986	0.996	0.995	0.998
Re	0.000	0.000	0.001	0.000	0.001
Total	0.996	0.985	0.996	0.995	0.998
W	0.968	0.967	0.926	0.973	0.991
Re	0.033	0.016	0.057	0.023	0.016
Total	1.000	1.003	0.983	0.995	1.007
W	0.874	0.888	0.814	0.880	0.855
Re	0.082	0.062	0.137	0.075	0.105
Total	0.956	0.950	0.950	0.954	0.960
W	0.733	0.736	0.765	0.777	0.718
Re	0.255	0.253	0.218	0.252	0.260
Total	0.987	0.988	0.983	1.029	0.977
W	0.701	0.736	0.730	0.712	0.737
Re	0.280	0.250	0.266	0.269	0.246
Total	0.981	0.985	0.996	0.981	0.983

size. Eventually, the macrohardness tests were conducted in the Rockwell Hardness tester. Table 4.11 gives the details of all the devices used in the metallography.

(iii) X-Ray chemical analysis

After machining the samples to the right size, each button was analysed in the X-ray Spectrometer using a chromium target. The intensities of the various elements in the 5 different alloys can be compared in Fig. 4.23 to get a qualitative estimate of the compositions.

4.4.4.4 Thermionic emission microscope

The apparatus used to determine the work function is a thermionic emission microscope. This apparatus was originally designed by XEROX in 1966 but subsequently has been subjected to a series of modifications in order to enhance its performance. The microscope, shown in Fig. 4.24, essentially consists of an electron source which is the sample surface itself that is heated in the neighborhood of 1500 to 2000°C by means of a filament. The electrons given out from the surface are drawn, through a system of lenses and drift tube, to the Faraday cage by the imposition of suitable potentials. The electrons collected at the Faraday cage are allowed to pass through an Electrometer which measures currents of the order of 10^{-11} to 10^{-14} Amps. The device is operated with a vacuum of 10^{-9} torr and the high temperature is measured with a calibrated optical pyrometer. There is a phosphor screen around the Faraday cage to observe real time grain boundary movements during the test. The entire system along with the microscope and accessories is shown in Fig. 4.25.

The diameter of the sample was less than that of the filament, so the sample was mounted in a step machined out from another sample holder. The

Table 4.11 Details of devices used for conventional metallgraphy.

Lapping machine :

        150V 60cs. 14 Amps
        Make: Buehler Ltd.

Microscope :

        Olympus system micrascope for metall-
        urgical use.
        Model: BHM.

Photography :

        Model: PM-6.
        Eyepieces available: P7x, P10x, P15x.
        Shutter speeds: B,1,1/2,1/4,1/8,1/15,
        1/30,1/60,1/125 & 1/250.
        Total magnification on film phase =
        0.4x (with P eyepieces).
        Picture size = 24 x 36mm.

Macrohardness :

        Rockwell type macromet hardness tester.
        Loads: 60, 100, 150 Kgs.
        Scales: a) B Scale, 1/16" Steel Ball,
        100Kg load.
        b) C Scale, Diamond cone, 150 Kg load.

Microhardness :

        Leitz wetzlar (Germany).
        Microhardness tester.
        Indentors: Knoop and Vickers.
        Loads: upto 2000 p.
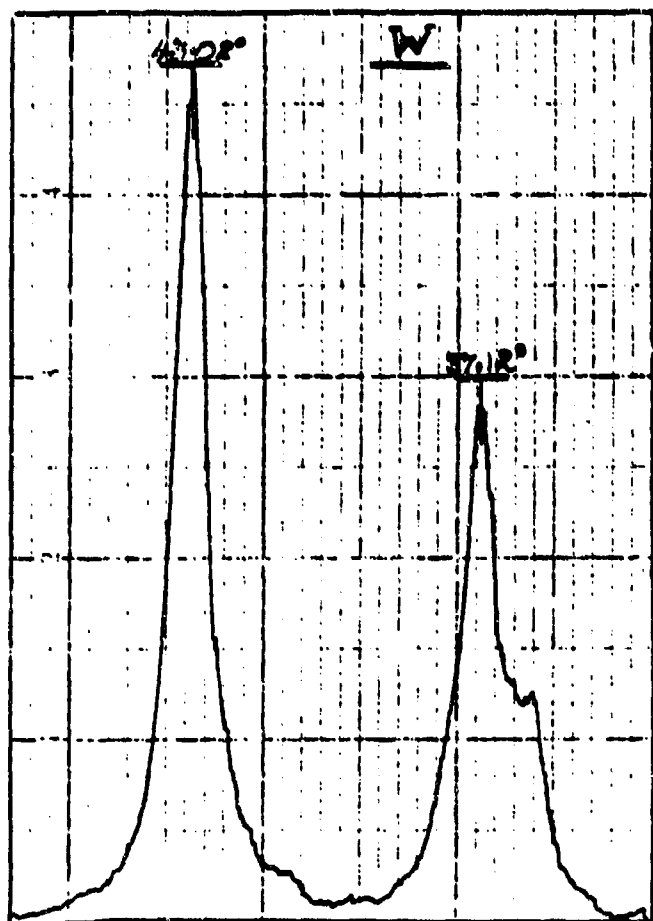
Fig. 4.23 Outputs for chemical analysis by x-ray spectrometry.
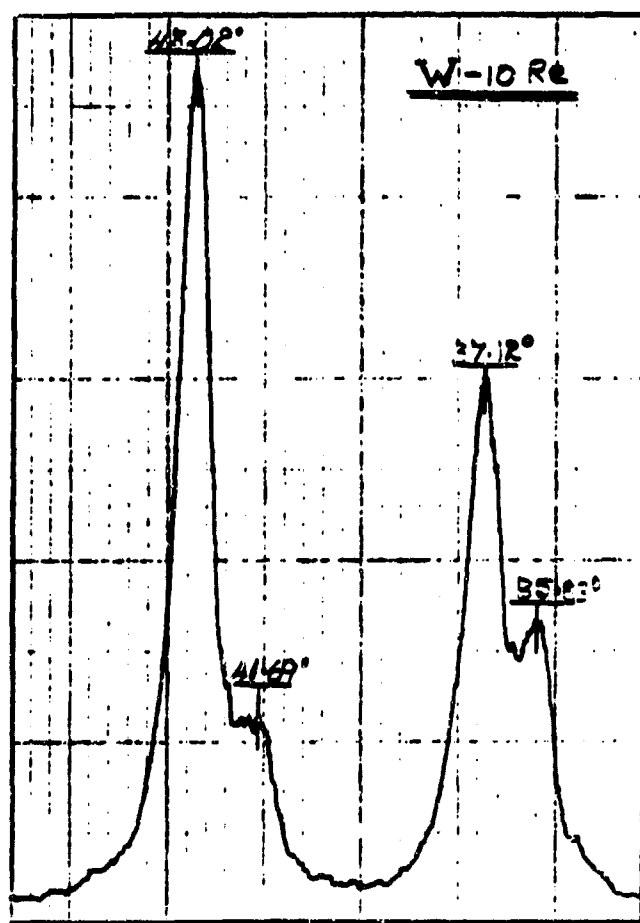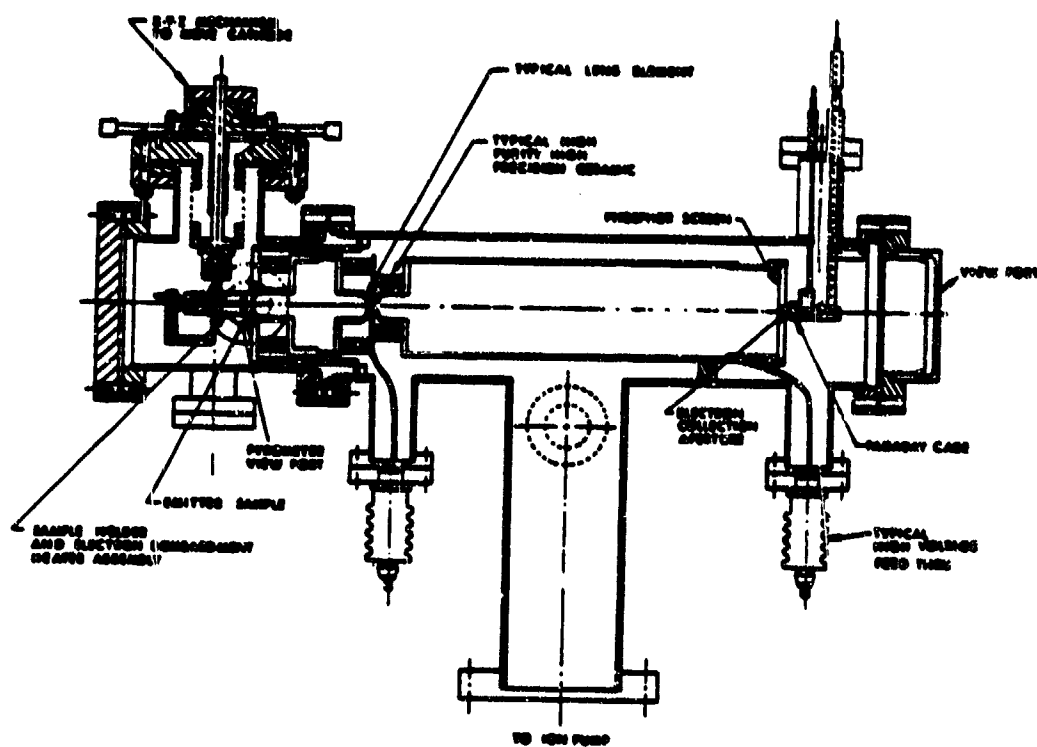
Fig. 4.24　A cross sectional view of the thermionic emission microscope.
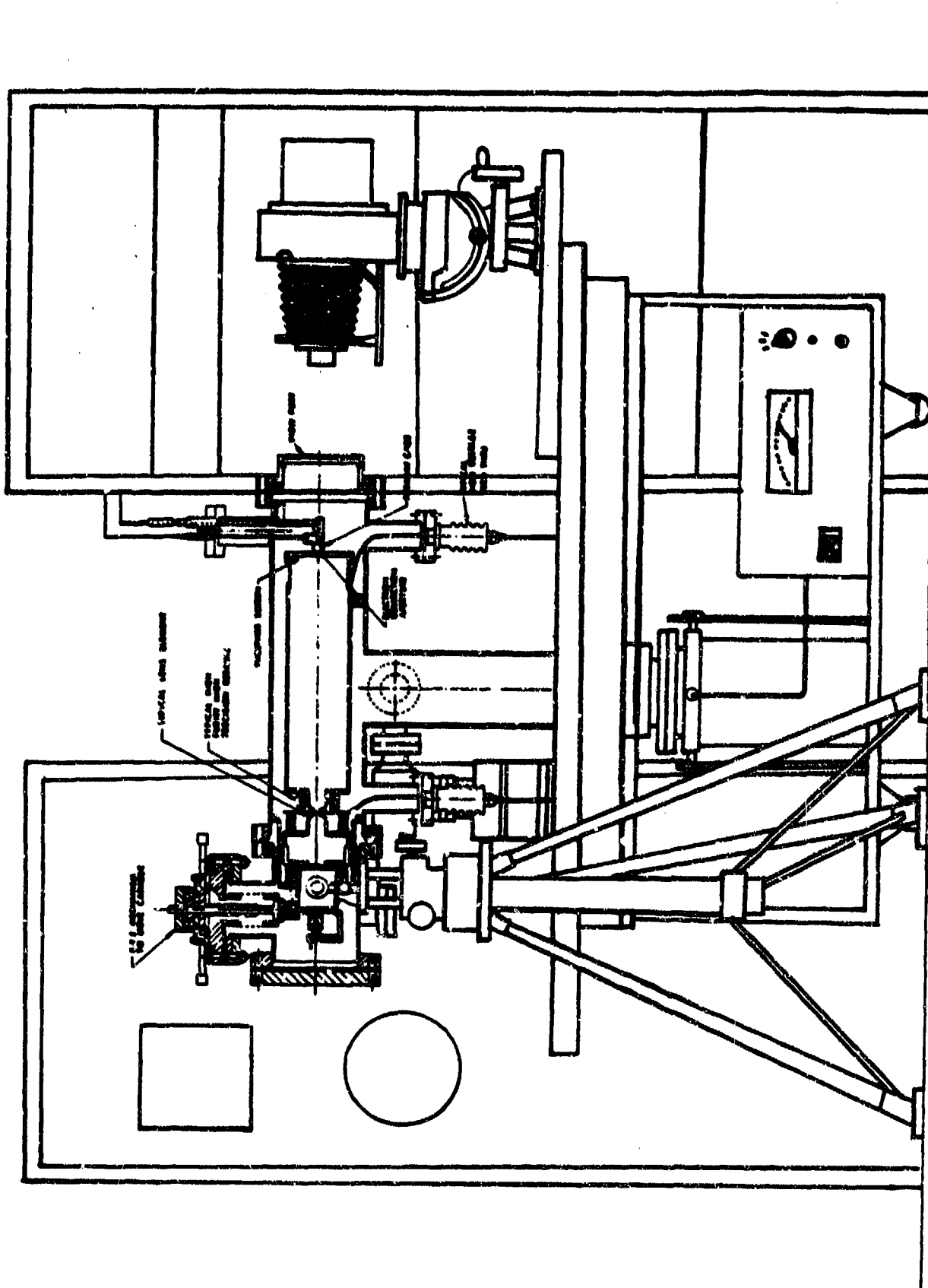
Fig. 4.25 Complete set up for high temperature thermionic emission microscopy.

Fig. 4.26 Emitter
Assembly.
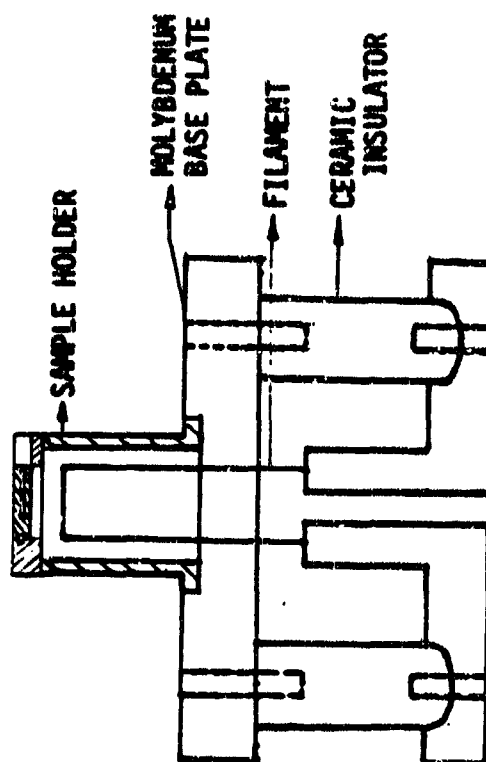
entire assembly consists of a molybdenum base plate and a tantalum disc, electron beam welded to a tantalum mounting tube, as shown in Fig. 4.26. The sample is held in position by a tungsten rod and a small grove at the top allows the Hohlraum to be seen from the side. Insulators are provided between the sample and filament because they are at different potentials.

There are 4 aspects to the instrumentation of the thermionic emission microscope in evaluating the work function of the examples under investigation.

1) Vacuum System:

It is absolutely essential that the environment within the microscope is extremely clean because the path of electrons is very susceptible to stray electrical and magnetic fields. Further, there should not be any contamination on the surface of the specimen while it is being tested. For this purpose, it is necessary to evacuate the entire chamber to less than 10^{-8} torr. This is accomplished in two stages; the roughing is done with a Sorption pump which utilizes molecular sieve material to absorb the air molecules when maintained at liquid nitrogen temperatures. This brings the vacuum to 10^{-3} torr. The ion pump is then switched on in order to bring down the vacuum to 10^{-7} torr. At this stage, the microscope is baked at about 250°C for 4 to 5 days so that all the adsorbed gases are removed and the vacuum eventually comes down to 10^{-9} torr when it is ready for testing. The details of the pumps used are given in Table 4.12.

ii) Electron Emission and Collection:

In addition to heating up the sample, it is necessary to provide progressively increasing potentials in the path of the electrons to make them move from the emitter to the collector with minimum losses. The

Table 4.12 Details of accessories of the thermionic emission Microscope.

1) Vacuum system:

    a) Sorption pump.

       Base pressure: Low micron range with normal use.

       Pumping capacity: 60000 torr-liters maximum.

       LN_2 consumption: 4.3 litres.

       Sorbent material: Type 5A molecular sieve.

       Sieve requirements: 3 lbs.

       Heater input: 115V, 50Hz., 350W.

       Bakeout Temperature: $250^{\circ}C$.

       Material: Aluminum.

    b) Vac ion pump.

       Pumping speed: 140 1/s at 10^{-6} torr.

       Operating life: 50000 hours at 10^{-6} torr.

       Materials: Body-304S.S., Cathode-Ti, Magnet-Ferrite.

       Internal volume: 17.9 litres.

       Weight: 120 lbs.

       Temperature limit: $400^{\circ}C$.

       Control unit: 7.5 kV. open circuit, 430 mA short cct.

2) Temperature measurement:

    a) NBS lamp.

       Filament: Tungsten filament (ribbon type).

       Reference: " The NBS photoelectric pyrometer and its use in realizing the international practical temperature scale above $1063^{\circ}C$," R.D.Lee, Metrologia 2, 150 (1966).

    b) Pyrometer.

       Micro optical pyrometer with red filter for higher ranges of temperature.

electrical schematic for the entire process is shown in Fig. 4.27. As seen in the schematic, the supplies to the filament are maintained at a floating negative potential with respect to the sample which is at ground potential. The electron drift tube is maintained at a high (KV) positive potential all the way to the collector and finally there are power supplies to the decelerating grid and the guard ring.

iii) Temperature Measurement

A calibrated micro-optical pyrometer will be used for measuring the temperature of the sample. The pyrometer was first calibrated with a NBS Calibrated Tungsten filament lamp. The NBS lamp was viewed through the pyrometer and temperatures were recorded. A plot of the lamp (true) temperature vs. pyrometer temperature was made. Then the viewport (sapphire) in the microscope was placed between the lamp and the pyrometer and the testing repeated to give a plot of temperature while viewing through viewport vs. true temperature. The plot of temperatures and the electrical schematic for the calibration are shown in Fig. 4.28. Details of the pyrometer and lamp are provided in Table 4.12.

iv) Photography - Emission Micrograph

A high speed Polaroid camera mounted directly behind the phosphor screen and viewport recorded the grain boundary movement at different temperatures.

4.4.5 Expected results and conclusions

The thermionic work functions will be evaluated for representative grains in each sample and the variation noted to determine the homogenity of the sintered samples. The pure tungsten and the tungsten alloys with higher percentages of rhenium should exhibit a homogeneous structure whereas there
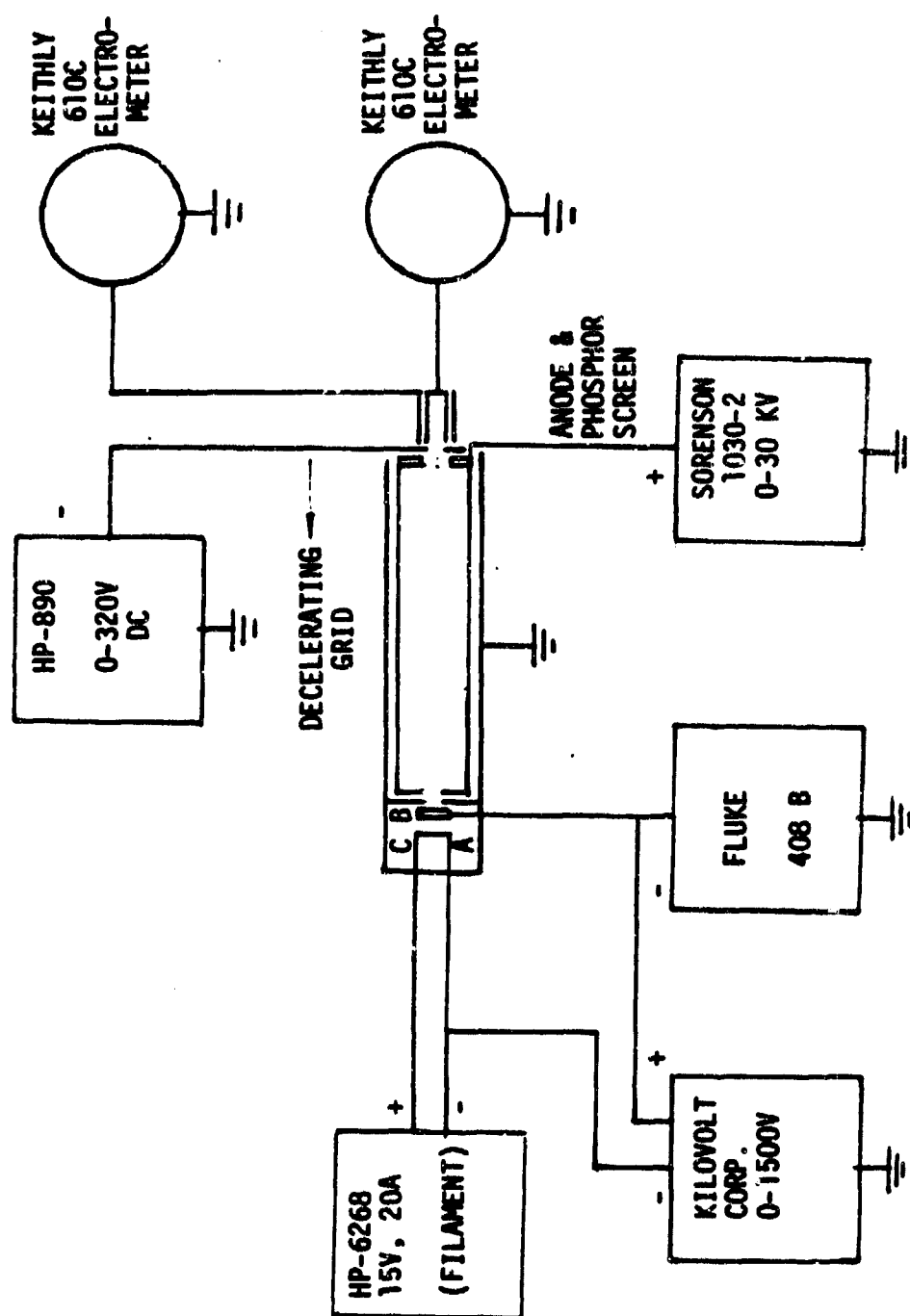
Fig. 4.27 Electrical schematic for the thermionic emission microscope.
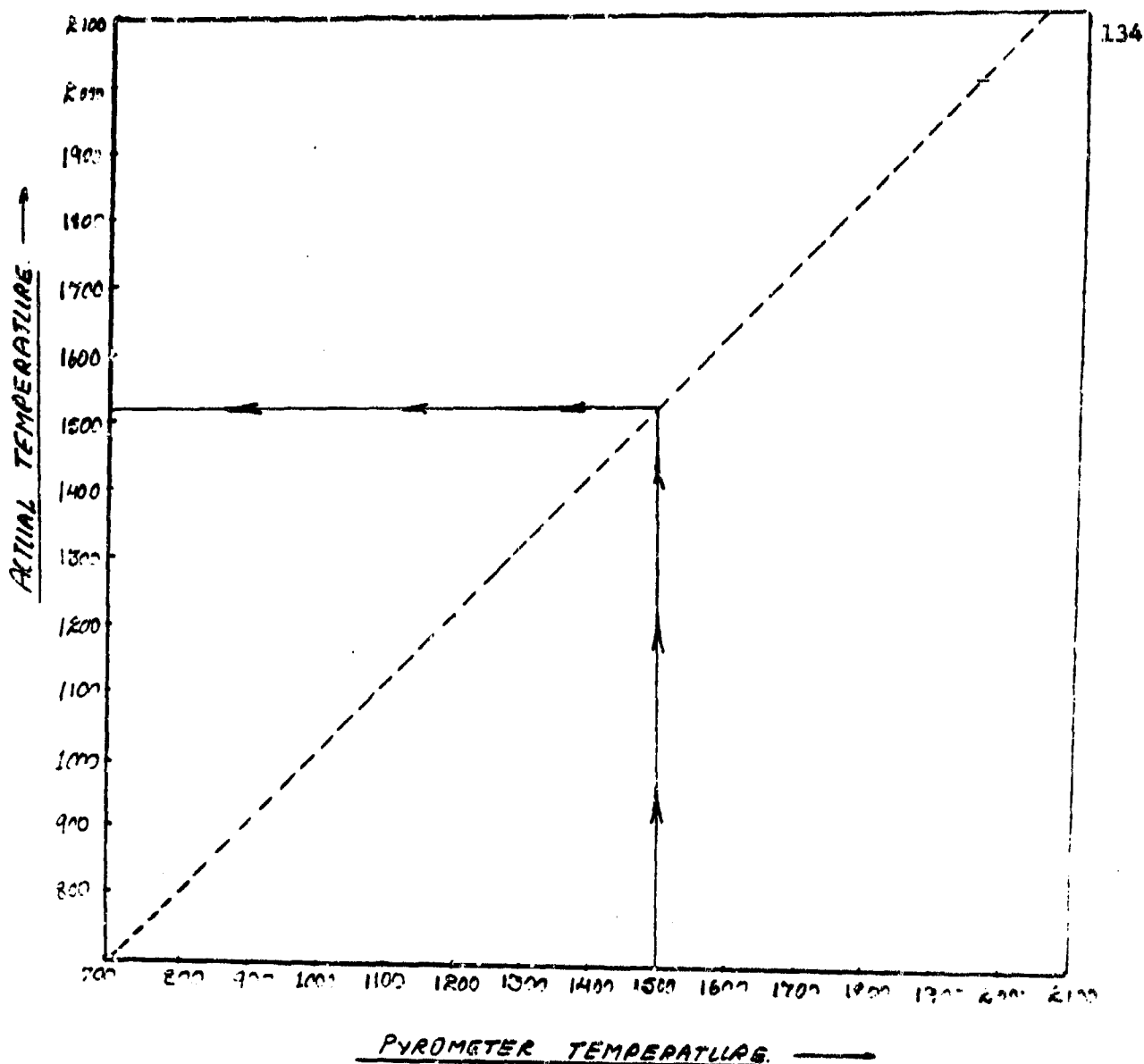
National bureau of standards.

Ribbon filament lamp.

Brightness temperatures at 0.655 um.

Maximum uncertainities in temperature:

$\pm 2.5^\circ$ at 800°C.

$\pm 1.5^\circ$ at 1100°C.

$\pm 3.0^\circ$ at 2300°C.

Center contact to be at 25°C.

Angle subtended at lamp filament by the entrance pupil of pyrometer = 0.14 rad.

Date: March 6. 1975.

Fig. 4:28 plot of true temperature vs. pyrometer temperature.

is some doubt as to whether the W, 3% Re and W, 10% Re will do so, as they did not have good homogeni.y at room temperature when they were subjected to electron microprobe analysis. As these sintered alloys have not been evaluated, we would imagine that it is difficult to predict the work functions based on previous experience on arc-cast material.

The alloys with ThO_2 and HfC, being stronger at higher temperatures should reveal interesting changes and trends in work functions from grain to grain and sample to sample. The grain sizes of the different alloys at the same temperature should reveal useful information in assessing certain qualities such as recrystallization, ductility, etc. Auger electron spectroscopy of the tested samples will provide ample information on grain boundary segregation.

4.4.5 Related activities in thermionic emission

As has already been stated, at a basic level a thermionic converter is a simple device: a heated electron emitter and a cooled electron collector positioned very close to one another. The space propulsion and weapons systems currently being studied would use nuclear reactors to produce the necessary heat. The gap between the 2 electrodes is enclosed in a gas-tight envelope which is either evacuated or filled with a metal vapor. As shown in Table 4.13, in order to maintain a continuous flow of electrons from the cathode to the anode, first of all, there must be a perfect vacuum and secondly there should not be any interelectrode space charge. Unless steps are taken to limit this charge buildup, it will severly limit the efficiency of a thermionic converter. There are two ways of getting by this inter-electrode space charge. It can be done by reducing the gap between the electrodes, which can only be done to a certain extent because of machining problems or a metallic vapor could be used, which readily ionizes and then

Table 4.13 Requirements for an efficient thermionic energy
converter.

Conditions for good thermionic emission.
1) Very good vacuum.
2) No inter electrode space charges.

Ways of reducing the effect of the negative space charge.
1) Reduce inter electrode gap.
2) Introduce positive ions.

Advantages of introducing positive ions.
1) They neutralize the negative space charge.
2) Being highly active in the plasma state, they act
as a conducting path for electrons.
3) They are adsorbed on the surface of the electrode.
4) They reduce the work function and increase the
electron yield.
5) Prevent contamination of the collector due to
degassing of the emitter.

Limitations on reducing the inter electrode gap.
1) The gap has to be a fraction of a mil. wide in
order to be really effective in maximizing emission
and collection. It is impossible to machine a
surface to such close tolerances.

Advantages of using Cesium over other metallic vapors.
1) Cesium has a low work function and a low ionization
potential.
2) It has the maximum ability to reduce the work
function of the parent material.
3) It has a melting point of $28^{o}C$ and so is in the
form of a liquid at room temperature.

neutralizes the electrons consituting the space charge. There are a lot of other advantages in introducing cesium vapor and these are presented in Table 4.13.

4.4.6.1 Thermionic emission from cesiated surfaces

Thermionic emission from cesiated surfaces, also known as the "plasma immersion technique" is a simple rapid method for studying the electron emission from metals immersed in cesium vapor. It was originally developed by Marchuk [4.24] and used to study the emission of molybdenum. The glass enclosure in which the test is conducted has since been known as the Marchuk-tube.

The construction of the entire tube as well as that of the probe configuration is shown in Fig. 4.29, 4.30 and 4.31. In this technique a small loop of wire is immersed in the plasma of a conventional cesium-vapor gas discharge tube and run a few volts negative with respect to the plasma potential. The small ion current arriving at the loop allows a much larger electron current to leave the loop, without encountering the electron pace charge. A pure alumina insulator is used to shield all except the tip of the emitting loop so as to expose only a small area having a uniform temperature. An advantage of this technique is that one can compare many metals in one experimental tube under identical conditions.

J.M. Houston [4.25] measured the thermionic emission of six polycrystalline refractory metals, in cesium vapor, using the plasma anode technique. The materials studied were W, Re, Ta, Mo, Nb, and a Mo-W alloy. He found that W and Re yield nearly the same emission; Mo, Ta, and Mo-W yield roughly a factor of three less emission than W, and Mo yields more than an order of magnitude less than W. Fig. 4.32 gives the typical S-curves for the different materials with the cesium at 150°C.
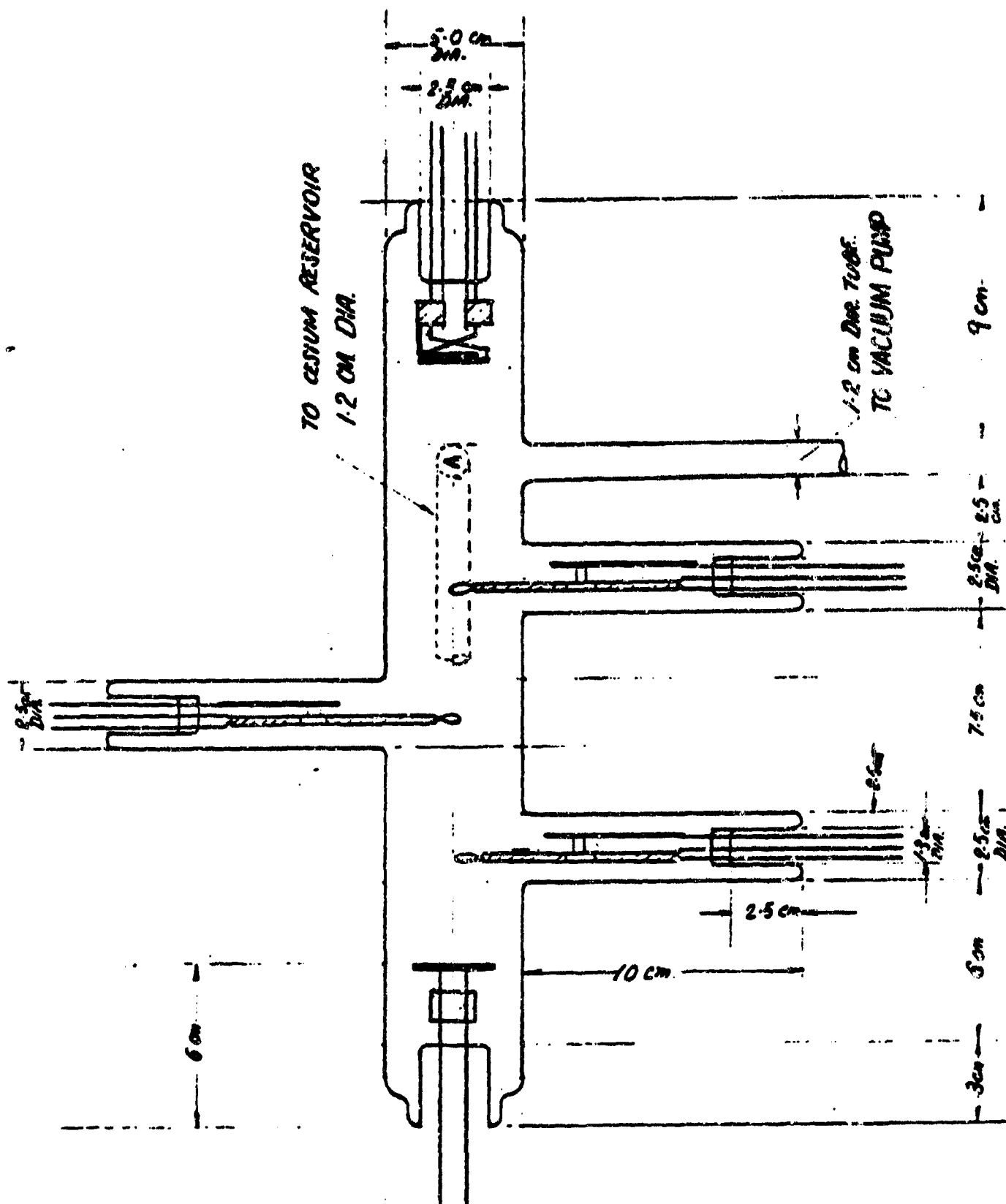
Fig. 4.29   The all-glass Marchuk tube.
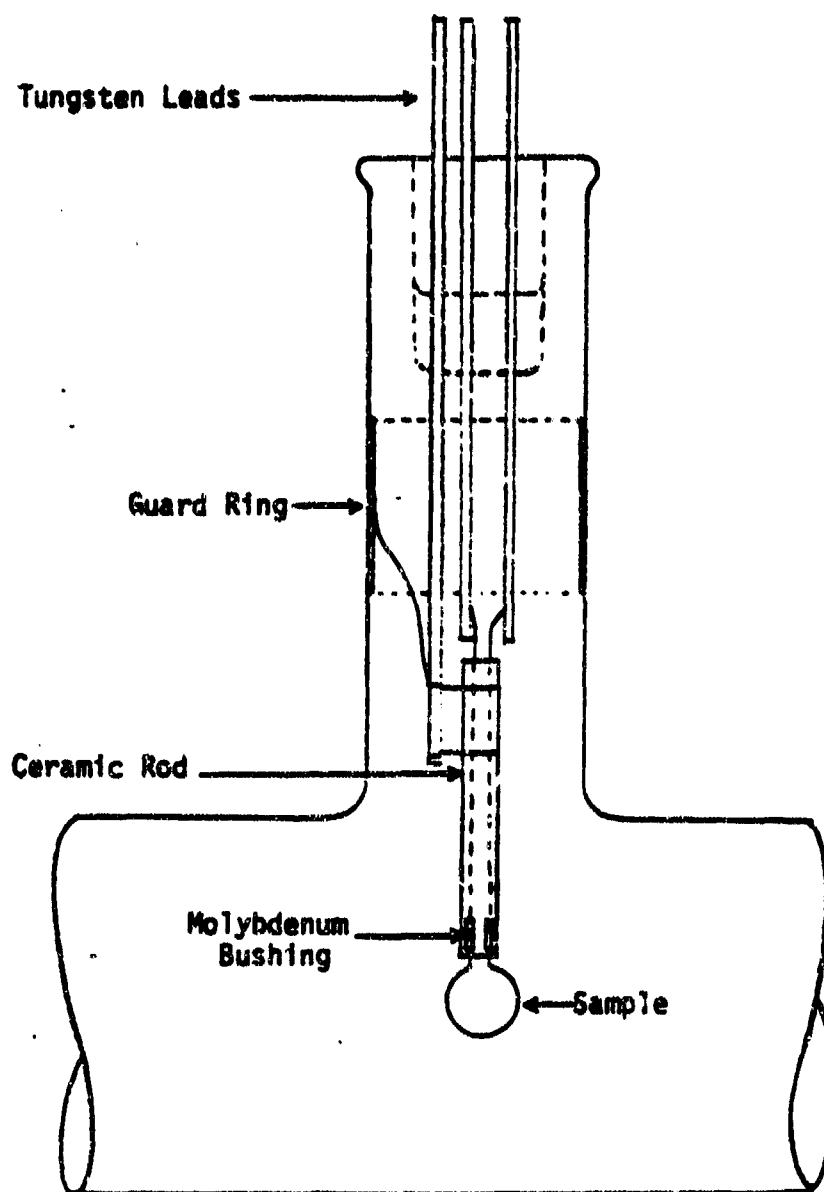
Fig. 4.30   The probe configuration.
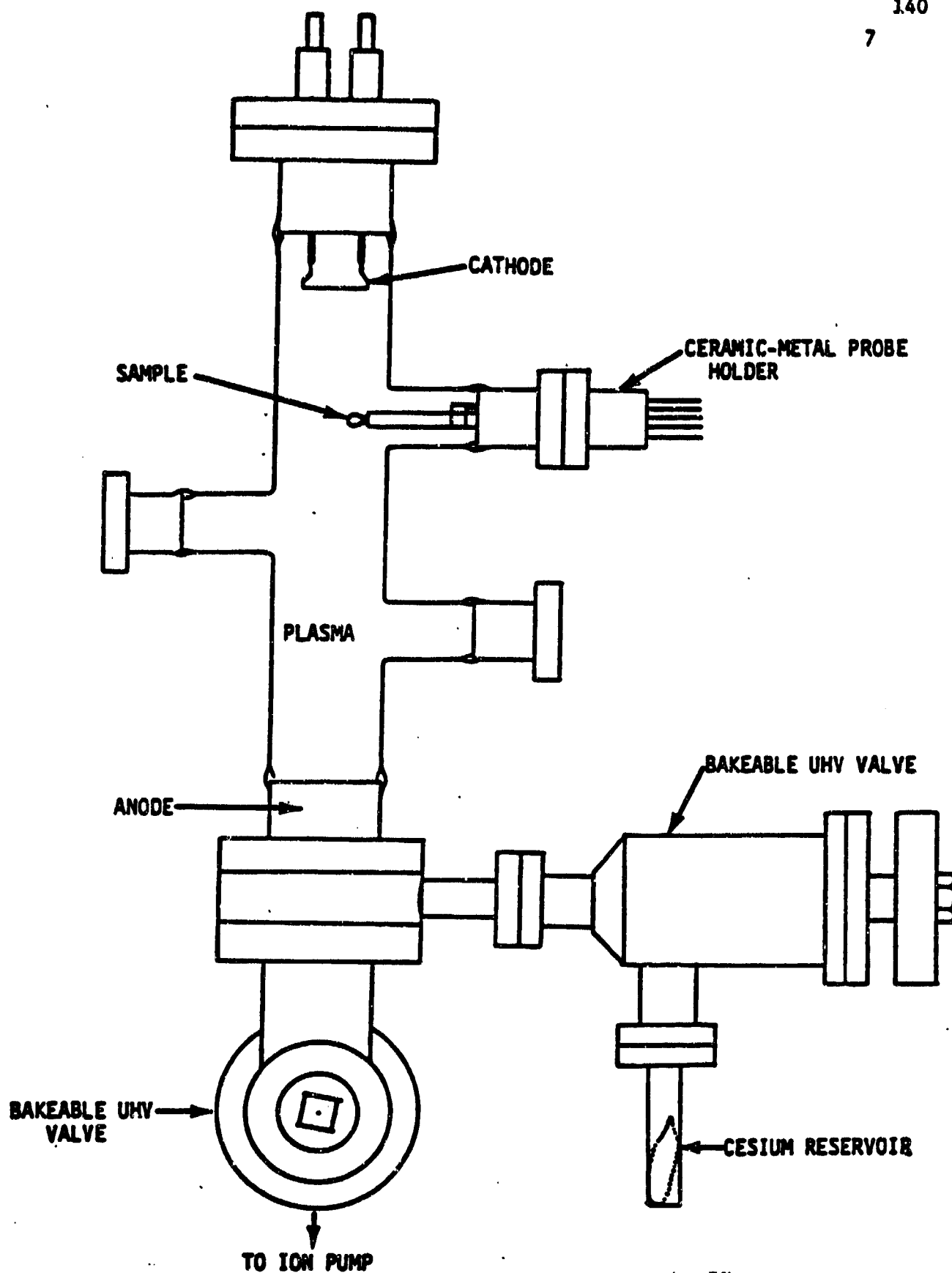
Fig. 4.31 A reusable metal-glass Marchuk tube.
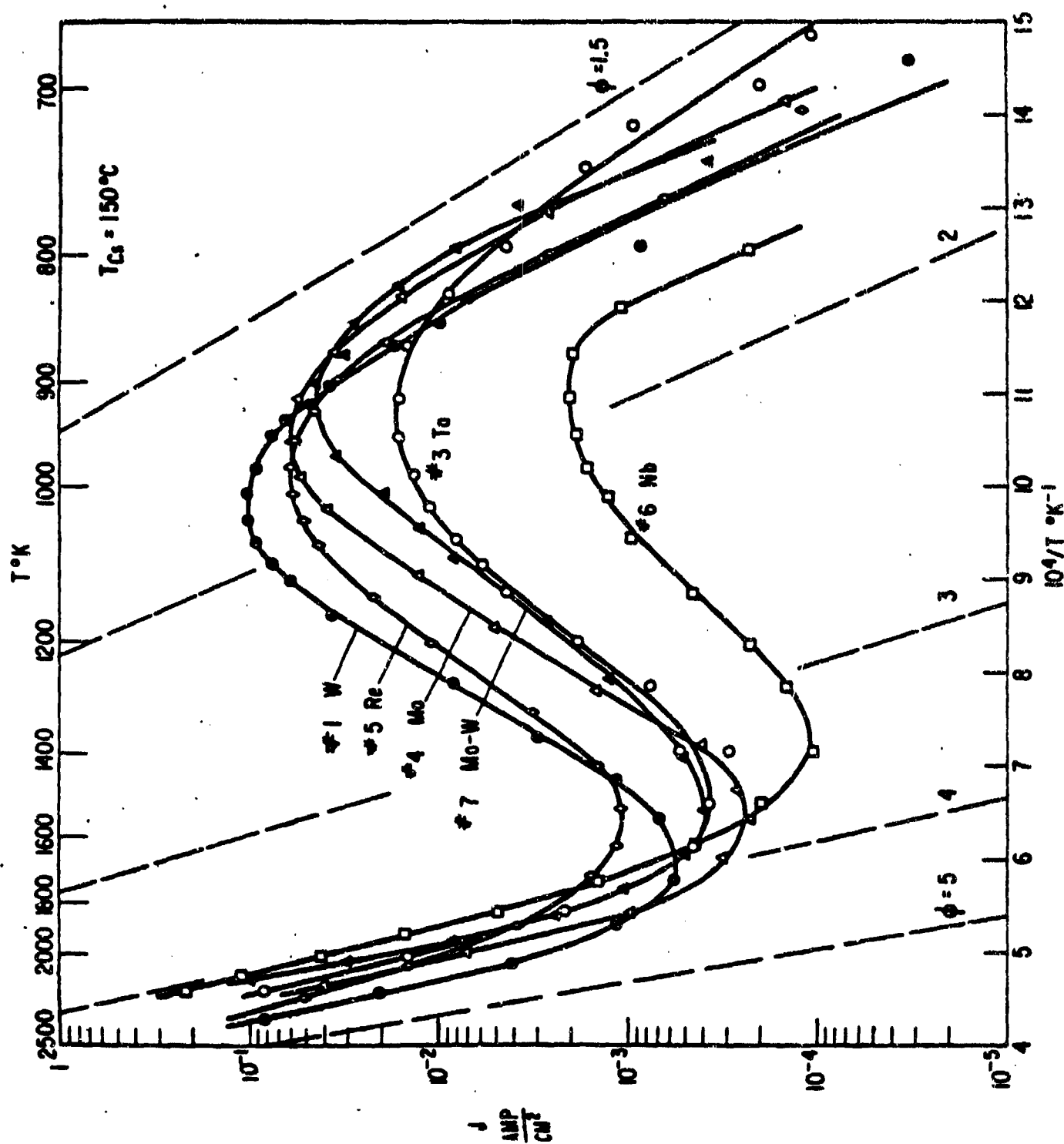
Fig. 4.32. S-curves for tungsten, rhenium, etc.

P.K. Dederick [4.26] and Houston used the plasma-immersion technique to measure the thermionic emission of non-atomically clean W, Ta, Mo, Ni, Ar, S.S. and Nichrome. They found that unflashed W had an emission of 0.045 to 0.76 amps/cm² with ϕ_{min} = 1.6 V. Mo had an emission of 1.0 amps/cm² with a ϕ of 1.5 V. Ta had an emission of 0.39 amps/cm² with a ϕ of 1.36 V. S.S. had an emission of 0.25 amps/cm² with a ϕ of 1.4 V. Ni had an emission of 0.01 amps/cm² with a ϕ of 1.5 V.

J.L. Coggins [4.27] et al., studied the thermionic emission characteristics of (110) and (112) single crystal tungsten. They determined the dependence of the thermionic emission in these two directions on filament temperature with a cesium reservoir temperature of 40°C. From the experimental results, they found that data for the (112) direction were not as reliable as those for the (110) direction because of the extreme susceptibility of the (112) face for contamination.

The cesiated electron emission was measured for three candidate electrodes for use as collectors in thermionic converters by M. Manda [4.28] and D.L. Jacobson. Nickel, Inconel 600 and Hastelloy were tested with a 412°K cesium reservoir. Peak emission from the alloys was found to be comparable to that from pure nickel. Both the Inconel and Hastelloy samples had work functions of 1.64 eV at peak emission. The minimum work functions were estimated to be 1.37 eV at a probe temperature of 750°K for Inconel and 1.40 eV for Hastelloy at 665°K. The bare work function for both alloys was estimated to be approximately 4.8 eV.

D. Tang [4.29] has been investigating the electron emission from cesiated 1% and 2% thoriated tungsten, with the help of a Pyrex Marchuk tube. A cesium pressure of 0.699 Pa was maintained with the cesium reservoir at 413°K. The peak emissions were measured to be 0.322 A/cm² at

1030°K for 1% thoriated tungsten and 1.139 A/cm² at 1120°K for 2% thoriated tungsten. The corresponding work functions were 1.75 eV and 1.78 eV respectively.

The main drawback of an all glass Marchuk tube is its inability to be used repeatedly for testing purposes. The whole tube in usually discarded if any parts or electrodes failed during fabrication or processing. It is useful for conducting one test after which it is rendered useless. In order to overcome this, it is proposed to build a metal-glass Marchuk tube with isolation valves as shown in Fig. 4.31. This will hopefully permit more than one test to be conducted on the same tube.

An Extranuclear Spectral 275 Mass Spectrometer is being set up in the lab in order to characterize our samples. For solid materials, a specially designed source inlet is used to introduce a sufficient amount of sample molecules into the ionizer chamber by evaporating the wire. However, no more than 1 µgrm. of the material should be raporized at once and introduced into the ionizer. The wires can be heated by direct resistance heating whereas larger chunks of material will have to be heated by induction heating or electron bombardment.

4.4.7 Recomendations for future research on thermionic emission

At the end of the present program we expect to have all the results on the W, Re and W, Re, ThO₂, HfC alloy combinations. Though this would give us a lot of useful information, the optimization study, would be complete if the W, Re alloys were studied individually with 1% ThO°₂ and 0.3% HfC additions.

The wires that have been procured would be ideal for testing in the metal-glass Marchuk tube as this would reduce the time and make the experimentation more economical. Further, the results of cesiated W, Re

together with the information obtained from the microscope should be useful in deciding emitter and collector materials for higher efficiency thermionic converters.

A motorized X, Y, Z mechanism would go a long way in making measurements on critical regions, a lot easier. The ion pump should be located closer to the emitter assembly. The Faraday pump guard ring and decelerating grid should be made integral. A permanent design for baking the entire system is absolutely essential.

4.5 HIGH TEMPERATURE, HIGH VACUUM MECHANICAL TESTING OF W, Re AND W, Re, ThO_2, HfC ALLOYS

The thermionic emission microscope is a very useful tool to acquire the surface characteristics (properties) of refractory metals and alloys that find application in Space Thermionic Energy conversion. However, the bulk properties of the materials are almost as useful as the surface properties, if they are to be exposed to the low pressure/low temperature environment in outer space. A significant quantum of data is available on the bulk properties of refractory materials at high temperatures but in most cases the tensile tests were conducted at room temperature and atmospheric pressure after annealing the sample to high temperatures for varying periods of time. Values obtained in this fashion do not really characterize the material at a given temperature because of a number of detrimental factors such as atmospheric contamination, irregular heating and so on. This has led a number of investigators to investigate real-time deformations and microstructural changes in refractory materials at high temperatures and moderate vacuum atmospheres.

Though W, Re cast materials have been mechanically tested at high temperatures, a complete study of the W, Re and W, Re, ThO_2, HfC sintered

materials family has not been examined in detail. This constitutes the latter half of the research activities for this program and what follows is a description of what was done so far, what is to be done in future and what results are expected with regard to high temperature, high vacuum mechanical testing of the respective alloys.

4.5.1 High temperature mechanical testing as opposed to conventional mechanical testing

Before we deal with high temperature testing, it would be appropriate to describe some of the mechanical properties that can be obtained by conventional testing under atmospheric conditions.

4.5.1.1 Mechanical properties in conventional mechanical testing

Deformation occurs where forces are applied to a material. Strain, e, is the amount of deformation per unit length and stress, σ, the force per unit area. Energy is absorbed by a material during deformation because a force has acted along the deformation distance. Strength is a measure of the level of the stress required to make a material fail. Ductility identifies the amount of permanent strain prior to fracture, while toughness refers to the amount of energy absorbed by a material during failure. All the pertinent mechanical properties are shown in Table 4.14. The initial strain (elastic) is essentially proportional to the stress; furthermore, it is reversible. The modulus of elasticity or Young's modulus is given by

$$E = \frac{\sigma}{e} \qquad (4.10)$$

It is a measure of the interatomic bonding forces. At higher stress permanent displacement occurs and this is termed plastic strain. The elastic strain is recovered when the material fractures but not the plastic

Property, or characteristic	Symbol	Definition (or comments)	Common units	
			SI	English
Stress	s	Force/unit area (F/A)	pascal* (N'/m^2)	psi* lb_f/in^2
Strain	e	Fractional deformation $(\Delta L/L)$	—	—
Elastic modulus	E	Stress/elastic strain	pascal	psi
Strength		Stress at failure		
Yield	S_y	Resistance to initial plastic deformation	pascal	psi
Tensile	S_t	Maximum strength (based on original dimensions)	pascal	psi
Ductility		Plastic strain at failure		
Elongation	e_f	$(L_f - L_0)/L_0$	$	$
Reduction of area	R of A	$(A_0 - A_f)/A_0$	$	$
Toughness		Energy for failure by fracture	joules	ft-lb
Hardness		Resistance to plastic indentation	Empirical units	

Table 4.14 Mechanical properties in conventional mechanical testing.

strain. In the present context, the single most important property that we are interested in determining for the W, Re and W, Re, ThO_2, HfC alloys is the DUCTILITY. Ductility, the plastic strain required for fracture, e_f, may be expressed as percent elongation. Like all strains it is dimensionless and is given by

$$e_f = \frac{\Delta L}{L} = \frac{L_f - L_0}{L_0}$$ (4.11)

However, since plastic deformation is commonly localized in the necked area, the percent of elongation depends on the gage length. So, one must be specific about the gage length whenever reporting ducility.

A second measure of ductility is the reduction in area given by

$$\text{ductility} = \frac{\Delta A}{A} = \frac{A_0 - A_f}{A_0}$$ (4.12)

at the point of fracture. Thus, elongation is a measure of plastic stretching whereas reduction in area is a measure of plastic contraction. The reduction in area is preferred in most cases, as a measure of ductility, because it does not require a gage length and it can be used to determine the true strain at the point of fracture.

The ability of a material to resist plastic deformation is called the yield strength S_y, and is the ratio

$$\sigma_y = \frac{F_y}{A}$$ (4.13)

where F_y is the force initiating the yield. In soft materials, the yield strength is marked by a definite yield point, but in harder materials it is common to define the yield strength as that stress required to give 0.2% plastic offset. The tensile strength, σ_t, of a material is calculated by dividing the maximum force by the original cross-sectional area. True

stress is based on actual area and nominal stress is based on the original area.

Toughness is a measure of the energy required to break a material in contrast to strength, which is a measure of the stress required to deform or break a material.

4.5.1.2 Subtleties involved in high temperature mechanical testing

All the properties mentioned above, can also be obtained in high temperature testing but this involves some subtleties not exhibited by conventional testing methods. First of all the specimen has to be heated. This can be done by resistance heating, induction heating or electron beam heating. Resistance heating was chosen in this case because of its simplicity and the small size of the sample. The fact that the specimen is heated to the order of 2500°K makes it absolutely necessary to house the tensile system in a vacuum chamber to prevent high tempera' ~e oxidation and imminent failure of the specimen. Special ceramics that have excellent electrical and thermal resistivity have to be used and the grips holding the specimen should also be made of a high temperature resistant material. Some means of cooling the grips have to be made available if there is excessive heat conduction from the specimen. Special vacuum chambers with flexibility to move while evacuated, had to be designed and procured for the testing. A high vacuum system should also be available.

4.5.2   Objectives of the research on high temperature mechanical testing

a)   Design a high vacuum system complete with instrumentation for temperature measurement and for heating the specimen.

b)   Fabricate the components of the system with suitable materials for the grips and the insulators.

c)   Using techniques such as Electron microprobe analysis, X-ray analysis, Metallography and Auger electron spectroscopy, characterize the materials received.

d)   Fabricate tensile test specimen using conventional machining and electrical discharge machining from the hot swaged, 0.25" rods with high density.

e)   Design fixtures, necessary for the precision machining of W, Re and W, Re, ThO_2, HfC alloys.

f)   Test the samples in an Instron testing machine.

        i)   Each alloy combination is to be tested at room temperature and and three other higher temperatures after maintaining the samples for a fixed period of time before deformation.

        ii)   Obtain stress-strain relationship for each specimen and the ductilities of the various material combinations.

        iii) Take replicas of the fractured surfaces and observe fracture characteristics in the TEM.

4.5.2.1 Present status on the activities with reference to stated objectives

    i)   Design of the entire system has been completed.

    ii)   95% of the components have been fabricated.

    iii) Techniques for machining W-alloys have been progressively refined and optimized.

    iv)   Part of the initial materials' characterization has been completed.

    v)   An Instron testing machine donated by Motorola is being readied for operation.

    vi)   The entire system is expected to be in operation during May 1985.

4.5.3 Literature survey on high temperature mechanical testing

As was stated earlier, prior to the 1960's most of the high temperature tensile test data were not really the output of real-time tests but values that were the result of extrapolations from room temperature data and high temperature annealing. However, there was some introductory work by Chester T. Sims [4.32] and P.I. Jaffee in the mid fifties that involved the testing of 50 mil rhemium wires at various temperatures under a controlled atmosphere of a mixture of 5% H in Helium. The results of the tenisle tests and stress rupture tests are shown in Fig. 4.33 and Table 4.15. In general they found that the elevated temperature strength properties of rhenium were high. Elevated temperature short time tests revealed that the elongation drops to a low value of about 1 to 3% above 500°C, whereas the stress-rupture tests showed elongations in excess of 4% at 2000°C. Improved ductility, which is normally observed at the recrystallization temperature in most metals seemed to occur at high temperatures in rhenium. The ductile to brittle transition [4.11] is of considerable importance in the case of tungsten because of the relatively high temperatures at which it occurs. As shown in Fig. 4.34, in general, the effect on the flow and fracture of annealed (recrystallized) tungsten as the deformation temperature drops through the transition zone is that of sharply increasing the yield strength. This resulted in a corresponding reduction in ductility over a narrow temperature range. The rapid increase in stress to produce yielding as temperature decreases is also illustrated. The relation between yield stress and temperature can be expressed by an equation of the form

$$\sigma = \exp[-q/RT] \qquad (4.14)$$
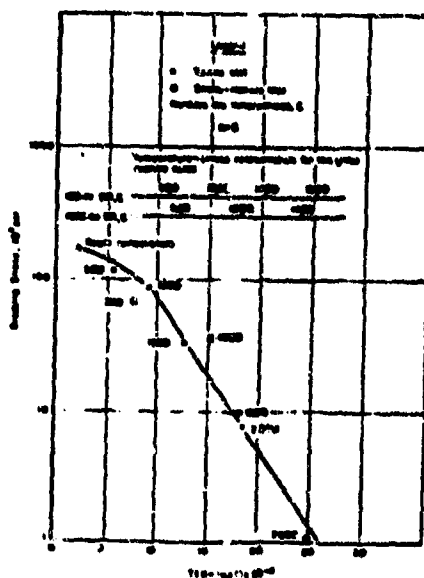
Fig. 4.33   Parametric plot of tensile and rupture data for pure rhenium metal.

Temperature, °C	Breaking Stress, Psi	Rupture Time	Elongation, Pct	Remarks
		100 hr	0.8, in 1.5 in.	Cased operation without rupture
25		Ruptured while loading		
500	105,000	2 sec		
500	90,000	3 min		
500	75,000	3.2 hr	0.6, in 1 in.	Oxidized badly
500	65,000	16.5 hr	2.0, in 4.5 in.	Oxidized badly
1000	40,000	18 min	0, in 2.2 in.	No oxidation, good test
1500	2,500	41 min	3.0, in 1.3 in.	Oxidized badly
1500	8,500	4.4 hr	1.0, in 2.3 in.	Oxidized badly
1500	8,500	23 min		No oxidation, good test
2000	1,100	48 min	0.5, in 1 in.	
2000	1,100	12.3 hr	4.4, in 2.5 in.	
2000	1,100			

Table. 4.15 Stress-rupture characteristics of 50 mil. Re wire at 1000°C.

Table .4.16 High temperature tensile properties of solid solution tungsten–rhenium–hafnium alloys.
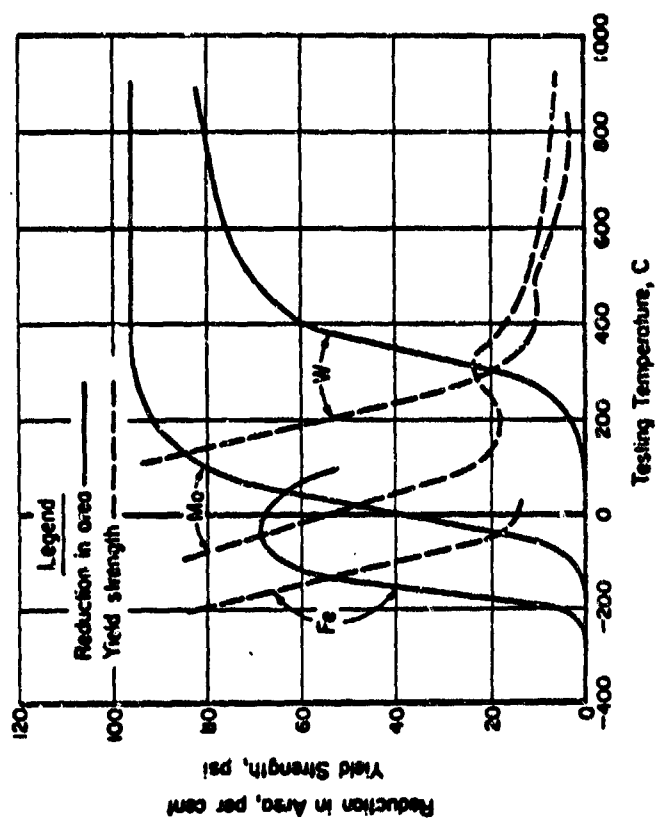
Fig. 4.34 Effect of temperature on the reduction in area and yield strength of annealed iron, molybdenum and tungsten.

The quasi activation energy for tungsten, calculated from the slope of Fig. 4.35 was about 5400 cals/mole for W, compared to 1700 cals/mole for Mo and 200 cals/mole for steel. Fig. 4.36 shows the effect of powder purity on ductile-brittle transition temperature of tungsten and this was investigated by Atkinson [4.31] and cited in this reference. It was found the interstitial atoms tend to increase the dbt temperature in tungsten. The figure shows that successively lower impurity levels reflect lower transition temperatures. Though this particular reference did not contain a lot of information on W-Re alloys, enough information was available to indicate that the ductile-brittle transition range for recrystallized 30 Re - 10 W extended down to 100°C. Fig. 4.37 summarized the tensile properties found by Jaffee [4.32] and associates for W-30 Re alloy. The strength of this alloy remained remarkably high up to just below the recrystallization temperature range.

In 1966, W.D. Klopp [4.33] and associates released a NASA document on the mechanical properties of solid-solution and carbide strengthened arc-melted tungsten alloys. They investigated the mechanical properties of several arc-melted tungsten alloys containing rhenium, tantalum, columbium, hafnium and/or carbon, in the temperature range of 2500°F to 4000°F. They found that solid-solution strengthening in W alloys was most effective in W-Hf alloys and least effective in W-Re alloys. Carbon additions to different W alloys produced various degrees of strengthening with the largest effect formed in W-Hf-C alloys. The strongest alloy W - 0.26a% C - 0.20a% Hf had a tensile strength of 62,500 psi at 3500°F. Table 4.35 gives the high temperature tensile properties of tungsten-rhenium-hafnium alloys. Tensile tests were performed in a vacuum of less than 5×10^{-5} torr at a constant crosshead speed of 0.05 ins./mt. The specimens were brought to temperature

Fig. 4.36 Effect of powder purity on the ductile-brittle tran. temperature of tungsten.

Fig. 4.35 Yield strength vs. temperature for recryst—allized tungsten.
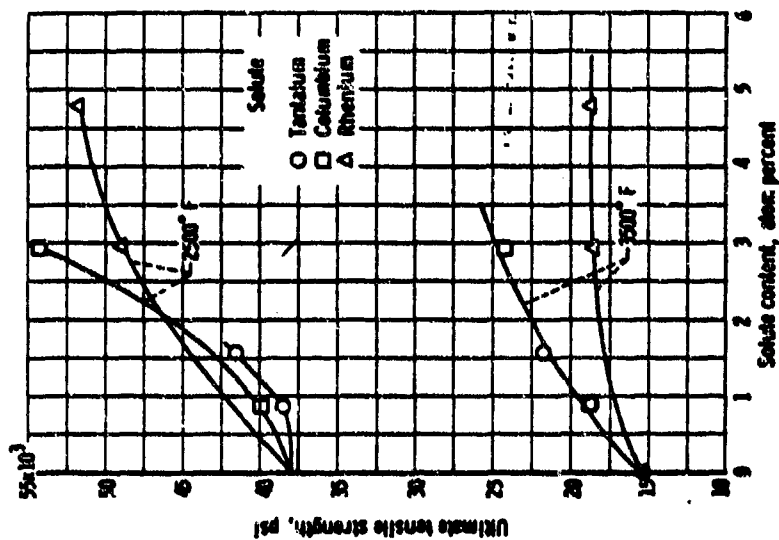
Fig.4.38 Effect of Ta,Co,Re on the tensile strength of W-0.37%Hf alloy at 2500°F and 3500°F.
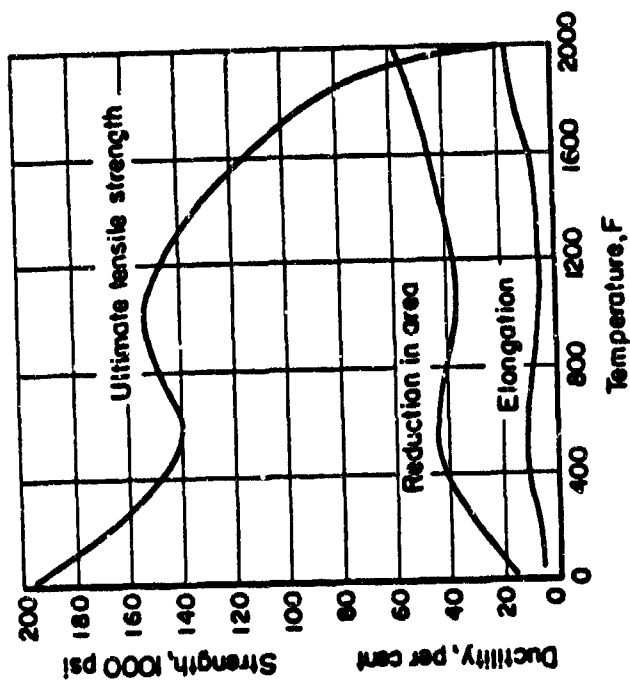
Fig.4.37 Tensile properties of W-30%Re wire at elevated temperatures.

in approximately one hour and held at that temperature for 30 minutes prior to testing. Fig. 4.38 shows the effect of rhenium on the tensile strength of nominal W-0.37a% Hf alloy at 2500°F and 3500°F.

Arc melted W alloys strengthened by a finely dispersed hafnium carbide precipitate have exhibited outstanding high temperature strength [4.34]. It was found that the addition of 40% rhenium to such alloys significantly improves their low temperature ductility. The alloy that exhibited optimum properties had the composition, W-4Re-0.35Hf-0.35 C. In the swaged condition, this alloy combined a tensile strength of approximately 10,000 psi at 3500°F, with a ductile-brittle transition temperature of 200°F. Fig. 4.39 a,b,c exhibits the results of the extensive studies of these investigators.

Sell [4.12] and Stickler investigated ingots of W-5Re-2ThO$_2$ alloy sintered from blended W, Re and ThO$_2$ powders containing a coarse ThO$_2$ dispersion, that could be swaged easily. The rods were evaluated in regard to solid solution and dispersion strengthening, the effect of rhenium and the ThO$_2$ dispersion on the dbt temperature and modes of fracture. Tensile tests were made in the temperature range from room temperature to 2400°C. In the ductile-brittle region, the crosshead speed was 0.005"/min to yield, followed by 0.05"/min to fracture. Tests above 800°C, were performed at a crosshead speed of 0.05"/min. Fig. 4.42 shows the temperature dependence of 0.2% yield stress of swaged and 1/2 hr/2400°C annealed W and W-alloy rods. Fig. 4.43 represents some of the light micrographs and electron micrographs of the fractured surfaces indicating the effect of test temperature on the mode of tensile fracture of swaged and annealed rods of W-5Re-2ThO$_2$. In an effort to determine if particle strengthening by a HfC precipitate could be obtained in a ductile W high Re alloy, an arc melted W-23.4% Re - 0.27 Hf -
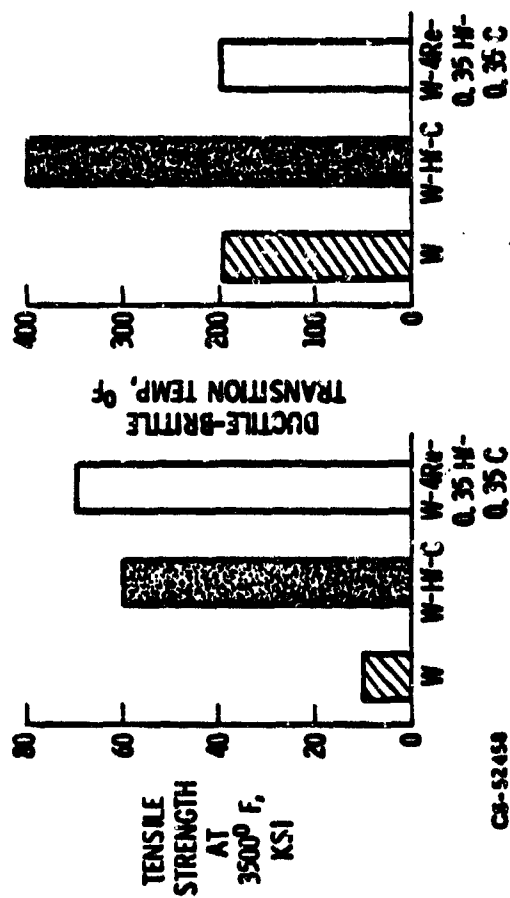
Fig. 4.39 Comparison of the mechanical properties of W-Re-Hf-C alloy with unalloyed tungsten and W-Hf-C alloy in swaged condition.
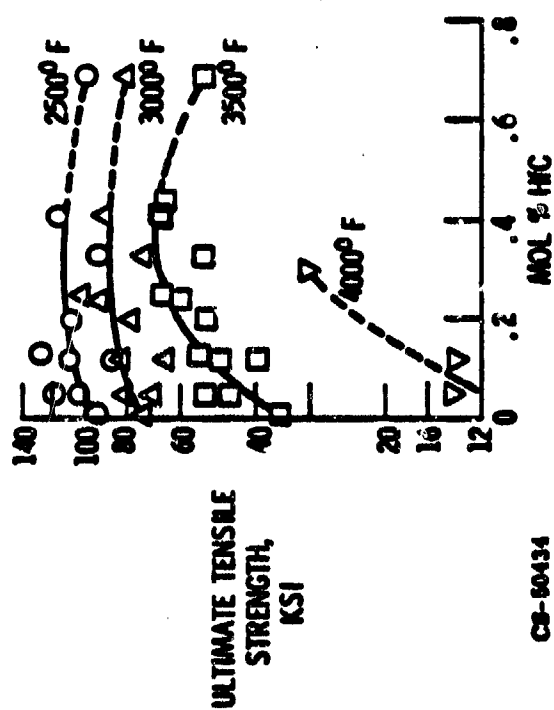
Fig. 4.40 Effect of hafnium carbide content on the high tempera-
ture tensile strength of W-4Re-Hf-C alloy.
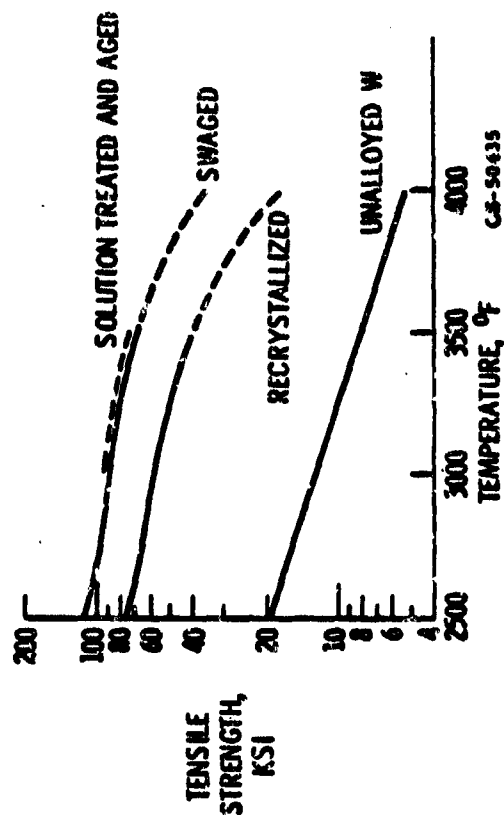
Fig. 4.41 Microstructure of swaged W-4Re-0.23Hf-0.3C alloy after tensile testing at 3500F, and comparison of the tensile strengths of W-4Re-0.35Hf-0.35C alloy in several microstructural conditions.
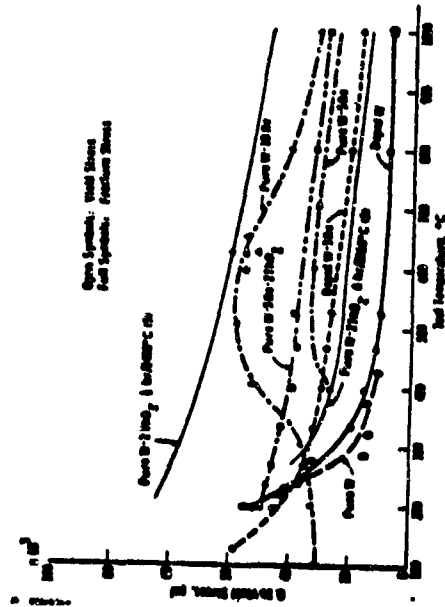
Fig.4.42 Temperature dependence of 0.2% yield stress of swaged W and W alloy rods.
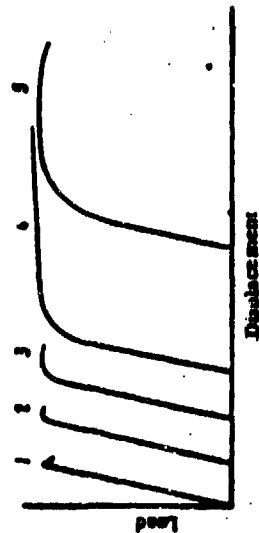
Fig. 4.44 Typical tensile curves of powder tungsten at increasing temperatures.
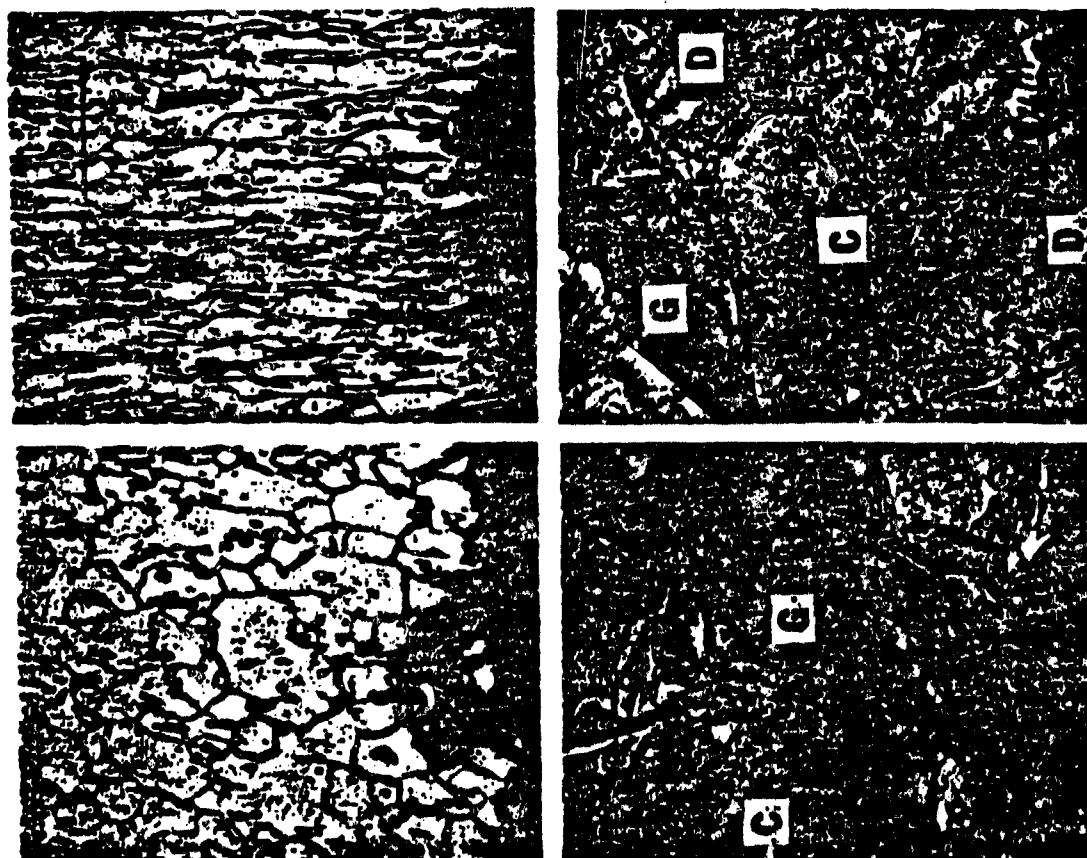
Fig. 4.43 Effect of test temperature on the mode of tensile fracture of swaged and 0.5hr./2400C annealed rods of W-5Re-2ThO$_2$.

C alloy was evaluated [4.35] by tensile testing. The alloy was found to exhibit good high temperature strength properties. At 3000°F, the HfC-strengthened alloy had a short time tensile strength of 62.7 ksi, more than double the strength of 28.1 ksi observed earlier for W-24 Re. However, the strength advantage decreases at higher temperatures due to HfC particle coarsening and grain boundary sliding. The tensile properties of the material are given in Table 4.17.

Arc melted tungsten-4 percent rhenium-hafnium-carbon alloys containing up to about 0.8 mol. percent-HfC were evaluated [4.36] for compositional effects on mechaincal properties in the as worked condition. The tensile properties of the W-4Re-Hf-C alloys, tested at 1930°C are given in Table 4.18. The data showed considerable scatter, especially for the alloys containing an excess of C. It was found that peak strengthening occurred at or near the calculated stoichiometric HfC composition (0.3 to 0.4 mol %) but decreased rapidly with excess of either carbon or hafnium.

F.I. Uskov [4.37] and A.V. Borbak investigated the temperature relationship of the characteristics of fracture toughness (crack resistance) of the powder metallurgy of tungsten. The samples were heated by radiation at a rate of 1 deg./sec. Before tension, a sample was held at the specified temperature for 30 minutes. Curves obtained in tests of compact samples of the powder metallurgy of tungsten under conditions of off-center tension at various temperatures (920-1600°C) in vacuum are shown in Fig. 4.44. Fig. 4.45 shows the characteristic features of failure of tungsten at different temperatures. From the features of the failure, it was concluded that the significant extent of the gently sloping portion on the tensile curves was not an indication of general plastic flow of the material. The failure of
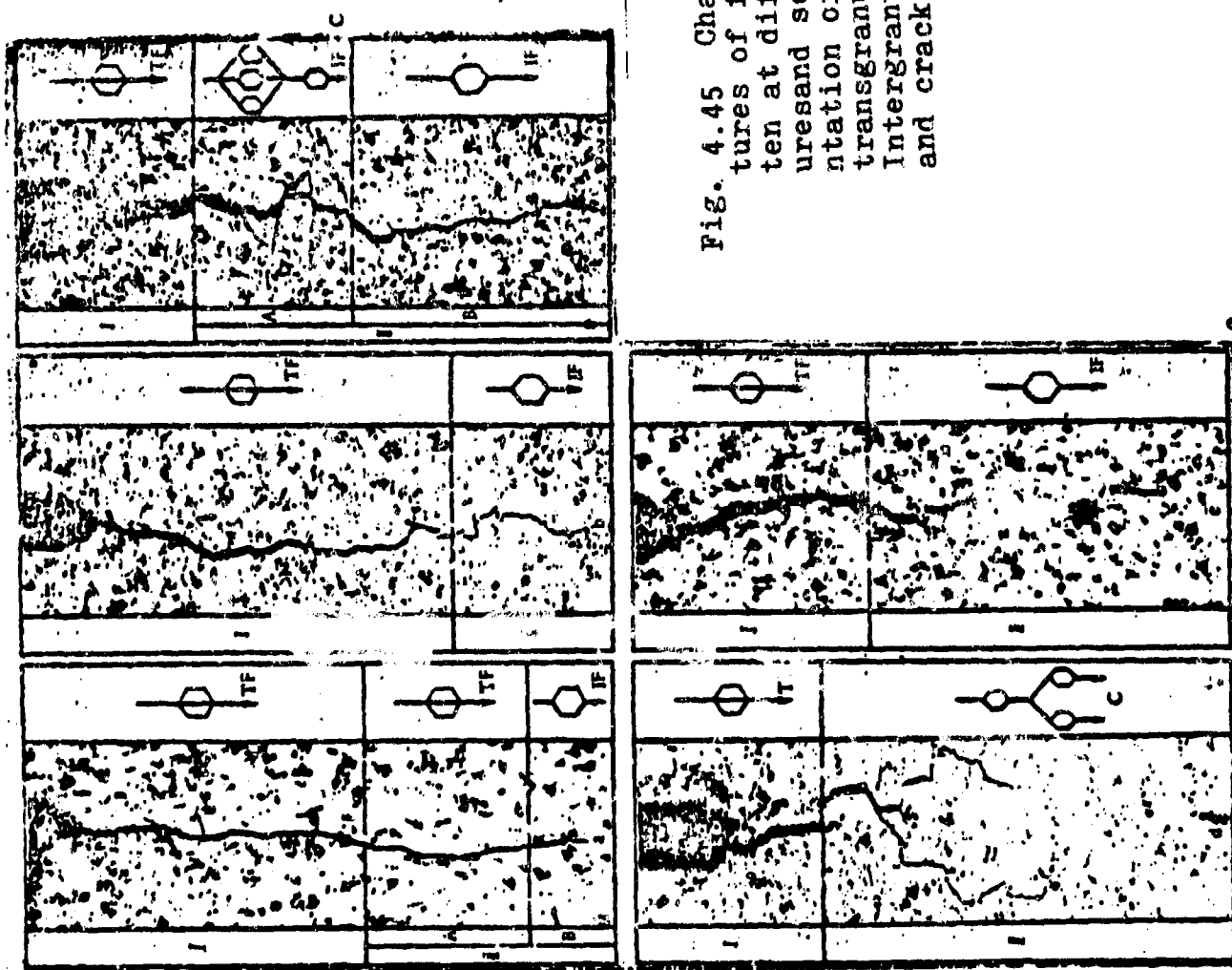
Fig. 4.45 Characteristic features of failure of tungsten at different temperatures and schematic representation of the processes of transgranular failure(TF), Intergranular failure(IF), and cracking (C).

Test temperature		Yield strength		Ultimate strength		Elongation (%)	Reduction in area (%)	Carbon content after test (at.%)	Median particle diam. after test (Å)(10⁻¹⁰ m)
(°F)	(°C)	(ksi)	(MN/m²)	(ksi)	(MN/m²)				
As swaged									
75	24	268	1850	289	1990	8	14	1.12	—
2000	1093	149	1030	172	1190	16	57	1.04	—
2500	1371	138	951	143	1000	23	65	1.00	—
3000	1649	56.9	392	62.7	432	39	84	0.78	—
3500	1927	15.5	107	16.7	115	92	87	0.81	700
Annealed 1 h at 3600°F (1892°C)									
2500	1371	59.3	409	67.9	468	60	91	0.99	—
3000	1649	32.9	227	34.7	239	73	>95	0.56	—
3500	1927	17.3	119	17.8	123	105	>95	0.64	840
Annealed 10 min at 4900°F (2704°C) and 1 h at 2500°F (1371°C)									
3500	1927	46.4	320	48.0	331	9	13	0.34	—

Table. 4.17 Tensile properties of W-23.4%Re-0.27Hf-C alloy.

Alloy	Calculated hafnium carbide content, mol%	Posttest carbon content, at. %	Excess solute, at. %		Ultimate tensile strength		Yield strength (0.2% offset)		Elongation, percent	Reduction in area, percent
			Hafnium	Carbon	MN/m²	ksi	MN/m²	ksi		
[a]A216	[b]0.20	[b]0.20	[b]0.10	----	361	52.4	322	46.8	21	85
[a]A234	.24	[b].30	----	[b]0.06	411	59.7	264	38.3	14	78
A263	.26	.46	----	.20	407	59.0	383	55.5	18	90
A272	.28	.35	----	.07	528	76.6	303	72.9	11	31
A272	.28	.39	----	.11	538	78.1	492	71.4	14	42
A270	.31	.66	----	.55	293	42.5	279	40.4	17	83
A261	.31	.31	.08	----	381	55.3	364	52.8	21	84
[a]A235	.31	.31	.04	----	458	66.5	413	59.9	20	76
[a]A219	.33	.67	----	.34	367	53.3	305	44.2	16	77
[a]A246	.34	.34	.06	----	452	65.6	426	61.8	22	88
A278	.36	.53	----	.17	349	50.6	307	44.5	7	81
A264	.39	.45	----	.06	426	61.8	399	57.9	17	89
A265	.39	.39	.15	----	383	55.6	362	52.5	22	88
[a]A245	.41	[b].46	----	.05	457	66.3	429	62.2	16	80
[a]A236	.44	[b].47	----	[b].03	443	64.6	381	55.3	20	88
A253	.55	.55	.14	----	319	46.2	289	41.9	24	79

Table.4.18 Tensile properties of swaged W-4Re-Hf-C alloys at 1930°C.

all the specimens were confirmed to be of a brittle nature, from the fractographic analysis at a test temperture of 1200°C.

The effect of excess hafnium or carbon in W-4Re-Hf-C alloys on the UTS [4.14] at 2200°K after a high temperature treatment at 2417°K is shown in Fig. 4.46. A maximum in UTS was found in compositions close to those having little or no excess of either Hf or C. Both excess Hafnium and excess carbon exhibit the same effect, that is the reduction in ultimate tensile strength.

4.5.4 Design and fabrication of the components of the high temperature tensile stage

The entire tensile stage can be divided in two parts, a) the external stage and b) the internal stage, for convenience in describing the system. Fig. 4.47 is a conception of what the entire system comprising of the high temperature stage, the Instron testing machine, the vacuum system, power supply, temperature measurement system, would look like when it is ready for testing.

4.5.4.1 The external stage

Fig. 4.48 shows all the parts that constitute the external part of the high temperature stage. It is essentially made up of the crossbars of the Instron, the load cell, the flexible bellows coupling and the 4-way cross chamber. The part nos. 1 through 8 are all supporting members which were designed to have minimum weight and were fabricated in the Mechanical Development Shop at Arizona State University. Since the test is expected to be conducted in a high vacuum atmosphere, the specimen has to be deformed in a leak tight chamber. The bellows system and the 4-way cross shown in Fig. 4.49 provide exactly this and at the same time, the necessary flexibility to deform the specimen up to 1.10 in. under a vacuum of better than 10^{-7} torr.
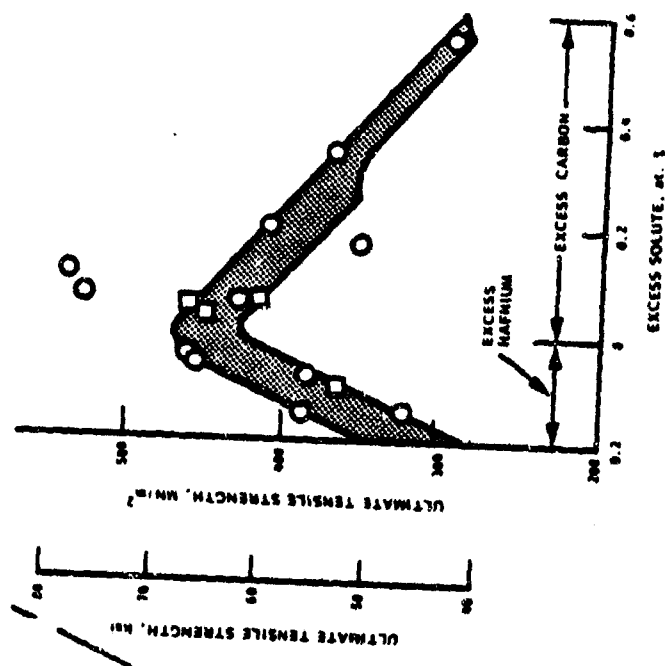
Fig. 4.46 Effect of excess Hf
or C in W-4Re-Hf-C alloys
on the UTS at 2000K after
a high temperature treat-
ment at 2477K.
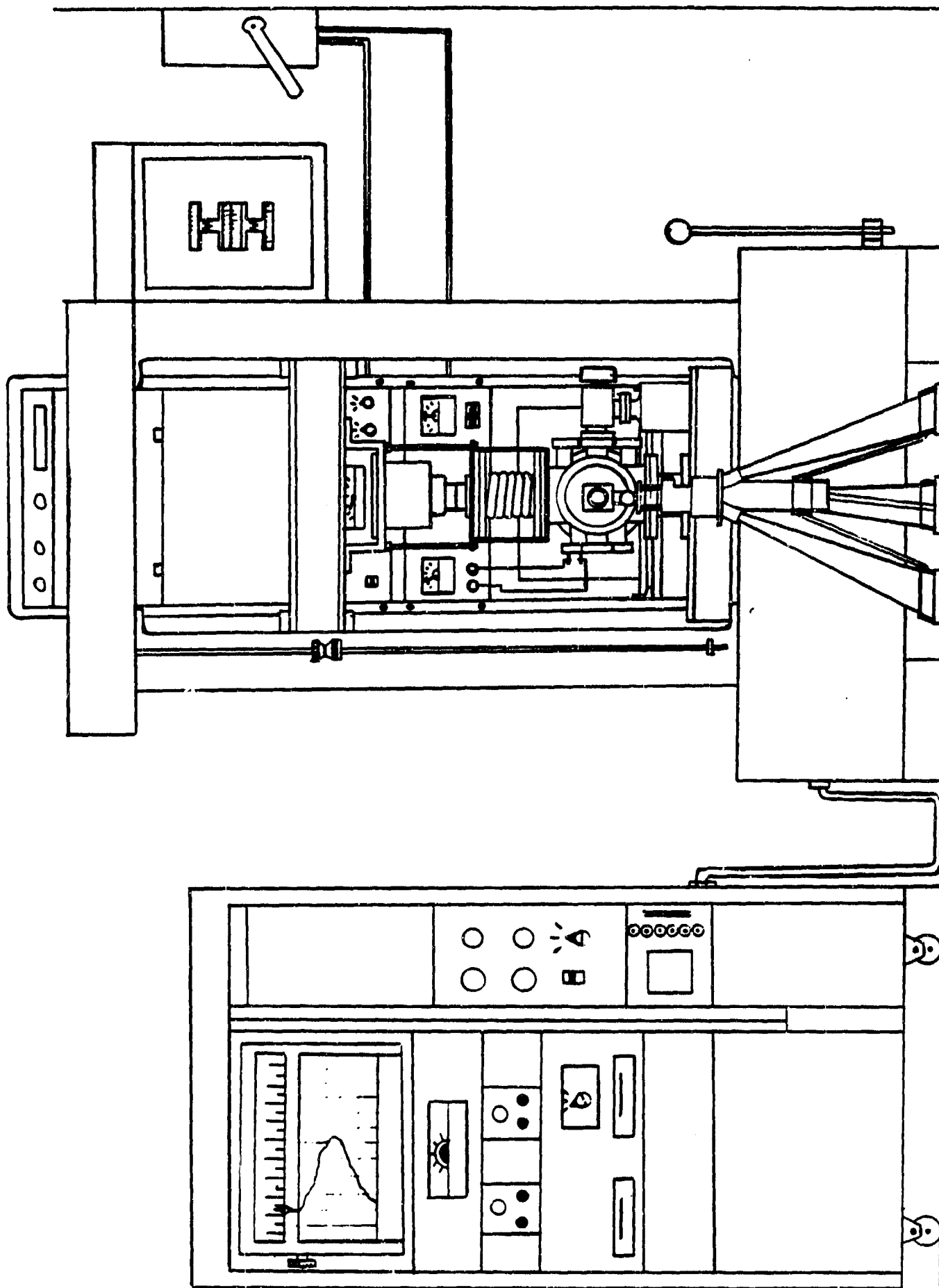
Fig. 4.47 Experimental layout for high temperature mechanical testing.

CROSSBAR

BASE
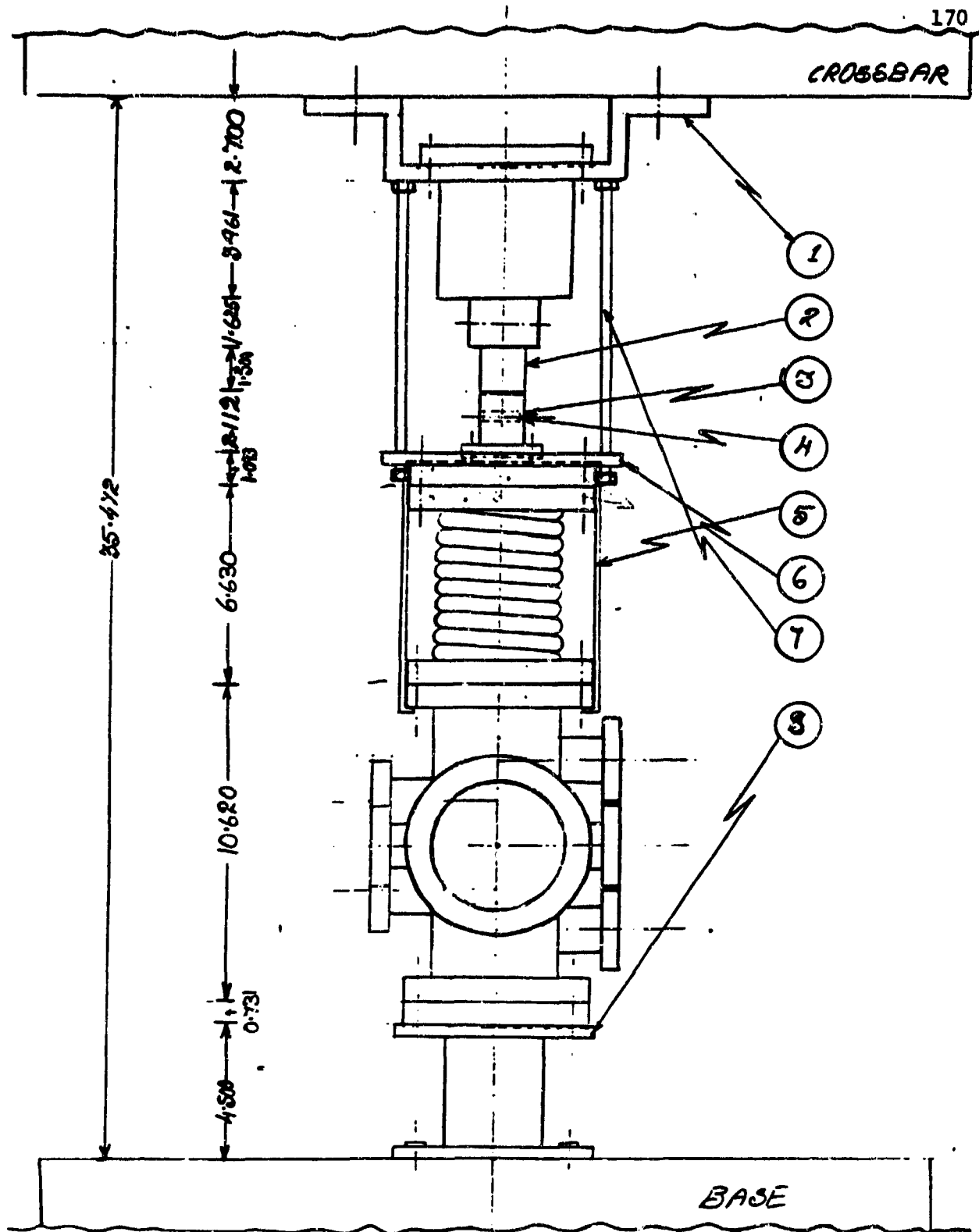
Fig. 4.48 External stage of the testing system.
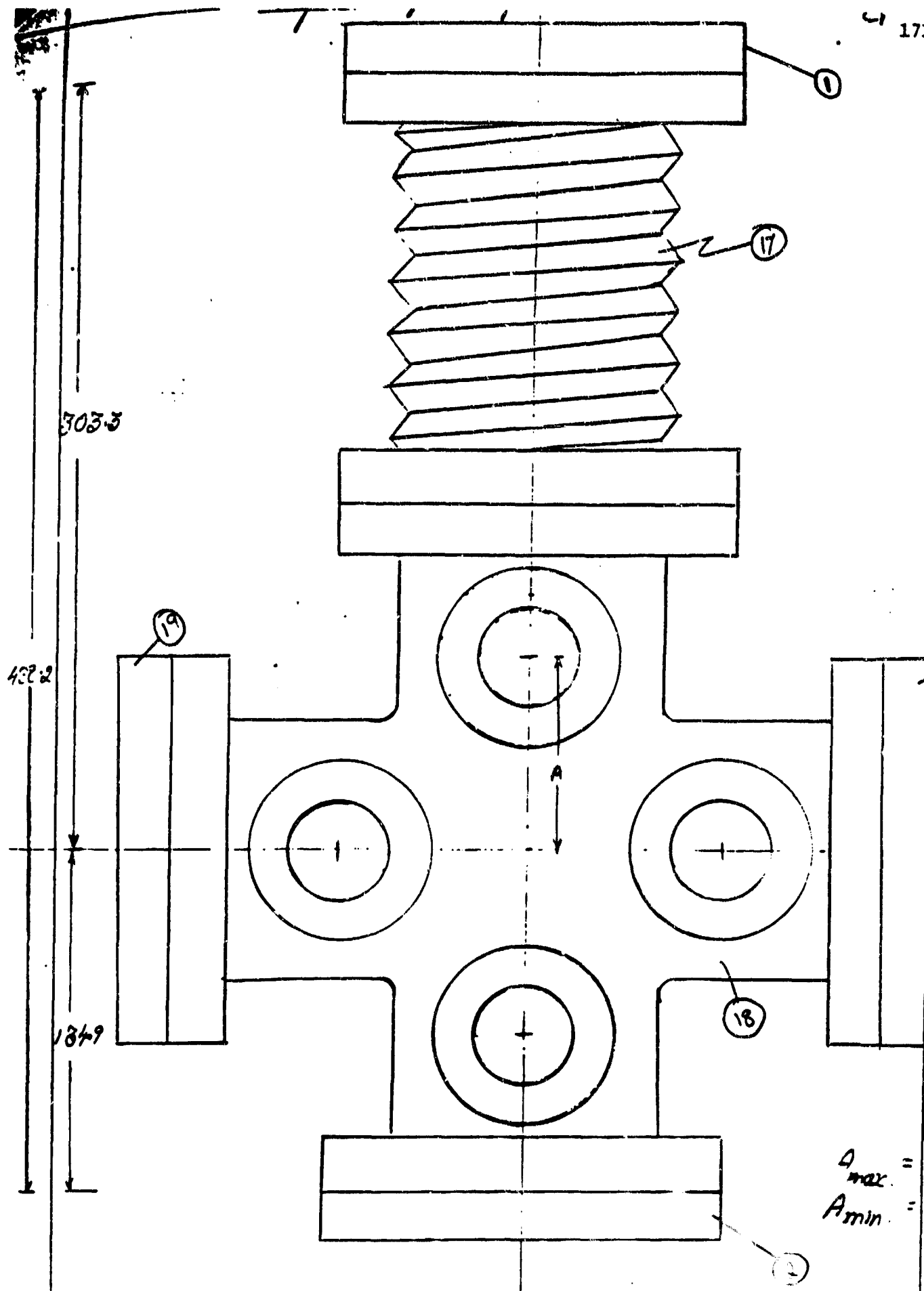
Fig. 4.49 4-way cross chamber and bellows system for housing the internal stage.

All the components in this stage were made of either mild steel or stainless steel. The 4-way cross was designed by us but fabricated and leak tested at LATEC Industries, 400 Bryce Avenue, Los Alamos, New Mexico 87544. An important precaution to be oserved here, while testing, is to be sure that the upper cross bar is limited to a movement of less than 1.0 in. This would prevent any damage to the flexible coupling.

4.5.4.2 The internal stage

The internal part of the high temperature stage is the nerve center for the entire system because this is the part where the heated specimen is held between grips, before deformation. Fig. 4.50 shows the top and bottom flange attachments of the grip assembly. The top flange is located at the top of the flexible coupling and the bottom flange is located under the 4-way cross chamber. Fig. 4.51 shows the critical grip assembly. There are two unique features of the design of this grip assembly.

a) Part No. 15 is part of a stainless steel ball which seats into a hemispherical depression in Part No. 7. This allows accurate alignment of the grip when the specimen is about to be loaded.

b) The ring 8 is threaded on to the grip 10 and when this is tightened against the bottom of part no. 7, the entire grip assembly from the flange, to the pin 12, becomes one rigid construction and this permits compression loads to be transmitted directly to the specimen without any relative movement in between.

The grip 10 and the pin 12 which are in direct contact with the specimen were made of Inconel-750X which has excellent high temperature resistance and strength. Part nos. 11 and 13 are special ceramic insulators made of Alumina AD-998. The properties of the Inconel and the ceramic are provided in Table 4.19 along with the addresses of the suppliers.
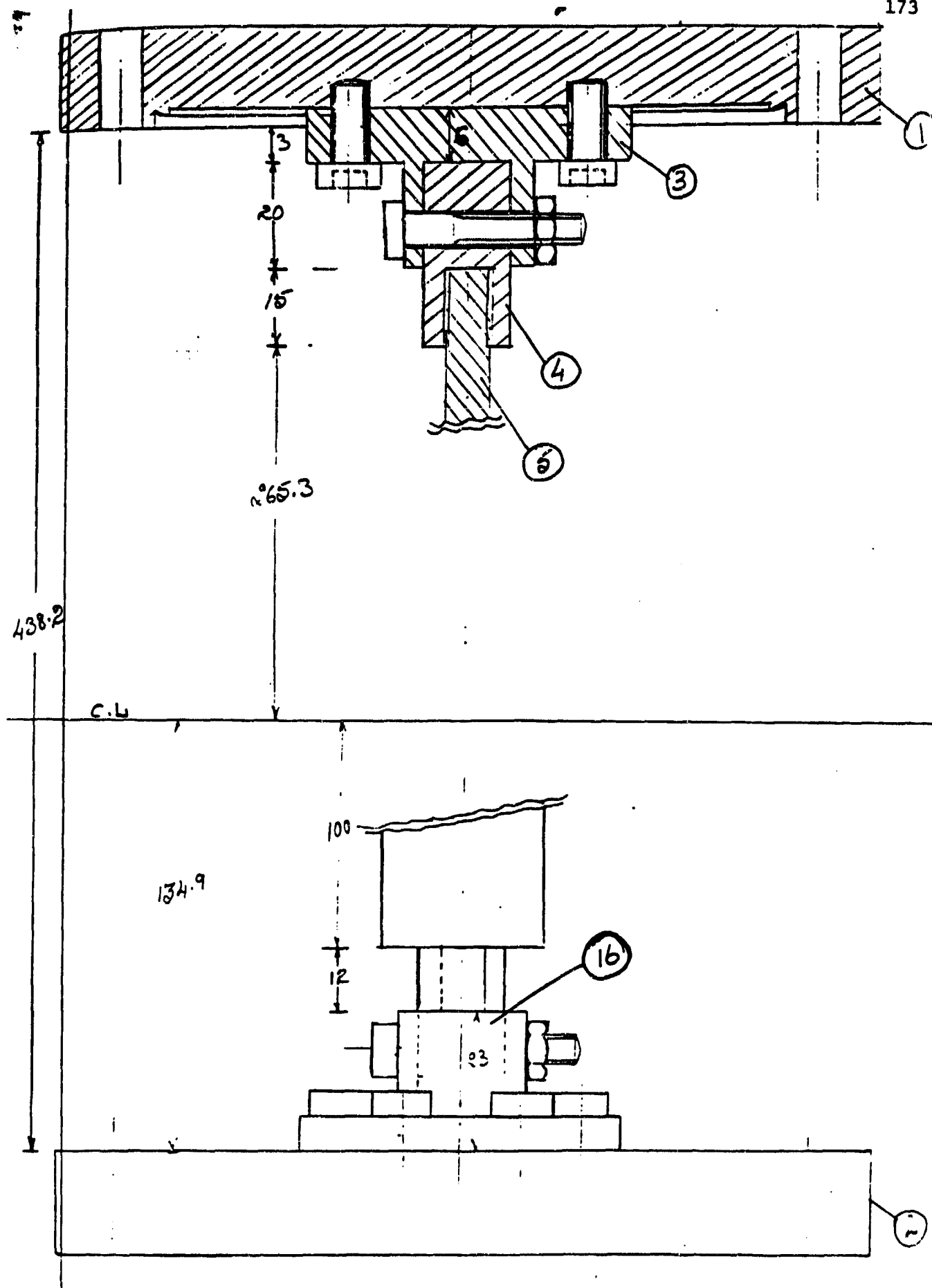
Fig. 4.50 Top and bottom flange attachments.
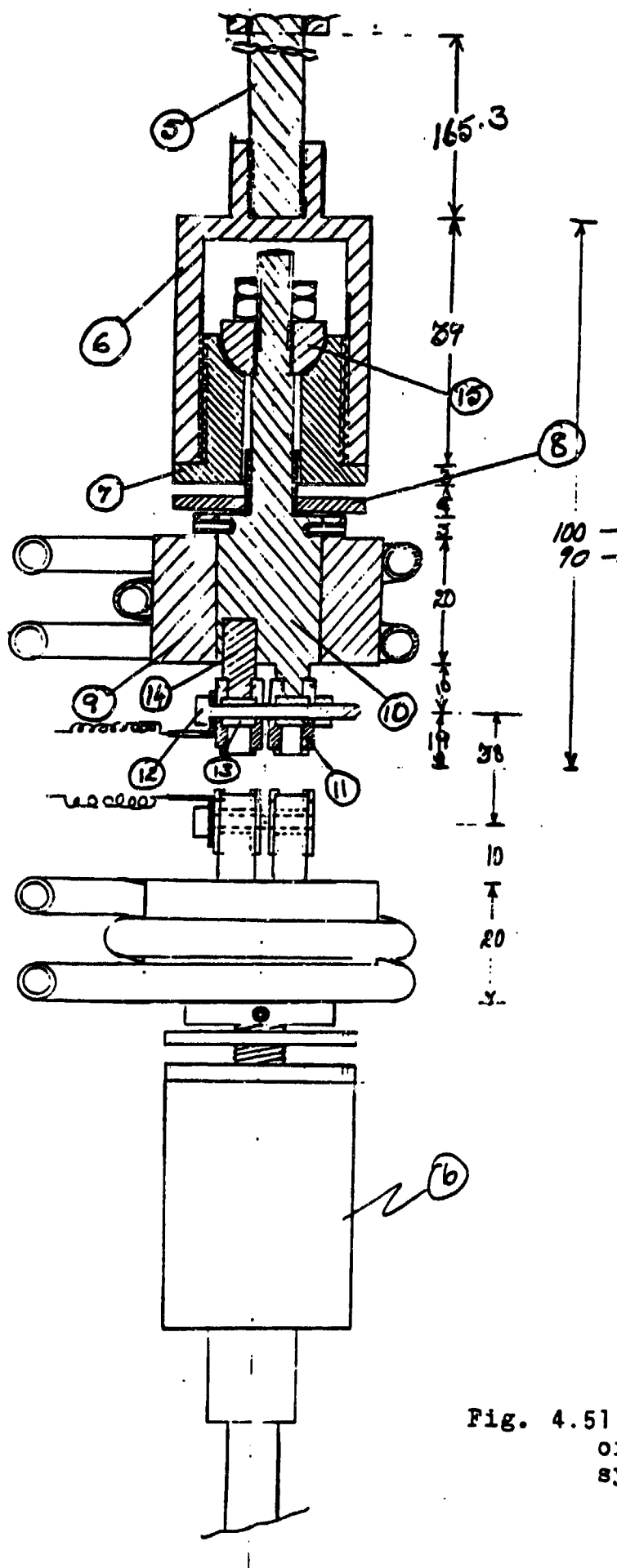
Fig. 4.51 Internal stage of the testing system.

Table 4.19 Important properties of Inconel 750X and ceramic AD-998.

1) Inconel 750X.

Description: It is an age hardenable alloy with good
corrosion and oxidation resistance.Also
possesses excellent relaxation resistance.

Major Applications: Gas turbine parts, Steam service and
nuclear reactor springs,bolts,vacuum enve-
lopes,extrusion dies, bellows forming tools.

Nominal chemical composition: Ni+Co -73%, Ti -2.5%,
Fe - 7%, Cr-15.5%.

Thermal conductivity: 12 W/m$^{\circ}$C at 20°C.
22.9 W/m$^{\circ}$C at 815°C.

Oxidation: Good to excellent.

Carburization: Good to excellent.

High temperature strength and stability: Good to Exc.

Tensile strength: 1117-1331 MPa.

Yield strength : 793-979 MPa.

Elongation in 2": 30 - 15%.

B.H.N. : 300 - 390

2) Ceramic AD-998.

Specific gravity: 3.96

Rockwell hardness: 90

Crystal size: 1 - 6 microns.

Color: Ivory

Compressive strength: 3792 MPa at 25°C.
1930 MPa at 1000°C.

Flexural strength: 283 MPa. ,TYP. 25°C.

Tensile strength: 207 MPa at 25°C.
103 MPa at 1000°C.

Modulus of elasticity: 393 GPa.

Shear modulus: 162 GPa.

Poisson's ratio: 0.22

Coeff. of linear thermal expansion: 3.44×10^{-6}/$^{\circ}$C. at 25C.

Thermal conductivity: 39.7 W/m-K at 20°C.
6.3 W/m-K at 800°C.

Specific heat: 880 J/Kg.-K at 100°C.

Part no. 9 is a copper annular cylinder with spiral copper tubes brazed on the external surface. Its purpose is to cool the grip if it gets too hot while heating the specimen. Because of the large thermal mass of the sink, it is anticipated that the grips would have to be cooled only if the temperature of the specimen exceeds 2500°K. As far as possible, we will refrain from using the cooling system as it becomes a potential source for water leakage and material degassing which would hinder the process of achieving a high vacuum. Every single component of the internal stage was designed with utmost caution and fabricated at the Mechanical Development Shop at Arizona State University.

4.5.5 Fabrication of tensile test specimen

The mechanical testing system was designed to accomodate both cylindrical specimen as well as plate type specimen, depending upon the availability of raw material. As the heating of the specimen was to be done by resistance-heating, a considerably large amount of current would be required to heat up the cylindrical samples. Thus, it was decided that the flat plate type specimen would be fabricated from the 0.25" dia. sintered rods procured from Rhenium Alloys Inc.

4.5.5.1 Flat plate specimen

Because of the extreme hard nature of W and W alloys, it is virtually impossible to grip the material between the jaws of the grip without providing a positive mechanical means of holding it. Invariably, the tungsten cuts through the grip material and slips out even before a moderate load is applied. Hence, it was necessary to design a configuration that would allow the specimen to be pulled by horizontal pins. The ASTM [4.38] Standard methods of tension testing of metallic materials was referred to,

in this connection and eventually the dimensions of the specimen were drawn out as indicated in Fig. 4.52. The specimen itself was fabricated by cutting out plates (24 mm x 6 mm x 0.75 mm) from the 0.25 ins. dia. rods. A special diamond embedded cutter, with a thickness of 0.025 ins. was used for this purpose. A lot of precautions were taken to maintain a feed rate that would not distort the vertical surface that was being cut. The plates were then mounted on an end milling machining and the right contours machined using a diamond core drill operated at a speed of about 10000 r.p.m. Inspite of the high speed and the fact that a diamond core drill was used, the machined surface was not smooth and so it had to be finished in the Electrical Discharge machine.

Fixtures and electrodes had to be designed before getting the sample electrically discharge machined. Figs. 4.53 and 4.54 give cross sectional views of the fixture for holding the specimen and the electrode assembly used for cutting, respectively. The specimen was then polished to remove rough surfaces that might act as stress concentrators. The polishing was done by using a paraffin mould to hold the specimen and Emery papers and eventually the lapping machine was used, to give a mirror finish. In order to polish all the surfaces uniformly, the sample was finally electropolished in 10% aqueous solution of sodium hydronide with an Inconel Cathode.

4.5.5.2 Cylindrical specimen

The cylindrical specimen was fabricated by turning the sintered rod in a lathe, with the help of a tungsten carbide cutting tool. A lot of problems had to be overcome before arriving at the optimum conditions for machining the sample. The tip of the cutting tool was wearing out very fast and it had to be sharpend every other minute. After rough machining in the lathe, the sample was mounted in a rotatable chuck, in the EDM (Fig. 4.55)
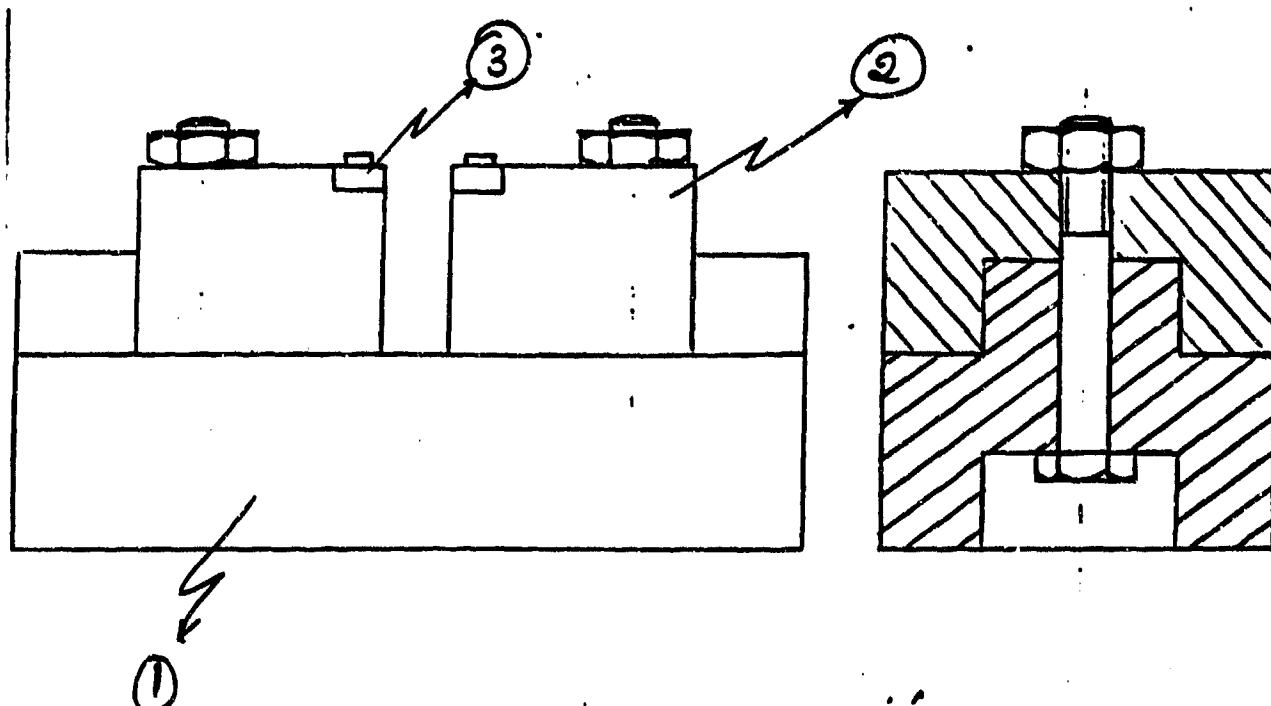
Fig. 4.53 Fixture for holding the specimen in the EDM.
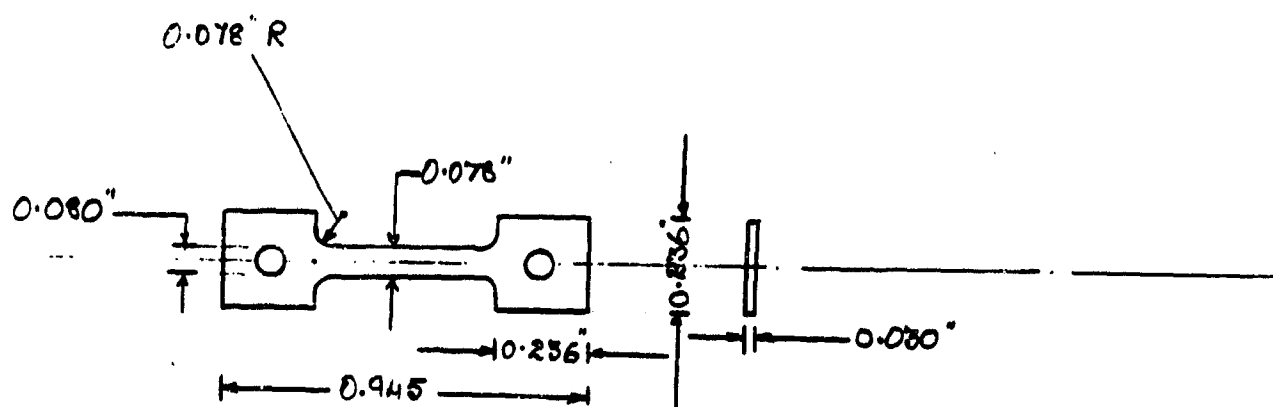
Fig. 4.52 Dimensions of the flat plate specimen.
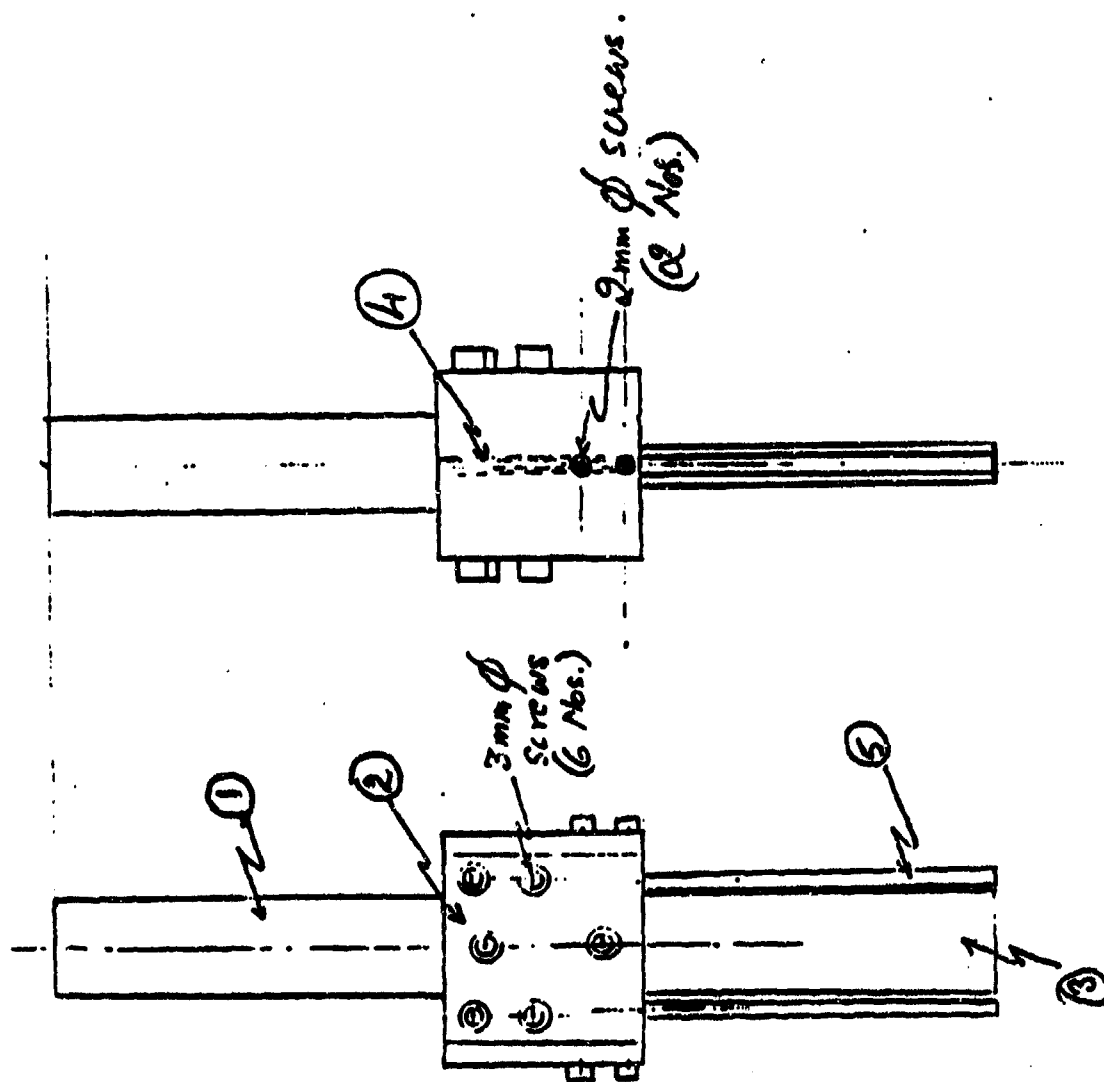
Fig. 4.54 Electrode assembly for final machining purposes.
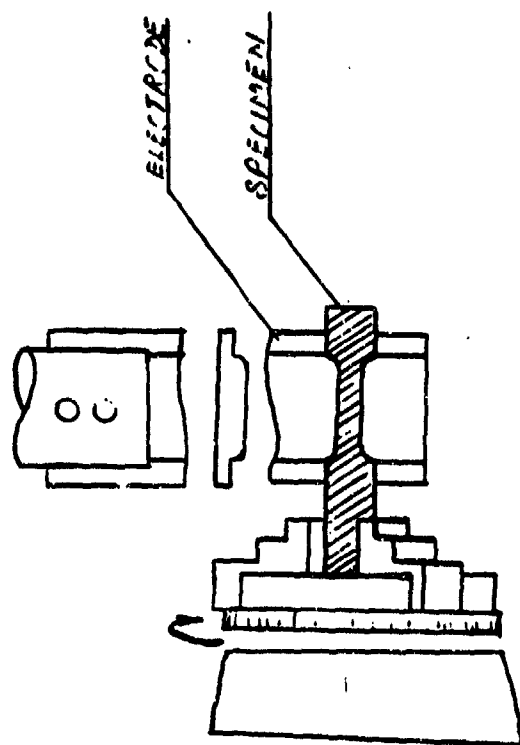
Fig. 4.55 Rotating assembly and electrode for cylindrical specimen.

and rotated while the electrode was gradually introduced from the top to effect the material removal. While designing the electrode, care was taken to ensure that its contour corresponded exactly to that of the gage section, of the sample.

4.5.6 Temperature measurement system

Because of the nature of the testing and the small dimensions of the specimen, it was impossible to drill a Hohlraum for temperature measurement. Further, since the specimen was going to be resistance heated, it is impossible to get any useful thermocouple output as the potential difference in the circuit introduces spurious signals which do not mean anything as far as the temperature is concerned. Thus, it was necessary to use induction heating to heat the sample and get actual temperatures using W-Re thermocouple wires. The microoptical pyrometer will be calibrated with the thermocouple readings and this calibration will be used to measure the temperature of the specimen, during real-time testing.

The induction heating system is being set up for use, later, for vacuum annealing purposes. Fig. 4.56 is a schematic of the induction heating system. The specimen is mounted in the glass tube and viewed with the optical pyrometer, as shown. The glass chamber is being fabricated at the glass-blowing section, Chemistry Department, Arizona State University. The mounting rack houses the ion-pump and the corresponding power supply and the roughing pump provides the necessary roughing vacuum before the ion-pump kicks on. A high frequency Lepel R.F. generator is being readied for this sytem. The accuracy of temperature measurements, by this method is expected to be better than ±10°C in the 2000 to 2500°K range.
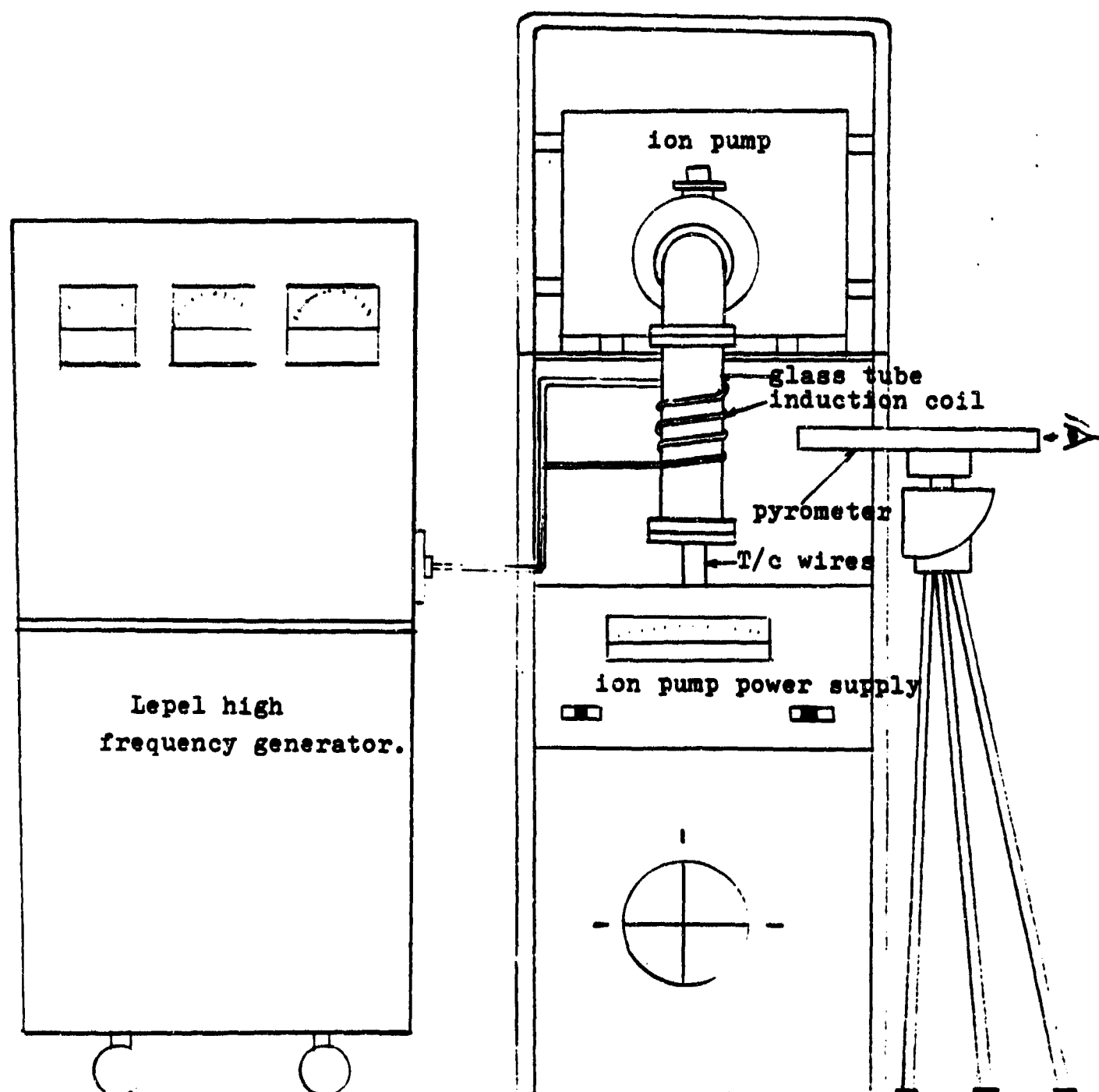
Fig. 4.56   The induction heating system.

4.5.7 General instrumentation and additional facility development

Other than the temperature measurement system there are 2 aspects of the general instrumentation that merit mentioning in this section. They are the vacuum system and the specimen heating system.

4.5.7.1 Ion-pump vacuum system

For the reasons mentioned earlier, it is necessary to conduct the test in an environment that is totally free from any contaminants. The best way to achieve this is to evacuate the entire chamber to a vacuum of better than 10^{-7} torr, the evacuating is done in two stages. The sorption pump brings the pressure down to about 10^{-3} torr and then the ion pump takes over until the pressure gets down to 10^{-6} torr. The entire system is then baked with I.R. lamps at 250°C for 48 to 72 hours to remove adsorbed gases.

4.5.7.2 Heating system for the specimen

The specimen will be heated up using a.c. current from a low voltage/high current power supply. The output from the power supply is carried to the two current feed troughs, at the side of the 4-way cross chamber, by means of copper wires as shown in Fig. 4.47. Inside the vacuum system, copper leads carry the current, through a tantalum sheet, the loading pin and then the specimen, and the circuit is completed back to the power supply, as shown in Fig. 4.51 Tantalum is used between the copper and the Inconel pin because it has a high melting point and will serve as a sink to the heat generated near the pin. If there is a lot of heat conducted to the copper, then the copper wires will be replaced with tantalum wires inside the vacuum system.

4.5.7.3 The electron-beam zone refining system

As a part of the study of material problems for high temperature, high-power space energy conversion systems, it was proposed that we build an electron-beam floating zone refiner, that could serve the dual purpose of purifying materials and also distributing a desired impurity uniformly throughout the material. Zone melting is a general term for controlling the distribution of soluble impurities or solutes in crystalline materials. Here, a short molten zone travels slowly through a relatively long solid charge and while travelling redistributes the solutes in the charge.

The vital part of the design of the zone-refining system is shown in Fig. 4.57. It essentially consists of a 4-way cross vacuum chamber with cooling water lines on its peripheral surface. The chamber is evacuated with an ion-pumped vacuum system. The specimen 5 is held in position by the two linear motion feedthroughs. The electron beam source is a filament 7 which surrounds the specimen. This electron gun can be moved up and down at different speeds with the help of the stepper motor operated UHV linear-motion drive 1. This unit is specially designed for high vacuum applications and supplied by MS. Kurt J. Lesker Co., from Pennsylvania. The various parts for the zone-refining system were procured in 1984 but all activities were temporarily shelved until early 1985 when we started working on it again.

In addition to zone-refining, the system is being modified to grow single crystals, bi-crystals and for electron beam melting purposes.

4.5.8 Conclusions

The tests conducted on the various alloy combinations should provide sufficient information on the following aspects:

1) Ductility

2) Modes of fracture

3) Grain boundary segregation of impurities.

The ductility of the materials is obtained from the change in length or cross section of the test specimen at various temperatures. The reduction in area would be zero below the DBTT and then it would increase with temperature only to a certain extent until it comes down again as grain boundary fracture dominates. It would be interesting to observe if the addition of ThO_2 and HfC provides an increase in the reduction of area over a wider temperature range.

As has been cited in literature, the modes of fracture are expected to be one or a combination of the following: transcrystalline cleavage, ductile tearing and grain boundary fracture. At temperatures of the order of 100/200°C, the fracture is expected to be of a brittle nature with a higher percentage of grain boundary fracture than the cleavage type. However, as the temperature increases, the cleavage will reduce and eventually disappear and most of the fracture becomes either ductile tearing or grain boundary fracture. The influence of Re on the mode of fracture of W-Re alloys has been observed to be one in which there is a decrease in the amount of cleavage failure. Further, the addition of ThO_2 and HfC is expected to promote ductile failure above the DBTT.

The yield stress and the ultimate stress are expected to increase with additions of Re, ThO_2, and HfC but this effect is expected to wear out after about 2500°C when most of the alloys tested exhibit the same properites as the parent material. It has already been established that the yield stress varies very little with increase in temperature for pure tungsten, but is increased considerably at lower temperatures with alloying additions. The tests will certainly reveal whether tungsten can be additively strengthened

at elevated temperatures by low concentrations of Re in solid solution and by dispersed ThO_2 and HfC. If there is an increase in strength due to the addition of ThO_2 and HfC, the major factors contributing would be the grain size and the dispersoid size.

Calculations of interparticle spacing using the Orowan relationship should give information leading to the discrepancy in stress values with and without the dispersoids. It will also show if it is the grain size or dispersoid distribution or substructure stabilization that contributes to the strengthening of the base metal. A plot of stress (without alloying) - stress (with alloying) vs. temperature should amply demonstrate the origin of incremental contributions to the UTS.

Post test Auger spectroscopy will be done in order to determine the grain boundary segregation of impurities on the fractured surface. This should reveal a qualitative and quantitative result of the dispersoids.

Eventually, an effort will be made to correlate the work functions from the microscope and the bulk properties from the high temperature mechanical testing, in order to arrive at some kind of a merit number for different types of TEC materials.

4.5.9 Related activities in Research on embrittlement of W-Re alloys

As we are interested in studying the ductility of W and W/Re alloys, it would be of utmost importance, to determine the factors that might possibly be the reason for making W as brittle as it is. Embrittlement of W alloys is caused by, among other things, grain boundary segregation and hydrogen embrittlement. To complete the study on recrystallization and ductility, of W-Re and W, Re, ThO_2, HfC alloys it is proposed to include, if time permits, an investigation of embrittlement by grain boundary segregation of

interstitial impurity products as well as the effect of hydrogen charging on the tensile strength of the alloys.

4.5.9.1 Grain boundary segregation

A major limitation in the usefulness of tungsten is its tenedency to be brittle. This difficulty is especially acute when it is in the polycrystalline form. Inspection of the fracture surfaces reveals that polycrystalline tungsten often fractures along the grain boundaries. Interstitial impurity products segregated in grain boundaries cause this kind of fracture due to embrittlement and recrystallization further diminishes ductility by localizing the brittle interstitial products in grain boundaries thereby increasing their intergranular concentrations.

The most embrittling component is carbon followed by oxygen, nitrogen and finally hydrogen. However, tungsten has been doped with a number of impurities for certain benefits and studies have been done on the effect of strength on the segregation of impurities in grain boundaries.

A. Joshi [4.39] and D.F. Stein used the Auger electron emission spectroscopy for direct chemical analysis of fracture surfaces. Substantial segregation of phosphorus to the grain boundaries was observed and it was found that the concentration of phosphorus could be related to the DBTT. The amount of segregation was also dependent on the grain size - the larger the grain size, the greater the concentration of phosphorus at the grain boundary and associated embrittlement. A combination of Auger electron spectroscopy and scanning electron microscopy was used [4.40] to identify the source of the unique interlocked elongated grains responsible for the high temperature sag resistance in doped W and W-Re alloys as due to bubbles formed by the volatilization of potassium during sintering. They found that by pinning grain boundaries, the bubbles raised the recrystallization

temperature. There was a thin layer of potassium remaining on the bubble surfaces. The size and distribution of the bubbles was related to the amount of material deformation during processing. Fig. 4.58 shows a typical Auger Electron spectra of W-3.25% Re taken in situ immediately after fracture at room temperature.

Incidentally, Th additions to Iridium +0.3%W alloys [4.41] are known to greatly increase their ductility during high temperature impact. Segregation of thorium to grain boundaries in alloys containing 5 and 1000 ppm. Th was studied using AES to analyse Th rich precipitates on intergranular fracture surfaces of an alloy containing 1000 ppm thorium. The thorium enriched region was only a few atom layers thick. No additional increase in grain boundary thorium level was observed as the overall thorium level was increased from 5 to 1000 ppm. This result indicated a solubility limit of thorium in Iridium +0.3% W of $\leq$ 5 ppm. Figs. 4.59 show the comparisons of the Auger spectra for undoped Ir +0.3% W, 5 ppm doped Ir + 0.3% W, and 1000 ppm doped Ir + 0.3% W.

We propose to use the Auger Electron Spectroscopy facility at the Centre for Solid State Sciences, to investigate the fracture surfaces of W, Re and W, Re, ThO_2, HfC alloy tensile test specimen and draw suitable conclusions on grain boundary segregation.

4.9.2 Hydrogen embrittlement

An important impurity, that contributes to the embrittlement of tungsten and tungsten alloys, is hydrogen. Hydrogen embrittlement has been observed in metallic alloys of hexagonal close-packed, face centered cubic, and body centered cubic crystalline structures and even in amorphous alloys. In particular, the hydrogen embrittlement susceptibility of the body centered cubic metals α-iron and the group VA elements have been well
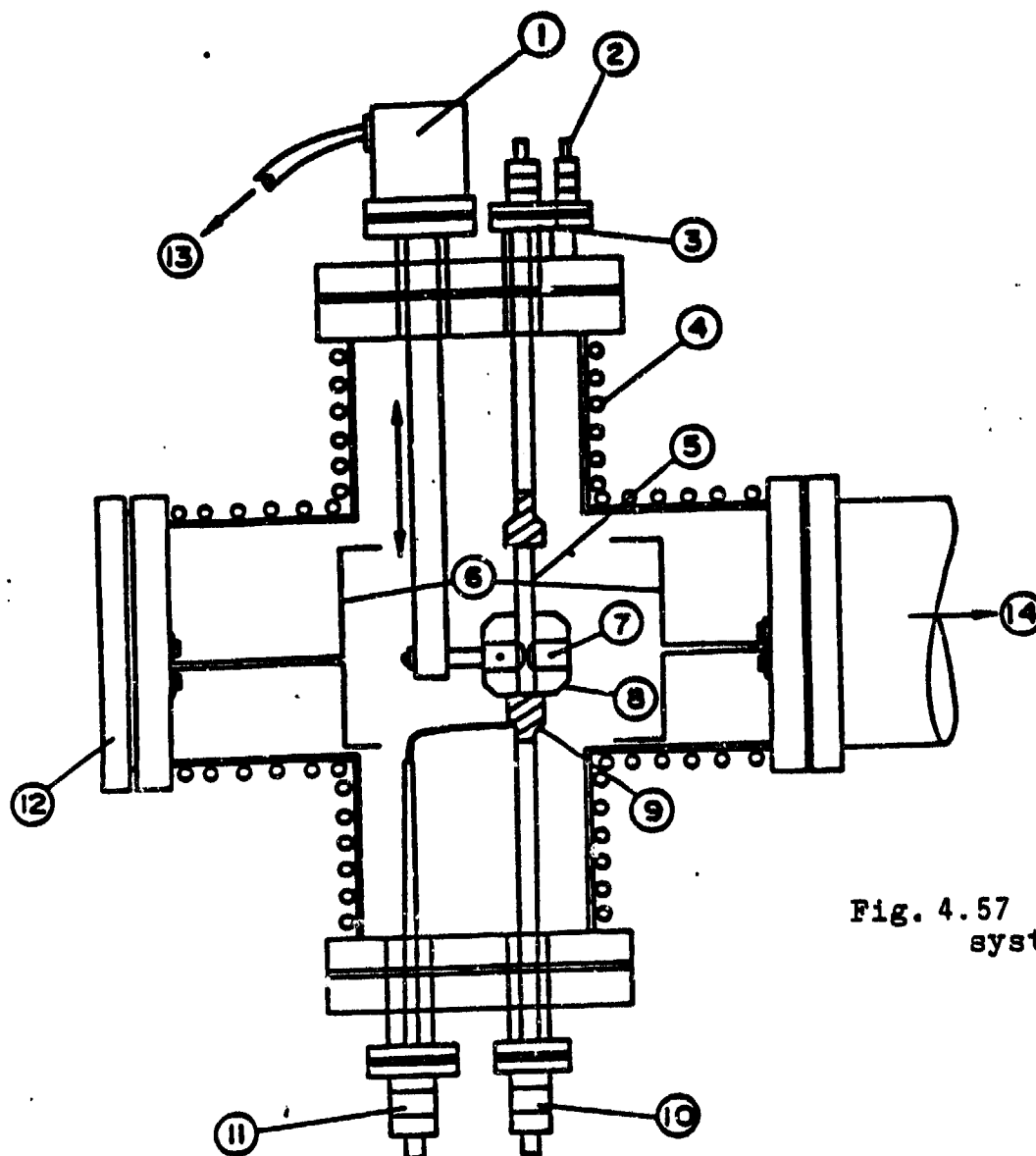
Fig. 4.57 Zone refining
          system components.

Fig.   4.58 Auger electron spectra
        of W-3.25%Re taken in situ
        after fracture at room
        temperature.
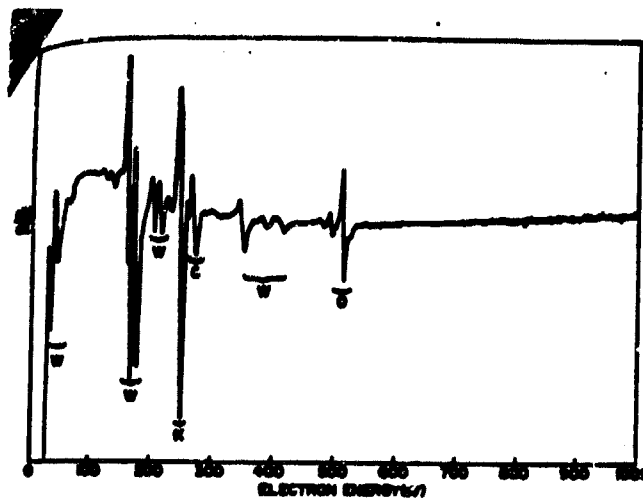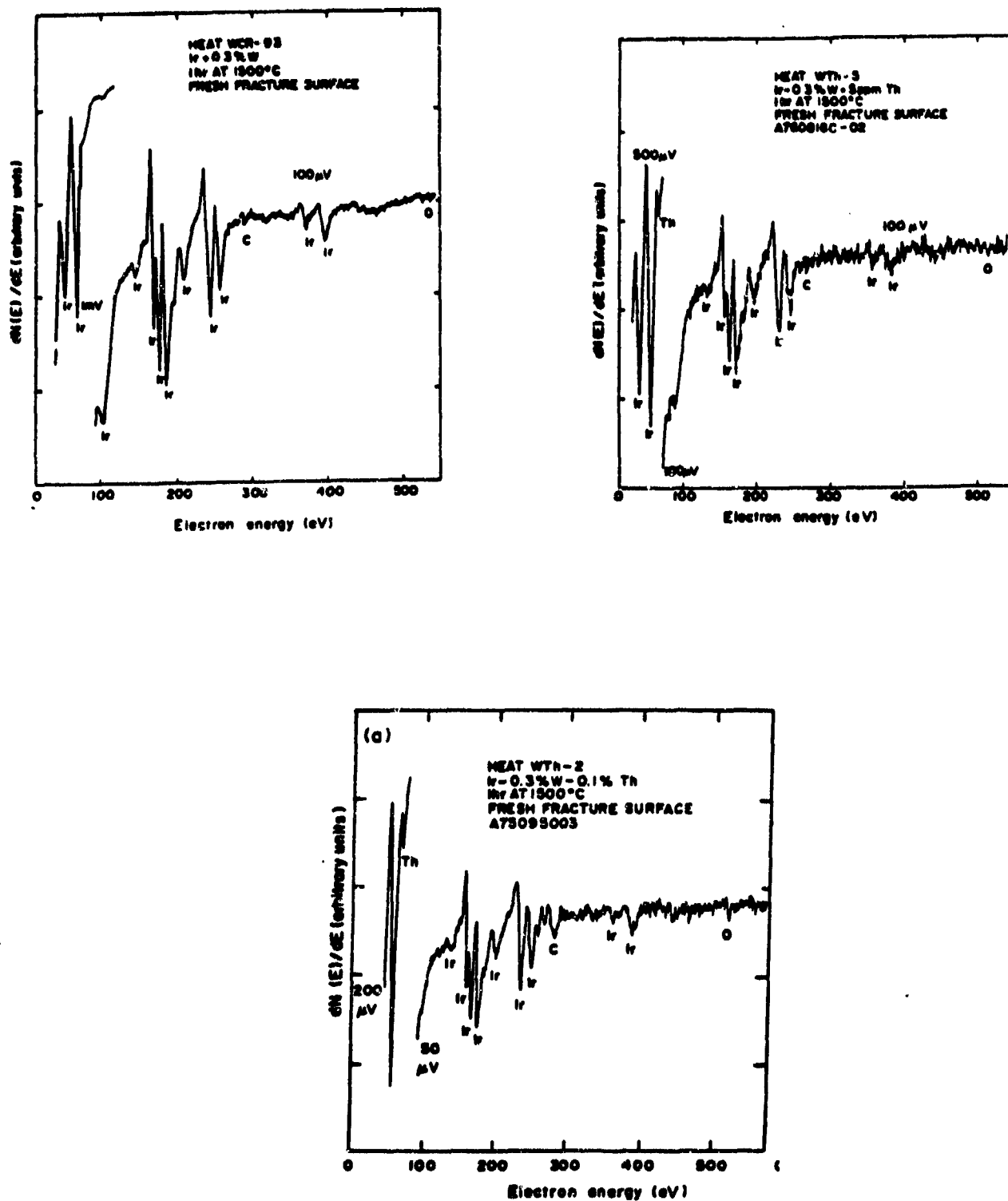
Fig. 4.59 Auger spectra of a) undoped Ir + 0.3% W. b) Ir + 0.3%W + 5ppm.Th., c) Ir + 0.3%W + 1000 ppm.Th.

documented. However, the body-centered cubic group VIA refractory elements have been considered the exception with very little, if not any, susceptibility to hydrogen embrittlement. However, recent investigations on chromium and molybdenum have shown otherwise and this leads us to believe that there would be an effect of hydrogen charging on the mechanical properties of tungsten.

F.E. Scyeryenie [4.42] and H.C. Rogers studied the effects of hydrogen embrittlement of tungsten base heavy alloys. The tested alloys of W-Cu-NMi and W-Fe-Ni that were heat treated in hydrogen and then quenched in water under an atmosphere of hydrogen, before tensile testing the samples. They found that the effect of hydrogen heat treatment varied with alloy composition the yield strength of all alloys remained unchanged. A 90W-YNi-3Fe alloy, however, showed a significant amount of strain rate sensitivity of ductility, as shown in Fig. 4.61 as compared to the 90W-5Ni-5Fe alloy in Fig. 4.60.

The effects of small additions of hydrogen on the mechanical properties of W was investigated by H.K. Birnbaum [4.43] et al. They found that the effect of hydrogen on group VA metals far outweighed the effect on VIA metals and this was attributed to the fact that the W system does not have any known hydride, a positive heat of solution in equilibrium with the hydrogen gas phase, and a hydrogen solid solubility which is extremely small even at rather high temperatures. The effect of other impurities like, O, N, and C, during hydrogen treatment have been found to be of greater significance than embrittlement by hydrogen. Further investigation [4.44] of hydrogen embrittlement of group VIA metals, resulted in the fact that under conditions of simultaneous tension testing and cathodic charging, the hydrogen was present at high fugacity at the tip of a crack or other stress

concentrations. Thus, hydrogen entry into the lattice in relatively high concentrations was possible at the point where it is most effective in causing fracture, the crack tip. Only under such conditons will there be significant hydrogen embrittlement in Mo and W. A similar conclusion was drawn [4.45] when T.M. Devine studied the hydrogen cracking of 218 tungsten wire. He found that, in view of the supposedly low mobility of hydrogen in molybdenum, as well as the apparent immunity of unnotched tungsten samples to embrittlement, the crack initiation time and its relative insensitivity to applied stress is the result of the entry of hydrogen as the rate controlling step into the metal at the notch root and the accumulation of a critical amount in the highly stressed region ahead of the notch.

As we are studying tungsten base heavy alloys and as it has been reported that there is some effect of hydrogen on such alloys, it appears that a study on the hydrogen embrittlement of W, Re and W, Re, ThO_2, HfC alloys would merit attention to some extent.

4.5.10 Recommendations for future activities on mechanical testing and related topics

High temperature testing should be conducted on W,Re alloys with separate components ThO_2 and HfC. This would make the optimization procedure more effective and would provide a completeness to the study.

A high temperature tensile stage should be built, that is capable of transferring the fractured specimen directly to the Auger chamber for analysis. This would prevent atmospheric contamination of the fractured surface which might lead to distorted conclusions regarding fracture characteristics.

The induction heating system that was built for calibrating the pyrometer temperature should be modified so that it could be used as a

vacuum annealing system. This will also enable one to study the ductile-brittle transition temperatures of various materials as temperatures below 800°C, could also be measured using W-Re thermocouples.

The grips used in the tensile stage should be modified to receive wires so that tensile testing on wires could be carried out at elevated temperatures. It is easier to heat up a wire than to heat up a mass of material using resistance heating.

4.7 REFERENCES

4.1 M. Cohen: High power requirements, p. 1-3, Proceedings of the AFOSR special conference on prime power for high Energy space systems; Norfolk, Virginia, Feb. 1982.

4.2 V. Kugnetsov: Operation of Thermionic Reactor converters TOPAZ-1 and TOPAZ-2, Proceedings of the 3rd International Conference on thermionic electrical power generation, Vol. 1, Juelich, Germany, June 1972.

4.3 J.F. Morris: Thermionic Energy Conversion topping thermoelectrics, IEEE Conference on Plasma Science (COPS) May 1981, DOE/NASA/1062-8, NASA TM-81677.

4.4 J.F. Morris: The Space Nuclear Reactor, Air Force AFWAL, Arizona State University, ERC-R-82004.

4.5 J.F. Morris: Ultralloys for current and future space powers, Air Force AFWAL, Arizona State University ERC-R-83025.

4.6 A. Hoppin: Investigation of Joining the Refractory Metals Tungsten and Niobium, GE contract with WADD, Materials Centre, USAF, 1960-62.

4.7 J.R. Stephens, W.R. Witzyk: Alloy Softening in Group VI A Metals Alloyed with Rhenium; Journal of Less Common Metals 23(1971) 325-342.

4.8 K. Sedlatschek, H. Braun: Tungsten Alloys of High Melting Points; Journal of Less Common Metals, 1, 19 to 33, 1959.

4.9 A.V. Logunov, A.I. Kovalev: Experimental Investigation of the Thermophysical Properties of W-Re Cast Alloys, High Temperature-High Pressures, Vol. 5, 1973, pp. 625-633.

4.10 W. Kingery: Property measurements at high temperatures, Wiley, 1959.

4.11 V.D. Barth: Physical and mechanical properties of Tungsten and Tungsten-base alloys; EMIC report 127, March 15, 1960.

4.12 H.G. Sell, R. Stickler: The effect of Rhenium on the mechanical properties of W-2w/o TLO$_2$, 6th Plansee Seminar, Reutte, Austria, June 1968.

4.13 .J. Smithells: Tungsten, Chapman & Hall, London, 1952.

4.14 J. Wadsworth: A reevaluation of the mechanical properties of Molybdenum and Tungsten based alloys containing Hafnium and Carbon, Metallurgical transaction, Vol. 14A, Feb. 1983, p. 285.

4.15 Erwin Eichen: Thermionic emission microscopy and its metallurgical applications.

4.16 E. Eichen: Thermionic emission microscope, high temperature, high resolution, Microscopy Symposium, Gordon and Breach, New York, 1967.

4.17 J.F. Morris: Thermionic energy conversion and metallic fluid heat pipes: High power densities from high temperature material interactions; Progress in Astronautics and Aeronautics, Vol. 83, 1982.

4.18 D.L. Jacobson, A.E. Campbell, : Molybdenum work function determined by electron emission microscopy; Metallurgical Transactions, Vol. 2, Nov. 1971, Pg. 3063.

4.19 D.L. Jacobson: Emission characteristics of some dilute Tungsten alloys; Metallurgical Transactions, Vol. 3, May 1972, p. 1263.

4.20 A. Modinos: The electronic work function of the different faces of Tungsten; Surface Science, 45(1978) 327-341.

4.21 J. Jaskie and D.L. Jacobson: Thermionic emission and surface composition of the Y-B System; Journal of Energy, Vol. 5, No. 3, May-June 1981, pg. 187.

4.22 C.V. Laudrith: Thermionic emission microscopy of polycrystalline Molybdenum and Mo-LaCrO$_3$; Thesis for M.S.; ASU, May 1982.

4.23 A. Subramanian: Thermionic emission microscopy of Mo-LaCrO$_3$ and LaB$_6$; Thesis for M.S.; ASU, May 1984.

4.24 Marchuk, P.M.: A study of the adsorption and thermoelectric qualities of Molybdenum in vapors of Cesium at increased pressures; Trudy Inst. Fig. Ak. Nauk. Ukraine, Vol. 7, No. 17, 1965.

4.25 J.M. Houston: Thermionic emission of refractory metals in Cesium vapor; Advances in electronics, 17, 125 (1962).

4.26 H.M. Houston and P.K. Dederick: Thermionic emission of thermionic converter collector materials in Cs vapor; IEEE, Proceedings of Thermionic Conversion Specialist conference, 1964, pg. 77.

4.27 J.L. Coggins, R.E. Stickney: Adsorption studies based on Thermionic Emission measurements; Surface science, 11 (1968) 355-369.

4.28 M. Manda, D.L. Jacobson: Electron emission from Nichel-alloy surfaces in Cesium vapor; IEEE transactions on Plasma Science, vol. PS-6, No. 2, June 1978.

4.29 M. Jang, D. Jacobson: Electron emission from Cesiated 1% and 2% Thoriated tungsten alloys, AIAA 19th Thermophysics Conference, June 25-28, 1984.

4.30 Chester T. Sims, R.I. Jaffee: Further studies of the properties of Rhenium metal, Transactions AIME, August 1956, Journal of metals, pg. 913.

4.31 R.H. Atkinson: "Tungsten alloy development," paper delivered at the Conference on Govt.-sponsored research in progress on Tungsten, Durham, North Carolina (1959).

4.32   R.I. Jaffee, S.T. Simms, J.J. Harowwd: "The effect of Rhenium on the fabricability and ductility of Mo and W," Third plansee seminar proceedings 1958, Pergamon Press (1959) pp. 380-411.

4.33   P.L. Raffo, W.D. Klopp: Mechanical properties of solid-solution and carbide-strengthened arc-melted Tungsten alloys, NASA Technical note, NASA TN D-3248, Feb. 1966.   .

4.34   Robert W. Hall, Peter L. Raffo, W.R. Wityke, W.D. Klopp: Carbide strengthening of Tungsten and Molybdenum alloys, Aerospace structural materials, NASA LeRC Conference, November 1969.

4.35. W.D. Klopp, W.R. Wityke: Mechanical properties of a Tungsten-23.4 percent Rhenium--0.27 percent Hafnium-Carbon alloy, J. less common metals, 24 (1971) 427-443.

4.36   Walter R. Wityke: Composition effects on mechanical properties of tungsten-rhenium-hafnium-carbon alloys; NASA technical note, NASA TN D-7210. Also Metallurgical transactions, Vol. 5, Feb. 1974.

4.37   F.I. Uskov and A.V. Babak: Features of the failure of powder metallurgy tungsten at different temperatures in vacuum, Institute of strength problems, Academy of sciences of the USSR, (Translated) Plenum Publishing Corporation, 1981.

4.38   ASTM Designation E8-82, American association State highway and transportation officials standards, ASHTO No.: T-68, Standard methods of tension testing of metallic materials.

4.39   A. Joshi and D.F. Stein: Intergranular brittleness studies in Tungsten using Auger spectroscopy, Metallurgical transactions, Vol. 1, Sept. 1970, pg. 2543.

4.40   Ronald P. Simpson, George J. Dooley III, T.W. Haas: Study of grain boundary fracture surfaces in doped Tunsten-Rhenium alloys, Metallurgical transactions, Vol. 5, March 1974, Pg. 585.

4.41   C.L. White, R.A. Padgett: Thorium segregation to grain boundaries in I$_r$ + 0.3% W alloys containing 5-100 ppm Thorium, Acta Metall. Vol. 31, pp. 111 to 119, 1983.

4.42   F.E. Scyerzenie, H.C. Rogers: Hydrogen embrittlement of tungsten base heavy alloys, Dept. of Defense, Thesis Grant # DAAA-25-69-C0136.

4.43   H.K. Birnbaum, M. Crossbeck, S. Grahr: The effects of Hydrogen on the mechanical properties and fracture of Ar and refractory metals, Hydrogen in Metals, ASM.

4.44   H.K. Birbaum, H. Wadley: Hydrogen Embrittlement in Molybdenum, Scripta Metallurgica, Vol. 9, pp. 1113-1116, 1975.

4.45   T.M. Devine: Hydrogen cracking of 218 Tungsten wire, Scripta Metallurgica, Vol. 10, pp. 447-450, 1976.

APPENDIX-4.1.

Derivation of the Richardson-Dushman Equation

~onsider an electron gas in equilibrium with a hot conductor. If we
kr... ne pressure of the gas, from kinetic theory we will know how many
electrons will strike on a unit area of hot conductor/sec. The electrons
that are absorbed must be compensated for by those that are emitted. Thus
the fraction of emitted electrons are 1-r where r is the so-called mean
reflection coefficient.

To get the pressure of the external electron gas, consider a Carnot
Engine operating between two temperatures T and T+dT, that evaporates
material from the saturated liquid state to the saturated vapor state during
the heat addition process. The efficiency of such an engineer is
approximately

$$n_t = \frac{\text{work out}}{\text{heat supplied}} = \frac{v_{fg} dp}{h_{fg}} = \frac{dT}{T} \tag{1}$$

$$\text{or} \quad h_{fg} = v_{fg} \cdot T \cdot \frac{dp}{dT} \tag{2}$$

which is the Clausius-Clopeyron Equation. The molecular volume of the
external electron gas is

$$v_{fg} = \frac{RT}{p} \tag{3}$$

From (2) we get

$$\frac{dp}{p} = \frac{h_{fg}}{RT^2} \cdot dT \tag{4}$$

We know that specific heat

$$C_p = (\partial h / \partial T)p \tag{5}$$

Thus for a subliming solid,

$$\frac{dh_{fg}}{dT} = C_{p_{gas}} - C_{p_{solid}} = C_p - C_p'$$ (6)

Using the principle of equipartition of energy states, elementary classical mechanics and Thermodynamics, we can show that the total energy of N molecules is

$$N\epsilon_M = \frac{f}{2} \cdot n'RT = \epsilon_{int}$$ (7)

Per mole, we have

$$\epsilon_{int}' = \frac{f}{2} RT$$ (8)

$$C_\nu = \frac{\partial \epsilon_{int}'}{\partial T})_\nu = \frac{f}{2} R$$ (9)

From thermodynamic considerations of a perfect gas,

$$C_p - C_\nu = R$$ (10)

and so

$$C_p = \frac{f+2}{2} \cdot R = \frac{5}{2} R$$ (11)

for a monatonic gas. (6) is now written as

$$h_{fg} = \int_o^T C_p dT + h_o$$ (12)

$$= \frac{5}{2} RT + h_o$$ (13)

Substituting (13) in (4) we get

$$\frac{dp}{p} = \frac{h_o}{RT^2} dT + \frac{5}{2} \cdot \frac{dT}{T}$$ (14)

Integrating,

$$\ln p = - h_0/RT + \frac{5}{2} \ln T + C \tag{15}$$

or $$p = T^{5/2} \exp. [-h_0/RT]\exp(C) \tag{16}$$

The number of particles $\dot{N}$, striking a unit area of wall per unit time coming in from all directions with all speeds is

$$\dot{N} = \frac{1}{4} n u_{av} \tag{17}$$

where $$n = p/kT \tag{18}$$

Making the usual kinetic theory assumption of a Maxwellian distribution, the mean speed is

$$u_{av} = [8kT/\pi m]^{1/2} \tag{19}$$

The above Equations may be combined to give

$$\dot{N} = p/(2\pi kT)^{1/2} \tag{20}$$

Eqtn. (16) can be converted into a current Eqtn. by dividing by $(2\pi m kT)^{1/2}$. the traction of emitted electrons are $(1-r)$ of those that impinge on the emitter; thus the emission current is

$$J = (1-r)A_0 T^2 \exp.[-h_0/(RT)] \tag{21}$$

Assuming r is independent of temperature, we have

$$J = A_1 T^2 \exp[-h_0/RT)] \tag{22}$$

Where A_1 is the emission constant.

Now $\quad \dfrac{\phi}{k} = \dfrac{h_0}{R}$. $\qquad\qquad$ (23)

$\therefore \quad J = A_r T^2 \, \exp. \, [-\phi/(kT)]$ $\qquad\qquad$ (24)

which is the Richardson-Dushman Equation.

APPENDIX-4.2

Nomenclature

r	– mean reflection coefficient.
1–r	– fraction of emitted electrons.
T	– Temperature (Lower) of Carnot engine.
η_t	– theoretical efficiency.
h_{fg}	– latent heat of evaporation one mole of electrons.
v_{fg}	– increase in volume of the system accompanying the evaporation of this quantity of electrons.
R	– The gas constant.
P	– Pressure of the gas.
C_p	– specific heat of constant pressure.
C_p	– Specific heat of constant pressure of subliming solid.
N	– total number of molecules.
ϵ_M	– mean total energy per molecule.
f	– number of degrees of freedom.
n'	– number of moles.
ϵ_{int}	– internal energy of the gas.
ϵ'_{int}	– internal energy per mole of the gas.
C_v	– molal specific heat at constant volume.
h_0	– constant of integration.
$\dot{N}$	– number of particles striking unit area of the wall per unit time.
n	– number of particles per volume.
u_{av}	– arithmetic mean speed.
k	– Boltzmann constant
m	– mass of the particle.
J	– emission current.
A_1	– emission constant = 120 Amps./cm^2/°K^2

ϕ - work function

σ - Stress or force per unit area.

e   - Strain on fractional deformation.

E   - Elastic modulus on the ratio of stress to strain.

σ_y - yield strength representing resistance to initial plastic deformation.

σ_t - Tensile strength representing the maximum strength.

e_f - Elongation or the ratio of change in length to the original length.

R of A   - Reduction of Area as the ratio of change in cross sectional area to the original area.

E   - Energy.

E_f - Fermi energy level.

h   - Plancks's constant.

ν - frequency of electromagnetic waves.

K_{max} - maximum of energy of the electron.

M   - Magnification

A_c - Area of collector.

V. EMISSIVITY DATA FOR METALS AT HIGH TEMPERATURES

5.1 ABSTRACT

A photon counting pyrometer has been built at Arizona State University based upon a similar device originated by Dr. E. K. Storms at Los Alamos National Laboratories. The pyrometers have proven accurate to $\pm 1°$ K at $2000°$ K. Emissivity data at high temperatures for hafnium, iridium, molybdenum, nobium, ruthenium, tantalum, tungsten and alloys of Hf, 3%-Zr and Nb, 45%-Ir have been generated with this pyrometer. The relationship of the emissivity to surface condition, grain size, alloying, crystal orientation and temperature are elements of investigation in this report. Requirements for high temperature materials for space systems such as thermionic energy converters requires accurate thermal radiation data, in particular emissivity, which is the primary objective of this work.

5.2 INTRODUCTION

The search for thermodynamic properties of various materials has proven to be a never ending process for the experimental engineer and physicist. Every experiment and every calculated correlation of data relies to some degree on the accuracy of the data published for the particular materials in sue at the time. As time has progressed the materials have become increasingly rare and much more specified in their uses. Requirements have specified higher temperatures, more stable compositions, and various mixtures of properties.

The temperatures of the materials used in thermionic energy conversion diodes are routinely over 2000 degrees Kelvin, with some reaching 3000 degrees. At these temperatures the properties of the materials used in the diodes are very difficult to find in published material. Since the measured efficiency of a diode is dependent upon the radiation losses and the radiation heat transfer between materials, the emissivity of the diode material is a very important property in the prediction of diode performance.

A thorough research of current published data was made in order to determine the extent of the problem in determining the exact properties of thermionic diode materials at very high temperatures. The first sources identified were the collected works of Gubareff, Janssen and Torburg [5.1] and the well known compilation of data by Touloukian and DeWitt [5.2]. These comprehensive publications are standard references for many radiation properties and have been in use for many years. Both publications contain a wealth of data in the higher temperature ranges for the more common materials such as tungsten, tantalum, and molybdenum. Another search

produced more publications of data that would substantiate the collected data and provide information on the less tested materials.

The data was assembled and a common problem emerged. Each paper or series of papers dealt with materials suitable for use in a specific field. For example, Kenisarin [5.3] studied different materials in order to find a new high temperature standard to replace the Gold furnace presently in use. Ratanapupech and Bautista [4] measured the emissivity of metals and their alloys in a molten state so that the temperature of a melt could be accurately determined. The materials used in thermionic diodes were not usually considered.

Several theories on the behavior of the emissivity were also discovered. Ratanapupech and Bautista [5.4] produced an expression that related the emissivity of a liquid metal alloy to the emissivities of the parent metals. If this could be extended to solid alloys the testing of every alloy mixture of two materials would not be required. Dimitriev and Chistyakova [5.5] described the dependence of the emissivity of metals on the temperature and wavelength. L. K. Thomas [6] estimated the wavelength dependence of the emissivity of tungsten and molybdenum alloys on the Fermi energy levels of the materials. The ability to calculate the emissivity of a material seemed to be possible.

The problem was defined. Experimentally determine the emissivity for materials currently under study for use in thermionic diode energy conversion. The measured data was examined for any correlations that may permit the prediction of the emissivity of a material without experimental measurement. The dependence of the emissivity on the temperature, crystal structure, crystal orientation, surface preparation, grain structure and annealing process were investigated.

Symbols

A   attenuation factor
e   emitted energy
R   pyrometer count rate
T   temperature
γ dead time of photomultiplier
ϵ emissivity
λ wavelength
C_1 Planck's first constant
C_2 Planck's second constant

Subscripts

C   of calibration furnace (corrected)
S   of specimen (corrected)
I   filter number
M   measured value
λ spectrally dependent

5.3 EQUIPMENT

5.3.1 Pyrometer

Once the requirement for temperature and thermal radiation measurement at very high temperatures was established the instruments necessary for the tas at hand were sought. A survey of current high temperature measurement devices produced several types of optical pyrometer.

Each of the pyrometers studied has its own shortcomings and advantages. The first pyrometer considered is the disappearing filament pyrometer. This device has been used for years in situations where the temperatures of a material are not measurable by thermocoupler. This pyrometer operates on the comparison principal, where the intensity of the sample is compared to a heated filament wire that is within the pyrometer. When the filament is heated to the same temperature as the target it disappears. Filters may be used to restrict the incoming radiation to a single wavelength, increasing the accuracy by elimination of the wavelength as a variable. These pyrometers are extremely accurate in the temperature range at which the instrument is calibrated. The accuracy suffers as the temperature varies from the calibration temperature. This is not usually critical since the instrument may be readily recalibrated, but, it is very time consuming when wide temperature ranges are being measured.

The major error in this pyrometer is the operator himself. The operator must compare the color of the reference filament in the pyrometer with the color of the test sample. Color perception and focusing are individual qualities of each person. Several measurements of temperatures with this type of pyrometer have been recorded as a temperature range instead of a specific temperature. Branstetter and Schaal [5.7] plotted the emissivities measured with a disappearing filament for a comparison to the

target temperature. The difference between the automatic pyrometer and the disappearing filament pyrometer is the detection device. Instead of an optical comparison by the operator a photomultiplier is used to compare the emission of the filament and the sample. The comparison is performed at high speed by the manipulation of mirrors, shutters or both. This type of device is used by several of the national bureaus of standards of other countries [10,11] and is also interfaced to microcomputers [5.8,5,11] providing the possibility for completely automatic laboratory functioning based on the pyrometer readings.

Initial work in the field of thermionic emissions brought contact with E. K. Storms [5.12], from Los Alamos National Laboratory, who encountered this same problem in his work on the determination of work functions of materials at high temperatures. His solution removed the reference heating filament from the automatic pyrometer. The photomultiplier recorded the electro-magnetic radiation emitted by a target directly. The thermal radiation emitted by a material is related to the temperature of the material by Wien's approximation

$$e_\lambda = 2 C_1/\lambda^5 \exp(C_2/\lambda T) \tag{5.1}$$

Given a measurement of the emitted energy the temperature can then be compared to the energy emitted by a calibrated source. From Wen's formula two equations are developed, one for the energy emitted by the calibrated source and another for the energy emitted by the specimen being measured.

$$e_C = 2 C_1/\lambda^5 \exp(C_2/\lambda T_C) \tag{5.2}$$

$$e_S = 2 C_1/\lambda^5 \exp(C_2/\lambda T_S) \tag{5.3}$$

The ratio of emitted energy for the calibrated source to the emitted energy for the unknown source can then be found.

$$e_C/e_S = \exp(C_2/\lambda T_S - C_2/\lambda T_C) \tag{5.4}$$

Solving for the unknown temperature yields

$$T_S = 1/[(\ln e_C/e_S)\ \lambda/C_2 + 1/T_C] \tag{5.5}$$

The instrument has proven accurate to within ±2° K at 2000° K without recalibration at any of the higher temperatures. The output is digitized, resulting in the ability to record the temperatures by simply connecting a printer or digital storage device. Since this met all of the requirements of the experiment a pulse counting pyrometer was constructed.

The construction of a pulse counting pyrometer was the next order of business. The details of the construction and operation of the pyrometer are outlined in appendix A. The photomultiplier measures a selected amount of radiation determined by the optical assembly. This assembly allows for: 1. selection of the wavelength of radiation to be sampled, 2. selection of the size of the sample area to be measured, 3. a ranging, measurement of broad temperature ranges, and 4. the ability to aim the pyrometer at the desired sample area.

The individual parts of the optical processing assembly are labeled in Fig. 5.1. The thermal radiation from the test specimen enters the camera lens (a) where the image is focused into the optical assembly. An interference filter (b) restricting the incoming radiation to a specific wavelength. A filter operating at a wavelength of 535nm is used in this device.

test camera interference mirrors neutral photomultiplier
sample lens filter aperature filters

eyepiece

discriminator-
amplifier

timer-
counter
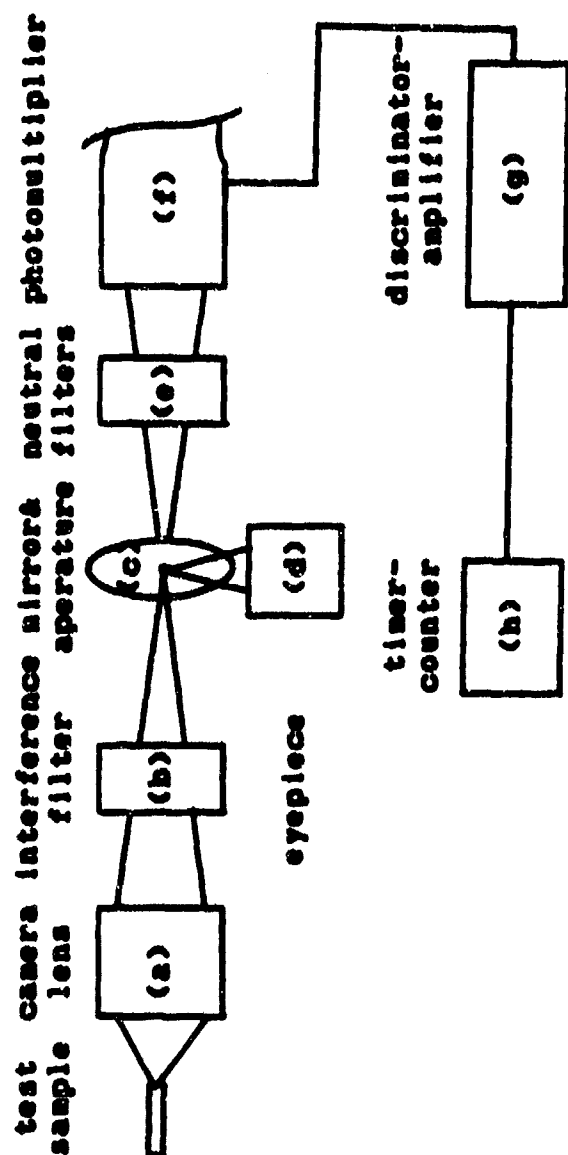
Figure 5.1 Photon/Pulse Counting Pyrometer
Block Diagram

The image of the specimen is foused onto a nickel mirror (c). The mirror serves three purposes. An aperature .1mm in diameter is drilled in the center of the mirror. The aperature restricts the amount of radiation that is admitted to the photomultiplier tube. The aperature also allows the pyrometer to be aimed at a very small area on the test specimen. Finally the mirror itself is used to aim the pyrometer at the test specimen. A 6 power eyepiece is used for the aiming process (d).

The filter section (e) is composed of three neutral density filters selectable with a lever on the side of the pyrometer. The three different filters attenuate the level of the radiation entering the photomultiplier tube. the attenuation provides three ranges of pyrometer operation permitting the measurement of temperatures from 1000 to 3000°K.

The photomultiplier (f) converts the thermal radiation into a series of electrical pulses. These pulses differ in voltage corresponding to the level of energy of the photons detected by the photomultiplier. The pulses are processed by a Princeton Applied Research [5.13] Model 1121 Discriminator-Amplifier (g). The discriminator section produces a signal based on the photomultiplier output. The amplifier section amplifies the discriminator output to a level compatible with the counting equipment. The output from the discriminator-amplifier if fed into a Hewlett-Packard [5.14] Model 5308 Frequency Counter-Timer (h). The frequency counter displays the number of pulses produced by the discriminator-amplifier in the form of a frequency (counts per second). The displayed reading is the measured count rate. The count rate is corrected and then converted to a temperature value or is used as is in emissivity calculations. Each of these processes are discussed in the procedures section.

5.3.2 Vacuum System

The testing of materials at very high temperatures required a vacuum system to prevent the oxidation of the materials. Shur and Peletskii [5.15] found that the minimum vacuum required to prevent this oxidation was a pressure of 3×10^{-8} Torr. A vacuum system that would reach this level was readily available in the form of a diffusion pump and bell jar vacuum chamber. The system is very fast and simple to operate.

5.3.3 Heating Apparatus

The heating method used in this series of experiments is electron bombardment (Fig. 5.2). This method uses a tungsten heating filament (a) that is heated by an AC current. The heating of the filament causes the "boiling off" of high energy electrons from the surface of the filament (b). The freed electrons are propelled toward the specimen by applying a high voltage potential (c) between the filament and the sample. The energy imparted to the sample by the impact of the high energy electrons heats the sample to very high temperatures. The power supply used in this apparatus incorporates a 10 Kilovolt DC supply operating at up to 0.5 Amperes [5.16]. This DC high voltage is the ground level for an AC power supply operating at up to 10 Volts and 20 Amperes. The AC supply provides the current to heat the tungsten filament and boil off the electrons while the DC supply provides the high voltage potential between the filament and the test specimen.

test sample
sample holder
heating chamber
heating filament

(b)

(a)

10V
AC

1500V
DC

(c)

−

+
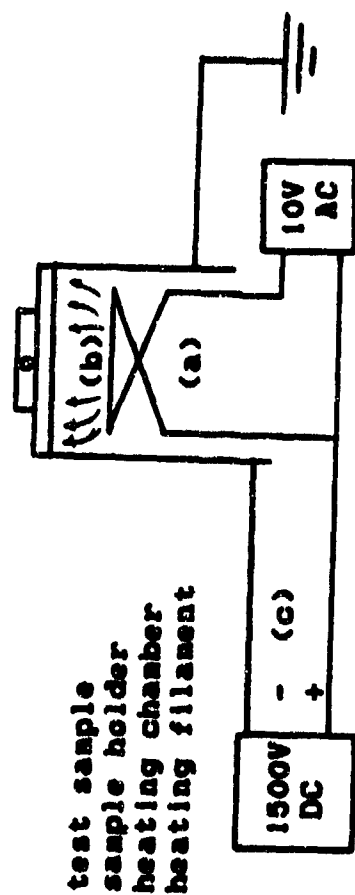
Figure 5.2 Test Apparatus

5.3.4 Sample Preparation

The materials used in this series of tests were selected based on availability and on their projected use in thermionic diode energy conversion research. The materials were hafnium, iridium, molybdenum, niobium, ruthenium, tantalum, tungsten and two alloys, Nb, 45%-Ir and Hf, 3%-Zr (percentage based on atomic weight).

Each sample was approximately 2mm thick and 12 to 20mm in diameter. A hohlraum 1mm in diameter and 10mm deep was drilled through the edge of the sample by electrical discharge machining (for the smaller diameter samples the hole was 0.6mm dia. and 6mm deep). The hohlraum was parallel to each flat surface and passed thorough the center of the sample (Fig. 5.3). The sample test area was polished with one or more grades of polishing compound: 600 grit carborundum wet/dry abrasive paper, 3 micron diamond or 0.5 micron diamond lapping compound. The test area produced by the polishing was on a plane perpendicular to the hohlraum centerline. The sample was bonded to a tantalum holder and placed in the test apparatus mounted to the vacuum chamber (Fig. 5.3d).
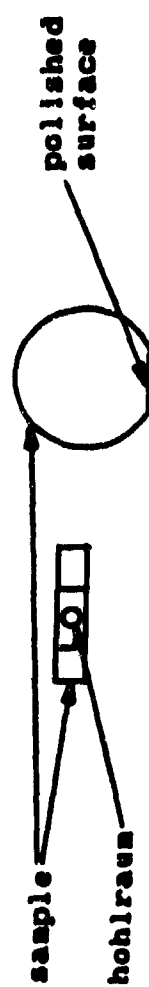
Figure 5.3 Specimen Preparation

5.4 PROCEDURE

Two steps were made before any of the measurements were taken. These were simple precautions to insure the proper functioning of the pyrometer and the validity of the measured data. First the attenuation of the bell jar was measured. A constant temperature source was placed in the vacuum chamber. The pyrometer measured the emission of the source. The bell jar was then placed in position and a second measurement was made. The ratio of these two measurements was included in the attentuation values for the pyrometer filters (see Appendix A).

The next step was the verification of the actual sample area of the pulse counting pyrometer. There was some doubt on my part as to the actual area of the sample that was measured by the pyrometer. A niobium sample was prepared with three different diameter hohlraums: 1.4mm, 0.7mm and 0.4mm. The 1.4mm hohlraum was only drilled to a depth of 10mm because of the size of the sample. The face of the sample was polished to provide a uniform surface around each of the hohlraums. The sample was heated to 1500° K and allowed to stabilize for a period of 1 hour. The emission of the sample was measured for 10 minutes to confirm that the temperature was stable. Measurements of each of the three hohlraums were made. The pyrometer was a fixed distance from the sample. The smallest emission measured was at the largest (1.4mm)hohlraum. This procedure confirmed the size of the sample area of the pyrometer to be approximately 0.4mm at a distance of 200mm from the sample.

The objectives of the test measurements were considered during the conduct of the heating process. The evaluation of the emissivity data required a knowledge of the changes that occurred in the emissivity and the material surface condition from the initial heating through extended

exposure to temperatures above 2000° K. The data assembled would reveal the change in microscopic surface condition and the effect that this change had on the emissivity of the material.

Two different heating processes were used to examine different effects on the emissivity and the surface conditions. Tungsten was used to test the effect of annealing on the emissivity and tantalum was used to test the effect of the surface preparation on the emissivity. The annealing process prescribed in many of the papers [5.6,5.7,5.15] included very long periods of time under extremely high temperatures. Neuer and Worner [5.17], in their study of the emissivity of steel alloys, carefully observed the time and temperature dependence of the annealing effect concluding that the annealing process was very fast. Most materials showed a change immediately after applying the heat. The annealing effect was complete after a maximum of 30 minutes at fairly low temperatures. The annealing effect at elevated temperatures was complete after 10-20 minutes. The examination of this process in the tungsten sample would require slow heating with frequent emissivity measurements.

The sample was initially heated to approximately 1300° K. Emissivity measurements were then taken up to a temperature of 2100° K. The temperature of the sample was decreased and stabilized at approximately 1500° K for a period of 2 hours. This annealing temperature was chosen based on results obtained by Shur and Peletskii in their measurements on the emissivity of titanium and titanium iodid [5.15]. The time factor chosen was half of the time used in their testing. The emissivity measurement continued from 1100 up to 2400°K.

The other heating procedure was designed to optimize the time of the test and allow checking for an annealing effect in the material. Each

sample was heated to approximately 1500° K for a period of 30 minutes. the temperature was decreased to 1100° K where emissivity measurements began. The temperature was increased and emissivity measurements made up to 2400° K. The temperature was decreased to approximately 2000, 1800, 1600 and 1400° K and emissivity measurements were taken. The second set of measurements recorded any change in the surface condition. The effect of the crystal orientation on the emissivity of a material was evaluated using a niobium single crystal specimen. This sample was polished on three faces 45° apart. The emissivity of each face was measured at every temperature level.

The recorded measurements of the pyrometer must be corrected for the dead time of the photomultiplier and for the attenuation of the bell jar and filters. The corrected count rates are converted into the temperature and emissivity values. The dead time and attenuation values are obtained experimentally. The process for obtaining these values is described in Appendix 5.9. The corrected count rate is found from the expression

$$R_S = A \ R_M / (1 - Y R_M) \tag{5.6}$$

The temperature is related to the corrected count rate through Wien's approximation

$$T_S = 1 / [(\ln R_C / R_S) \ \lambda / C_2 + 1 / T_C] \tag{5.7}$$

The emissivity of a material is defined as the energy emitted from a surface compared to the energy emitted by a black body at the same temperature and wavelength. Since the pyrometer measures a relative level of emitted energy, the emissivity is a simple comparison of the corrected count rates measured at the hohlraum and at the surface

$$c_\lambda^i = R_S/R_H \qquad (5.8)$$

5.5 ERROR REDUCTION

The measurement of any quantity involves comparison of the measurement in one set of conditions to a recognized standard of measurement. This series of tests involves two measurements, the sample temperature and emmissivity. Both of the measurements are dependent on the accuracy of the pulse counting pyrometer. The errors associated with the operation of the photomultiplier are discussed in detail in Appendix 5.9 The effect of these errors on the test results are discussed in this section. Other errors in emissivity and temperature measurement are also presented, as well as the steps taken to reduce the effects of those errors.

5.5.1 Pyrometer Error

The pyrometer contains two sources of error. The calibration is the first source of error in any type of measuring device. Pyrometers are normally calibrated against a tungsten strip lamp resident in the laboratory. The strip lamp is sent to the National Bureau of Standard for calibration against the national temperature standards. The national temperature standards are calibrated against a gold furnace, the international standard for high temperature calibration. The strip lamp is then installed in the laboratory in a controlled environment chamber with an adjustable power supply.

The possibility of error introduced by this system is enormous. The extension of the gold standard to very high temperatures introduces an error that has been discussed in many papers. Kenisarin [5.3], Jones and Tapping [5.18] and Ruffino [5.19] have all proposed the use of a different material with a higher freezing point as the international temperature standard for

this very reason. Also, every transfer of the initial calibration standard results in the introduction of a small error in temperature measurement. The lest number of transfers is two: one from a gold furnace to a strip lamp at the National Bureau of Standard and the other from that strip lamp to the user's strip lamp. the calibration by the National Bureau of Standards provides the user with a sheet of temperature readings at 100° K steps. These temperatures are recorded for a pyrometer using a wavelength of .655 microns. The pyrometer is calibrated at these temperatures.

The calibration of the pulse counting pyrometer reduces the usual level of pyrometer error by calibrating the device with a copper furnace operated by E. K. Storms at Los Alamos National Laboratory [5.12]. This pyrometer also operates in a controlled and predictable manner above the copper melting point. The result is a pyrometer that is accurate to less than $\pm 1°$ K at temperatures above 2000° K [5.12].

5.5.2 Black Body Cavity

The hohlraum drilled into the edge of each of the test specimens serves as the point of measurement of the temperature of the sample. The use of hohlraums as black body cavities has been studied at great length for its simplification of the measurement of very high temperatures. Branstetter and Schaal at NASA Lewis experimentally measured the emissivities of several geometries of cavity [5.7]. The results indicated that a cylindrical cavity with a length to diameter ratio of 7 to 1 would yield an emissivity of .99. A mathematical formulation of the same problem was made by Y. Ohwada at the Japanese National Research Laboratory of Metrology. His results incorporated both isothermal and nonisothermal cavities of cylindrical and conical geometries. His mathematical formulation for isothermal cavities indicated an emissivity of .9938 [5.20]. The evaluation of a nonisothermal

cavity indicated an emissivity of .990 [5.21]. The experimental and mathematical calculations indicate an error of less than 1% is introduced by the assumption of the hohlraums as black cavities.

5.5.3 Temperature Gradient

The measurement of the emissivity was a comparison between the energy emitted at the hohlraum to the energy emitted at the surface. An error was introduced because of the physical method used to make the energy level measurements at the hohlraum and the surface. The measurement of both energy levels were made by the same pulse counting pyrometer.

The hohlraum was measured first then the pyrometer was aimed at the surface of the sample to obtain the surface emission. the pyrometer was again aimed at the hohlraum for a second temperature measurement. This process required a certain amount of time to perform. The normal time required for hits process was five seconds to measure the temperature, two seconds to move the pyrometer and stabilize the reading, five seconds to measure the surface emission, two seconds to move the pyrometer again, and five seconds to measure the temperature for a total time of nineteen seconds. This length of time was enough to allow the power supply to drift slightly from the initial value causing a change in the temperature of the sample. The temperature change was usually less than 2° K. However, the variation did reach levels of 10° K. The evaluation of the temperature for each emissivity measurement was an average of six to ten readings made by the pyrometer, half from before the surface measurement and half after. Any data recorded that had a temperature change of more than 5° K was discarded. This threshold guaranteed a temperature measurement accurate to within 1% of the temperature of the surface at the time of the surface measurement.

The calculation of the emissivity presented a larger error than that considered for the temperature measurements. The source of this error was based in the operational characteristics of the pulse counting pyrometer. The actual number of pulses counted at higher temperatures (above 1500° K) was between one and two million counts per second. All seven of the digits were recorded and used in calculations. A 1° K temperature change at 1500° K caused a change of about 10,000 counts per second. This results in the high accuracy of the pulse counting pyrometer for measuring temperatures. However, this also causes problems with any temperature instability in the test specimen. The temperature change during the measurement process described above resulted in a large difference in the energy readings made by the pyrometer. This difference affected the calculated emissivity. Changing the temperature by 5° K resulted in a variation of the calculated emissivity by 5%. This variation increased with an increase in temperature. Combining all of the factors in this section the recorded data should be accurate to approximately 7%.

5.6 RESULTS

Figures 5.4 through 5.9 show the measured emissivity of the materials tested. Data collected from other papers and publications are shown as bands or curves of emissivity as a function of temperature. Note that most published data for the normal spectral emissivity of a material was measured at a wavelength of .655 microns. The data was adjusted to a wavelength of .535 microns by Planck's Law

$$e_\lambda = 2 \, C_1 / \{\lambda^5 [\exp(C_2/\lambda T - 1)]\}$$

Where there are several sources of data the emissivities measured in this series compare favorably with the results obtained by others. Table 5.1 lists the measured data for each of the materials tested.

Figure 5.4 shows the plots of the tungsten data and the expected data for this wavelength. The data for the polished surface lies within the range of past test results, verifying the experimental method being used and the operation of the pulse counting pyrometer. Figures 5.5 and 5.6 show the tantalum and molybdenum data which also fall near the expected results.

The variable with the greatest effect on the emissivity is, not surprisingly, the surface condition. With various surface preparation, and before annealing took place, the emissivity varies by more than 40%. This is much greater than the differences between materials. It can also be seen from the tantalum and tungsten plots that there is a definite effect from the annealing process. Curves 1 were obtained during the initial heating cycle. Curves 2 were obtained after a period of 2 hours at approximately 1500° K. The effects of the annealing process can be observed both in the differences in emissivities and in a comparison of the surface condition before and after the heating cycle. The before-and-after inspections of each of the specimens revealed a smoothing effect caused by the annealing process. The annealing time turned out to be much less than reported in various other experiments [5.6,5.7,5.15]. Consultation with James Morris (recently at NASA Lewis, currently at Arizona St. Univ.) revealed that there seems to be a definite relation between the annealing characteristics of the material and the recrystallization temperature of the material. Because the measurements were taken only at the surface the effects of the recrystallization process made themselves known within minutes, not hours. This is supported by the results obtained by Neuer and Worner in their tests on steel alloys [5.17]. Due to different definitions of the

Tungsten	ϵ =	.5437 - .4066e-7 T
Tantalum	ϵ =	.5245 - .7926e-4 T
Molybdenum	ϵ =	.5656 - .9566e-4 T
Niobium		
single crystal	ϵ =	.5246 - .7673e-4 T
polycrystalline	ϵ =	.5646 - .8986e-4 T
Niobium-46% Iridium	ϵ =	.6237 - .1282e-3 T
Iridium	ϵ =	.4078 - .4382e-4 T
Hafnium	ϵ =	.5874 - .1149e-3 T
Hafnium-3% Zirconium	ϵ = 1.0406 - .3846e-3 T
Ruthenium	ϵ =	.5858 - .1480e-3 T

Table 5.1. Line fit of emissivity data as a
function of temperature (° Kelvin).

Tungsten

Temp	Emiss	Temp	Emiss	Temp	Emiss
curve 1					
1689	.549	1979	.545	2073	.548
1762	.539	1990	.537	2084	.548
1856	.541	2006	.538		
curve 2					
1604	.470	2155	.440	2327	.427
1750	.448	2235	.431		

Tantalum

Temp	Emiss	Temp	Emiss	Temp	Emiss
curve 1					
1814	.646	1859	.587	1851	.511
1825	.645	1888	.568		
1842	.665	1973	.534		
curve 2					
1434	.417	1942	.379	2099	.346
1528	.405	1995	.378	2115	.341
1584	.397	2001	.369	2163	.336
1606	.392	2011	.362	2226	.323
1717	.362	2031	.367	2285	.318
1860	.347	2041	.361	2329	.310
1898	.365	2050	.362	2383	.312
1938	.375	2057	.361	2415	.312

Molybdenum

Temp	Emiss	Temp	Emiss	Temp	Emiss
1013	.458	1735	.396	1968	.377
1374	.449	1778	.388	1982	.372
1416	.438	1812	.385	2027	.370
1481	.430	1839	.385	2042	.373
1546	.419	1846	.382	2077	.373
1601	.415	1883	.380	2082	.372
1724	.398	1927	.380	2091	.372

Table 5.2. Emissivity data

Niobium
single crystal

Temp	Emiss		Temp	Emiss		Temp	Emiss
1589	.355		1936	.324		2217	.309
1731	.347		1985	.320		2310	.297
1777	.337		2057	.320		2331	.260
1848	.339		2065	.315		2365	.250
1857	.334		2136	.319		2407	.249

polycrystalline

Temp	Emiss		Temp	Emiss		Temp	Emiss
1476	.523		1758	.402		2086	.373
1580	.462		1772	.406		2088	.378
1669	.414		1848	.403		2148	.374
1708	.405		1914	.380		2206	.363
1728	.405						

Niobium-45% Iridium

Temp	Emiss		Temp	Emiss		Temp	Emiss
1431	.536		1698	.423		1817	.376
1515	.520		1788	.394		1827	.365
1601	.475		1799	.389		1887	.344
1641	.436		1809	.384		1916	.319

Iridium

Temp	Emiss		Temp	Emiss		Temp	Emiss
1526	.336		1639	.338		1845	.333
1614	.341		1822	.324		1933	.320

Hafnium

Temp	Emiss		Temp	Emiss		Temp	Emiss
1506	.450		1755	.381		1892	.392
1552	.400		1815	.372		1914	.382
1630	.383		1817	.374			

Table 5.2. Emissivity data (continued)

Hafnium-3% Zirconium

Temp	Emiss	Temp	Emiss	Temp	Emiss
1342	.465	1631	.450	1790	.333
1487	.478	1673	.439	1853	.296
1527	.471	1738	.411	1918	.269

Ruthenium

Temp	Emiss	Temp	Emiss	Temp	Emiss
1624	.333	1832	.297	1940	.307
1700	.334	1873	.299		

Table 5.2. Emissivity data (continued)

Figure 5.4 Tungsten

Figure 5.5 Tantalum
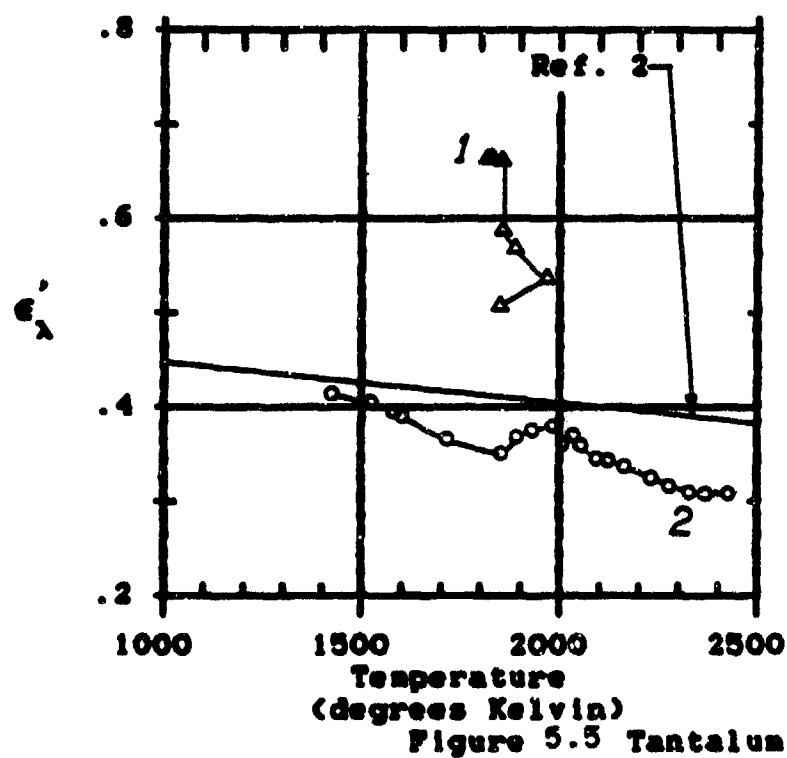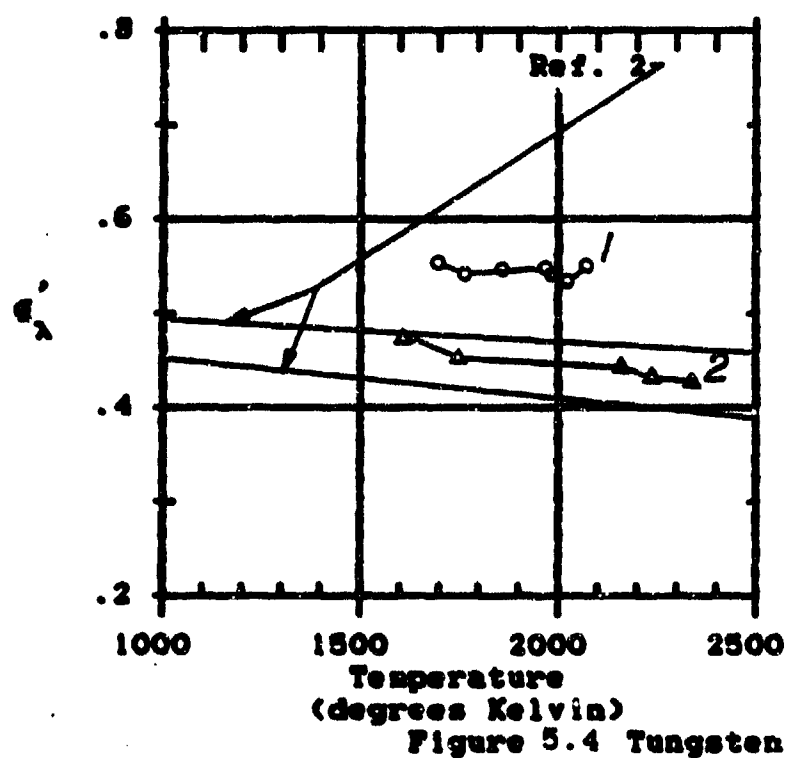
recrystallization temperature a definite annealing temperature cannot be defined. A guideline of 0.4 times the melting point of the material is used for evaluating these test results.

It appears that a linear relationship exists between the normal spectral emissivity of some materials and the temperature of the material. Dimitriev and Chistyakova [5.15] and Zhorov [5.22] have found relationships for the emissivity of a material as a function of temperature. Since the data collected here is linear in nature a least squares method of curve fitting is applied to each of the plots yielding the results in Table 5.2. Several of the materials were sampled over too small a temperature difference to provide a good line fit of the data (Ru, Nb-Ir, Hf, Hf-Zr). A future investigation in other wavelength bands could yield the same kind of results. L. K. Thomas at the Westinghouse R & D Center predicted the wavelength dependence of material emissivity based on the Fermi energy level of the material [5.6]. With his work and the theory set forth here, it may be possible to describe the emissivity of a material based only on the material properties and a known surface environment.

Ratanapupech and Bautista [5.4] determined an expression for the emissivity of a mixture of liquid metals in terms of the mole fractions and emissivities of the elements that compose the mixture. An attempt is made to find a similar expression for solid alloys. The results of the alloy measurements are in Fig. 5.7 and 5.8. There seems to be no relation at all between the emissivity of a solid alloy and the emissivities of the constituents. Instead the surface condition dominates the property of emissivity. The Nb, Ir plot is close to the Nb plot at low temperature, then it moves toward the Ir plot as the temperature rises. The melting point of the material was reached at a temperature reading of 2130° K (this alloy is
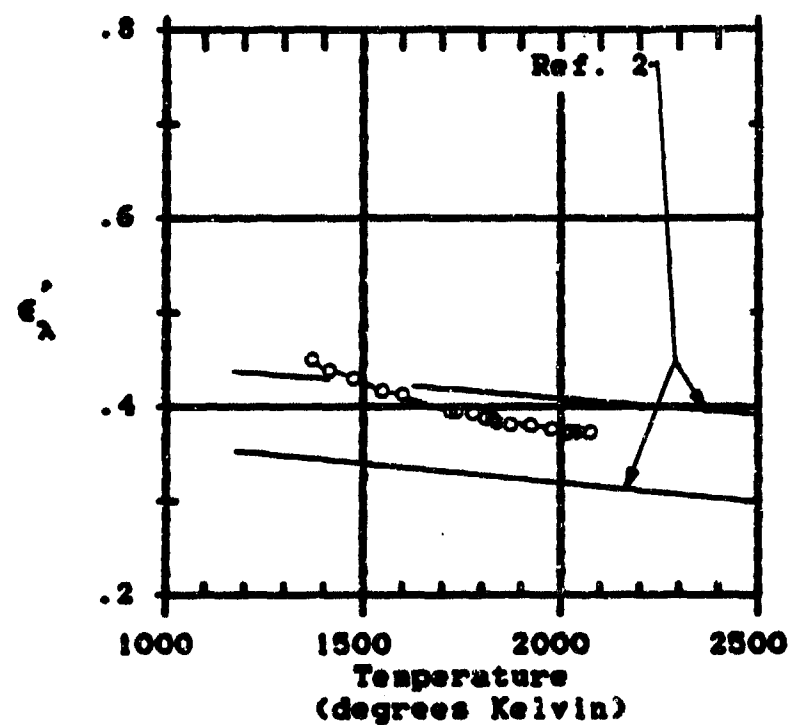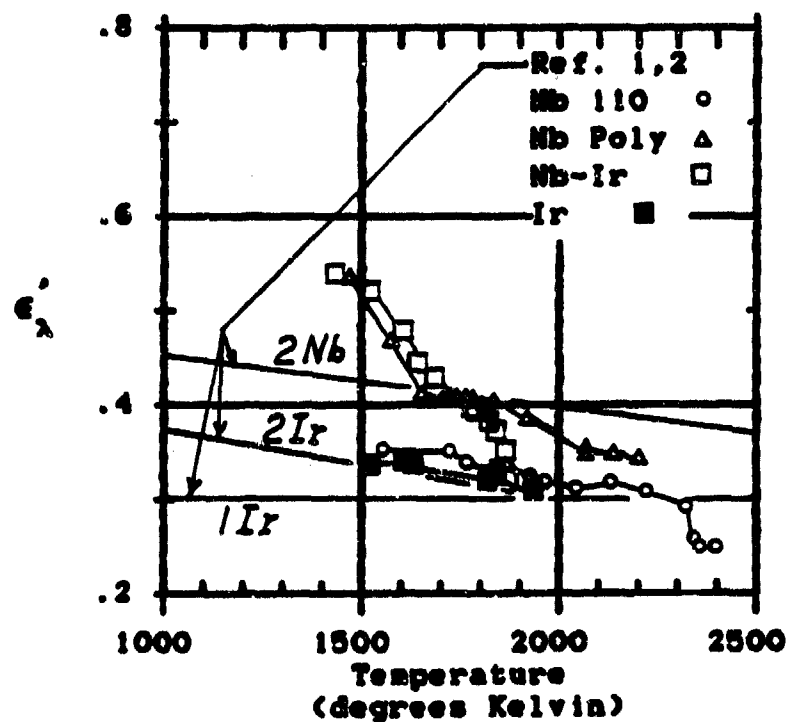
31

Figure 5.6 Molybdenum

Figure 5.7 Niobium, Iridium and Nb-46% Ir

a eutectic with a melting point of 2137° K). The Hf, Zr (Fig. 5.8) alloy showed a strong relationship to the emissivity plot of the Hf. This could be a function of the small percentage of Zr in this particular alloy. the comparison of the samples after testing revealed that the Hf and Hf,Zr have completely different microscopic surface conditions. Data published for other alloys (Mo-W, W-Re, W-Ta, W-Nb, Ta-Mo among others) also have no relationship to the properties of the base metals.

The relationship of the emissivity to the microscopic surface area is hampered because of problems in measurement of the surface roughness. Shestakov, et. al. [5.23] performed an analytical evaluation of the effect of the roughness on the emissivity but did not provide a solution for the measurement of the roughness itself. Neuer and Worner [5.17] performed a regular etching of steel surfaces using the electrical machining process. The analytical calculations of the emissivity of these samples closely followed the experimental results. These investigations show the possibility of calculating the emissivity based on surface condition. the relationship of the surface roughness to the emissivity did not appear in these tests. The surface roughness caused by a relatively rough polish does not prevail over the annealing effect.

The effect of the crystal orientation on the emissivity is explored by testing a Niobium single crystal at three different orientations. The measurements show less variation than the accuracy of the measurement process. However the difference between the single crystal and polycrystalline samples is surprising. Microscopic analysis reveals that the polycrystalline sample acquired numerous surface pits from the annealing process accounting for the higher emissivity values over the single crystal sample (Fig. 5.7).
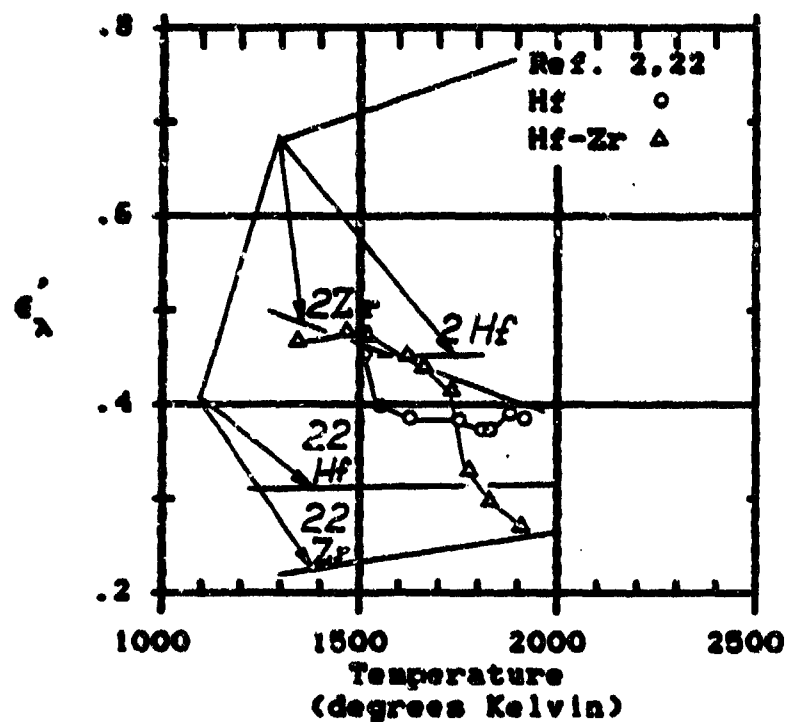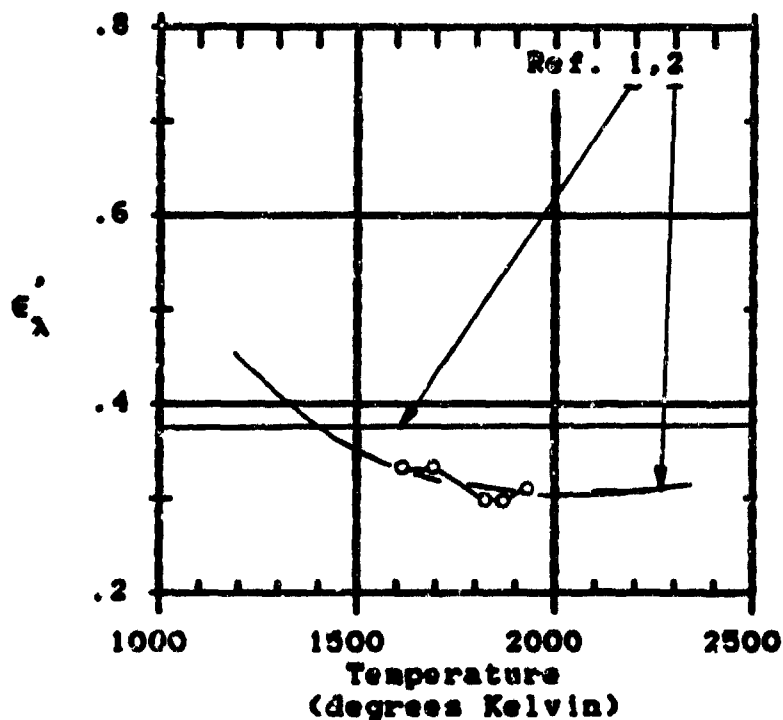
Figure 5.8 Hafnium and Hf-3% Zr

Figure 5.9 Ruthenium

5.7 CONCLUSIONS

The pulse counting pyrometer proved to be an excellent instrument for measuring the energy emitted by a material. The resulting data can be used to directly measure emitted energy rather than requiring inference from a measured temperature. Material properties which are based on an emitted energy can be calculated.

The emissivity of materials has been shown to be a strong function of the surface preparation with the temperature a weak function at any one wavelength. A possible expression for the emissivity as a function of temperature is given for some of the materials tested. The crystal orientation does not effect the material emissivity. However the difference between a single crystal structure and a polycrystalline structure does affect the emissivity. The emissivity of an alloy is not related to the constituents but is determined by the surface conditions. The annealing process and its effect on the emissivity is related to the grain structure of the material and the growth of the grains during heating. The normal spectral emissivities of hafnium, iridium, molybdenum, niobium, ruthenium, tantalum and tungsten, Hf, 3%-Zr and Nb,45%-Ir are recorded.

The determination of the emissivity from the material properties seems to be within grasp. Further study into the effect of the recrystallization temperature and the annealing process is necessary to accurately predict the transition point and the properties of a material before and after that point. The grain size and structure should be accurately measured during each step of the heating process. Then the prediction of the emissivity from the surface roughness may be made. The final product should be an accurate emissivity value of any desired metal at any temperature. The extension of this to the total and hemispherical emissivities also seems

possible. The end result would be a savings of many man hours of testing and research and would allow the pursuit of more meaning studies.

5.8 Appendix

Pulse Counting Pyrometer

The photon/pulse counting pyrometer was designed by Dr. E. K. Storms at Los Alamos National Laboratory [5.27]. It was designed to provide a very accurate and easy to use pyrometer for the laboratory. The device uses a photomultiplier to detect the thermal radiation emitted from a source. The electrical pulses produced by the photomultiplier are counted and compared to the number of pulses produced at a calibration temperature. The results is the temperature of the source. The detailed construction, calibration and operation of the pulse counting pyrometer is presented.
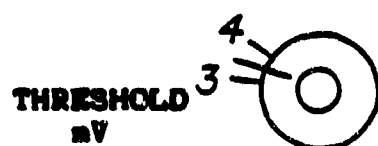
5.8.1 Construction

The first step in construction is obtaining a photomultiplier tube and housing assembly. The assembly used is a 9813B photomultiplier and a RFI/B-213F housing [5.28]. This assembly is mounted on a base plate of aluminum to allow the mounting of the optical assembly. The pyrometer is shown in Figure 5.10. The optical assembly is composed of an inexpensive camera lens (a), an interference filter (b), a nickel mirror (c), an eyepiece (d), and a neutral density filter assembly (e).

The camera lens may be of any variety. A fixed focal length model was used. The use of a variable focal length may be possible but has not been attempted. The lens is attached to an aluminum box with a bayonet mount. The aluminum box may be of any size and shape. The interference filter is mounted just behind the camera lens. The nickel mirror is mounted on a aluminum block at an angle of 45° to the incident radiation. A .1mm hole is drilled in the center of the mirror parallel to the incident radiation. The neutral density filter assembly is from a Northrup & Leeds optical pyrometer. It contains two filters and one opening without a filter. The

camera   interference   mirror   neutral   phototube
             filter   filters
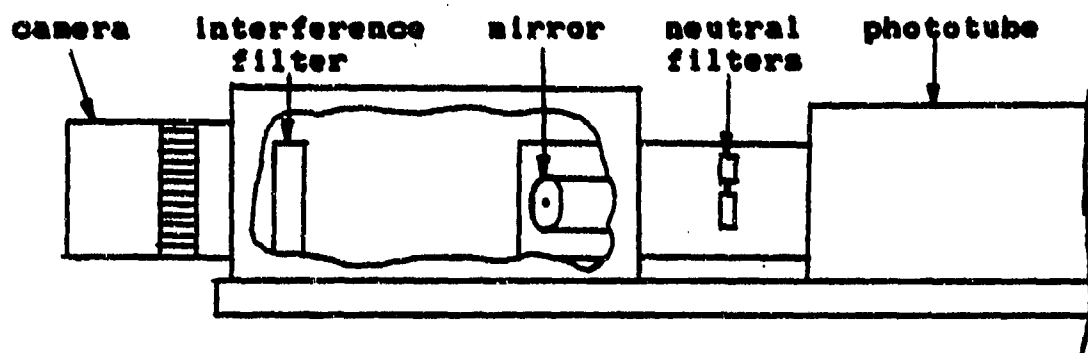
Discriminator-Amplifier Front Panel

SINGLE	WINDOW	CORRECT	PHA	PRESCALE

THRESHOLD   mV   ATHRESHOLD   mV

0.1	0.3	1.0	3.0	10.0

Figure 5.10   Pulse/Photon Couting Pyrometer

eyepiece is positioned at 90° to the incident radiation and is focused on the mirror.

The only critical alignment is in the positioning of the mirror and the camera lens on the center line of the photomultiplier. Care should be taken to keep all three components on the same axis. The distance of the mirror from the camera lens should be checked to insure the ability to focus an image onto the mirror at a distance of 15 to 25 cm from the camera lens. A 6 power eyepiece is used in this instrument and is more than adequate.

5.8.2 Theory of Operation

The operation of the pyrometer is broken down into three major sections. The optical section of the pyrometer is the selector section of the pyrometer, restricting the incoming thermal radiation to a single wavelength and sampling a small area of the source. Each portion of the optical section serves a specific purpose. The camera lens gathers the radiation emitted by the source. As the radiated beam enters the optical assembly the interference filter acts to admit only a specific wavelength of the radiation. The mirror positions an image of the source in the focal axis of the eyepiece for aiming the pyrometer. The aperature drilled in the mirror restricts the sampled portion of the source to a very small area. The exact area is determined by the distance the pyrometer is from the source. The neutral density filters attenuate the incoming radiation to a level that is within the linear operating range of the photomultiplier detector.

The detector section is the photomultiplier assembly. The photomultiplier works on the principle of photoemission and secondary-electron emission in order to detect very low levels of light [5.29]. The incoming thermal radiation strikes the photocathode at the front of the

photomultiplier tube. The photoelectric emission in the photocathode material send electrons into the photomultiplier tube. The number of electrons released is proportional to the energy of the incoming radiation. The electrons are accelerated and focused onto a dynode. This material will emit two or more electrons for each incident electron. These secondary electrons are again accelerated and focused onto another dynode providing another level of aplification. Several of these stages may be placed in a photomultiplier resulting in an amplification of several orders of magnitude. The acceleration of the electrons and the operation of the dynodes are powered by an excitation voltage supplied external to the tube. The focusing apparatus in this device is performed by the permanent magnets mounted in the phototube housing.

The signal processing section is composed of a Princeton Applied Research Model 1121 Discriminator-Amplifier [5.30] and a Hewlett-Packard Model 5308 Timer-Counter [5.31]. The signal produced by the photomultiplier is routed to the discriminator-amplifier. The discriminator produces and output pulse based on the signal from the photomultiplier. The threshold level and count mode may be selected from the front panel. The threshold level sets the minimum signal level that will be processed by the discriminator. A threshold difference level may also be set that controls a second threshold level. The count mode may be one of three selections. the SINGLE count position provides a single output pulse for each input that exceeds the low threshold level. The WINDOW count position produces an output pulse only if the incoming signal is between the high and low threshold levels. The CORRECT count position produces a single output pulse for each input signal that is between the high and low threshold levels,

and, produces two output pulses for any input signal that is above the high threshold level.

The output signal from the discriminator-amplifier is input to the timer-counter. This device is operated as a frequency counter providing an output that is the number of counts per second. Any type of frequency counter may be used. The Hewlett-Packard 5308 was chosen because of the standard interface connection and the ability to use it in other systems. A Hewlett-Packard printer is connected via the interface providing a hard copy of the pyrometer measurements.

5.8.3 Calibration

A pyrometer is only as good as the calibration. For this reason the pulse counting pyrometer was transported to Los Alamos National Laboratory and the laboratory of Dr. E. K. Storms for calibration. Dr. Storms operates a copper furnace specifically for calibration of his two photon counting pyrometers [5.27].

The initial step in calibration was to determine the operation parameters that would provide the most linear operation over the widest temperature range. This was a trial and error process using a tungsten strip lamp and an adjustable power supply for the photomultiplier excitation voltage. The reading of the pyrometer was plotted against the strip lamp temperature. This process was repeated for each excitation voltage, threshold level, threshold difference level and count mode. The most linear operating mode was obtained at the following settings:

Excitation voltage	1400V
Threshold	0.975mV
Threshold difference	0.300mV
Count Mode	CORRECT

The next step was the actual calibration. The pyrometer was aimed at the copper furnace and connected to a computer. The computer recorded and plotted each reading of the pyrometer. The copper furnace was turned on. When the copper began to melt the plot of the pyrometer readings leveled off indicating the phase change of the copper. When the phase change was complete the pyrometer readings again increased indicating the completion of the phase change. The power to the furnace was turned off. The readings again leveled off during the phase change of the copper. When the phase change was complete the process was halted. The entire sequence required a period of three hours. The start and end points of each of the phase changes were designated and the computer calculated the average pyrometer reading at the calibration temperature.

The last step in the calibration was the determination of the dead time of the photomultiplier and the attenuation of each of the neutral density filters. The dead time of the photomultiplier is the recovery rate of the detector within the photomultiplier tube. The detector has a certain recovery time during which it will not detect an impacting electron. The dead time is a value that corrects for this characteristic behavior.

The process requires an adjustable temperature source, in this case a tungsten strip lamp. The pyrometer count rate is measured without a filter in place. At the same temperature a new measurement is made with a filter in the light path. The process is repeated for each filter and for a series of temperature. A plot of the ratio of the count rates versus the count rate without the filter is made. A least squares curve fit is used to relate the measurements to the expression

$$R_I/R_{I+1} = A_{I+1} + R_I \, \gamma \, (A_{I+1}^{-1}) \tag{9}$$

I indicates the filter number. Two filters are used in this instrument with a third position without a filter. 0 was designated the measurement without a filter, 1 for the first filter and 2 for the second filter.

The plot of the two sets of data points is in Figure 5.11. Also shown is the line fitted to equation 3. The resulting dead time is an average of the values calculated for each filter. The attenuation of the pyrex bell jar is used as the attenuation of the 0 filter position. The attenuation values and dead time for this instrument are:

```
Dead time          1.1044E-7  1/sec
Attenuation 0      1.0607
Attenuation 1      4.7780
Attenuation 2      98.6840
```

The calibration measurement is corrected for dead time (Eqn. 6) and used in the expression for determining the temperature of other pyrometer measurements (Eqn. 7).

This completes the details of the pulse/photon counting pyrometer. Dr. Storms has used two of these instruments for over five years without difficulty. The calibration has proven to be good for at least a three year period. The dead time and attenuation calculations are repeated about every six months. The long term drift in calibration is better than 1° K. The reproducibility of a temperature measurement is better than ±0.2° K. The accuracy of the instrument is better than 1° K based on gold furnace measurements [5.27].
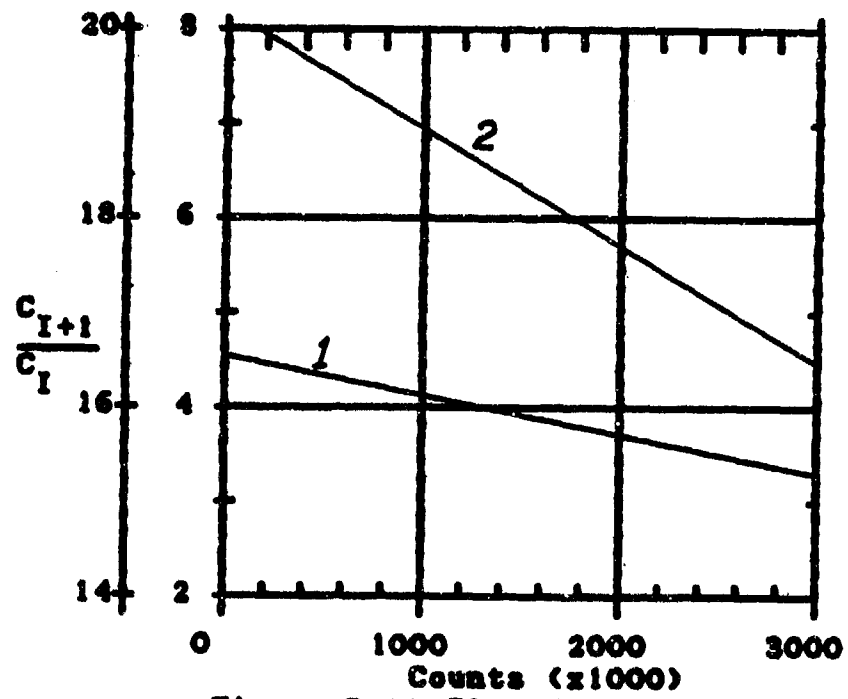
Figure 5.11 Plot for calculation of dead time

5.9 REFERENCES

5.1 Gubareff, G. G., J. E. Janssen and R. H. Torburg: "Thermal Radiation Properties Survey," 2d ed., Honeywell Research Center, Minneapolis, Minn, 1960.

5.2 Touloukian, Y. S. and D. P. DeWitt: "Thermophysical Properties of Matter," Vol. 7,8,9 – Thermal Radiative Properties, New York IFI Plenum, 1970.

5.3 Kenisarin, M. M.: Transfer of the IPTS Above 2000K, High Temperature-High Pressure, vol. 8, no. 4, pp. 367-376.

5.4 Ratanapupech, P. and R. G. Bautistia: Normal Spectral Emissivities of Liquid Iron, Liquid Nickel, and Liquid Iron-Nickel Alloys, High Temperature Science, vol. 14, pg. 269, 1981.

5.5 Dimitriev, V. D. and I. G. Chistyakova: Analytic Dependence of the Spectral Emissivity of Tantalum on Wavelength and Temperature, High Temperature, vol. 18, pp. 742-746.

5.6 Thomas, L. K.: The Thermal Radiation of Tungsten Alloys at Temperatures Up to 3000° K, Westinghouse Research and Development Center, Pittsburgh, Pennsylvania.

5.7 Branstetter, J. R. and R. D. Schaal: Thermal Emittance Behavior of Small Cavities Located on Refractory Metal Surface, NASA TM X-52147, Oct 1965.

5.8 Foley, G. M.: High Speed Optical Pyrometer, Review of Scientific Instruments, vol. 41, no. 6, pp. 827-834, 1970.

5.9 Ruffino, G.: High-Speed Radiation Pyrometry, High Temperatures-High Pressures, vol. 8, pp. 143-154, 1976.

5.10 Jones, T. P. and J. Tapping: A Precision Photoelectric Pyrometer for the Realization of the IPTS-68 above 1064.43° C, Metrologica, vol. 18, pp. 23-31, 1982.

5.11 Righini, F., A. Rosso and G. Ruffino: System for Fast High-Temperature Measurement, High Temperature-High Pressure, vol. 4, no. 5, pp. 597-603, 1972.

5.12 Storms, E. K. and B. A. Mueller: A Very accurate Pyrometer for General Laboratory Use, Natl. Bur. Std. Sp. Pub. 561, Oct 1979, pg. 143.

5.13 Manufactured by Princeton Applied Research Corp., P. O. box 2565, Princeton, NJ 08540.

5.14 Manufactured by Hewlett-Packard, 1820 Embarcadero Rd., Palo Alto, CA 94303.

5.15 Shur, B. A. and V. E. Peletskii: Emissivity of Titanium Iodide and Technical-Grade Titanium in the Temperature Interval 1100-1900° K, High Temperature, vol. 19, Nov-Dec 1981, pg. 841.

5.16 Manufactured by Hipotronics, Inc., Brewster, NY.

5.17 Neuer, G. and B. Worner: Influence of Surface Properties on the Total Emittance of Steel, "Proceedings of the Seventh Symposium on Thermophysical Properties," 1977, pp. 250-255.

5.18 Jones, T. P. and J. Tapping: The Freezing Point of Platinum, Metrologia, vol. 12, pp. 19-26.

5.19 Ruffino, G.: Primary Temperature Measurement Above the Gold Standard, High Temperature-High Pressure, vol. 12, no. 3, pp. 241-246, 1980.

5.20 Ohwada, Y.: Evaluation of the Integrated Emissivity of a Black Body, Japanese Journal of Applied Optics, vol. 23, no. 3, pp. 1167-1168, 1984.

5.21 Ohwada, Y.: Evaluation of Effective Emissivities of Nonisothermal Cavities, Applied Optics, vol. 22, no. 15, pp. 2322-2325, 1983.

5.22 Zhorov, G. A.: Emissivity of Metals of the 4B Subgroup at High Temperature, High Temperature, vol. 8, no. 3, pp. 501-504, 1970.

5.23 Shestakov, E. N., V. S. Stolbov, L. N. Latyev, and V. Ya. Chekhovskoi: Emittance of Rough Surfaces, "Proceedings of the Seventh Symposium on Thermophysical Properties," pp. 279-284, 1977.

5.24 Siegel, R. G. and B. A. Howell: "Thermal Radiation Heat Transfer," Hemisphere Publishing Corp., Washington, D. C., 1981.

5.25 Sparrow, E. M. and R. C. Cess: "Radiation Heat Transfer," Augmented Edition, Hemisphere Publishing Corp., Washington, D. C., 1978.

5.26 Goldsmith, A., T. E. Waterman and H. J. Hirschhorn, "Handbook of Thermophysical Properties of Solid Materials," Vol. I - Elements, Pergamon Press, New York, 1961.

5.27 E. K. Storms and B. A. Mueller: A Very Accurate Pyrometer for General Laboratory Use, Natl. Bur. Std. Sp Pub 561, Oct 1979.

5.28 Available fromm Gencom Division/Emitronics, Inc., 80 Express St., Plainview, NY 11803

5.29 Susskind, C.: "The Encyclopedia of Electronics," pp. 599-604, Reinhold Publishing Corp., New York, 1962.

5.30 Manufactured by Princeton Applied Research Corp., P. O. box 2565, Princeton, NJ 08540.

5.31 Manufactured by Hewlett-Packard, 1820 Embarcadero Rd., Palo Alto, CA 94303.

VI. Mass Spectrometer Solid Probe

6.1 Abstract

The proposed solid probe design uses induction heating to sublime refractory metal samples to be analyzed in a quadruple mass spectrometer. A copper induction coil is used to induce a high frequency, alternating current into the sample material. A tantalum tube, holding the sample, ha a 0.050 inch orifice in the end of it to ensure the ionizer is not flooded with sample molecules. Ceramic insulators are used to thermally and electrically insulate both the tantalum tube and copper tubing from the body of the probe. Besides the high frequency, (radio frequency) a generator provides cooling water, run through the copper tubing.

6.2 INTRODUCTION

This project involves the design of a solid heating probe for the mass spectrometer in the thermionics lab at Arizona State University. Before a solid probe design could be generated, a complete understanding of the mass spectrometer and the function of the probe was necessary. Factors, such as the high vacuum and cleanliness requirements were experimented with in the lab. They theory behind the mass spectrometer and induction heating was studied, so an effective design could be implemented. The following design constraints were used in the solid probe design. The function of the mass spectrometer is to analyze surface composition of refractory metals and high temperature alloys. This means a temperature requirement of approximately 2000 C to 3000 C is necessary. The probe must vaporize the materials, by sublimination, in a high vacuumed chamber. The probe must have a two and three quarters inch flange attachment for interfacing with the mass spectrometer. Lastly, the probe must not introduce contamination resulting from foreign matter or vacuum leaks in the chamber of the mass spectrometer.

6.3 THEORY OF THE MASS SPECTROMETER

The mass spectrometer is a device for analyzing material composition by measuring the mass of ionized atoms. There are several different types of mass spectrometers, but the one in the thermionics lab is a quadrupole mass spectrometer. It consists of three separate parts; the ionizer, the mass filter and the detector plate. All of these components are contained in a chamber at low pressure (high vacuum). The following process describes the analysis of a sample.

The sample is placed in the tantalum tube of the solid probe and the probe is attached to the flange on the mass spectrometer. The primary pump is started to initiate a vacuum in the chamber. Once a pressure of 10^{-3}

torr is achieved, the turbo-pump increases the vacuum to as low as 10^{-6} torr. The sample is then heated and sublimed by the solid probe. A fine stream of sample molecules leave through the orifice at the end of the tantalum tube and enter the ionizer. A stream of electrons bombard the gaseous molecules producing positively charged parent ions and fragment ions. A series of lenses in the ionizer collimate the cloud of sample molecules toward the mass filter.

The quadrupole mass filter is composed of four cylindrical rods, arranged parallel and symmetrical with one another, with opposite rods electrically connected (Fig. 6.1). A radio frequency and direct current voltage, of equal potential but opposite charge, is applied to each set of rods. A stream of ions with a given m/z (mass-to-charge) ratio can be transmitted through the quadrupole filter and all other ions stopped, by varying the absolute potential applied to the rods. The ions transmitted trough the filter are said to be in stable orbits, while the ions absorbed or deflected by the quadrupoles are said to be in unstable orbits.

Finally, the ions flowing down the quadrupole in stable orbits strike the collector plate (Faraday plate) and the signal is multiplied and displayed on the oscilloscope. A spectrum of signal intensity versus m/z value can be obtained from the oscilloscope screen (Fig. 6.2).

6.4 Contamination of the Mass Spectrometer

In order to obtain accurate results from the mass spectrometer, the mass spectrometer chamber must be kept free from all contamination. Contamination can result from foreign matter, such as oil fom a human hand, and/or vacuum leaks.

Since the solid probe interfaces directly with the chamber, the possibility of contamination must be taken into consideration. Every part
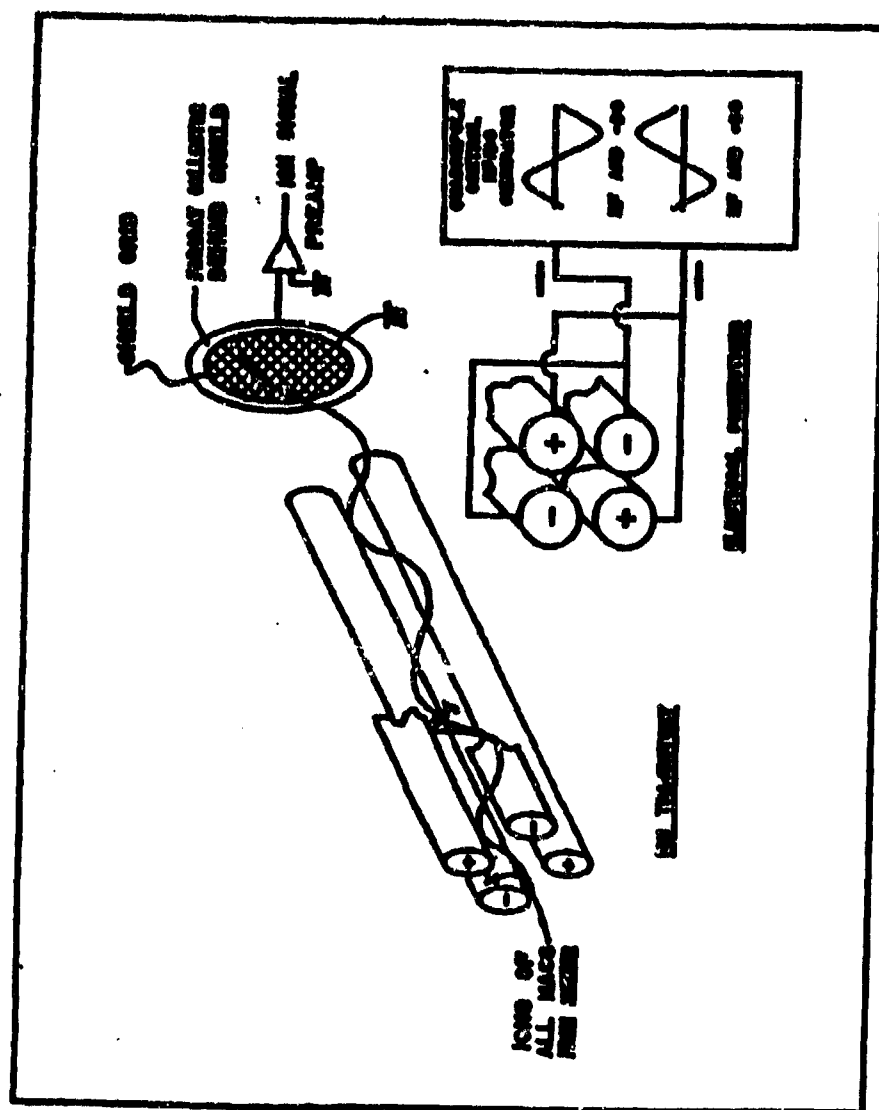
Fig. 6.2 Signal intensity versus m/z value.

Fig. 6.1 Quadrupole mass spectrometer wiring and configuration diagram.
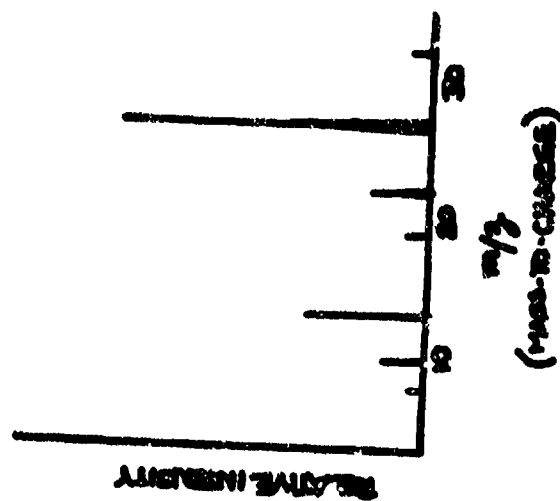
of the solid probe must be cleaned thoroughly, to ensure no residues (unwanted oxides) are left on the part's surface. For each material used in the solid probe, including the sample, an appropriate cleaning procedure must be used.

While working in the thermionics lab, several cleaning processes and spot welding techniques were demonstrated by graduate student Derek Tang. This instruction included the cleaning of tungsten electrode rods and the fabrication of collectors and emitters used in a Marchuk tube. The cleaning procedures for tungsten and tantalum are given on the following page. Most metal cleaning processes are similar to that of tungsten and tantalum are given on the following page. Most metal cleaning processes are similar to that of tungsten and tantalum, differing only in the type of cleaning agent used.

Beside "surface residues," contamination can occur form vacuum leakage. When the probe is attached to the mass spectrometer, a copper "O-ring" must be placed between the probe and mass spectrometer flanges to provide the proper seal against leakage. Vacuum is necessary because the mass spectrometer either predicts the trajectory or measures the time flight on an ion. Without vacuum, neither function could be accomplished because of scattered collisions from unmeasured molecules.

Chemical Cleaning Procedures

I. Tungsten

1. General oakite cleaning procedure

2. Boil in sodium hydroxide bath for approx. 20 minutes

3. Rinse in distilled water

4. Ultrasonic in distilled water for 30 seconds

5. Hot air dry

6. Store in plastic bag

II. Oakite

1 - part powdered oakite

8 - parts distilled water

Stir and partially dissolve oakite in cold water, then heat to 80 C and use at that temperature. Place parts to be cleaned in oakite.

III. Tantalum

1. General oakite cleaning procedure

2. Boil in hydrochloric acid for 15 minutes

3. Rinse with distilled water

4. Rinse in two baths of boiling distilled water

5. Ultrasonic in alcohol for 30 seconds

6. Hot air dry

7. Wrap in lint free, sulphur free paper

8. Store in a plastic bag

6.5 INDUCTION HEATING

Induction heating is the heating of an electrically conducting material by eddy currents induced by a varying electro-magnetic field. The induction heater principle is similar to that of a transformer. The copper coil can be considered the primary winding and the tantalum tube, a single wind secondary. When a high-frequency, alternating current flows in the primary coil, secondary currents (eddy currents) will be induced in the material. Since the current flowing in the sample material is a summation of the eddy currents induced, the copper coil is wrapped closely around the tantalum tube. This ensures maximum induced eddy currents and therefore, high heating rates.

The advantages of induction heating over conventional heating processes are; the heating is very rapid because the heating is induced directly into the material. The heating is localized and heating area easily controlled by the size and shape of the inductor coil. Because of the generator, the heating is easily controllable. It lends itself to automation, in-line processing, and automatic-process cycle control. The start-up time is short and the working conditions are favorable because of the absence of noise, fumes, and radiated heat.

The induced currents in the sample material decrease exponentially from the surface toward the center of the material being heated. Since the heating is maximum at the surface, and the mass spectrometer will be used for surface composition analysis, induction heating lends itself as the most effective method of heating. With induction heating the heat is generated by the current flowing through the material's own resistivity.

6.6 Solid Probe Design

The final design of the solid probe incorporates induction heating to vaporize solid samples at a temperature of approximately 2000 C to 3000 C. The induction coil, made of copper, carries radio frequency and induces current directly into the sample material. Cooling water is run through the copper tubing to minimize the effects of radiation. a generator provides both the radio frequency and cooling water to the solid probe. the tube holding the sample is made of tantalum and has a 0.050 inch orifice in the end of it. The probe flange and body are made of stainless steel. The flange is a standard two and three quarters inch flange. Ceramic insulators are used to thermally and electrically insulate the base of the tantalum tube and the copper tubing from the body of the solid probe. The probe and a schematic of its relationship with the mass spectrometer are shown in Figs. 6.3, 6.4, and 6.5.

6.7 DESIGN RATIONALE

Of the three basic types of heating methods; induction heating, resistive heating and electron bombardment, induction heating was chosen because of the geometry of the application. The induction heating probe is a self-contained unit that has the capability of heating a sample to the very high temperature requirement (2000 C to 3000 C).

Furthermore, induction heating was chosen for the probe because of it's advantages previously stated, such as; extremely high heating rates, easily controllable heating, short start-up time, and absence of fumes and radiated heat.

Copper tubing is used for the induction coil because of it's high electrical conductivity. The sample holding tube is made of tantalum because of it's capability to withstand high temperatures and ease of
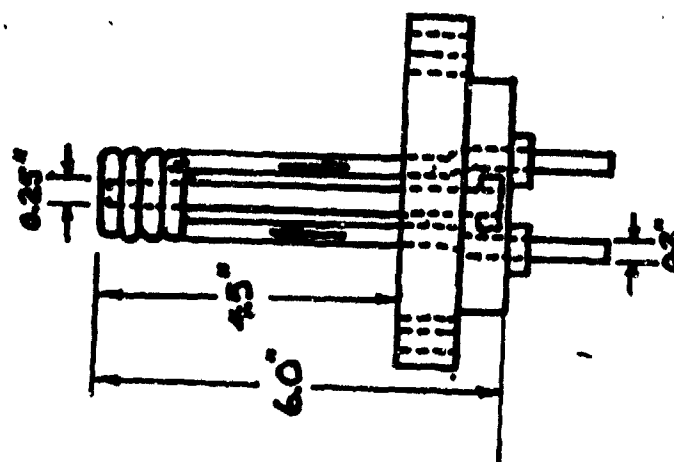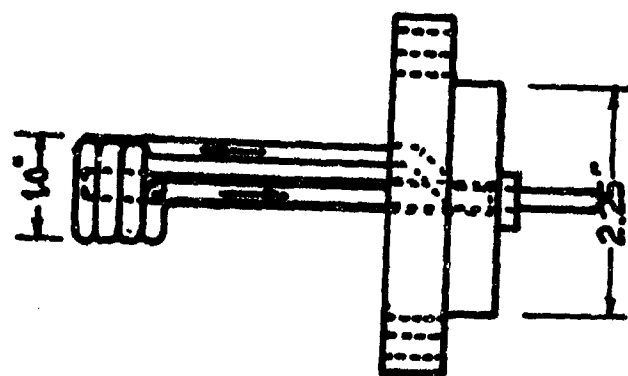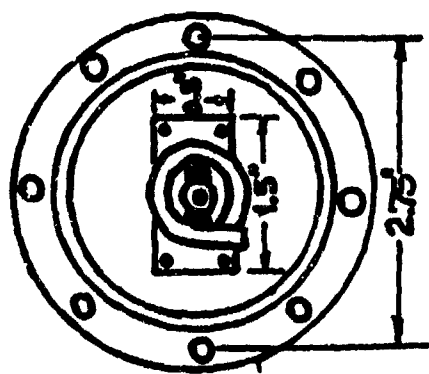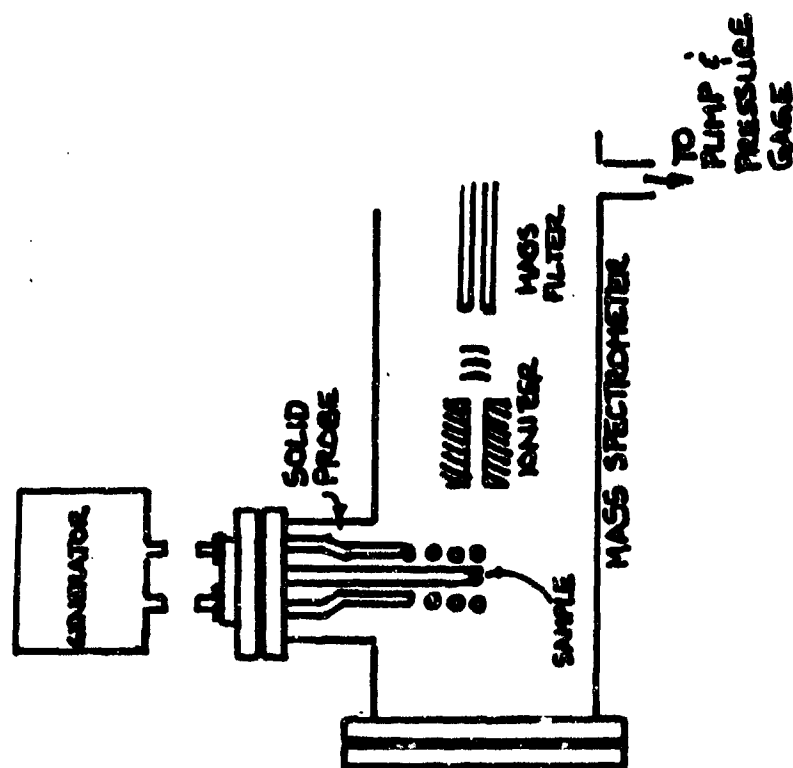
Fig. 6.3 Orthographic views of the solid probe.

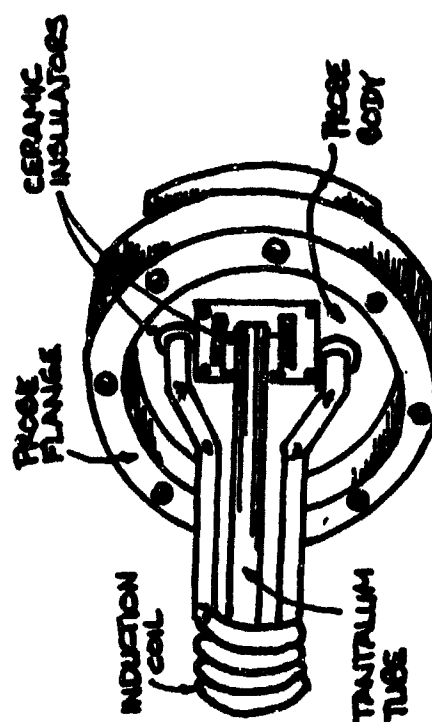Fig. 6.5 Schematic of solid probe in the mass spectrometer.

Fig. 6.4 Perspective view of solid probe.

machining. A small orifice (0.050 inch) is drilled in the end of the tantalum tube to permit only a small stream of sample molecules to enter the ionizer. This is important because the ionizer must not be flooded with sample molecules.

Because of it's ability to both thermally and electrically insulate, ceramic is chosen for insulation between the base of the tantalum tube and the body of the probe. The ceramic insulators are also employed between the copper tubing and the body of the probe.

The copper induction coil is wound only at the end of the tantalum tube to localize the heating at the sample location in the tube. The spacing between the copper coil and tantalum tube is close to ensure maximum induced eddy currents and therefore, high heating rates. The induction coil and sample holding tube extend approximately six inches into the mass spectrometer chamber to allow the heating to take place directly in front of the ionizer.

6.8 CONCLUSION

The objective of this project was to develop a design for a solid probe to interface with the mass spectrometer in the thermionics lab. to initiate the design procedure for the probe, the method of heating had to be chosen. Induction heating was chosen because of it's advantages in this application. The configuration of the probe was then generated and the materials chosen.

6.6 REFERENCE

6.1 J. R. Branstetter & R. D. Schaal, "NASA Technical Memorandum: Thermal "Emittance of Small Cavities Located on Refractory Metal Surfaces," Lewis Research Center, Cleveland, Ohio.

6.2 "Probe for Direct Exposure of Solid Samples in a Ionization Mass Spec.," Analytical Chemistry, Vol. 51, No. 2, February 1979, pages 316-318.

6.3 Extranuclear manual on the mass spectrometer.

6.4 "Simple Ion Probe Attachment for Existing Mass Spectrometer," Analytical Chemistry, Vol. 10, No. 14, December 1974, pages 172,173.